2014

Grid integration of solar photovoltaic resources: impact analysis and mitigation strategies

Md Jan-E Alam
University of Wollongong

GRID INTEGRATION OF SOLAR PHOTOVOLTAIC RESOURCES: IMPACT ANALYSIS AND MITIGATION STRATEGIES

A Thesis Submitted in (Partial) Fulfilment
of the Requirements for the Award of the Degree

DOCTOR OF PHILOSOPHY

from

UNIVERSITY OF WOLLONGONG

by

MD. JAN-E-ALAM, M SC (EEE)
School of Electrical Computer and Telecommunications Engineering
Faculty of Engineering and Information Sciences
2014

CERTIFICATION

I, Md. Jan-E-Alam, declare that this thesis, submitted in partial fulfilment of the requirements for the award of Doctor of Philosophy, in the School of Electrical Computer and Telecommunications Engineering, Faculty of Engineering and Information Sciences, University of Wollongong, is wholly my own work unless otherwise referenced or acknowledged. The document has not been submitted for qualifications at any other academic institution.

Md. Jan-E-Alam

15th May, 2014

DECLARATION OF PUBLICATIONS

This thesis includes chapters that have been written as the following journal articles:

Chapter 2:

M. J. E. Alam, K. M. Muttaqi, and D. Sutanto, "A Three-Phase Power Flow Approach for Integrated 3-Wire MV and 4-Wire Multigrounded LV Networks with Rooftop Solar PV," *IEEE Transactions on Power Systems*, Vol. 28, No. 2, pp. 1728-1737, May 2013.

Chapter 3:

M. J. E. Alam, K. M. Muttaqi, and D. Sutanto, "A SAX-Based Advanced Computational Tool for Assessment of Clustered Rooftop Solar PV Impacts on LV and MV Networks in Smart Grid," *IEEE Transactions on Smart Grid*, Vol. 4, No. 1, pp. 577-585, March 2013.

Chapter 4:

M. J. E. Alam, K. M. Muttaqi, and D. Sutanto, "An Approach for On-line Assessment of Rooftop Solar PV Impacts on Low Voltage Distribution Networks," *IEEE Transactions on Sustainable Energy*, Vol. 5, No. 2, pp. 663 - 672, April 2014.

Chapter 5:

M. J. E. Alam, K. M. Muttaqi, and D. Sutanto, "A Versatile Volt-VAr Control Strategy for Solar PV Inverters to Support Distribution Networks while Mitigating Voltage rise at Mid-day and Voltage Fluctuations during Passing Clouds," under 2nd review by the *IEEE Transactions on Power Systems*, manuscript ID: TPWRS-01537-2013.R1.

Chapter 6:

M. J. E. Alam, K. M. Muttaqi, and D. Sutanto, "Mitigation of Rooftop Solar PV Impacts and Evening Peak Support by Managing Available Capacity of Distributed Energy Storage Systems," *IEEE Transactions on Power Systems*, Vol. 28, No. 4, pp. 3874-3884, November 2013.

Chapter 7:

M. J. E. Alam, K. M. Muttaqi, and D. Sutanto, "A Novel Approach for Ramp-rate Control of Solar PV Using Energy Storage to Mitigate Output Fluctuations Caused by Cloud Passing," accepted for a future issue of the *IEEE Transactions on Energy Conversion*, Digital Object Identifier 10.1109/TEC.2014.2304951.

Chapter 8:

M. J. E. Alam, K. M. Muttaqi, and D. Sutanto, "Mitigation of Neutral Current and Neutral Potential Rise in 4-wire Multi-grounded LV Networks under Unbalanced Allocation of Rooftop Solar PV Using Distributed Storage," submitted to the *IEEE Transactions on Power Systems*, manuscript ID: TPWRS-00657-2014.

M. J. E. Alam, K. M. Muttaqi, and D. Sutanto, "Community Energy Storage for Mitigation of Neutral Current and Neutral Potential Rise in 4-wire Multi-grounded LV Networks under Unbalanced Allocation of Rooftop Solar PV," under preparation for submission to the *IEEE Transactions on Smart Grid.*

As the primary supervisor, I, A/Prof. Kashem M. Muttaqi, declare that the greater part of the work in each article listed above is attributed to the candidate, Md. Jan-E-Alam. In each of the above manuscripts, the candidate contributed to development of the main idea or concept, which has been extended, refined and tuned for improvement with advice from myself and his co-supervisor Prof. Danny Sutanto, both contributing as co-authors. The candidate has prepared the first draft of each of the manuscripts and revised those according to the suggestions provided by the supervisors. The candidate has been responsible for submitting each of the manuscripts for publication to the relevant journals, and he has been in charge of responding to the reviewers' comments, with assistance from his co-authors.

Md. Jan-E-Alam	A/Prof. Kashem M. Muttaqi
Candidate	Principal Supervisor
15th May, 2014	15th May, 2014

ACKNOWLEDGEMENT

I would like to gratefully acknowledge the guidance and support provided by my supervisors A/Prof. Kashem M. Muttaqi and Prof. Danny Sutanto in conducting the research works presented in this thesis. In addition, I would like to appreciate the support of the Australian Power Quality and Reliability Centre technical staff members, especially the assistance of Mr. Sean Elphick. The supports of the Australian Research Council (ARC) and Essential Energy, NSW, Australia, under the linkage project grant are also acknowledged.

KEYWORDS

Solar Photovoltaic (PV)

Distribution Networks

Low Voltage Multigorunded Network

Medium Voltage Network

Voltage Regulator

3-Wire / 4-Wire

Voltage Rise

Reverse Power Flow

Neutral Current

Neutral Potential Rise

Reactive Power Control

Battery Energy Storage

Distributed Energy Storage

Community Energy storage

Charging/Discharging

State of Charge

Ramp-rate

Dynamic Model

ABSTRACT

There is already strong evidence that rooftop solar photovoltaic (PV) units at low voltage (LV) distribution networks are creating major impacts on the operation of the electricity networks, both at the low and medium voltage (MV) levels. With the proliferation of solar PV penetration, LV distribution grids are experiencing the issues of reverse power flow and voltage rise. As a result, the hosting capacities of many distribution feeders are already close to their maximum limit. This prompts many utilities to impose a barrier to the installation of new solar PV units at the LV distribution level and to reduce the PV size allocated for household. In addition, fluctuations in PV power output due to passing clouds can result in significant voltage fluctuation, especially in weak distribution grids. With an unbalanced allocation of single phase PV units, 4-wire LV distribution networks can experience an increase of neutral current and therefore the neutral potential (or neutral-to-ground voltage) can exceed the acceptable limit.

In the context of the problems outlined above, an accurate assessment of the impact of solar PV on distribution networks is becoming necessary so that effective mitigation actions can be taken, and the PV penetration level can be increased. With such a background, this thesis aims at: developing a comprehensive and realistic assessment approach for the impact of solar PV on distribution networks, analysing the impact using the developed approach in real network environment with smart grid measurements, and proposing mitigation strategies for the particular problems identified above.

First, this thesis has developed a comprehensive modelling and analysis approach for integrated medium voltage (MV) and multigrounded low voltage (LV) distribution networks for an accurate assessment of solar PV impact. Using this approach, PV integrated networks can be modelled by retaining their wiring configurations, such as 3-wire configurations for MV networks and 4-wire configurations for LV networks, including the delta-wye transformers and neutral grounding impedances in the LV networks. The three-phase modelling capabilities cater for load and network unbalances and asymmetries. A voltage dependent load modelling approach has been adopted. Capabilities have been incorporated to model solar PV resources based on PV panel *I-V* characteristics using PV panel parameters, inverter efficiency, irradiance and ambient

temperature data. With such a detailed modelling capability, this approach is able to provide an accurate assessment of solar PV impact on the LV and upstream MV networks compared to other methods where such details are not considered.

An intelligent approach has been developed to analyse solar PV impact with a proposed power flow approach using smart grid measurements in a computationally efficient manner. A time series approximation technique in combination with data-mining techniques has been proposed for extraction of the dataset that is more effective for PV impact analysis from a large volume of smart-grid measurements.

An on-line approach has been proposed to assess the PV impact using real-time models of distribution networks constructed using on-line network data so that a more accurate analysis of the impact could be performed under the varying load and network conditions. In addition, a dynamic type "what-if" analysis feature has been proposed to investigate the network behaviour in a potential PV generation scenario and also to understand the effectiveness of a prospective mitigation action.

This thesis has proposed new mitigation strategies against the particular PV impacts identified.

A versatile reactive power control strategy has been proposed in this thesis that is suitable to provide appropriate network support under various conditions associated with PV power generation. In addition to a dynamic reactive power compensation for voltage support during low or no PV period, the proposed strategy is able to mitigate voltage rise during excess PV generation period using a reverse power flow based droop characteristic, and to provide a fast and appropriate reactive power support using a ramp-rate based approach for voltage fluctuation mitigation during cloud passing.

To effectively utilise limited capacities of energy storage devices for PV impact mitigation and evening peak load support, a new charging/discharging control strategy has been developed in this thesis. Unlike the traditional constant rate strategy, the proposed strategy can control the shape of the charging/discharging profile to ensure an effective use of the storage capacity. The charging rate is also adjusted dynamically to consider the effect of unstable weather conditions to ensure that the available capacity is exploited wisely.

This thesis has proposed a new strategy where the PV inverter ramp-rate can be controlled to a desired level by deploying energy storage. Traditionally, energy storage devices are used to smooth PV output fluctuations using moving average control. However, moving average does not control the ramp-rate directly; rather the ramp-rate depends on previous values of the PV output. According to the proposed strategy, the desired ramp-rate during the ramping event is governed by controlling the energy storage based on an inverse relationship with the PV panel output ramp-rate to improve the fluctuation mitigation performance. In contrast to the moving average method, the proposed strategy is able to control the desired ramp-rate, independent of the past history of the PV panel output, and therefore a storage device is operated for a comparatively small amount of time.

Finally, in the context of exacerbated neutral current and neutral potential problems under a high penetration of single phase PV systems allocated in an unbalanced pattern, and the limitations of the traditional mitigation strategies against these impacts, this thesis has proposed new mitigation strategies using energy storage. Distributed storage connected to each PV system, and a central community storage system for the whole feeder, both have been considered as potential strategies. A power balancing algorithm has been developed to balance the net power exchange with the grid utilising the minimum amount of storage power. A control strategy has been developed based on the balancing algorithm to control the energy storage devices to provide an appropriate balancing effect under varying load and PV unbalance.

CONTENTS

LIST OF FIGURES

LIST OF TABLES

Chapter 1

INTRODUCTION

A high penetration of distributed solar photovoltaic (PV) resources is becoming a reality for many electricity distribution utilities world-wide. In Australia, the installed PV capacity forecast by the Australian Electricity Market Operator (AEMO) shows that PV capacity will be increased to 5.1 GW by 2020 from 1.45 GW in February 2012 [1]. This high PV penetration can introduce new challenges for distribution networks that need to be addressed.

The increase of PV penetration level into the distribution systems has created situations where PV power generation can exceed the load demand, and hence can produce power flow from customers to the grid. This is in opposition to the direction of power flow in a traditional distribution grid without a high PV penetration. A reverse power flow creates voltage rise problems in distribution systems, particularly in weak radial systems.

Passing clouds can cause PV power generation to fluctuate because of its dependency on the ambient sun irradiance level. This can cause the PV output to ramp-up or ramp-down at high rates. Weak distribution systems are vulnerable to voltage fluctuations created by such high ramp-rate PV output fluctuations.

An unbalanced allocation of PV units at different phases of a distribution feeder can create a high neutral current, particularly in the midday, when reverse power flow is at the peak level. In the presence of neutral grounding resistance, this high neutral current may produce considerable neutral potential.

Due to the potential impacts of PV integration, distribution utilities are imposing network PV penetration limits [2] which refer to the maximum amount of PV generation that can be integrated with a distribution network without violating power quality and system security limits [3]. In Australia, some utilities are imposing PV hosting limits using PV unit size (3.5 to 5 kW per phase per residential connection)

whereas, some other utilities are imposing limits in terms of the infrastructure loading level (30% of low voltage feeder capacity, 20% of zone substation capacity, etc.) [4]. Limiting the PV penetration level is, however, contradictory to the Australian Government's Renewable Energy Target [5]. Therefore, a comprehensive analysis of PV impacts is required and, based on the results from the analysis, new mitigation approaches need to be developed to increase the PV penetration level in the distribution networks.

Distribution systems, especially at the low voltage level, have not received much attention in the past due to their passive nature and less interaction with the upstream medium/high voltage networks. However, modern distribution grids are becoming more active due to integration of distributed generation. Therefore, it has become necessary to revisit the distribution network analysis approaches to investigate the solar PV impacts more accurately. Commercial tools for distribution network analysis may not be fully equipped for the necessary analysis for PV impact assessment.

Smart metering technologies are being integrated with distribution grids at a significant level, and more importantly, these technologies are being extended to the low voltage customer level [6]. Using an appropriate analysis tool, data available from the smart metering devices can offer a potential advancement in realistic assessment of PV impacts using offline and online approach.

In recent days, reactive power capability is being incorporated with "smart" PV inverters [3, 7] to provide network ancillary support. Although an individual PV inverter size is limited, with an appropriate control, the collective capacity of the distributed inverters can provide various system support benefits for the low voltage and upstream medium voltage feeders.

Battery energy storage devices can also be integrated with residential PV systems to increase the viability of PV generation by mitigating the intermittency effect. Using suitable control strategies, the PV integrated storage devices can be an invaluable resource to mitigate the potential PV impacts, such as voltage rise, reverse power flow, voltage fluctuation and neutral potential rise.

In the context of the topics discussed above, the backgrounds of the specific challenges that will be addressed in this thesis are discussed below.

1.1 BACKGROUND OF THE PROBLEMS AND RESEARCH MOTIVATIONS

1.1.1 Limitations of the Traditional Three-Phase Power Flow Approaches for a Comprehensive Assessment of Solar PV Impacts

Analysis of the PV impacts is a key step to design effective mitigation options. The accuracy and usefulness of the distribution network analysis results will depend on the network modelling techniques adopted. Analysis results would be more accurate and would represent the practical situation better if the network models with less approximation are used for analysis. Three-phase power flow methods have been traditionally used to analyse distribution systems to consider the impact of load and network unbalances. However, the traditional three-phase power flow approach mainly considers a 3-wire configuration of the distribution networks. In recent years, three-phase 4-wire power flow methods, e.g., [8], have been reported to include the effect of the neutral wire and the neutral grounding resistances in the analysis. However, in these methods, the integration of 3-wire and 4-wire power flow methods and the detailed modelling of the interfacing distribution transformer with 3-wire primary and 4-wire secondary sides are not explicitly considered. While it is important to explicitly model the neutral wire and the neutral grounding resistances to accurately analyse a high penetration of solar PV impacts on distribution networks, it is also important to investigate whether and how severely these impacts are propagated to the upstream medium voltage (MV) networks. This motivates for the development of an analysis approach where a distribution network can be modeled with a reasonable accuracy by including the lines and transformers with the actual wiring configurations (such as 3-wire/4-wire), neutral grounding impedances and voltage control devices in the upstream MV networks, such as voltage regulators.

1.1.2 Computational Burden of Using a Large Volume of Smart Grid Data for PV Impact Analysis

In addition to an appropriate modelling and analysis technique, the effectiveness of the mitigation options will also depend on the data used for the PV impact analysis. Real network data would be preferable than synthetic data for an accurate estimation of the PV impacts on a given network. With the advent of smart metering infrastructure in

distribution systems, real network data are becoming available. However, to analyse the PV impacts from an archive of network data, a huge computational effort would be necessary. For example, a database containing a week's or a month's voltage profiles and power flow profiles at different buses of a given network may need to be analysed for PV impact assessment. However, due to overcast cloudy days and spatial diversity, all the profiles may not show voltage rise and reverse power flow. A technique to filter out only the profiles showing a specific PV impact will aid in analysing the PV impacts in a more computationally efficient way. Therefore, it is necessary to develop an intelligent approach that can extract the relevant portion of the data from an archive which then can be studied in details for PV impact analysis.

1.1.3 Need for an Online Approach of PV Impact Assessment for Designing Effective Mitigation Strategy

Due to the high growth rate of PV penetration level, distribution network scenarios are changing rapidly. Therefore, offline analysis of PV impacts using archived historical data may not be able to provide sufficient information to design an effective mitigation options against PV impacts. Previous efforts on quantifying distributed generation impacts on distribution networks, e.g. [9] are mainly useful for planning oriented studies using offline data. As the Advanced Metering Infrastructure (AMI) is being extended to the LV feeder level, it is anticipated that real time information on individual customer connections would be available in the near future. To effectively utilise such online data for PV impact assessment in real time for more accurate design of the impact mitigation strategies, especially at the LV level, an online impact assessment approach using suitable indices for online quantification of PV impacts would be necessary.

1.1.4 Need for an Appropriate Reactive Power Control Strategy for Network Support under Intermittent PV Power Generation

The incorporation of reactive power capability with solar PV inverters is becoming popular in recent days. This reactive power capability is mainly intended to be used to mitigate voltage rise and also to support voltage during the evening peak load. As PV power generation is dependent on the ambient irradiance level, more reactive capacity can be made available during cloud passing periods due to the unused capacity from less active power generation. This increased reactive capacity can be useful for voltage support during cloud passing periods. Previous works, e.g. [10], mainly concentrated on

reactive power control for PV impacts related to slow variations of PV output, such as voltage rise mitigation or voltage support. Incorporation of a reactive power control feature for fast acting phenomenon, like PV output fluctuation during cloud passing, and its coordination with traditional control features for slow variation of PV output would be challenging. This motivates to develop a versatile reactive power control strategy to provide network support under various situations of PV power generation using the available reactive capability which will vary depending on the PV power generation.

1.1.5 Limitations of the Traditional Charging/Discharging Strategies to Effectively Use the Battery Capacity for PV Impact Mitigation

Battery energy storage devices are being integrated with PV systems to mitigate solar PV impacts. Energy storage devices are charged over the day with the surplus power from solar PV systems which result in reducing the reverse power flow and mitigating the voltage rise. The stored energy can be used for providing evening peak load support. As the energy storage devices have limited capacity, an appropriate control of charging/discharging rates is essential to ensure an effective and wise use of the available storage capacity [11]. The reverse power flow and voltage rise become significant mostly during the midday period when the PV power is at its peak level and the load demand is typically low. However, the traditional charging strategies do not consider such dynamic variations while charging the energy storage devices. Similarly, the traditional discharging strategies do not consider the variations of evening load to discharge at the highest rate during the occurrence of the peak load. Also the storage device may need to be discharged for short time periods to provide active power support during cloud passing. If this short term discharge is performed, an adjustment of charging rates for the post-discharge periods needs to be carried out so that the available storage capacity can be effectively used. This dynamic adjustment of charging rate for an effective use of the limited storage capacity is not considered in the traditional strategies. Therefore, instead of the traditional constant or pre-specified charging/discharging methods, new charging/discharging strategies need to be developed so that the charging/discharging patterns can be controlled to match the load and PV generation patterns, with the provision for necessary dynamic adjustment to account for unanticipated events, such as, cloud passing.

1.1.6 Drawbacks of Traditional Moving Average based Algorithms to Control PV Inverter Ramp-rate for Fluctuation Mitigation

Traditionally, moving average [12] based algorithms are used for controlling energy storage devices for smoothing the PV output fluctuations. Moving average based methods are subject to memory effect which means, depending on the length of the averaging window, the smoothened version of the PV output would highly depend on the previous values of the PV output. Therefore, even if the actual PV output does not fluctuate significantly during some periods, the moving average based control will continue to provide fluctuation mitigation support. Also, a moving average based smoothing algorithm does not control the ramp-rate at any specific value; rather, the ramp-rate depends on the previous PV panel outputs within the averaging window. Therefore, a less amount of control over the fluctuation mitigation performance is available if a moving average based strategy is used. Considering these limitations, new strategy needs to be developed that will provide the fluctuation mitigation support only when it is necessary by the ramp-rate tracking, and also the fluctuation mitigation performance can be controlled by controlling the ramp-rate.

1.1.7 Limitations of the Traditional Strategies in Mitigating Neutral Current and neutral potential Rise in LV Distribution Networks

The existing neutral current and the neutral potential (neutral-to-ground voltage - NGV) problems can be aggravated by a highly unbalanced allocation of customer installed rooftop PV systems in distribution feeders. Traditional mitigation techniques [13] against neutral current and neutral voltage problems have not been designed to give any particular attention to the contributions of neutral current produced by a combined effect of load and PV unbalance. Moreover, the traditional mitigation strategies are of static type and do not change the mitigation effect with the variability of PV generation. Therefore, the traditional mitigation strategies may not be sufficient in the new distribution network environment with a high penetration of single phase PV units allocated in an unbalanced form. In this context, it is necessary to develop new solution strategies that would be able to provide an appropriate balancing effect under dynamic variations of load and PV unbalance. Battery energy storage devices are already being integrated with single rooftop PV systems, and can be used for mitigation of neutral current and neutral potential rise problems by power balancing. For this purpose, an appropriate control strategy needs to be developed.

1.2 OBJECTIVES AND SPECIFIC CONTRIBUTIONS

Based on the background of the problems and research gaps identified in the previous section, the objectives of this thesis are listed below.

- Development of a power flow approach for PV impact analysis using distribution network models preserving actual wiring configurations of lines and transformers, including neutral grounding impedances.
- Development of an intelligent approach to use a large volume of smart grid data for PV impact assessment using data dimensionality reduction and data mining techniques.
- Development of an on-line approach for solar PV impact analysis in low voltage distribution networks.
- Development of a versatile reactive power control strategy for providing network support under various conditions of PV power generation over the day, including absence of PV in the night.
- Development of a charging/discharging strategy for energy storage devices integrated with solar PV systems to control the shape of charging/discharging profile for an effective use of limited storage capacity for PV impact mitigation and evening peak load support.
- Development of a ramp-rate control strategy using energy storage for mitigation of PV output fluctuations avoiding the memory effects associated with moving average based algorithms.
- Development of a strategy using energy storage, either in distributed or in concentrated form, for mitigation of neutral current and voltage problems created by an unbalanced allocation of PV resources in distribution networks.

The specific contributions of this thesis are summarised below.

A power flow approach has been developed for analysing integrated MV and mutigrounded LV segments of distribution networks preserving the 3-wire and 4-wire configurations and incorporation of neutral grounding impedances. A per unit primitive admittance matrix model of the delta-wye transformer for interfacing the 3-wire MV

and 4-wire LV systems has been developed. The proposed approach will be useful for performing PV impact analysis with more accuracy than the approaches where 3-wire approximations of 4-wire network segments are used and effect of the neutral wire and grounding impedances are not explicitly considered. The developed approach will also be useful for investigating the PV impacts propagating to the upstream MV networks, including the impacts on voltage regulator operation.

An approach has been developed combining SAX (Successive Aggregate Approximation – a data dimensionality reduction technique) and data-mining algorithms to intelligently extract effective data for PV impact analysis from a large volume of smart grid measurements. This will aid to perform PV impact analysis using the developed power flow approach with less computational burden.

A variable width sliding window based approach has been proposed for the analysis of solar PV impacts using on-line measurements from smart monitoring devices. The width of the assessment window can be made narrow when PV impacts are intense, whereas in other times, assessment can be performed with a wide assessment window to reduce computational and monitoring burden. A dynamic "what-if" analysis feature has been included in the proposed approach to understand how the network would behave if the network conditions at the present time instant are altered. The dynamic "what-if" analysis would be instrumental to understand the effectiveness of a prospective mitigation action more accurately.

A versatile reactive power control approach has been proposed for solar PV inverters for providing reactive power support to distribution networks under different conditions of PV power generation over the day and at the absence of PV power in the night. Using the proposed approach, PV inverters would be able to mitigate voltage rise in the excessive PV generation period using a droop-based mode, mitigate voltage fluctuations using a ramp-rate based mode, and improve voltage during low or no PV period using a grid power import based mode. A coordination approach has been developed for smooth transition among the control modes. A dynamic model of the inverter current control system has been developed to investigate the performance of the proposed approach in a fast ramp-rate based mode.

A method has been developed to control the shape of the charging/discharging profiles of battery energy storage units integrated with solar PV systems to ensure an

effective use of the limited storage capacity. A system of non-linear equations has been developed using the constraints of capacity and time limitation of storage operation, and also the user defined parameters to control the charging/discharging profiles. The charging/discharging rates obtained by solving the developed system of equations are also adjusted at each instant of time to consider any unplanned operation (such as any short-term discharge to provide support during unstable weather conditions) so that the limited available capacity can be used wisely.

A ramp-rate control approach for solar PV inverters has been proposed for the mitigation of PV output fluctuation. The ramp-rate of the PV panel output is used to control the PV inverter ramp-rate to a desired level by deploying energy storage. During the ramping event, the desired ramp-rate is governed by controlling the energy storage based on an inverse relationship with the PV panel output ramp-rate to improve the fluctuation mitigation performance. In contrast to the moving average method, the proposed strategy is able to control the desired ramp-rate independent of the past history of the PV panel output and therefore will need to operate a storage device less amount of time, compared to a moving average based algorithm. A dynamic model of the PV-storage integrated system is developed to verify the proposed strategy in the presence of physical device time lags.

The possibility of applying energy storage as a potential strategy to reduce the neutral current and voltage problems under an unbalanced allocation of single phase PV units has been explored. Distributed energy storage integrated with individual PV systems (suitable for existing networks), and a Community Energy Storage (CES) system for the whole feeder (suitable for new networks or future grids) – both have been considered as potential strategies. A methodology is developed based on constrained minimisation method for both forms of storage devices to perform the charging/discharging in such a manner that the balancing operation, and hence the mitigation of neutral current and neutral potential rise problem, is accomplished by spending the minimum power from the battery storage.

1.3 THESIS ORGANISATION

The organisation of the thesis is outlined below.

Chapter 1 provides a background of the problems that has been particularly focused

in this thesis, and identifies the objectives and specific contributions in the context of the problems.

Chapter 2 develops a comprehensive network modelling approach preserving the wiring configurations of the MV and LV segments of the network, and also shows the modelling approaches used for load and solar PV modelling. Then, a generalised approach for formulating the power flow problems of integrated MV and mutigrounded LV networks with solar PV is presented and a method to solve the power flow problems using the current-mismatch variant of the Newton-Raphson algorithm is discussed.

Chapter 3 develops an intelligent approach using SAX and data mining techniques for extracting the appropriate portion of the data from a large volume of smart grid measurements so that solar PV impacts can be analysed with less computational burden. A brief description of the SAX method is provided and following this, the proposed intelligent approach is described to show how SAX, time series clustering, and anomaly detection algorithms can be used for reducing computational efforts of PV impact assessment.

Chapter 4 develops an on-line approach for PV impact assessment using the data available from smart monitoring devices in LV distribution networks. The architecture of the proposed online approach has been described including the concept of the variable width sliding window. The application of the on-line approach for PV impact assessment using numerical indices, for aiding to design mitigation actions using accurate real time information, and for dynamic "what-if" analysis to understand the threats of a potential PV penetration scenario are described.

Chapter 5 develops a reactive power control strategy to mitigate voltage related impacts of a high penetration of solar PV resources on distribution networks. The development of the proposed strategy is presented under various conditions of PV generation to show how the strategy can mitigate voltage rise during surplus PV generation period and voltage fluctuation by providing fast reactive power support during cloud passing periods, and provides voltage support during low or no PV period.

Chapter 6 a charging/discharging strategy for use with energy storage devices integrated with solar PV systems to control the power consumption/delivery of battery power to ensure an effective use of limited energy storage capacity for PV impact

mitigation and evening peak load support. This chapter initially provides an analytical background of the effectiveness of using energy storage units for PV impact mitigation. Then the method to obtain the appropriate charging/discharging rates is presented, which is followed by a battery operation strategy including the adjustment of charging/discharging rates to consider unplanned events, such as cloud passing.

Chapter 7 develops a strategy to control the charging/discharging of energy storage devices to mitigate PV output fluctuations caused by cloud passing. Initially, the limitations of the moving average based methods for ramp-rate control has been investigated. Then the proposed strategy has been presented where the new features (application of an inverse characteristic between PV ramp-rate and battery power ramp-rate during the ramping events and a "State-of-Charge" based approach outside the ramping events) have been explained.

Chapter 8 develops an energy storage based approach to mitigate the neutral current and neutral potential problem arising from a high penetration of PV resources allocated in an unbalanced pattern. The limitations of traditional mitigation techniques against neutral voltage problems under a high PV penetration scenario have been presented. Then, the applications of distributed and community energy storage, including control algorithms for charging/discharging are presented to show how the surplus power from PV units at all the phases over the day and the power drawn by the unbalanced loads over evening peak load period could be balanced.

General conclusions and directions for future works are provided in **Chapter 9**.

REFERENCES

[1] Australian Electricity Market Operator. (2012). *Rooftop PV Information Paper: National Electricity Forecasting* [Online]. Available: http://www.aemo.com.au/Reports-and-Documents/Information-Papers/Rooftop-PV-Information-Paper-National-Electricity-Forecasting

[2] R. A. Shayani and M. A. G. de Oliveira, "Photovoltaic Generation Penetration Limits in Radial Distribution Systems," *Power Systems, IEEE Transactions on,* vol. 26, pp. 1625-1631, 2011.

[3] D. Premm.IEA PVPS Task 14 Workshop, Kassel, Germany. (May 8, 2012). *PV System Technology Review - How smart PV Inverters Increase the Hosting Capacity of Distribution Grids*.

[4] N. Ben.The Australian PV Association. (September, 2013). *PV Integration on Australian*

Distribution Networks [Online]. Available: http://ceem.unsw.edu.au/sites/default/files/documents/APVA%20%20PV%20and%20DNSP%20Literature%20review%20September%202013.pdf

[5] Australian Government, Department of Climate Change and Energy Efficiency. (August 2012). *Renewable Energy Target* [Online]. Available: http://www.climatechange.gov.au/ret

[6] R. C. Dugan and M. McGranaghan, "Sim City," *Power and Energy Magazine, IEEE,* vol. 9, pp. 74-81, 2011.

[7] J. W. Smith, W. Sunderman, R. Dugan, and B. Seal, "Smart inverter volt/var control functions for high penetration of PV on distribution systems," in *IEEE/PES Power Systems Conference and Exposition (PSCE)*, Phoenix, AZ, USA, 20-23 Mar., 2011, pp. 1-6.

[8] D. R. R. Penido, L. R. de Araujo, S. Carneiro, J. L. R. Pereira, and P. A. N. Garcia, "Three-Phase Power Flow Based on Four-Conductor Current Injection Method for Unbalanced Distribution Networks," *IEEE Transactions on Power Systems* vol. 23, pp. 494-503, 2008.

[9] L. F. Ochoa, A. Padilha-Feltrin, and G. P. Harrison, "Evaluating distributed generation impacts with a multiobjective index," *Power Delivery, IEEE Transactions on,* vol. 21, pp. 1452-1458, 2006.

[10] E. Demirok, P. González, K. H. B. Frederiksen, D. Sera, P. Rodriguez, and R. Teodorescu, "Local Reactive Power Control Methods for Overvoltage Prevention of Distributed Solar Inverters in Low-Voltage Grids," *IEEE Journal of Photovoltaics* vol. 1, pp. 174-182, 2011.

[11] M. J. E. Alam, K. Muttaqi, and D. Sutanto, "Distributed Energy Storage for Mitigation of Voltage-rise Impact caused by Rooftop Solar PV," in *IEEE PES General Meeting*, San Diego, California, USA, 22-26 July, 2012.

[12] N. Kakimoto, H. Satoh, S. Takayama, and K. Nakamura, "Ramp-Rate Control of Photovoltaic Generator With Electric Double-Layer Capacitor," *IEEE Transactions on Energy Conversion* vol. 24, pp. 465-473, 2009.

[13] EPRI. *Elevated Neutral-to-Earth Voltage, Urban Contact Voltage and Other Perceptibility Concerns for Humans and Animals* [Online]. Available: http://strayvoltage.epri.com/index.asp

Chapter 2

A THREE-PHASE POWER FLOW APPROACH FOR INTEGRATED 3-WIRE MV AND 4-WIRE MULTIGROUNDED LV NETWORKS WITH ROOFTOP SOLAR PV

ABSTRACT

With increasing level of rooftop solar PV penetration into LV distribution networks, analysis with realistic network models is necessary to adequately capture the network behaviour. The traditional three-phase 3-wire power flow approach lacks the capability of exact analysis of 4-wire multigrounded LV networks due to the approximation of merging the neutral wire admittance into the phase wire admittances. Such an approximation may not be desirable when neutral wire and grounding effects need to be assessed, especially in the presence of single-phase solar power injection that may cause a significant level of network unbalance. This thesis proposes a three-phase power flow approach for distribution networks while preserving the original 3-wire and 4-wire configurations for more accurate estimation of rooftop PV impacts on different phases and neutrals. A three-phase transformer model is developed to interface between the 3-wire MV and the 4-wire LV networks. Also an integrated network model is developed for an explicit representation of different phases, neutral wires and groundings of a distribution system. A series of power flow calculations have been performed using the proposed approach to investigate the impacts of single-phase variable PV generation on an Australian distribution system and results are presented.

2.1 INTRODUCTION

Integration of solar photovoltaic (PV) resources in high penetration level may introduce a multitude of adverse impacts [1-2] on distribution networks. Voltage rise [3], reverse power flow [4], voltage unbalance [1] can be listed as some of the major impacts. Analysis of network behaviour with PV penetration is essential for understanding these impacts. Three-phase power flow is often deployed as a tool for the analysis of network asymmetry and load imbalance in distribution networks. With an increasing level of single phase rooftop solar PV penetration, phase domain analysis is essential not only for incorporating the load unbalance and network asymmetries, but also to assess the impacts of single-phase solar PV units installed in the three-phase distribution networks. Without the direct control of distribution utilities over the sizes and locations of customer-installed rooftop PV units, unbalanced allocation of PV resources will produce different level of impacts on different phases of a feeder, such as unbalanced impacts of voltage rise [3] and reverse power flow [4]. Unbalanced operation of networks can also affect induction motors, power electronic converters [5], and, may also decrease network voltage stability margins [6].

Medium voltage (MV) segments of distribution networks are typically constructed with 3-wire configuration whereas low voltage (LV) segments are constructed with 4-wire configuration, where the fourth wire is the neutral wire which is grounded at multiple locations along the feeder. Using the assumption of zero neutral voltage with a perfectly grounded neutral in the LV part, matrix reduction technique is typically applied to reduce the 4x4 admittance matrices corresponding to LV line-segments into 3x3 matrices [7]. However, in practical LV distribution feeders, neutral grounding resistances can vary from less than 1 Ohm to several tens of Ohms depending on the type and condition of grounding system [8-10]. Further, the unbalance in load and line impedance and the unbalanced allocation of PV resources can produce high neutral current in LV feeders, sometimes even higher than the phase currents [7, 11]. High neutral current can produce significant neutral-to-ground voltage in the presence of neutral grounding resistance. Therefore, the traditional assumption that the neutral-to-ground voltage is zero and merging the neutral line admittances into the phase line admittances in the modelling may not be realistic. High neutral current may produce voltage distortion, and may overload neutral conductor [12]. Further, the neutral-to-ground voltage can act as a common-mode noise in sensitive electronic equipment [13].

Neutral-to-ground voltage beyond manufacturer specified tolerance level [13] may cause mal-operation [14] of sensitive equipment. To avoid such issues, the accurate determination of neutral current and voltage is essential, especially for planning distribution networks with PV integration. Therefore, preserving the 4-wire configuration in the network model would be desirable and development of a power flow approach capable of retaining the original wiring configurations of the MV and LV network segments is necessary.

Extensive research has been performed on 3-phase power flow algorithms for distribution networks with distributed resources [15], however, most of those are based on a 3-wire power flow approach. A forward-backward substitution based 4-wire power flow method is developed in [11] considering the ground-wire impedance. A three-phase 3-wire power flow based on a current-mismatch variant of Newton-Raphson algorithm is presented in [16]. Authors in [17] have developed a current-mismatch based 4-wire power flow approach. However, in [17], a combined 3-wire and 4-wire power flow formulation corresponding to MV and LV networks is not explicitly presented.

This thesis proposes a three-phase power flow approach developed for the analysis of single phase rooftop solar PV impacts on distribution networks by preserving the realistic configurations of MV and LV networks. With this technique, the PV impacts on the host LV network and the upstream MV network can be performed without modifying the model of the original wiring configurations. LV network modelling will be performed based on the original 4x4 matrix representation of LV line segments, and MV networks will be modeled using 3x3 matrices. A primitive admittance model of delta-wye transformer will be developed based on the technique presented in [18] to satisfy the modelling requirements of the 3-wire (MV) and 4-wire (LV) systems. The integrated system of power flow equations corresponding to the 3-wire and 4-wire networks will be solved using the current-mismatch variant of Newton-Raphson algorithm. It is worth mentioning that a network model retaining the original 3-wire and 4-wire configurations could be solved using other power flow solution algorithms with minor adjustments to incorporate 3- and 4-wire configuration where the neutral line and ground resistances need to be included. To investigate the impacts of single-phase variable PV generation, a series of power flow calculations will be performed over a 24-hour period. A practical distribution system in Australia will be used to verify the

applicability of the proposed approach in real-world distribution networks. Though this thesis has concentrated on rooftop PV systems, the problems presented can be experienced with any type of distributed generation resources, such as small residential wind power units or fuel cells, installed in an unbalanced pattern in a distribution feeder. Therefore, the proposed approach can be extended to other distributed generation resources.

2.2 SYSTEM MODELLING

A distribution feeder can be represented as a combination of series elements (overhead and underground line segments, transformers etc.) connected between, and shunt elements (line susceptances, grounding impedance, capacitor / reactor banks, etc.) connected at, different system nodes. Admittance matrix models of the series and shunt components assembled in the form of a total system admittance matrix are used for network analysis. A simple 4-bus distribution test feeder shown in Fig. 2.1(a), similar to the IEEE 4-bus test system [19] will be used in this thesis to formulate the modelling approach of 3-wire and 4-wire systems; a similar approach can be followed for the general extended form of the test system shown in Fig. 2.1(b). The 4-bus feeder is configured to have a 3-wire MV section from bus 1 to 2, a delta-wye step-down transformer from bus 2 to 3, and a 4-wire LV section from bus 3 to 4. Detailed modelling aspects of the network components are discussed below.

2.2.1 Modelling of the MV Lines

Three wire MV distribution lines can be represented using 3×3 admittance matrices consisting of the self admittances of three phases *a*, *b*, and *c* as the diagonal elements and the mutual coupling admittances among them as off-diagonal elements. Following this model, the MV line admittance of the 4-bus test system, $\mathbf{Y}_{12}^{MV}$, can be written as,

$$\mathbf{Y}_{12}^{MV} = \mathbf{y}_{ij}^{abc} = \begin{bmatrix} y_{ij}^{aa} & y_{ij}^{ab} & y_{ij}^{ac} \\ y_{ij}^{ba} & y_{ij}^{bb} & y_{ij}^{bc} \\ y_{ij}^{ca} & y_{ij}^{cb} & y_{ij}^{cc} \end{bmatrix} \tag{2.1}$$

where, the subscripts *i* and *j* are used for generic modelling purpose, that represents the buses 1 and 2, respectively, in the network given in Fig. 2.1(a). It is to be noted that to construct the total system admittance matrix with 3-wire and 4-wire lines, the MV line admittance model needs to be accommodated into the 4-wire line model. Therefore,

order of the admittance matrix in (2.1) is increased to 4×4 using all *zero* elements, as given below.

$$\mathbf{Y}_{12}^{MV} = \mathbf{y}_{ij}^{abc} = \begin{bmatrix} y_{ij}^{aa} & y_{ij}^{ab} & y_{ij}^{ac} & 0 \\ y_{ij}^{ba} & y_{ij}^{bb} & y_{ij}^{bc} & 0 \\ y_{ij}^{ca} & y_{ij}^{cb} & y_{ij}^{cc} & 0 \\ 0 & 0 & 0 & 0 \end{bmatrix} \tag{2.2}$$

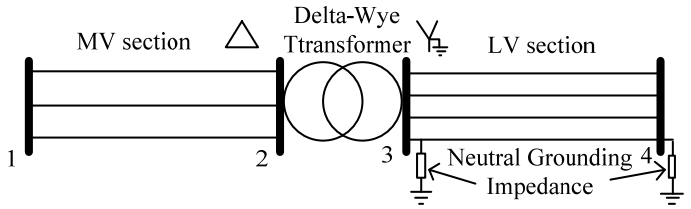

(a) 4-bus, 3-wire and 4-wire test system

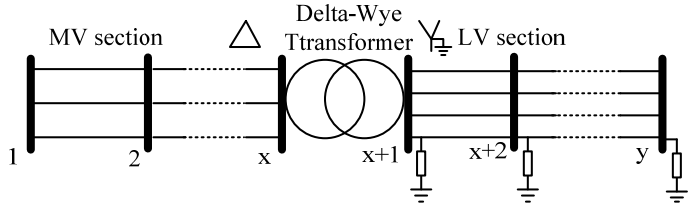

(b) A general extended form of 3-wire and 4-wire test system

Fig. 2.1. Three Wire and Four Wire Test System (a) 4-bus, 3-wire and 4-wire test system. (b) General extended form of 3-wire and 4-wire test system.

2.2.2 Modelling of the LV Lines

Low voltage distribution feeders are typically constructed with four wire line segments where the fourth wire is the neutral wire. Similar to the phase conductors, the neutral conductor has self and mutual impedance components with the other phase wires, and these need to be included in the admittance model. The LV line admittance matrix, $\mathbf{Y}_{34}^{LV}$ of the test system is given below using a 4×4 matrix model.

$$\mathbf{Y}_{34}^{LV} = \mathbf{y}_{ij}^{abcn} = \begin{bmatrix} y_{ij}^{aa} & y_{ij}^{ab} & y_{ij}^{ac} & y_{ij}^{an} \\ y_{ij}^{ba} & y_{ij}^{bb} & y_{ij}^{bc} & y_{ij}^{bn} \\ y_{ij}^{ca} & y_{ij}^{cb} & y_{ij}^{cc} & y_{ij}^{cn} \\ y_{ij}^{na} & y_{ij}^{nb} & y_{ij}^{nc} & y_{ij}^{nn} \end{bmatrix} \tag{2.3}$$

Here, *i* and *j* are used as subscripts for the generic modelling purpose, similarly as described for (2.1), which represents buses 3, and 4, respectively. The neutral wire is explicitly modeled in this matrix model, as reflected in the 4th row and column.

2.2.3 Modelling of the MV/LV Transformer

A primitive admittance matrix model of a delta-wye transformer is developed based on the relationship of transformer terminal currents with the internal winding currents, in a similar fashion discussed for wye-delta connection in [18]. The per unit impedance matrix model of a three-phase transformer with three-phase short circuit impedances, z_T^a, z_T^b, and z_T^c, can be described in a matrix form as,

$$\mathbf{Z}_T^{abc} = \begin{bmatrix} z_T^a & 0 & 0 \\ 0 & z_T^b & 0 \\ 0 & 0 & z_T^c \end{bmatrix} \tag{2.4}$$

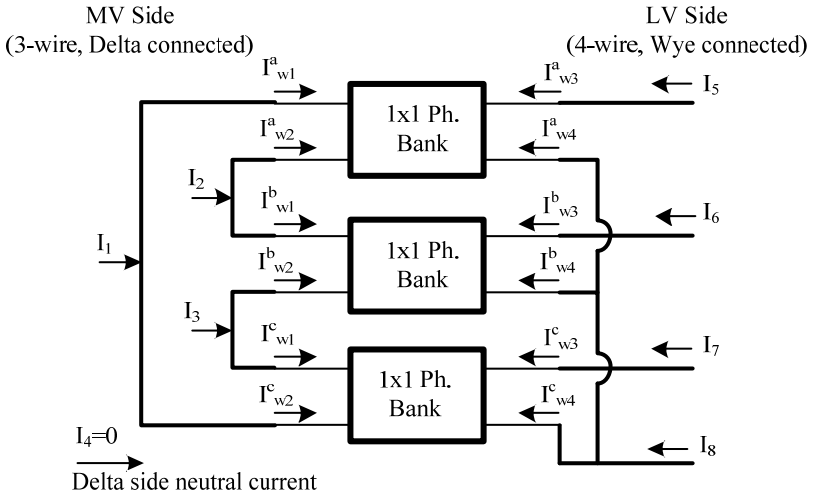

Fig. 2.2. Terminal connection and currents of delta-wye transformer.

The ground referenced nodal admittance matrix [18], $\mathbf{Y}_T^L$, can be obtained using the incidence matrix, *B*, relating the short circuit currents with the terminal currents [18], as given below.

$$\mathbf{Y}_T^L = B\left(\mathbf{Z}_T^{abc}\right)^{-1} B^T \text{ where, } B = \begin{bmatrix} 1 & 0 & 0 \\ -1 & 0 & 0 \\ 0 & 1 & 0 \\ 0 & -1 & 0 \\ 0 & 0 & 1 \\ 0 & 0 & -1 \end{bmatrix} \tag{2.5}$$

The winding admittance matrix $\mathbf{Y}_T^W$ can be obtained from $\mathbf{Y}_T^L$ by using the following equation,

$$\mathbf{Y}_T^W = N\mathbf{Y}_T^L N^T \tag{2.6}$$

where,

$$N = \begin{bmatrix} N^a & \mathbf{0} & \mathbf{0} \\ \mathbf{0} & N^b & \mathbf{0} \\ \mathbf{0} & \mathbf{0} & N^c \end{bmatrix} \tag{2.7}$$

and,

$$N^a = N^b = N^b = \begin{bmatrix} 1 & 0 \\ -1 & 0 \\ 0 & 1 \\ 0 & -1 \end{bmatrix} \tag{2.8}$$

In (2.7), **0** denotes a 4×2 matrix of *zero* elements, and in (2.8) 1 corresponds to nominal per unit turns ratio. The terminal currents in the delta-wye transformer shown in Fig. 2.2 can be related to the winding currents by,

$$\begin{bmatrix} I_1 \\ I_2 \\ I_3 \\ I_4 \\ I_5 \\ I_6 \\ I_7 \\ I_8 \end{bmatrix} = \overbrace{\begin{bmatrix} 1 & 0 & 0 & 0 & 0 & 0 & 0 & 0 & 0 & 1 & 0 & 0 \\ 0 & 1 & 0 & 0 & 1 & 0 & 0 & 0 & 0 & 0 & 0 & 0 \\ 0 & 0 & 0 & 0 & 0 & 1 & 0 & 0 & 1 & 0 & 0 & 0 \\ 0 & 0 & 0 & 0 & 0 & 0 & 0 & 0 & 0 & 0 & 0 & 0 \\ 0 & 0 & 1 & 0 & 0 & 0 & 0 & 0 & 0 & 0 & 0 & 0 \\ 0 & 0 & 0 & 0 & 0 & 0 & 1 & 0 & 0 & 0 & 0 & 0 \\ 0 & 0 & 0 & 0 & 0 & 0 & 0 & 0 & 0 & 0 & 1 & 0 \\ 0 & 0 & 0 & 1 & 0 & 0 & 0 & 1 & 0 & 0 & 0 & 1 \end{bmatrix}}^{\mathbf{A}} \times \begin{bmatrix} I_{w1}^a \\ I_{w2}^a \\ I_{w3}^a \\ I_{w4}^a \\ I_{w1}^b \\ I_{w2}^b \\ I_{w3}^b \\ I_{w4}^b \\ I_{w1}^c \\ I_{w2}^c \\ I_{w3}^c \\ I_{w4}^c \end{bmatrix} \tag{2.9}$$

It is to be noted that the 4th row of **A**, corresponding to the neutral current of delta side, is a vector of all zero elements as there is no neutral current for the delta side. This row is inserted for making the 3-wire side of the admittance matrix compatible with the 4-wire system calculation, as discussed earlier in the MV and LV line modelling. The primitive admittance matrix of the transformer, $\mathbf{Y}_T^{prim}$, is found as,

$$\mathbf{Y}_T^{prim} = \mathbf{A}\mathbf{Y}_T^{prim}\mathbf{A}^T = \begin{bmatrix} \mathbf{Y}_T^{PP} & \mathbf{Y}_T^{PS} \\ \mathbf{Y}_T^{SP} & \mathbf{Y}_T^{SS} \end{bmatrix} \tag{2.10}$$

where, $\mathbf{Y}_T^{PP}$ is the primary (delta) side self admittance matrix;

$\mathbf{Y}_T^{SS}$ is the secondary (wye) side self admittance matrix;

$\mathbf{Y}_T^{PS}$ and $\mathbf{Y}_T^{SP}$ are the mutual admittance matrices between primary and secondary sides.

To develop the per-unit model, $\mathbf{Y}_T^{PS}$ and $\mathbf{Y}_T^{SP}$, each has to be divided by $\sqrt{3}$ and $\mathbf{Y}_T^{PP}$ has to be divided by 3, as described in [20].

2.2.4 Admittance Matrix of the Integrated System

The total system admittance matrix, $\mathbf{Y}$, for a *k*-bus three-phase power system can be constructed as a $4k \times 4k$ matrix to accommodate both 3-wire and 4-wire admittance matrices. The diagonal and off-diagonal elements of $\mathbf{Y}$ are obtained by,

$$\mathbf{Y}_{ii} = \sum_{i=1}^{k} \mathbf{y}_{ij}^{abcn}, \text{ and } \mathbf{Y}_{ij} = -\mathbf{y}_{ij}^{abcn} \tag{2.11}$$

where, i and $j = 1, 2, ..., k$.

Self admittance matrices of the transformer primary and secondary are added with the self admittance matrices of the primary bus and the secondary bus, respectively, and the mutual admittances are added with the mutual admittances between primary and secondary buses. Following this method, the system admittance matrix for the 4-bus test system with integrated MV and LV networks can be written as,

$$\mathbf{Y} = \begin{bmatrix} \mathbf{Y}_{12}^{MV} & -\mathbf{Y}_{12}^{MV} & 0 & 0 \\ -\mathbf{Y}_{12}^{MV} & \mathbf{Y}_{12}^{MV} + \mathbf{Y}_T^{PP} & -\mathbf{Y}_T^{PS} & 0 \\ 0 & -\mathbf{Y}_T^{SP} & \mathbf{Y}_{34}^{LV} + \mathbf{Y}_T^{PS} & -\mathbf{Y}_{34}^{LV} \\ 0 & 0 & -\mathbf{Y}_{34}^{LV} & \mathbf{Y}_{34}^{LV} \end{bmatrix} \tag{2.12}$$

Buses with grounded neutral, such as bus 3 and 4 in Fig. 2.1(a), are modeled by adding the neutral grounding admittances with the self admittances of the neutral wire at the respective buses. This is given in the equation below for an arbitrary bus i, where the neutral grounding admittance is y_{ii}^{N-G}.

$$\mathbf{Y}_{ii} = \mathbf{Y}_{ii} + \begin{bmatrix} 0 & 0 & 0 & 0 \\ 0 & 0 & 0 & 0 \\ 0 & 0 & 0 & 0 \\ 0 & 0 & 0 & y_{ii}^{N-G} \end{bmatrix} \tag{2.13}$$

2.2.5 Modelling of Loads

Realistic modelling of distribution network loads is a complex task involving comprehensive study of the types, ratings and consumption trends of electrical

appliances. Lighting, cooking, cooling, heating, computer, telecommunication and entertainment systems are some of the common types of appliances in residential households and all of these applications vary throughout the day based on consumer behaviour. Practical modelling of distribution feeder loads, especially at LV level, would therefore require modelling of load variations of each of the individual end-use applications. Total load profile of the households then could be performed by aggregation of the individual load profiles. ZIP representation of typical residential loads [21-22] will be used for modelling the loads in this chapter of the thesis.

A ZIP load model includes proportions of constant power, constant current, and constant impedance loads as given below.

$$P^{\mathrm{ZIP}} = P_0\left(p^{\mathrm{P}} + \left|\frac{V_{Ph-N}}{V_0}\right| p^{\mathrm{I}} + \left|\frac{V_{Ph-N}}{V_0}\right|^2 p^{\mathrm{Z}} \right) \tag{2.14a}$$

$$Q^{\mathrm{ZIP}} = Q_0\left(q^{\mathrm{P}} + \left|\frac{V_{Ph-N}}{V_0}\right| q^{\mathrm{I}} + \left|\frac{V_{Ph-N}}{V_0}\right|^2 q^{\mathrm{Z}} \right) \tag{2.14b}$$

$$\text{where}, p^{\mathrm{P}} + p^{\mathrm{I}} + p^{\mathrm{Z}} = 1 \,\text{and}\, q^{\mathrm{P}} + q^{\mathrm{I}} + q^{\mathrm{Z}} = 1 \tag{2.14c}$$

Here, P_0 and Q_0 are the nominal real and reactive power at nominal voltage V_0; and $p^{\mathrm{P}}, p^{\mathrm{I}}, p^{\mathrm{Z}}$, and $q^{\mathrm{P}}, q^{\mathrm{I}}, q^{\mathrm{Z}}$ are, respectively, the constant power, constant current and constant impedance proportions of active and reactive load and termed as ZIP parameters, and V_{Ph-N} is the phase-to-neutral voltage. To obtain the aggregate load model for the household, aggregate ZIP parameters for active and reactive components of loads, ZIP^{P}_{agg} and ZIP^{Q}_{agg}, where, $\mathrm{ZIP}^{P} \in \left\{p^{\mathrm{P}}, p^{\mathrm{I}}, p^{\mathrm{Z}}\right\}$ and $\mathrm{ZIP}^{Q} \in \left\{q^{\mathrm{P}}, q^{\mathrm{I}}, q^{\mathrm{Z}}\right\}$, will be determined using weighted average of individual ZIP parameters, as given below.

$$\mathrm{ZIP}^{P}_{agg} = \sum_{i=1}^{n}\left(\frac{P_i}{P_{total}}\right)\mathrm{ZIP}^{P}_{i} \tag{2.15a}$$

$$\mathrm{ZIP}^{Q}_{agg} = \sum_{i=1}^{n}\left(\frac{Q_i}{Q_{total}}\right)\mathrm{ZIP}^{Q}_{i} \tag{2.15b}$$

Here, i = 1, 2, ... n, for n number of loads corresponding to different household activities.

2.2.6 Modelling of Rooftop Solar PV

Solar PV systems installed in LV feeders typically contain rooftop PV modules and associated single phase inverter modules. The inverter output is connected between the phase and neutral conductor, as shown in Fig. 2.3, where current injection models of three single phase PV sources connected at phases *a*, *b* and *c* are presented. Current injection of PV inverter, I_{inv}, depends on the complex output power of the inverter, $P_{inv} + j\sqrt{S_{inv}^2 - P_{inv}^2}$, where, P_{inv} is the inverter real power, S_{inv} is the PV inverter apparent power capacity, and V_{Ph-N} is the phase-to-neutral voltage:

$$I_{inv} = \left(\frac{P_{inv} + j\sqrt{S_{inv}^2 - P_{inv}^2}}{V_{Ph-N}} \right)^* \tag{2.16}$$

Here, * represents complex conjugate. It is to be noted, the inverter can be designed to provide reactive power based on utility requirements or standards; and the apparent capacity of inverter S_{inv} is not directly related to the DC power coming out from the PV modules. The P_{inv} is the AC power generated by the inverter for a given value of DC power generated by the PV modules, P_{DC}, taking into account efficiency of the inverter, η_{inv}, mismatch among multiple PV modules, η_m, and dirt effects, η_d, as given below [23].

$$P_{inv} = \eta_{inv} \times \eta_m \times \eta_d \times P_{DC} \tag{2.17}$$

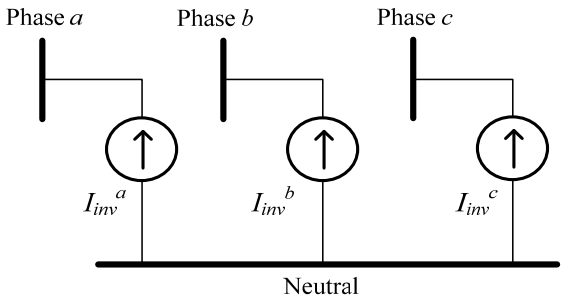

Fig. 2.3. Current injection model of solar PV inverter.

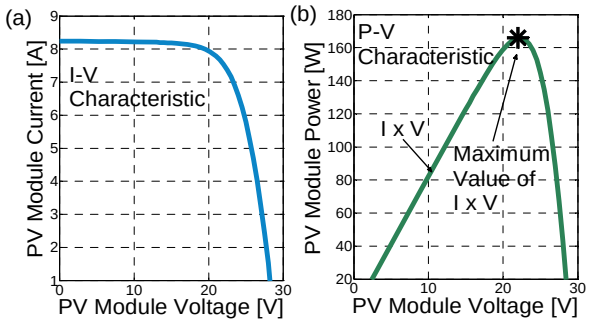

Fig. 2.4. Implementation of MPPT function; (a) *I-V* characteristic (b) *P-V* characteristic.

The inverter controls the amount of reactive power output that can be generated from the inverter, and is given by $\sqrt{S_{inv}^2 - P_{inv}^2}$. For a larger reactive power output required from the inverter, S_{inv} should be made larger, for the same P_{inv}. P_{DC} can be obtained from the *I-V* characteristic of the solar PV module as given by the following equation,

$$P_{DC} = max(V_{DC} \times I_{DC}) \tag{2.18}$$

where, V_{DC} is the PV module voltage, I_{DC} is the PV module current and $max(\cdot)$ implements the Maximum Power Point Tracking (MPPT) function. The function $max(\cdot)$ given in (2.18), is a function used to select the maximum value from a series of $V_{DC} \times I_{DC}$ values to obtain the maximum power point of the *P-V* characteristic, as shown in Fig. 2.4. PV module voltage V_{DC}, depends on ambient conditions and PV module electrical parameters, whereas the PV module current I_{DC} depends on the ambient conditions, the module voltage, and the PV current itself, as derived in [23-24]. Mathematically this can be described as,

$$V_{DC} = \phi(t, \mathbf{p}) \tag{2.19}$$

$$I_{DC} = \psi(t, G, \mathbf{p}, V_{DC}, I_{DC}) \tag{2.20}$$

where,

- t is the ambient temperature;
- G is the ambient sun irradiance level;
- $\mathbf{p}$ is a vector of PV module electrical parameters, such as module resistances, short-circuit current, voltage-temperature and current-temperature coefficients etc;

ϕ is a function to determine the PV module voltage from ambient conditions and PV parameters;

ψ is a function to determine the PV module current from ambient conditions, PV parameters, module voltage and module current.

An observation of (2.20) indicates that it is a transcendental expression and an analytical form of solution is not available [24]. Therefore, numerical technique is applied to solve (2.20) to find the *I-V* characteristic of PV modules at any given ambient conditions. The *I-V* characteristic is then used to find out the current injection from PV inverters into the network.

2.3 PROPOSED 3-PHASE POWER FLOW FOR INTEGRATED 3-WIRE AND 4-WIRE SYSTEMS WITH SOLAR PV

The power flow approach proposed in this thesis is developed based on the current mismatch variant [16-17] of Newton-Raphson algorithm to utilise the advantage of less computational burden as compared to the power mismatch variant. For a converged power flow problem, the mismatch between specified current and calculated current should be nearly *zero*. Such mismatch, denoted by $\Delta\mathbf{I}_m$ at an arbitrary bus *m* of a three-phase feeder can be expressed as,

$$\Delta\mathbf{I}_m = (\mathbf{I}_m)^{spec} - (\mathbf{I}_m)^{calc} \approx 0 \tag{2.21}$$

Here, $(\mathbf{I}_m)^{spec}$ is the vector of specified currents and $(\mathbf{I}_m)^{calc}$ is the vector of calculated currents at the bus *m*. If the three-phase bus *m* is of 3-wire configuration, then the length of the mismatch vector and the current vectors is 3, and, for a 4-wire configuration the length is 4, where the 4-th element corresponds to the neutral current. Specified currents at bus *m* can be obtained from current contributions from ZIP load and solar PV as given in (2.22) based on the current injection model shown in Fig. 2.5.

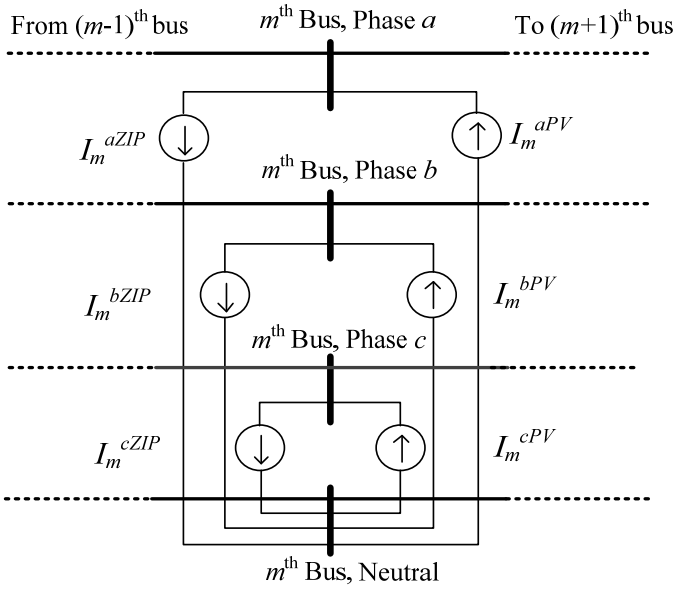

Fig. 2.5. Current injection model of load and PV for power flow formulation.

$$(\mathbf{I}_m)^{spec} = -\mathbf{I}_m^{\text{ZIP}} + \mathbf{I}_m^{\text{PV}} \tag{2.22}$$

where,

$$\mathbf{I}_m^{\text{ZIP}} = \left(\frac{\mathbf{P}_m^{\text{ZIP}} + j\mathbf{Q}_m^{\text{ZIP}}}{\mathbf{V}_m} \right)^* \tag{2.23}$$

and,

$$\mathbf{I}_m^{\text{PV}} = \left(\frac{\mathbf{P}_m^{\text{PV}} + j\mathbf{Q}_m^{\text{PV}}}{\mathbf{V}_m} \right)^* \tag{2.24}$$

where,

$\mathbf{I}_m^{\text{ZIP}}$	is the vector of phase currents contributed by ZIP load at phases *a*, *b*, *c*;
$\mathbf{I}_m^{\text{PV}}$	is the vector of phase currents contributed by ZIP load at phases *a*, *b*, *c*;
$\mathbf{P}_m^{\text{ZIP}} + j\mathbf{Q}_m^{\text{ZIP}}$	is the vector of complex powers corresponding to loads at phases *a*, *b*, *c*;
$\mathbf{P}_m^{\text{PV}} + j\mathbf{Q}_m^{\text{PV}}$	is the vector of complex powers corresponding to solar PV inverters at phases *a*, *b*, *c*;
$\mathbf{V}_m$	is the vector of complex voltages at phases *a*, *b*, *c*.

The minus sign in (2.22) with $\mathbf{I}_m^{\text{ZIP}}$ represents the difference in the direction of current injections from the ZIP load and solar PV. In (2.24), $\mathbf{Q}_m^{\text{PV}}$ will be *zero* if unity power

factor operation of PV is considered. It is to be noted that for 3-wire networks, $\mathbf{V}_m$ comprises of the phase voltages, whereas, for 4-wire networks it contains the phase-to-neutral voltages. The specified current through the neutral wire, $\left(I_m^{\mathrm{N}}\right)^{spec}$ can be found by adding the specified phase currents I_m^a, I_m^b, and I_m^c, obtained from the vector of specified phase currents, $(\mathbf{I}_m)^{spec}$:

$$\left(I_m^{\mathrm{N}}\right)^{spec} = -\left(I_m^a + I_m^b + I_m^c\right) \tag{2.25}$$

The calculated currents can be obtained using the total system admittance matrix and the vector of system voltages using the following classical network current equation.

$$(\mathbf{I}_m)^{calc} = \sum_{n=1}^{k} \mathbf{Y}_{mn}\mathbf{V}_n \tag{2.26}$$

Here, $\mathbf{Y}_{mn}$ is the admittance matrix from bus m to n, where, n=1, 2, ..., k, and k is the total number of system buses. Mismatch in the specified and calculated current injection components in phase and neutral nodes of a three-phase feeder can be expressed in terms of their real and imaginary components using the following equations.

$$\Delta\mathbf{I}_{m_{Re}} = \frac{\mathbf{P}_m\mathbf{V}_{m_{Re}} + \mathbf{Q}_m\mathbf{V}_{m_{Im}}}{\left(\left|\mathbf{V}_{m_{Re}} + j\mathbf{V}_{m_{Im}}\right|\right)^2} - \left(\sum_{n=1}^{k}\mathbf{G}_{mn}\mathbf{V}_{n_{Re}} - \mathbf{B}_{mn}\mathbf{V}_{n_{Im}}\right) \tag{2.27}$$

$$\Delta\mathbf{I}_{m_{Re}} = \frac{\mathbf{P}_m\mathbf{V}_{m_{Im}} - \mathbf{Q}_m\mathbf{V}_{m_{Re}}}{\left(\left|\mathbf{V}_{m_{Re}} + j\mathbf{V}_{m_{Im}}\right|\right)^2} - \left(\sum_{n=1}^{k}\mathbf{G}_{mn}\mathbf{V}_{n_{Im}} + \mathbf{B}_{mn}\mathbf{V}_{n_{Re}}\right) \tag{2.28}$$

$$\Delta I_{m_{Re}}^{\mathrm{N}} = -\left(I_{m_{Re}}^a + I_{m_{Re}}^b + I_{m_{Re}}^c\right) - \left(\sum_{n=1}^{k}\mathbf{G}_{mn}^N\mathbf{V}_{n_{Re}} - \mathbf{B}_{mn}^N\mathbf{V}_{n_{Im}}\right) \tag{2.29}$$

$$\Delta I_{m_{Re}}^{\mathrm{N}} = -\left(I_{m_{Re}}^a + I_{m_{Re}}^b + I_{m_{Re}}^c\right) - \left(\sum_{n=1}^{k}\mathbf{G}_{mn}^N\mathbf{V}_{n_{Im}} + \mathbf{B}_{mn}^N\mathbf{V}_{n_{Re}}\right) \tag{2.30}$$

The subscripts $_{Re}$ and $_{Im}$ in (2.27)-(2.30) stand for *Real* and *Imaginary*, respectively. In (2.27) and (2.28), $\mathbf{G}_{mn}$ and $\mathbf{B}_{mn}$ are 3×4 matrices consisting of the corresponding real and imaginary parts of the admittance matrix from bus m to n, with respect to the phase conductors. In (2.29) and (2.30), $\mathbf{G}_{mn}^N$ and $\mathbf{B}_{mn}^N$ are 1×4 vectors consisting of the respective real and imaginary parts of the admittance matrix from bus m to n corresponding to the neutral conductor. The system of non-linear equations (2.27)-(2.30) can be solved using Newton-Raphson (N-R) iterative algorithm that needs to

relate the incremental changes in voltages with incremental changes in currents in terms of real and imaginary components, as given in the following:

$$\begin{bmatrix} \Delta \mathbf{V}_{m_{Re}} \\ \Delta V^{N}_{m_{Re}} \\ \Delta \mathbf{V}_{m_{Im}} \\ \Delta V^{N}_{m_{Im}} \end{bmatrix} = inv(\mathbf{J}) \times \begin{bmatrix} \Delta \mathbf{I}_{m_{Im}} \\ \Delta I^{N}_{m_{Im}} \\ \Delta \mathbf{I}_{m_{Re}} \\ \Delta I^{N}_{m_{Re}} \end{bmatrix} \tag{2.31}$$

The incremental voltage vector in (2.31) refers to the updates in voltages to be used in the power flow iterations of N-R algorithm, and the incremental current vector refers to the current mismatches. The 1st and 3rd row of voltage vector contains the real and imaginary components of phase voltage updates, respectively, and the 2nd and 4th row contains the updates of neutral voltage; **J** is the Jacobian matrix. For 3-wire segments of distribution networks, the neutral components are not present and therefore, the 2nd and 4th rows are not included in the N-R equations. Following this, the N-R equation for the 4-bus test system under consideration can written as,

$$\begin{bmatrix} \Delta V_2^{abc} \\ \Delta V_3^{abcn} \\ \Delta V_4^{abcn} \end{bmatrix} = inv \begin{pmatrix} J_{22}^{abc} & J_{23}^{abcn} & J_{24}^{abcn} \\ J_{32}^{abcn} & J_{33}^{abcn} & J_{34}^{abcn} \\ J_{42}^{abcn} & J_{43}^{abcn} & J_{44}^{abcn} \end{pmatrix} \times \begin{bmatrix} \Delta I_2^{abc} \\ \Delta I_3^{abcn} \\ \Delta I_4^{abcn} \end{bmatrix} \tag{2.32}$$

where,

V_2^{abc} is the 6-element incremental voltage vector consisting of $\left[\Delta V_{2_{Re}}^{abc} \quad \Delta V_{2_{Im}}^{abc}\right]^T$, corresponding to the 3-wire bus, Bus-2. *T* represents transpose;

V_3^{abcn} is the 8-element incremental voltage vector consisting of $\left[\Delta V_{3_{Re}}^{abcn} \quad \Delta V_{3_{Im}}^{abcn}\right]^T$, corresponding to the 4-wire bus, Bus-4. The similar notations hold for the other 4-wire bus, Bus-4;

I_2^{abc} is the 6-element current mismatch vector consisting of $\left[\Delta I_{2_{Re}}^{abc} \quad \Delta I_{2_{Im}}^{abc}\right]^T$, corresponding to the 3-wire bus, Bus-2;

I_3^{abcn} is the 8-element current mismatch vector consisting of $\left[\Delta I_{3_{Re}}^{abcn} \quad \Delta I_{3_{Im}}^{abcn}\right]^T$, corresponding to the 4-wire bus, Bus-4. The similar notations hold for the other 4-wire bus, Bus-4;

In (2.32), '*inv*' represents the inversion of the Jacobian matrix. The first element in

the Jacobian matrix, J_{22}^{abc}, is a 6 × 6 matrix block corresponding to the 3 wire section of the system, while J_{33}^{abcn}, J_{34}^{abcn}, J_{43}^{abcn} and J_{44}^{abcn} are 8 × 8 matrix blocks corresponding to the four wire section. The remaining, J_{23}^{abcn}, J_{24}^{abcn} and J_{32}^{abcn}, J_{42}^{abcn} are, respectively, 6 × 8 and 8 × 6 matrices, corresponding to the delta-wye transformer between the three wire and four wire network segments. It is to be noted that Bus 1, being the slack bus, has been excluded from (2.32). Following a similar type of notations, the N-R equation of the general form of 3-wire and 4-wire feeder in Fig. 2.1(b) containing *x* number of 3-wire buses and (*y*-*x*) number of 4-wire buses can be developed as given below.

$$\begin{bmatrix} \Delta V_2^{abc} \\ \vdots \\ \Delta V_x^{abc} \\ \Delta V_{x+1}^{abcn} \\ \vdots \\ \Delta V_y^{abcn} \end{bmatrix} = inv(\mathbf{J}) \times \begin{bmatrix} \Delta I_2^{abc} \\ \vdots \\ \Delta I_x^{abc} \\ \Delta I_{x+1}^{abcn} \\ \vdots \\ \Delta I_y^{abcn} \end{bmatrix} \tag{2.33}$$

Where,

$$\mathbf{J} = \begin{bmatrix} J_{22}^{abc} & \cdots & J_{2x}^{abc} & J_{2(x+1)}^{abcn} & \cdots & J_{2y}^{abcn} \\ \vdots & \ddots & \vdots & \vdots & \ddots & \vdots \\ J_{x2}^{abc} & \cdots & J_{xx}^{abc} & J_{x(x+1)}^{abcn} & \cdots & J_{xy}^{abcn} \\ J_{(x+1)2}^{abcn} & \cdots & J_{(x+1)x}^{abcn} & J_{(x+1)(x+1)}^{abcn} & \cdots & J_{(x+1)y}^{abcn} \\ \vdots & \ddots & \vdots & \vdots & \ddots & \vdots \\ J_{y2}^{abcn} & \cdots & J_{yx}^{abcn} & J_{y(x+1)}^{abcn} & \cdots & J_{yy}^{abcn} \end{bmatrix} \tag{2.34}$$

Methods of calculating Jacobian elements described in [16-17] will be deployed in this thesis. Updates of real and imaginary components of voltages are found using (2.33) in each iteration of the N-R algorithm that continues until the current mismatch in (2.21) is satisfied with an acceptable tolerance. This power flow approach using N-R algorithm works for both mesh and radial networks.

2.4 APPLICATION OF THE PROPOSED POWER FLOW APPROACH TO ASSESS PV IMPACTS

2.4.1 The IEEE 4-Bus Test Case

The IEEE 4-bus system [19] is a standard distribution test feeder to verify power flow programs with different transformer connections. The unbalanced loading scenario [19]

with delta-wye step-down transformer connection is used in this thesis. The 12.47 kV line segment is configured as 3-wire and the 4.16 kV segment is configured as 4-wire. Power flow results for the 3-wire and 4-wire segments of the test system obtained using the proposed approach are presented in Table 2-I.

TABLE 2-I

IEEE 4-BUS TEST RESULTS WITH DIFFERENT GROUNDING OPTIONS

Grounding Type	Ph.	Bus 2 [V]	Bus 3 [V]	Bus 4 [V]
Solidly Grounded	A	12350	2293	2163
	B	12360	2263	1939
	C	12285	2206	1837
	N	N/A	≈ 0	≈ 0
Resistance Grounded	A	12350	2325	2161
	B	12363	2316	2012
	C	12271	2105	1719
	N	N/A	74	74

Neutral voltages in the order of 10^{-3} V are obtained for a solidly grounded neutral (10^{-4} ohm) and are assumed as *zero*, as shown in Table 2-I for the 4-wire buses, 3 and 4. On the other hand, even a low grounding resistance of 0.3 ohm, which is within acceptable limit [7], produced a 74 V of neutral voltages at bus 3 and 4 in the presence of high unbalance in loads. The neutral voltages presented in Table 2-I cannot be directly obtained as a power flow result using a traditional 3-wire power flow approach. This neutral voltage calculation capability would be useful for distribution feeders with imperfect neutral grounding and containing unbalanced integration of solar PV.

2.4.2 Practical Test Network

The proposed power flow approach is tested on a real distribution feeder in New South Wales (NSW), Australia. It is important to note that the introduction of non-metallic under-ground water reticulation system in Australia is contributing to increased grounding impedance in the LV feeders, as many of the service drops are bonded with previously metallic water piping system for neutral grounding purpose. Unbalanced PV allocation at a high penetration level will produce increased neutral current and hence

will increase the neutral voltage in the presence of elevated neutral impedance. Therefore, the proposed power flow approach could be useful for PV impact analysis on such a network with high neutral grounding impedances.

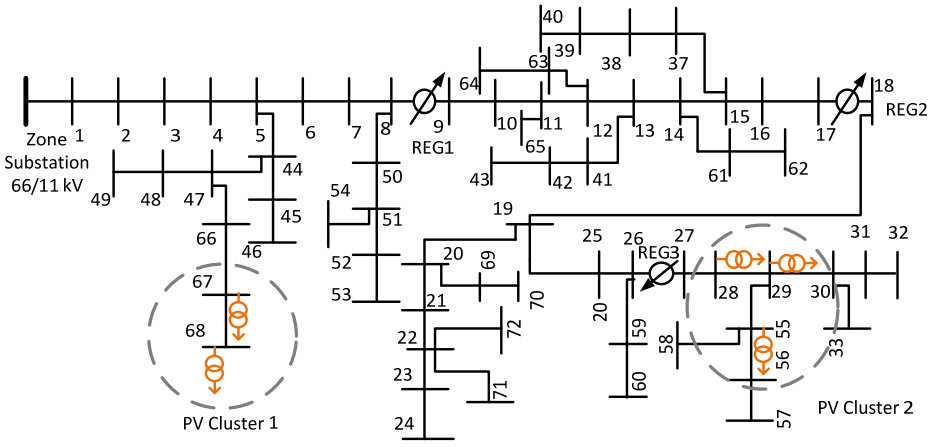

Fig. 2.6. A practical distribution feeder in NSW, Australia.

The test feeder is an 80 km long 11 kV rural feeder with 3 series voltage regulators, as shown in Fig. 2.6. The 0.4 kV LV feeders are connected at different buses along the MV feeders through 11/0.4 kV delta-wye transformers. Residential loads in the LV feeders are distributed in an unbalanced pattern among the phases. Load data measured on a practical Australian feeder are used for simulation. PV resources are integrated in a clustered form, i.e., numerous PV units are installed in a small geographical area. Transformer symbols are used to identify the feeders that form the PV clusters. Size of PV units at different residential households ranges from 2 to 5 kW. PV outputs are generated using the April irradiance data given in [23] and applied to obtain the I-V characteristic of Kyocera KC200GT [25] PV module. Numerical values of neutral grounding resistances in PV cluster 1 have been set much higher than the ones in PV cluster 2 for analysing the effects of high neutral grounding resistance. Analysis is performed using both idealistic and realistic values of neutral to ground resistance in PV cluster 2. IEEE Std. 182-1991 [8] suggests that neutrals of LV systems are typically grounded solidly. For a solidly grounded neutral, phase-to-ground fault current can be equal to 100% or greater than the three-phase fault current [8]. Based on this criterion, and using the MV/LV substation and LV feeder data of the test system under study, an idealistic value of the neutral to ground resistance for solidly grounded neutral was determined as 0.05 ohm. A realistic value of 0.5 ohm is selected according to the recommended value of neutral grounding resistance in a Combined Multiple Earthed

Neutral (CMEN) system for Australian distribution utilities [9-10]. To consider a 10-times increase in neutral grounding resistance due to bonding with non-metallic water piping system as discussed in [26], neutral grounding resistance of 5 ohm is used in PV cluster 1.

2.4.3 PV Impacts on LV Networks

Solar PV resources generate at their peak capacity during midday, depending on the ambient sun insolation and temperature. Household load demand is comparatively lower during this time. Power generation from PV resources, therefore, may exceed the load level at the PV connection point at this time, and voltage rise may be observed. Such a scenario is shown in Fig. 2.7 at one of the LV feeder ends selected from both of the PV clusters in the network. The upper plot in Fig. 2.7(a) shows voltage from PV cluster 1, which shows significant rise in voltage at midday, and phase *a* voltage exceeds the upper limit. The lower plot in Fig. 2.7(b) shows the voltage rise in PV cluster 2, which is maintained within the limit by the action of voltage regulator REG3 (in Fig. 2.6).

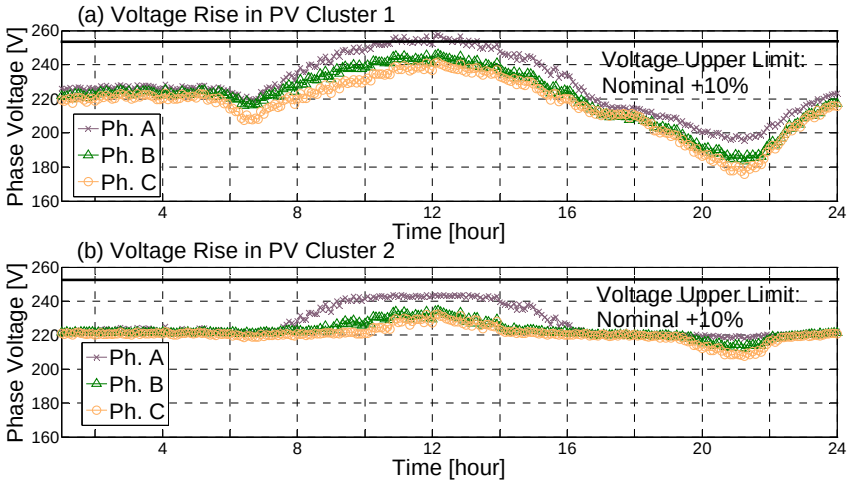

Fig. 2.7. Daily voltage profile at LV feeder end (a) PV cluster 1 (b) PV cluster 2.

Due to unbalanced allocation of PV units, voltage rise is different at different phases of the feeder. This unbalance in power injection produces significant increase of neutral current in the LV feeder at midday, as shown in Fig. 2.8. The upper plot in Fig. 2.8(a) shows the phase and neutral currents at an LV substation bus in PV cluster 1, and the lower plot in Fig. 2.8(b) shows the same for PV cluster 2. It is observed that in PV cluster 1, the neutral current exceeds phase *b* and *c* currents, and nearly reaching the phase *a* current at midday. The situation is less severe in PV cluster 2 with much lower grounding resistance. The high neutral current produced by unbalanced PV injection

increases the neutral voltage as shown in Fig. 2.9; the upper plot in Fig. 2.9(a) shows neutral voltage in PV cluster 1 that remains nearly at 1 V during high PV generation period. This is already higher than the common-mode noise limit of 0.5 V [13] for sensitive equipment. With the idealistic value of neutral resistance of 0.05 ohm in PV cluster 2, the neutral voltage in cluster 2 does not exceed 0.15 V, as shown in Fig. 2.9(b). However, using the realistic value of 0.5 ohm in PV cluster 2, the neutral voltage in cluster 2 slightly exceeds the common-mode voltage limit of 0.5 V. Such neutral to ground voltages may exceed the tolerance level with further increase in unbalanced PV allocation which would impose potential safety hazards and may also cause damage of sensitive equipment [13-14]. Despite the results presented in this thesis, utilities endeavour to change the connection of customers to ensure a more balanced allocation of PV inverters across the phases.

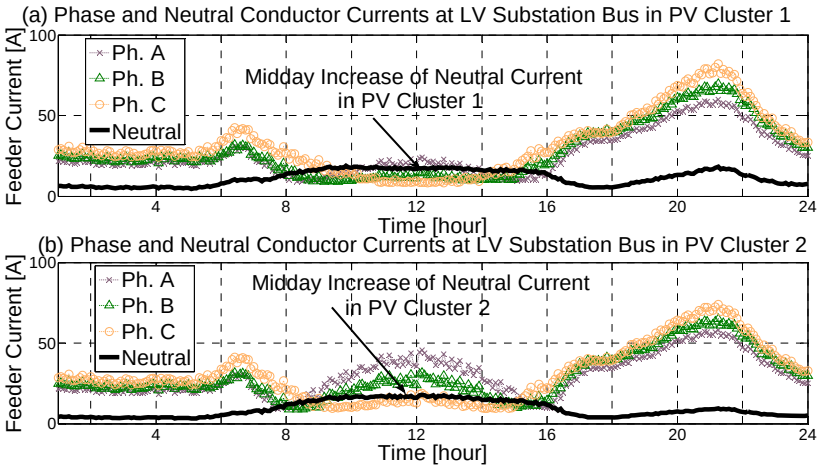

Fig. 2.8. Daily variation of neutral current (a) PV cluster 1 (b) PV cluster 2.

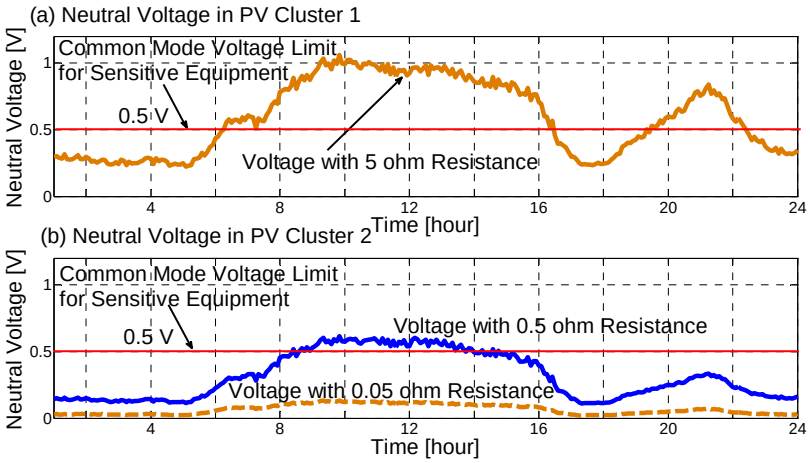

Fig. 2.9. Daily variation of neutral voltage (a) PV cluster 1 (b) PV cluster 2.

Although the simulation results presented in this chapter are related to the demand

curve at a single location in the network, the proposed power flow tool is developed in such a way that it can consider the diversity of loads at different locations, if the diversified load data is available.

A case study is conducted for a scenario where the total PV generation in the feeder is higher than the feeder demand and the results are presented in Fig. 2.10. In this case, surplus power from PV resources is injected into the upstream MV network. This is shown in the upper plot of Fig. 2.10(a) with a reverse power flow at one of the LV substation buses in a PV cluster. This suggests that a voltage rise is created in the MV feeder at the immediate upstream of the PV clusters due to the reverse power flow. The reactive power flow at the substation bus, however, remains nearly unchanged as shown in the lower plot of Fig. 2.10(b), because the PV inverters are modeled to operate at unity power factor.

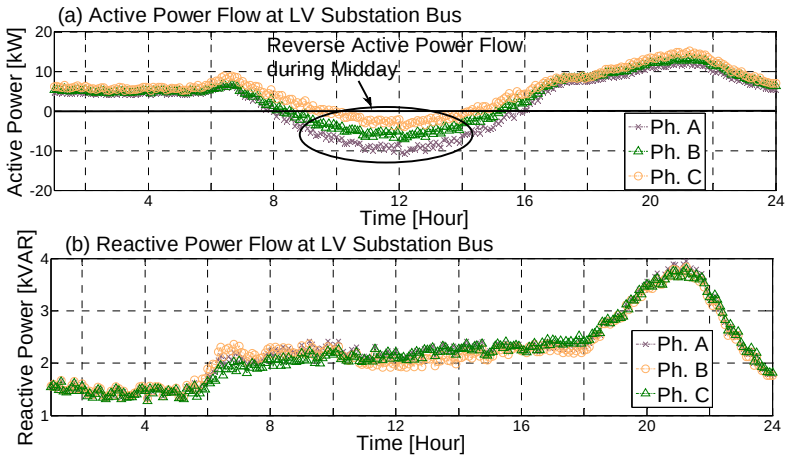

Fig. 2.10. Daily variation of active and reactive power flow at substation node (a) active power (b) reactive power.

It is to be noted, if the neutral grounding resistances are approximated to be *zero*, then the power flow results obtained by including the neutral wire would not be different than the results obtained using a 3-wire representation of a 4-wire LV feeder. The grounding resistances need to be non-zero to observe the effect of including neutral wire in the network model.

2.4.4 PV Impacts Propagated to MV Networks

PV impact propagation to the MV network is presented in this thesis using MV level voltage profiles. Fig. 2.11 shows the voltage profile of the MV feeder along the feeder length that contains the two PV clusters. This voltage profile corresponds to the time of

peak PV generation in the cluster. Voltage rise is observed along one of the spurs of the MV feeder (through the buses 47, 66, 67 and 68 in Fig. 2.6) due to the absence of voltage regulator at the immediate upstream.

On the other hand, voltage rise produced by the PV cluster 2 is bucked down by REG3. This effect is also observed in Fig. 2.12 that shows the tap operations of the REG3; Fig. 2.12(a), (b) and (c) shows the tappings of phase *a*, *b*, and *c*, respectively. The positive tap numbers indicate voltage bucking operation, whereas, the negative tap numbers mean voltage boosting. It is observed that at midday, from about 11 am to 1 pm, the tapping of phase *a* is positive that indicates the action of REG3 to reduce the voltage rise caused by the PV cluster downstream; phase *b* and *c* however, remains mostly at the neutral state as voltage in these phases remain within the limits. In the evening, tap numbers in all the phases are negative indicating a voltage boosting operation.

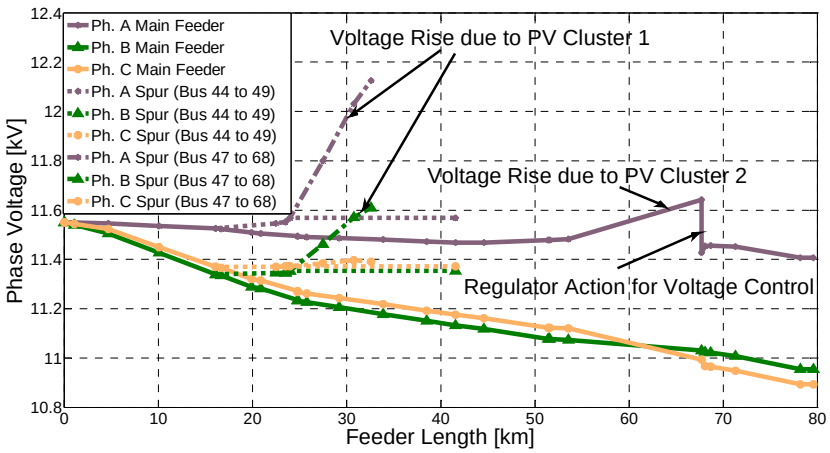

Fig. 2.11. Midday voltage profile along the 11 kV feeder.

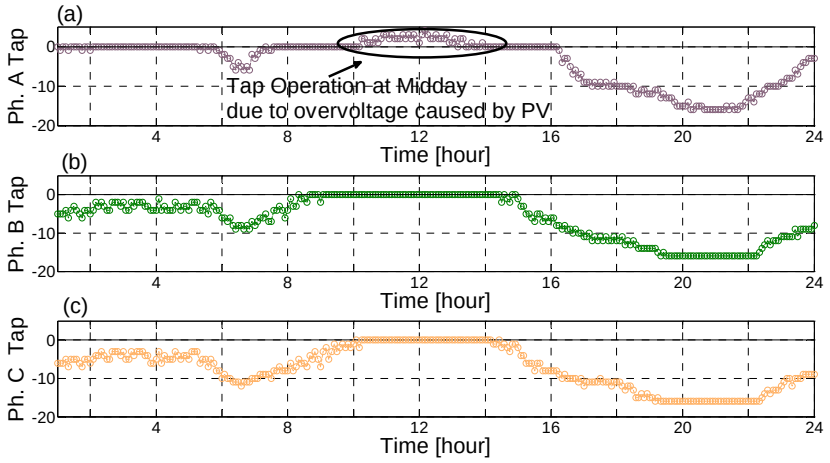

Fig. 2.12. Daily tap operations of REG3 (a) phase *a* tap (b) phase *b* tap (c) phase *c* tap.

2.5 CONCLUSIONS

A three-phase power flow approach capable of distribution network analysis by preserving the actual wiring configuration of MV and LV networks has been proposed for realistic analysis of solar PV impacts. This approach would be particularly useful for multigrounded LV networks where the neutral wire needs to be modeled explicitly due to the presence of neutral grounding impedances. A real distribution network, consisting of 3-wire MV and 4-wire LV feeders with multiple neutral groundings, has been used to verify the applicability of the proposed power flow approach. Unlike the traditional 3-wire power flow, the proposed approach is able to provide the neutral current and voltage caused by unbalanced allocation of single-phase rooftop PV units, and hence would be able to provide information regarding possible safety issues. With the peak level of PV output during midday, the neutral current and voltage impacts become more significant, as verified through a series of power flow calculations corresponding to a 24-hour load and PV output variations. Simultaneous modelling of 3-wire and 4-wire systems using the proposed approach enables the investigation the PV impacts propagated to the upstream MV level. Further research can be carried out using the proposed approach to investigate the voltage regulation coordination and protection issues against high neutral to ground voltage related to 3-wire MV and 4-wire multigrounded LV systems with distributed resources.

REFERENCES

[1] F. Katiraei, K. Mauch, and L. Dignard-Bailey, "Integration of photovoltaic power systems in high-penetration clusters for distribution networks and mini-grids," *International journal of distributed energy resources,* vol. 3, pp. 207-224, 2007.

[2] R. A. Walling, R. Saint, R. C. Dugan, J. Burke, and L. A. Kojovic, "Summary of Distributed Resources Impact on Power Delivery Systems," *IEEE Transactions on Power Delivery* vol. 23, pp. 1636-1644, 2008.

[3] M. Thomson and D. G. Infield, "Network Power-Flow Analysis for a High Penetration of Distributed Generation," *IEEE Transactions on Power Systems* vol. 22, pp. 1157-1162, 2007.

[4] A. Canova, L. Giaccone, F. Spertino, and M. Tartaglia, "Electrical Impact of Photovoltaic Plant in Distributed Network," *IEEE Transactions on Industry Applications* vol. 45, pp. 341-347, 2009.

[5] A. von Jouanne and B. Banerjee, "Assessment of voltage unbalance," *IEEE Transactions on Power Delivery* vol. 16, pp. 782-790, 2001.

[6] P. Juanuwattanakul and M. A. S. Masoum, "Voltage stability enhancement for unbalanced

multiphase distribution networks," in *IEEE Power and Energy Society General Meeting*, Detroit, MI, USA, 24-29 Jul., 2011, pp. 1-6.

[7] T. H. Chen and Y. Wen-Chih, "Analysis of multi-grounded four-wire distribution systems considering the neutral grounding," *IEEE Transactions on Power Delivery* vol. 16, pp. 710-717, 2001.

[8] "IEEE Recommended Practice for Grounding of Industrial and Commercial Power Systems," *IEEE Std 142-2007 (Revision of IEEE Std 142-1991),* pp. 1-225, 2007.

[9] Ausgrid, "Design Standard for Distribution Earthing," June 2005.

[10] Ergon Energy. *Distribution System Earthing Guidelines* [Online]. Available: https://www.ergon.com.au/__data/assets/pdf_file/0018/6615/Distribution-System-Earthing-Guidelines.pdf

[11] R. M. Ciric, A. P. Feltrin, and L. F. Ochoa, "Power flow in four-wire distribution networks-general approach," *Power Systems, IEEE Transactions on,* vol. 18, pp. 1283-1290, 2003.

[12] J. C. Balda, A. R. Oliva, D. W. McNabb, and R. D. Richardson, "Measurements of neutral currents and voltages on a distribution feeder," *IEEE Transactions on Power Delivery,* vol. 12, pp. 1799-1804, 1997.

[13] T. M. Gruzs, "A survey of neutral currents in three-phase computer power systems," *IEEE Transactions on Industry Applications* vol. 26, pp. 719-725, 1990.

[14] Power & Systems Innovation, Inc. *Power Quality - The Basics* [Online]. Available: http://www.psihq.com/iread/pqbasics.htm

[15] J. A. Martinez and J. Mahseredjian, "Load flow calculations in distribution systems with distributed resources. A review," in *IEEE PES General Meeting*, Detroit, Michigan, USA, 24-29 July, 2011, pp. 1-8.

[16] P. A. N. Garcia, J. L. R. Pereira, S. Carneiro, Jr., V. M. da Costa, and N. Martins, "Three-phase power flow calculations using the current injection method," *Power Systems, IEEE Transactions on,* vol. 15, pp. 508-514, 2000.

[17] D. R. R. Penido, L. R. de Araujo, S. Carneiro, J. L. R. Pereira, and P. A. N. Garcia, "Three-Phase Power Flow Based on Four-Conductor Current Injection Method for Unbalanced Distribution Networks," *IEEE Transactions on Power Systems* vol. 23, pp. 494-503, 2008.

[18] R. C. Dugan and S. Santoso, "An example of 3-phase transformer modeling for distribution system analysis," in *Transmission and Distribution Conference and Exposition, 2003 IEEE PES*, 2003, pp. 1028-1032 vol.3.

[19] W. H. Kersting, "Radial distribution test feeders," in *IEEE Power Engineering Society Winter Meeting*, Columbus, Ohio, USA, 2001, pp. 908-912 vol.2.

[20] J. Arrillaga and N. R. Watson, *Computer Modelling of Electric Power Systems (including Facts)*. New York, NY, USA: John Wiley & Sons, Inc. , 2001.

[21] L. Ning, X. Yulong, H. Zhenyu, F. Puyleart, and S. Yang, "Load component database of household appliances and small office equipment," in *IEEE Power and Energy Society General Meeting - Conversion and Delivery of Electrical Energy in the 21st Century*, Pittsburgh, PA, USA, 20-24 July, 2008, pp. 1-5.

[22] K. P. Schneider and J. C. Fuller, "Detailed end use load modeling for distribution system analysis," in *IEEE Power and Energy Society General Meeting*, Minneapolis, MN, USA, 25-29 July 2010, pp. 1-7.

[23] G. M. Masters, *Renewable and Efficient Electric Power Systems*. New Jersey: Wiley-IEEE Press, 2004.

[24] M. G. Villalva, J. R. Gazoli, and E. R. Filho, "Comprehensive Approach to Modeling and Simulation of Photovoltaic Arrays," *IEEE Transactions on Power Electronics,* vol. 24, pp. 1198-1208, 2009.

[25] Kyocera. *KC200GT High Efficiency Multicrystal Photovoltaic Module* [Online]. Available: http://www.energymatters.com.au/images/kyocera/KC200GT.pdf

[26] J. Werda, J. Chan, and P. Freeman. *Electrical Earthing - Risk Management Strategies for the Water Industry, presented at the 2nd Annual Water Industry Engineers and Operators Conference, Newcastle, NSW, Australia, 8-10 April, 2008.* [Online]. Available: http://www.wioa.org.au/conference_papers/08_nsw/documents/johnwerda.pdf

Chapter 3

A SAX-BASED ADVANCED COMPUTATIONAL TOOL FOR ASSESSMENT OF CLUSTERED ROOFTOP SOLAR PV IMPACTS ON LV AND MV NETWORKS IN SMART GRID

ABSTRACT

Future distribution networks with increasing level of solar PV penetration will be managed using smart grid technologies capable of producing appropriate and timely response during normal and abnormal operational events. Distribution feeder loads vary throughout the day according to the trend of consumption of the customers. Solar PV outputs fluctuate in proportion to irradiance level of sun. Simultaneous occurrence of both of these variations would result in various operating conditions that may lead to unexpected events, and would require a large amount of network data to be processed and analysed for decision making. It is envisaged that such data will be available in the future grids with the availability of smart technologies and advanced communication in residential dwellings, commercial buildings and industrial complexes. In this thesis, an advanced intelligent computational tool is developed to characterise and analyse the large amount of data associated with wide variations in network behaviour using SAX (Symbolic Aggregate Approximation) and pattern recognition. The proposed tool is capable of dealing with network asymmetry, load unbalance, single-phase solar PV integration and their impacts on upstream networks and will assist in making right and timely decisions to mitigate adverse impacts of solar PV. The proposed tool has been tested with a practical three-phase distribution system in Australia and can provide an extensive assessment with less computational effort and time.

3.1 INTRODUCTION

A large number of single phase solar photovoltaic (PV) units are expected to be integrated with future distribution grids in clustered form [1]. Conventional distribution networks are typically designed to supply electric power from upstream high or medium voltage networks to consumers through low voltage feeders. With integration of multiple numbers of solar PV units, normally expected network behaviour may be changed [2]. For example, voltage profile may rise along the feeder with high PV penetration, whereas traditionally voltage drop along the feeder is observed. Similarly, power could flow from load (consumers) to source (substation), whereas in traditional distribution grids power flow from source (substation) to load (consumers) is typically found. The degree of change in network behaviour will vary throughout the day depending on the variation in load demand and PV output. The highest amount of change could typically be expected at noon time when solar PV units would generate at the peak level of the available capacity. With high PV penetration, the risk of violating system operation limits caused by changes in network behaviour may therefore arise at this period of the day. Considering the possibility of operation limit violation, it is important to investigate the potential impacts of PV clusters on distribution network to take corrective actions so that solar PV penetration can be increased to the desired level.

At present, the assessment of solar PV impacts is typically performed by applying a number of assumptions on network data, especially the load demand data on LV feeders. Simplification of network is also performed by aggregating all the feeder loads and PV generation at the LV substation secondary side [3]. In future, under smart grid environment, numerous smart meters with integrated communication facilities are anticipated to be installed to collect distribution feeder operational data throughout the day that would be available for analysis of normal and abnormal events. Impact analysis of solar PV cluster then could be performed with realistic data on the original network topology retaining detailed model of LV networks. This would produce results with higher accuracy and would aid in more effective decision making for implementing corrective actions. However, a massive amount of high resolution time series data will be collected by the smart meters and need to be analysed. The task of impact assessment would be easier and would incur less computational time if the assessment tool is capable of data mining to detect hidden patterns and anomalies from the stored database and identify clusters that are of interest for PV impact assessment. These clusters will

contain smaller dataset and can be studied in more details with less computational efforts and time. Intelligent clustering and pattern recognition techniques may be used to achieve this.

Further, performing data mining tasks on raw data may require extensive computational efforts. Approximation of the high resolution time series data can be performed to decrease the size of the database so that the computational performance of the tool can be improved. A number of time series approximation techniques have been proposed in the data mining literature [4]. Recently, a symbolic approximation technique, namely SAX (Symbolic Aggregate Approximation) method, for time series data representation has been proposed [4], that features data dimensionality reduction and lower bounding capability [5] which are essential for data mining tasks. Only a few applications of this method in power systems [6] have been observed so far. Authors in this paper have reduced a number of electricity price time series data into SAX form prior to clustering resulting in improved computational performance. The SAX method, however, has been applied extensively in other disciplines with reportedly excellent results [7]. Based on the beneficial features of this method discussed in literature, the purpose of this thesis is to explore the usefulness of this method for the assessment of solar PV impacts using large amount of time series data available from smart meters and other smart appliances in future distribution grids.

The major contribution of this thesis is to propose a comprehensive rooftop solar PV impact assessment tool to analyse a large database of future smart grid measurements. The novelty of the contribution lies in the application of SAX algorithm combined with data mining and pattern recognition techniques for PV impact analysis by extracting the behaviour of a particular PV impact of interest (such as voltage rise, reverse power flow, cloud passing etc.) at a given location and time of occurrence from a large database of smart grid measurements. This offers a new way of analysing data, impact characterization and feature extraction from a huge volume of high-resolution recorded data collected from a distribution system containing solar PV. The tool will be capable of PV impact analysis based on a large set of realistic time series data available from numerous smart meters installed in the networks. SAX approximation of time series data will be performed to reduce the dimensionality of the database. Time series clustering and anomaly detection techniques will then be applied to identify only the data that are important for PV impact analysis. With a large number of single phase PV

units integrated into distribution feeders, the tool will also be capable to evaluate the solar PV impacts on individual phases in LV systems, as well as on the upstream MV networks.

3.2 CLUSTERED ROOFTOP SOLAR PV IMPACTS ON DISTRIBUTION NETWORKS

Solar PV impacts on distribution networks are experienced in terms of changes in operational behaviour of the networks, such as, changes in voltage, power flow, power loss, etc. The impacts of the integration of solar PV in clustered form may propagate to the upstream networks. Hence, the changes produced by the solar PV units in the LV networks may impact the operation of the voltage control devices in the MV networks. For example, tap operation of voltage regulators may be influenced by the change in voltage profile caused by solar PV units. Several impacts of clustered solar PV on distribution networks are briefly described below.

3.2.1 Voltage Rise

In the traditional distribution networks, voltage along a distribution feeder typically reduces from the voltage at the substation bus, along the feeder, due to voltage drop across the line segments. If solar PV resources are integrated, loads are served locally resulting in less current flowing through the feeders. This reduces the amount of voltage drop and power losses and as a result voltage profile is improved. However, if the generation from PV resources are high enough to offset the loads on the feeder, the surplus power will create voltage rise. This effect may be observed at midday when total PV generation in the feeder is higher than the feeder load demand. With cluster based installation of PV, the voltage rise impact may propagate to upstream MV networks.

Voltage profile throughout the day at a given bus of a hypothetical distribution feeder, shown in Fig. 3.1(a), would look like the one given in Fig. 3.1(b); the voltage profiles with and without solar PV are identified with arrows showing the voltage rise at midday caused by solar PV output. Fig. 3.1(b) clearly indicates that two different types of time series patterns are produced with and without PV inclusion.

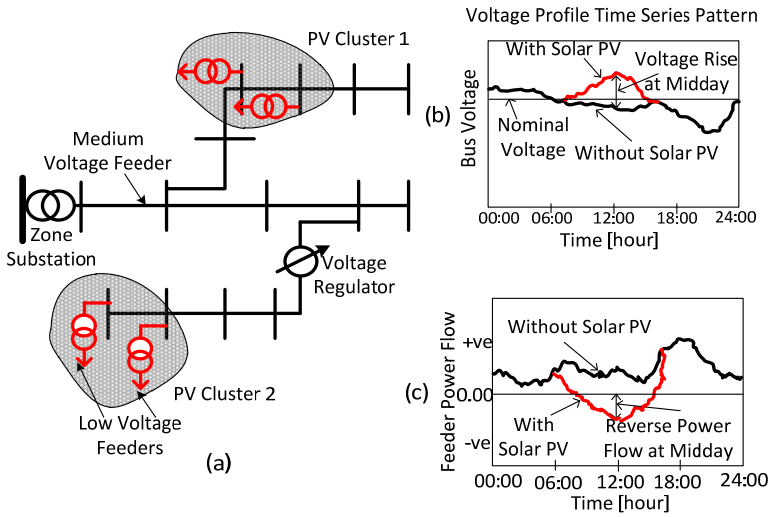

Fig. 3.1. Time series patterns of solar PV impacts; (a) simple distribution feeder (b) voltage profile pattern (c) power flow pattern.

3.2.2 Reverse Power Flow

LV distribution feeders are typically radial and the direction of the power flow is, therefore, from substation towards the loads. Similar to the voltage rise impact, power flow direction would be changed when PV generation exceeds the load demand. Active power flow profile throughout the day at the secondary side of an LV distribution feeder is shown in Fig. 3.1(c). Reverse power flow is observed at midday due to excess output from solar PV. The difference in power flow time series patterns due to PV integration is obvious from Fig. 3.1(c).

3.2.3 Variation of Feeder Power Loss

Power losses would typically decrease in distribution feeder with solar PV resources integration as less amount of power is imported from the substation. However, with a high penetration of PV cluster, if the reverse power flow is higher than the power flow without PV, an increase in feeder power loss may be observed [8]. Power loss may vary due to the variation of the PV output at the different time of the day.

3.2.4 Voltage Unbalance

Allocation of PV inverters among different phases of a distribution feeder is mainly controlled by the choice of the customers. The distribution of PV generation in a PV cluster therefore may not be equal at all the phases. This may deteriorate the existing voltage unbalance factor of the network [9]. The unbalance factor may vary from time to time due to the variations of solar irradiance and PV output.

3.2.5 Change in Tap Operations

Tapping operation of voltage regulators in the MV distribution feeders is performed in response to changes in voltage at a remote position downstream to the regulator (or often referred to as the "load centre"). Voltage regulators may tap up or down their tap positions to keep voltage at the load centre within a bandwidth of voltage upper and lower limits. Voltage rise caused by PV clusters may require the regulators to operate during midday to keep the voltage profile below the upper limit.

3.3 PROPOSED COMPUTATIONAL TOOL FOR SOLAR PV IMPACT ASSESSMENT IN SMART GRID ENVIRONMENT

As stated earlier, huge computational effort will be necessary to perform PV impact assessment using the entire volume of data stored by numerous meters installed in a future smart grid environment. For example, the length of a voltage profile time series data measured at a 5-minute interval for a week at some arbitrary bus in a three-phase feeder will be 2016, for each phase. If the feeder contains 100 buses, then the weekly voltage profile database will contain at least 100×2016 pieces of data for each phase. However, the analysis of the entire volume of the stored data may not be of significance for the investigation of solar PV impacts. This is due to the fact that the level of PV impact on the network behaviour will depend on many factors, such as, the location of the PV cluster, penetration level, clearness of sky, sun insolation level, temperature, etc. Therefore, solar PV impacts, such as voltage rise or reverse power flow, may not be significantly visible in all the stored time series data. If the times and the PV locations can be found when the PV impacts are more intense, then detailed analysis can be carried out for those scenarios only.

To select the time series data of particular importance for PV impact assessment from a large database, data mining using clustering and pattern recognition techniques would be necessary. Such a method can identify hidden patterns (such as incidents of voltage rise) and anomalies in the time series database. However, performing this sort of data mining tasks on the original time series data will impose significant computational burden on the tool. A time series approximation technique that can reduce the dimensionality of the data while retaining its features at the same time can be useful in this purpose. A new symbolization based time series approximation technique termed as Symbolic Aggregate Approximation (SAX) has attracted much attention of the data

mining research community due to its capability to reduce the computational effort in data mining applications. The proposed tool in this thesis will use SAX method to reduce data dimensionality prior to applying data mining techniques. Once the patterns of interest and times of anomalies have been identified, these smaller set of database can be analysed in greater details to understand why they occur, to help in predicting such future events, and to design corrective measures to reduce the impacts of the rooftop solar PV.

Usually, the detailed analysis is to be carried out using load flow analysis to further investigate the daylong behaviour of distribution networks with time varying load and PV generation data. Adoption of a load flow calculation algorithm that needs less computational time and effort would be necessary in this part to make the analysis tool practically useful. Current-mismatch based Newton-Raphson algorithm [10] will be used in the proposed tool that will speed up the computational process.

The advantage of using SAX method in data mining through pattern recognition and the current-mismatch based Newton-Raphson load flow method will be described in the following subsections.

3.3.1 A Brief Review of SAX Method

Time series data consists of patterns of an event sampled over a time period at some specified interval. The length of the data would typically be huge, particularly if high resolution in measurement is used. Working with a huge amount of time series database for data mining applications would impose a high computational burden on the analysis tool. To reduce this burden, SAX method can be applied to symbolise the time series data to reduce its dimensionality. Moreover, it can ensure the lower bounding of the data. Both of these features will be explained below briefly [4].

Consider a time series data S of length n that has the elements s_1, s_2, … s_n. The first step in SAX approximation is to normalise the original n-dimensional time series data and then to convert it into a w-dimensional time series T with elements t_1, t_2, … t_w, where, typically, $w<<n$. This can be performed using a Piecewise Aggregate Approximation (PAA) [11] of the original time series S using the following expression.

$$t_i = \frac{w}{n} \sum_{j=\frac{n}{w}(i-1)+1}^{\frac{n}{w}i} s_j \tag{3.1}$$

Once the PAA representation of the data is obtained using (3.1), the lower dimensional time series T is then transformed into discrete form through a number of equiprobable symbols. This is performed using Gaussian distribution, as normalised time series data usually show a highly Gaussian distribution characteristic [4]. To obtain the symbols having equal probability, breakpoints need to be defined that will divide the Gaussian curve into equal sized areas.

For example, if the PAA representation of a time series is desired to be symbolised using "a" number of letters from the alphabet, then a-1 number of break points have to be obtained that will divide the Gaussian curve into "a" number of equal sized areas. This method is demonstrated in Fig. 3.2 for a time series that is symbolised using 3 letters of the alphabet, that is, a = 3.

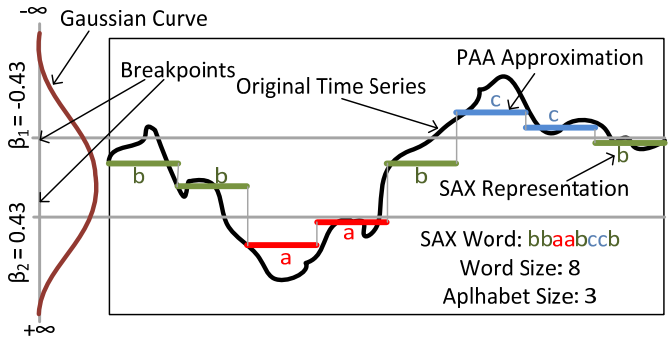

Fig. 3.2. SAX representation of time series data

To perform this, the Gaussian curve $N(0,1)$ is divided into 3 areas using the breakpoints at β_1 and β_2. Values of the breakpoints are obtained from standard normal distribution tables [4]. In general, if the symbolization is to be performed using "a" number of alphabets, the breakpoints of the Gaussian curve will be located at $\beta_1, \beta_2, \ldots, \beta_{a-1}$.

Symbolization of the time series is performed in ascending order of breakpoints. For example, the PAA coefficients below the smallest breakpoint are symbolised with alphabet 'a'; similarly, the PAA coefficients greater than or equal to the smallest breakpoint and less than the second smallest breakpoint is symbolised with alphabet 'b', and so on. The concatenation of all the symbols representing the PAA version of the

original time series is defined as *word* and the total number of different letters of the alphabet used is called *word size* [12]. The total number of different alphabets used in the word is defined as *alphabet size* [12]. The word size represents the total number of segments into which the original time series will be divided and the alphabet size indicates the granularity of the data. Fig. 3.2 shows the SAX representation of an original time series using an 8-word and 3-alphabet SAX data.

Dimensionality reduction of original time series data using an approximation technique needs to be performed in such a way that any essential feature of the data is not lost [5]. In time series data mining, distances among multiple time series are usually obtained using different types of distance measures. The most commonly used distance measure is the Euclidean distance [4, 12] as shown in Fig. 3.3(a), for two time series S_1 and S_2. Essential features for data mining in the approximated data are retained if the distance measures of the approximated data are less than or equal to the distance measures of the original data [5]. This is defined as *Lower Bounding* of the distance. For the SAX representations of SW_1 and SW_2 in Fig. 3.3(b) of the original time series in Fig. 3.3(a), the lower bounding will ensure that,

$$D(SW_1, SW_2) \leq D(S_1, S_2) \tag{3.2}$$

where, $D(SW_1, SW_2)$ is the lower bounding distance measure of the SAX data and $D(S_1, S_2)$ is the distance between original time series data.

For the SAX representation, the lower bounding distance measure is obtained from the breakpoints of the Gaussian curve using a function named '*mindist*' [4] defined as follows,

$$mindist(SW_1, SW_2) = \sqrt{\frac{n}{w}\sum_{i=1}^{w}[dist(sa_{1i}, sa_{2i})]^2} \tag{3.3}$$

where, sa_{1i} and sa_{2i} are the elements (alphabets) of the SAX words SW_1 and SW_2, and '*dist*' is the distance function whose values can be obtained by table-lookup method [4] from a table containing the breakpoints of the Gaussian curve used for symbolization of the original time series.

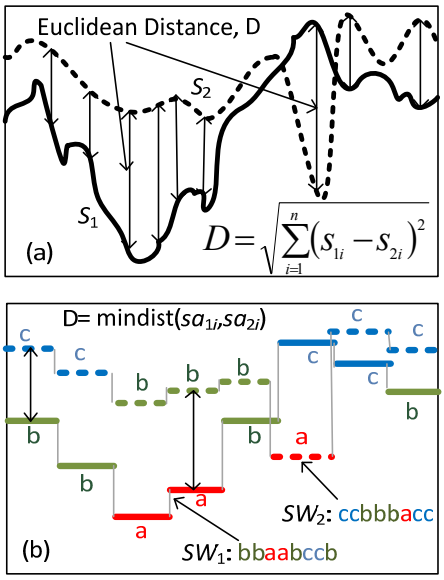

Fig. 3.3. Distance measure of time series data; (a) Euclidean distance for original data (b) Gaussian curve breakpoint distance for SAX word.

3.3.2 SAX Representation of Network Behaviour Data

The selection of the word and alphabet size for SAX representation is highly data dependent and may be infeasible to determine analytically [4]. Determination of the suitable word and alphabet size is therefore performed experimentally. It is anticipated that the smart meters will store network behaviour data (e.g., voltage, current) in the normally used units (e.g., Volt, Ampere). To perform SAX conversion, this data has to be normalised to have values between *zero* and *one*. Then a suitable size of word and alphabet has to be determined experimentally to obtain SAX representations that reduce the dimensionality yet retains the main features of the data. An example of SAX conversion of a daylong voltage profile of a distribution feeder node with solar PV is presented in Fig. 3.4.

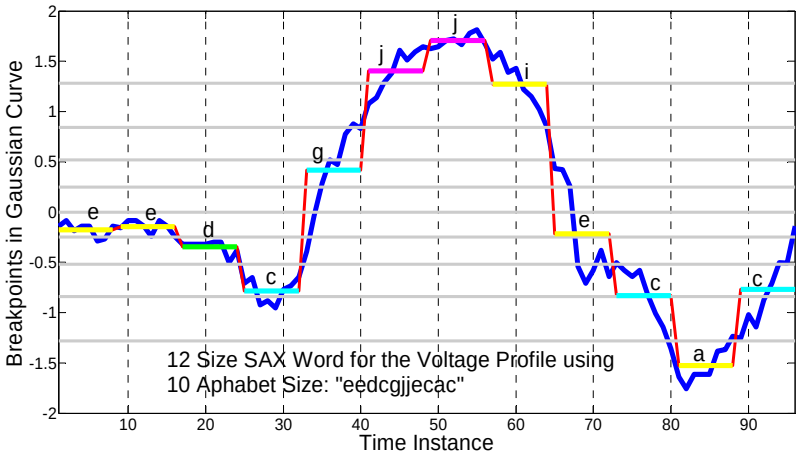

Fig. 3.4. SAX approximation of a time series voltage profile data.

3.3.3 Clustering of Patterns from the Time Series Datasets

Clustering of the time series data containing network behavioural patterns will be needed to find out which group of data is of interest for detailed impact assessment of solar PV.

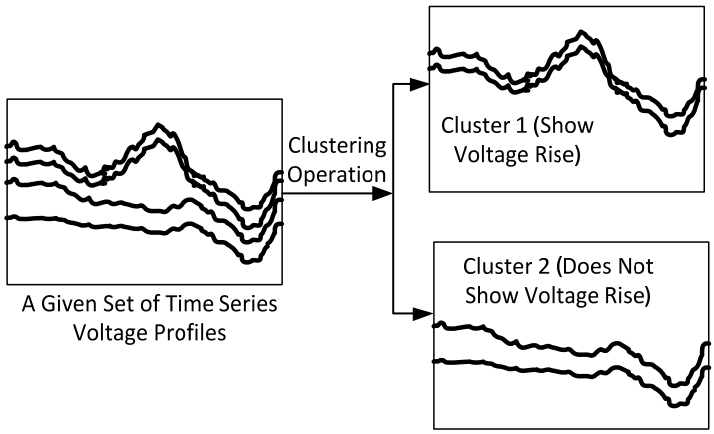

Fig. 3.5. Identification of voltage rise patterns using clustering technique.

For example, Fig. 3.5 shows that a given set of time series patterns containing voltage profiles with and without rising trend can be separated into two different clusters. For solar PV impact assessment, the cluster containing voltage rise profiles will only be used for further analysis.

Several methods of time series clustering have been reported in literature [13]. The proposed tool will use the partitional clustering technique using k-means algorithm. The k-means technique is an iterative clustering algorithm that first determines the cluster centroids and then minimises the sums of the data-point to cluster centroid distances, summed over all the clusters, iteratively [13]. For example, S_k, k=1, 2, … n represents n-

number of time series patterns that needs to be grouped into c number clusters. Using k-means algorithm, c number of cluster centroids are first defined. An objective function, J, is then defined using the sums of data-point to cluster centroid distances over all clusters, as shown below [13].

$$J = \sum_{i=1}^{c} \sum_{k=1}^{n} \left\| S_k - v_i \right\|^2 \tag{3.4}$$

where, v_i, i=1, 2 … c are c-number of cluster centroids. These cluster centroids are updated iteratively until J is minimised.

The number of points in each of the cluster centroids is equal to the length to the time series data. Therefore, the computational effort to calculate the cluster centroids and to perform the iterative adjustment is reduced when lower dimensional approximation of the time series is used. Application of k-means on SAX representation of data also produces better results as the initialization of the cluster centroids with a lower dimensional data improves the quality of the results [4].

3.3.4 Detection of Anomalies in Datasets

In some cases, time series data collected and stored by the smart meters may contain unusual or exceptional network behaviour. For example, passing clouds may introduce fluctuations in the smooth rising trend of the voltage profile time series data. Detection of the unusual patterns is necessary for performing further analysis. Standard algorithms for unusual pattern recognition can be used for this purpose. For simplicity, Brute Force [12] algorithm is used in this thesis that measures the non-self match distances of each of the time series from each other and the time series that possesses the largest distance from its nearest match is detected as the most unusual pattern. This algorithm is explained below for finding the most unusual pattern from 3 voltage profiles.

The voltage profiles are arranged in a matrix form as shown in Fig. 3.6. For the 3 voltage profiles, size of the matrix is 3x3. The diagonal cells are left crossed as only the non-self match distances are of use for anomaly detection. The off-diagonal elements in each column give the non-self distances of the voltage profiles from each other. The smallest distance in each column provides the nearest match distance of each voltage profiles. The largest of the three smallest distances from the three columns in the matrix thus indicates the most anomalous voltage profile, which is, VP_3. Similarly, the second

most anomalous profile can be found using the second largest of the nearest match distance. In this way, a ranking of the anomalous time series profiles can be made.

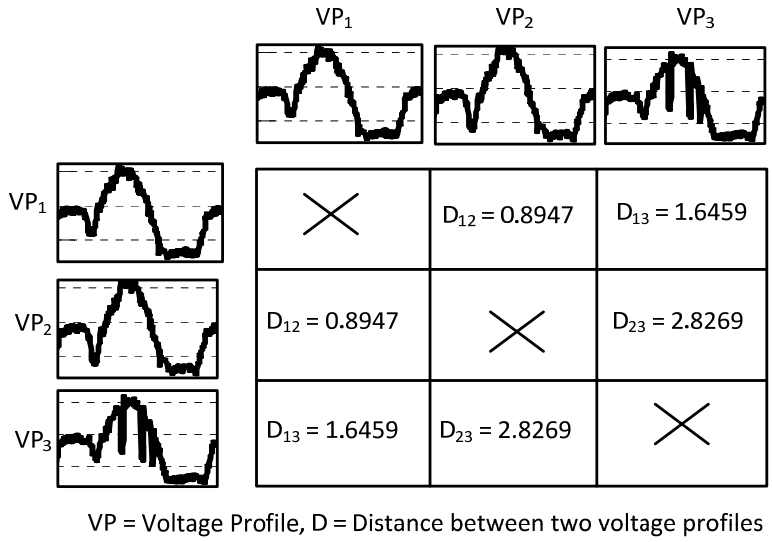

Fig. 3.6. Algorithm for finding unusual voltage profile

3.3.5 Time Series Power Flow Analysis with Solar PV

Once the time series with the patterns of interest and anomalies have been identified, power flow calculations have to be conducted. The formulation of current mismatch based load flow equation with solar PV output at *k*-th time instant, where $k = 1, 2, \ldots n$ (*n* is the length of time series data), is shown below. An arbitrary bus *i* of a *b* bus distribution feeder is considered, as shown in Fig. 3.7, where the load demands and PV generation at the *i*-th bus and *k*-th time instant is specified from the available system data. The specified current at the *i*-th bus in the *k*-th instant can be obtained using (3.5).

$$I_i^{spec}(k) = \frac{\left[\left\{P_i^{PV}(k) - P_i^{L}(k)\right\} + j\left\{Q_i^{PV}(k) - Q_i^{L}(k)\right\}\right]^*}{V_i^*(k)} \tag{3.5}$$

where,

$I_i^{spec}(k)$ = Specified current vector

$P_i^L(k)$ = Active load vector

$Q_i^L(k)$ = Reactive load vector

$P_i^{PV}(k)$ = PV active power output vector

$Q_i^{PV}(k)$ = PV reactive power output vector

$V_i(k)$ = Node voltage vector

The vectors mentioned here are corresponding to the *i*-th bus at the *k*-th time instant, and * indicates the complex conjugate operator.

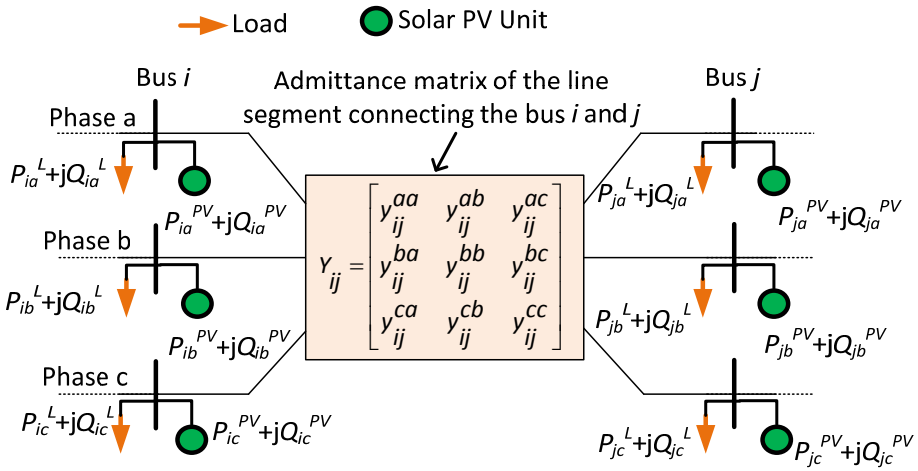

Fig. 3.7. Part of a three-phase distribution feeder connected by two arbitrary buses *i* and *j*

Current at *k*-th time instant can also be calculated from network admittance matrix using,

$$I_i^{calc}(k) = \sum_{j=1}^{b} Y_{ij}(k) V_j(k) \tag{3.6}$$

where,

$I_i^{calc}(k)$ = *Calculated* current vector

$Y_{ij}(k)$ = *Admittance* matrix between *i*-th and *j*-th bus

$V_j(k)$ = *Voltage* vector at the *j*-th bus

If node *voltage* values used in (3.5) and (3.6) are correct, then the mismatch between specified and calculated current would be nearly *zero*, that is,

$$\Delta I_i(k) = I_i^{spec}(k) - I_i^{calc}(k) \approx 0 \tag{3.7}$$

Newton-Raphson method is applied at each time instant *k* to obtain the node voltages that satisfies the condition in (3.7), by relating the incremental changes in node current with incremental changes in node voltage with system Jacobian, as given below.

$$\Delta I_i(k) = J(k) \Delta V_i(k) \tag{3.8}$$

where,

$\Delta I_i(k)$ = incremental change in current resulting from mismatch between specified and calculated current at the *k*-th time instant

$J(k)$ = system Jacobian matrix at the *k*-th time instant

$\Delta V_i(k)$ = incremental change in voltage used as the update in voltage for power flow iterations corresponding to the *k*-th time instant

The details of power flow iterations are not the main focus in this chapter, rather it emphasises only the computational advantage of current-mismatch based formulation of load flow equations. Details of this algorithm can be obtained in [10]. The elements of the Jacobian matrix shown in (3.8) can be obtained from the system admittance matrix with modifications of the diagonal blocks by adding contributions from loads [10]. Therefore, once the system admittance matrix is formed, it can be used for all the instances in the time series data, unless the network topology is changed. This reduces the computational burden for time series load flow analysis with a given set of load and PV generation patterns.

3.3.6 Flowchart of the Proposed Advanced Computational Tool

It is obvious that analysis of a large amount of measured data to assess the presence of network issues and concerns, and also the severity of the solar PV impacts would be highly computational intensive and time consuming. The analysis tool, therefore, need to have a "sense making" capability [14] to find out which part of the database is to be used for in-depth analysis. Voltage and power flow variations can be considered as the primary impacts that are directly caused by solar PV. Variations of power loss, voltage unbalance factor and tap changer operation are rather secondary impacts that are generally caused by the primary impacts. Detection of the changes in voltage and power flow patterns will therefore be used as the main criteria to identify the time series data that can be used for detailed analysis and extraction of the features.

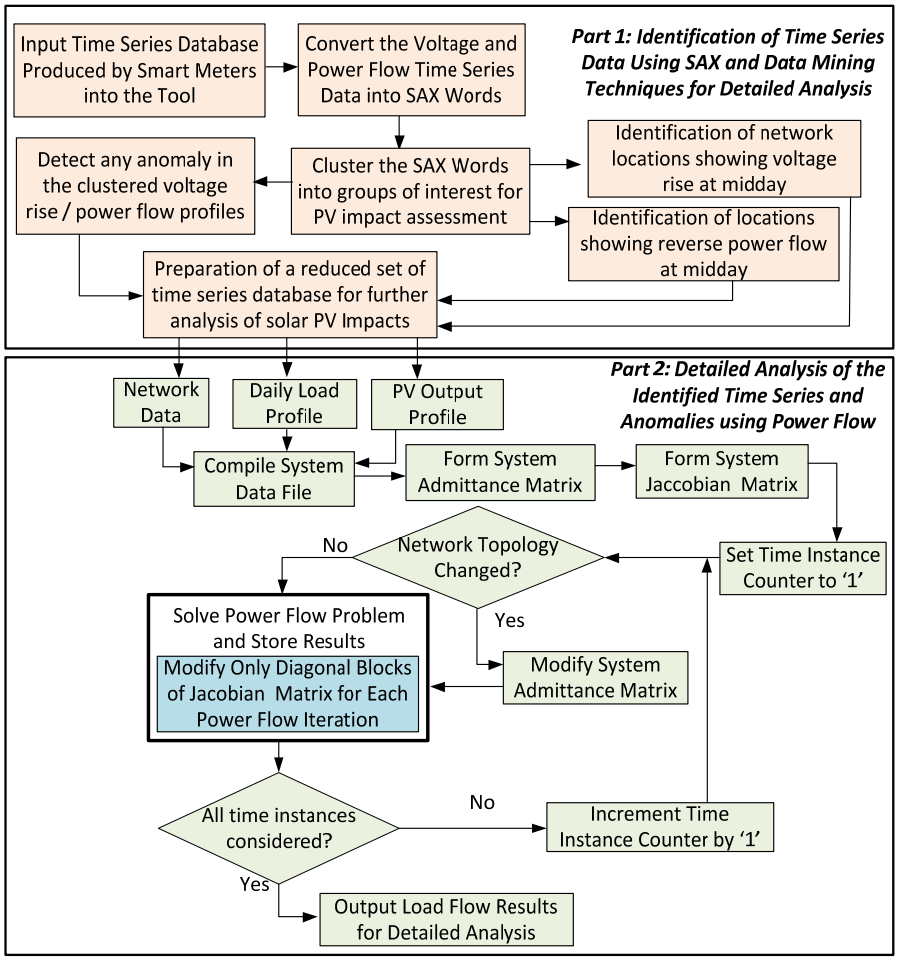

Fig. 3.8. Flowchart of the proposed analytical tool.

Functionality of the proposed tool consists of two main parts as shown in Fig. 3.8. In the first part, the large volume of voltage profile and time series data archived by smart meters will be taken as input. The data will be then be converted into SAX words prior to performing clustering and anomaly detection. Once the network locations and times of interest for PV impact analysis are obtained from the discovered patterns and anomalies, the corresponding load demand, PV generation and network data will be extracted from the large database to perform load flow analysis in the second part of the tool.

3.4 APPLICATION EXAMPLE

The proposed tool has been tested on a practical distribution network in New South Wales, Australia. Results will be presented in the following subsections.

3.4.1 Test Network

The test distribution network consists of an 80 km 11 kV backbone with 18 spurs of

different lengths in the range of 5 to 30 km. This rural network serves several sparsely populated areas. Three series voltage regulators are installed along the main feeder to control the voltage at remote ends. A simplified schematic diagram of the test network is shown in Fig. 3.9. The transformer symbols shown inside the PV cluster indicate the downstream LV feeder contains solar PV units. LV feeders are modeled using four-wire configuration and neutral wire is considered as solidly grounded at the customer service drop. Voltage and power flow profiles for the investigation are generated by performing load flow analysis of the test network.

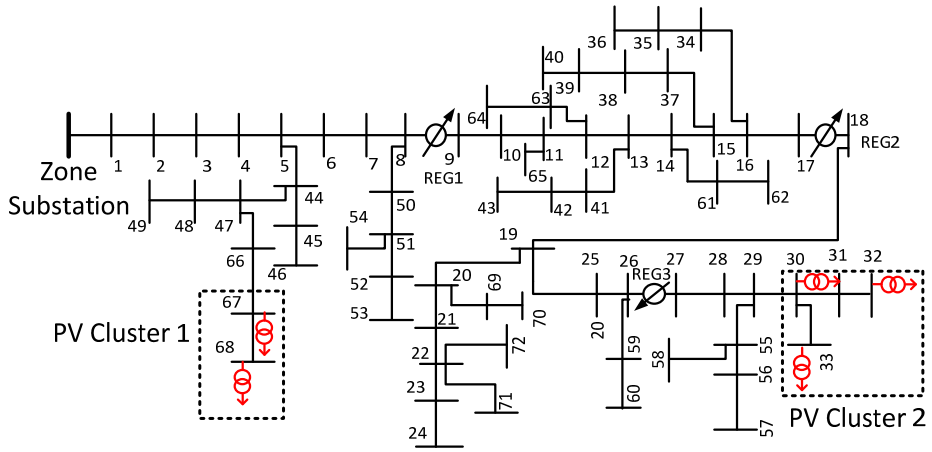

Fig. 3.9. Test distribution network with locations of PV clusters.

3.4.2 Dimensionality Reduction of Results Database using SAX

For a 24 hours voltage profile with 5-min resolution data, the length of the time series is 288. Using SAX, the voltage profile time series can be reduced to a lower dimension, w, where w is the size of the SAX word. The compression ratio achieved using SAX can be defined as,

$$\text{compression ratio} = \frac{n}{w} \tag{3.9}$$

where, n is the length of original data and w is the SAX word size. With a 20 word SAX representation, the compression ratio achieved for 1 day's voltage profile data is 14.4. Similarly, line flow data can be converted to SAX word and considerable reduction in data dimensionality can be achieved. Reduced data dimension will incur less computational effort in clustering and pattern recognition tasks to be performed on the data collected by smart meters.

3.4.3 Identification of Network Location Affected by Solar PV Clusters

Voltage profile time series data was clustered into 4 groups using k-means algorithm and the results are presented in Fig. 3.10. Clustering results of the original raw data are shown in Fig. 3.10(a) and that from SAX representations are shown in Fig. 3.10(b). It is observed in Fig. 3.10(a) that all of the four clusters created from the original data include voltage rise behaviour, and cluster 1 contains a mix (low and high) of voltage rise patterns. However, Fig. 3.10(b) shows that based on SAX representation of the data, the profiles with significant voltage rise are now grouped into cluster 4 only. The node locations corresponding to these voltage profiles can be identified using the cluster indices and further analysis of voltage rise now can be performed.

Similarly, daylong power flow profiles from the system nodes have been clustered using the original data as shown in Fig. 3.11(a) and using the approximated time series data shown in Fig. 3.11(b). Cluster 3 in Fig. 3.11(a) shows that the reverse power flow profiles due to solar PV have been clustered together with the ones that have not been affected by PV operation. On the other hand, when clustered using time series data obtained from SAX approximation, Fig. 3.11(b) shows that all the time series dataset with reverse power flow profiles at midday have been grouped into cluster 2 only.

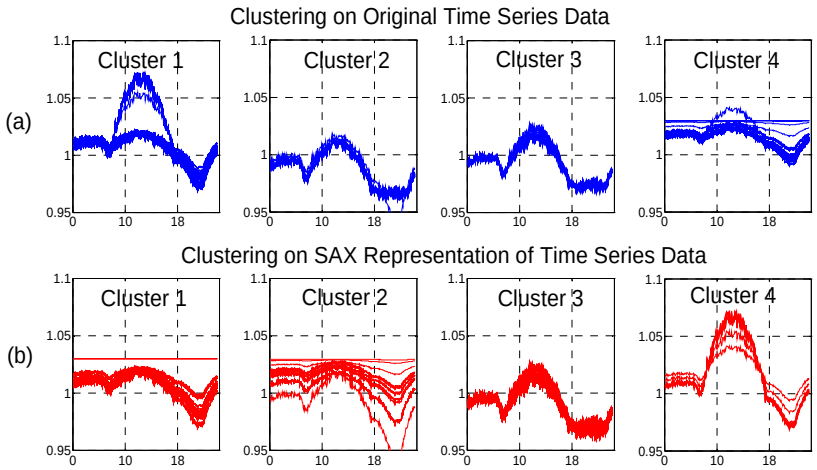

Fig. 3.10. Clustering of voltage profiles for identification of network locations showing voltage rise: (a) using original time series data (b) using SAX approximation.

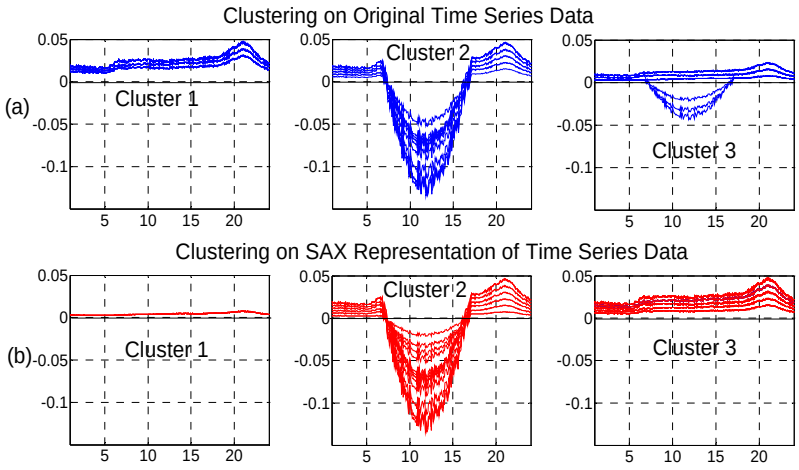

Fig. 3.11. Clustering of power flow profiles for identification of network locations showing reverse power flow: (a) using original time series data (b) using SAX approximation.

The main advantage of applying SAX was found in reduction of computational time. A comparison was made on average runtime of k-means routine for 10 consecutive runs with original and SAX data. Reduction in elapsed time was about 16 times and 10 times for voltage and power flow profiles, respectively.

3.4.4 Detection of Abnormal Voltage Profile

Consecutive 14 days voltage profile time series data of one of the network buses affected by solar PV were analysed as 14 time series patterns. The original time series data of each day's voltage profile was converted into SAX words. The distances of each of the SAX time series from each other were calculated to determine the time series that possesses the largest distance from its nearest non-self match. For simulation tests, cloud passing effects have been embedded (by incorporating sharp reductions in the PV output) in the time series data for two of the 14 days considered. The levels of reductions in the PV output are selected based on historical data. Detection of the voltage profile anomaly due to distortion by cloud passing effect was performed successfully, as shown in Fig. 3.12 below.

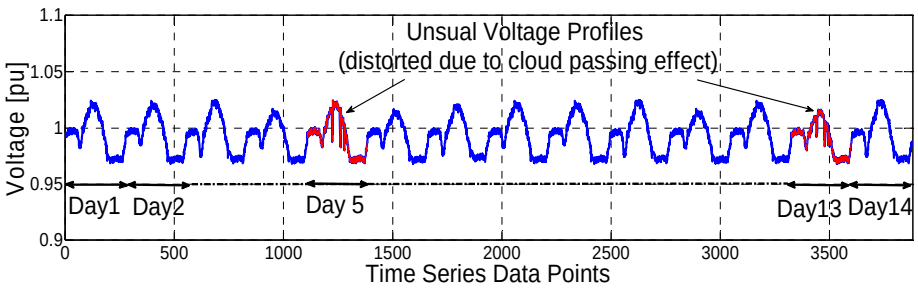

Fig. 3.12. Detection of unusual voltage behaviour.

3.4.5 Detailed Analysis of Identified Dataset Related to Solar PV Impacts

Once the patterns and anomalies of interest for PV impact assessment have been obtained from a large set of time series database, more detailed analysis can be carried out. The application of such detailed analysis may include determination of better network operation strategy with high PV penetration, or, design of corrective actions to mitigate PV impacts, etc. The type and methodology of the next stage of analysis will depend on its application. Load flow solution will be commonly required to perform such detailed analysis. This thesis will only show an example related to the PV impact on upstream voltage regulator operation.

Clustering of voltage profiles of the test system has identified that the LV feeders downstream to the third voltage regulator is experiencing voltage rise issues. Based on this information, it is important to investigate how the load centre voltage of this regulator is being affected by the voltage rise in the downstream LV feeders and how is this affecting the tap changer operation. The voltage profile at the load centre of this regulator was studied and presented in Fig. 3.13(a) which shows that the voltage is marginally equal to the upper limit set in the controller. This makes an intuitive suggestion that tap operation may have been performed by the regulator to keep the voltage within upper limit and this is verified by the tap operation profile shown in Fig. 3.13 (b). With the load and PV generation data corresponding to this scenario available at hand, load flow analysis was performed to investigate how the tap operation would be without solar PV. The load center voltage without PV is shown in Fig. 3.13(a) that shows the voltage is well below the threshold and no tap operation would have been performed without PV.

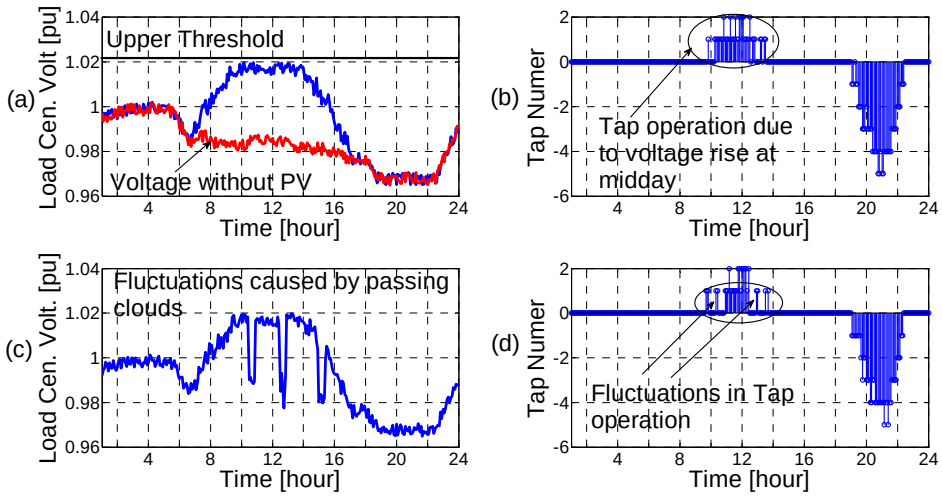

Fig. 3.13. Impact of midday voltage rise on tap changer operation: (a) Voltage profile at the load center of the third voltage regulator (b) Tap operation corresponding to the voltage profile in Fig. 3.13(a) (c) Fluctuations introduced by passing clouds in the load center voltage (d) Tap operation corresponding to the voltage profile in Fig. 3.13(c).

Passing clouds introduce fluctuations in the distribution feeder voltage with solar PV and may also produce fluctuations in the tap changer operation. The load and PV generation data corresponding to the most anomalous day identified in Fig. 3.12 by the anomaly detection technique were used in the load flow analysis. Tap operation of the third voltage regulator with this data was examined. Passing cloud induced fluctuations were observable from the load center voltage, as shown in Fig. 3.13(c), and fluctuation in tap operations were observed at the same time periods, as shown in Fig. 3.13(d). It is to be noted that the voltage fluctuation at about 15:00 hours did not impact the regulator operation as voltage rise at this moment was not so high as to cause the tap changer to operate.

Since archived data from real-time measurements is used in the PV impact analysis, more accurate results should be obtained when compared to those using assumption based synthetic data. This will help utility planning engineers to understand the PV impacts on the distribution systems better. The proposed approach can be used to track and visualise the identified PV impacts of interest, and also identify unique signatures within the utility system. This can be achieved using the three-phase load flow analysis, capable of dealing with network asymmetry, load unbalance, single-phase solar PV integration, and their impact on upstream network, described in section 3.3.5. Using the unique signatures of the identified PV impacts, the proposed approach can assist in providing distribution system infrastructure security via early warning systems of solar PV impacts in real-time.

3.5 CONCLUSION

An advanced analysis tool for the assessment of clustered rooftop solar PV impacts in the future distribution networks under smart grid environment is proposed. With a large volume of real time network data collected from monitoring systems or smart meters, this tool will be able to intelligently decide which part of the data would be effective for analysis of solar PV impacts on distribution networks. To identify the hidden patterns and anomalies in the archived time series database, this tool will apply data mining techniques. However, to reduce the computational efforts while applying the pattern discovery algorithms, the proposed tool will use SAX representation to reduce the dimensionality of the database. Further, the tool will also deploy a load flow algorithm demanding less computational effort while performing in-depth analysis of the identified data of interest. A practical distribution network in Australia was used in this thesis to verify the applicability of the proposed computational tool. It was observed that the developed tool is able to identify the useful portions of the large database for further detailed analysis and feature extraction to characterise the response. It is envisaged that the proposed tool can identify the unique signatures associated with different types of PV impacts which can be used in real-time for warning of the PV impacts in the networks.

REFERENCES

[1] S. Morozumi, N. Inoue, Y. Arashiro, Y. Chiba, and T. Iwasaki, "Strategies and status of grid-connection Technology Development in NEDO," in *Power and Energy Society General Meeting - Conversion and Delivery of Electrical Energy in the 21st Century, 2008 IEEE*, 2008, pp. 1-6.

[2] R. A. Walling, R. Saint, R. C. Dugan, J. Burke, and L. A. Kojovic, "Summary of Distributed Resources Impact on Power Delivery Systems," *IEEE Transactions on Power Delivery* vol. 23, pp. 1636-1644, 2008.

[3] Y. Liu, J. Bebic, B. Kroposki, J. de Bedout, and W. Ren, "Distribution System Voltage Performance Analysis for High-Penetration PV," in *Energy 2030 Conference, 2008. ENERGY 2008. IEEE*, 2008, pp. 1-8.

[4] J. Lin, E. Keogh, L. Wei, and S. Lonardi, "Experiencing SAX: a novel symbolic representation of time series," *Data Mining and Knowledge Discovery,* vol. 15, pp. 107-144, 2007.

[5] E. Keogh, "Mining shape and time series databases with symbolic representations," 2007, p. 7.

[6] H. Mori and Y. Umezawa, "A SAX-based method for extracting features of electricity price in power markets," in *Transmission & Distribution Conference & Exposition: Asia and Pacific, 2009*, 2009, pp. 1-4.

[7] E. Keogh, J. Lin, F. Ada Waichee, and H. Van Herle, "Finding Unusual Medical Time-Series Subsequences: Algorithms and Applications," *Information Technology in Biomedicine, IEEE Transactions on,* vol. 10, pp. 429-439, 2006.

[8] V. H. M. Quezada, J. R. Abbad, and T. G. S. Roman, "Assessment of energy distribution losses for increasing penetration of distributed generation," *Power Systems, IEEE Transactions on,* vol. 21, pp. 533-540, 2006.

[9] F. Shahnia, R. Majumder, A. Ghosh, G. Ledwich, and F. Zare, "Sensitivity analysis of voltage imbalance in distribution networks with rooftop PVs," in *Power and Energy Society General Meeting, 2010 IEEE*, 2010, pp. 1-8.

[10] P. A. N. Garcia, J. L. R. Pereira, S. Carneiro, Jr., V. M. da Costa, and N. Martins, "Three-phase power flow calculations using the current injection method," *Power Systems, IEEE Transactions on,* vol. 15, pp. 508-514, 2000.

[11] E. Keogh, K. Chakrabarti, M. Pazzani, and S. Mehrotra, "Locally adaptive dimensionality reduction for indexing large time series databases," 2001, pp. 151-162.

[12] L. Wei, E. Keogh, X. Xi, and M. Yoder, "Efficiently finding unusual shapes in large image databases," *Data Mining and Knowledge Discovery,* vol. 17, pp. 343-376, 2008.

[13] T. Warren Liao, "Clustering of time series data--a survey," *Pattern Recognition,* vol. 38, pp. 1857-1874, 2005.

[14] G. Venayagamoorthy, "Dynamic, Stochastic, Computational, and Scalable Technologies for Smart Grids," *Computational Intelligence Magazine, IEEE,* vol. 6, pp. 22-35, 2011.

Chapter 4

AN APPROACH FOR ON-LINE ASSESSMENT OF ROOFTOP SOLAR PV IMPACTS ON LOW VOLTAGE DISTRIBUTION NETWORKS

ABSTRACT

Assumption based off-line analysis tools may not be able to provide sufficient and accurate information for corrective decision-making to mitigate solar PV impacts in the future distribution grids. This is mainly due to the increasing penetration level of intermittent power generation resources and also the fluctuating behaviour of consumer demand. On-line assessment tools can assist to manage PV impacts and aid to mitigate those on real time basis. This thesis proposes an approach for on-line assessment of rooftop PV impacts on low voltage (LV) networks using real-time network data. A variable-width sliding window will be used to provide the analysis outcomes based on-line data. The width of the sliding window can be varied according to user input so that the changes in network behaviour caused by PV integration can be investigated conveniently. Several numerical indices are proposed in this thesis to assess solar PV impacts on the LV networks. This approach also uses the on-line data to develop real time distribution network models for a dynamic "what-if" analysis. The usefulness of the proposed on-line assessment approach is verified using an Australian LV distribution feeder.

4.1 INTRODUCTION

The penetration of rooftop solar PV resources is increasing in the low voltage (LV) distribution networks day by day. With the capability to serve loads at the connection point, PV resources have the potential to change the normal network behaviour. While the integration of solar PV can provide different system support benefits [1], a high penetration of PV on the other hand may impact the network in several ways [2], such as voltage rise, reverse power flow, and increased energy loss [3]. In many countries around the world, the integration of PV resources at a high penetration level is a comparatively new issue. Many utilities are yet to fully understand the consequences of the cascaded impacts in a real time operation. Network operators therefore deploy analytical tools to assess the potential impacts of PV resources on the distribution networks. In general, off-line impact analysis is performed during the processing of a prospective PV connection request using assumption based synthetic data, and/or, historical data collected and archived through monitoring devices installed in the networks. While the impact studies during acceptance of a PV connection request can provide a preliminary estimation of PV impacts, the real scenario in the presence of varying load and network conditions are still unknown. Also, new PV connections are being accepted regularly, leading to change of the prevailing conditions during the acceptance of the connection requests. Therefore, an off-line investigation performed before may not be adequate for the present scenario. Similarly, off-line analysis using the historical data may not be sufficient for taking appropriate mitigation actions due to the changes in network condition with time, such as addition of loads and network equipment, and installation of new generation resources.

With the increasing level of solar PV penetration in distribution networks, advanced tools would be needed that are capable of online impact assessment so that sufficient information on PV impacts are available from the most recent network condition with an acceptable accuracy. This will require a collection of real time system operation data and the ability to perform the impact analysis on-line so that network operators can take immediate decisions and implement necessary actions (such as issuing a command to operate the devices that can mitigate PV impact, for example, a community energy storage device) at the time of occurrence of any detrimental impact.

Extensive research has been carried out on modelling and analysis of distribution

networks with Distributed Generation (DG) resources based on a general off-line approach; a review is provided in [4]. Several numerical indices have been developed in [5] for the analysis of network impacts of DG resources to investigate the best locations for DG units in the network using a steady-state analysis approach. This type of approach is useful for off-line analysis, typically performed in planning oriented studies for DG integration. A general approach to quantify the benefits of DG integration has been discussed in [6] using a parametric study where the variations of different DG impact indices have been observed with the variations of DG ratings and DG power factor. Again, the analytical approach used is more suitable for an off-line type analysis using previously archived data. In contrast, the motivation of the research in this thesis is to assess the PV impacts on-line using real-time data so that a more accurate analysis of the impacts could be done under the varying load and network conditions. This would also be helpful to take a more effective decision (as the impact estimation is more accurate) on the spot for immediate mitigation by available means.

This thesis proposes a variable-width sliding window based on-line assessment approach for solar PV impacts on LV distribution networks. The proposed approach will use the data available from numerous smart meters installed in the future smart grid environment to assess solar PV impacts online. Communication delays associated with smart meters will be ignored in the present version of the work. However, it is anticipated that with the advancement of smart grid technologies, such delays will become negligible in future. Using the variable-width sliding window allows the width of the assessment window to be varied depending on the situation. For example, when the PV output is at its peak level, the width of the assessment window can be reduced to obtain a closer view of the situation, because the threat of the voltage limit violation could be high at this time. On the other hand, when the PV output is consistently decreasing or unavailable, for example during late afternoon or at night, the width of the sliding window can be increased to avoid unnecessary monitoring activities. Different numerical indices will be defined based on key network parameters that are influenced by the PV integration. Real time network models will be compiled using the most recent network information to investigate the impact of PV penetration by incorporating any desired changes in the PV output or network parameters. The proposed approach will be able to perform a “what-if” analysis using a time-varying base case scenario to advise the user how a given operating network would behave in a potential PV generation

scenario. The information obtained using the proposed approach would be beneficial (in terms of a more accurate impact analysis) to take mitigation actions against adverse impacts of high PV penetration, including fluctuations caused by sudden variations in PV output. The applicability of the approach will be tested using a practical LV distribution feeder in Australia.

4.2 THE PROPOSED ON-LINE ASSESSMENT APPROACH

Offline analysis of rooftop solar PV impacts on LV networks is typically performed using assumption based data due to unavailability of detailed operational data on the LV networks. Scenario analysis is performed using load flow solution with the load and PV generation data modified to fulfill the analysis objectives, such as the analysis of worst-case scenario. The proposed on-line approach on the other hand, will perform the impact investigations using real time data collected by smart meters installed at different locations in the network, and the usage of assumption will be kept as low as possible. Functionalities of the proposed approach are described below.

4.2.1 Architecture of the Proposed On-line Approach

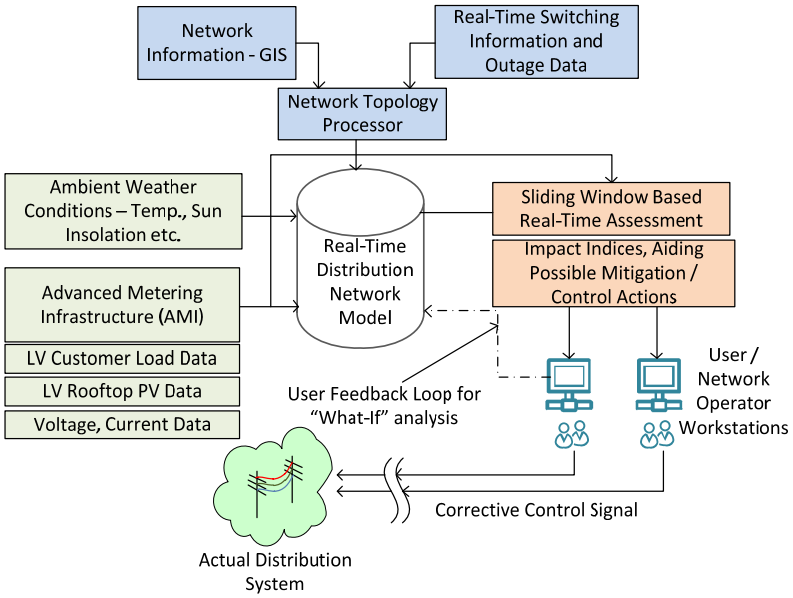

Fig. 4.1. The architecture of the proposed online assessment approach

The proposed approach will consist of on-line data input functionalities, as shown in Fig. 4.1, that will receive real time data related to distribution networks and also the weather information that is related to PV power output. The approach will also have the ability to update the network topology using the most recent switching and outage information. Combining the available on-line network data and topological information,

the proposed approach would be able to make use of real time models of distribution networks. Solar PV impacts on networks will be assessed by the approach using several numerical indices based on network variables that are mostly affected by solar PV, such as, bus voltage, line power flow, and feeder power loss. The proposed approach and indices will be highly useful to assess the impact of an increasingly high penetration of solar PV.

4.2.2 Collection and Processing of Real Time Data with AMI

Real time system operation data will collected from numerous smart meters and monitoring devices anticipated in the future distribution networks using an Advanced Metering Infrastructure (AMI) [7]. Resolution of the data will depend on the technical specifications of the AMI devices. If required, data pre-processing techniques [8] will be applied to improve the quality of the measured data.

4.2.3 Sliding Window Based Assessment

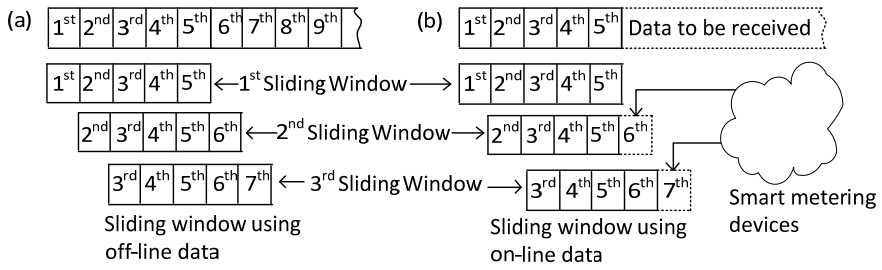

Fig. 4.2. Illustration of sliding window; (a) using off-line data; (b) using on-line data.

Sliding windows are normally used for extracting sub-sequences from stored (i.e. offline) time-series data. Fig. 4.2 shows an illustrative example of how this can be applied for extraction of time series sub-sequences from on-line data. An off-line time series data of an arbitrary length is considered in Fig. 4.2(a), where up to the 9th data point is shown. In general, the i^{th} sub-sequence, $\mathbf{S}_i$, of length W from an N-dimensional time series data set, $\mathbf{D}$, can be extracted using (4.1).

$$\mathbf{S}_i = \mathbf{D}(i : m) \tag{4.1}$$

where, $m = (i+W-1)$ and, $i = 1, 2, \ldots, N - (W-1)$.

Following this and using a sliding window of length 5, for example, the 1st sub-sequence is a vector of 1st to 5th data points; the 2nd one is a vector of 2nd to 6th, and so on. It is observed that the m^{th} data point is always available as long as archived off-line

data is considered. This is, however, not the case with on-line data, where the m^{th} data has to be obtained from real time measurements. The example in Fig. 4.2(b) shows that the 2nd sub-sequence is formed by combining the 2nd to 5th previously received data points with the 6th recently received data; similarly, the 3rd sub-sequence is obtained from the 3rd to 6th previously received data with the recently received 7th data, and so on. These sub-sequences of time series data are used as the sliding windows for the proposed on-line approach.

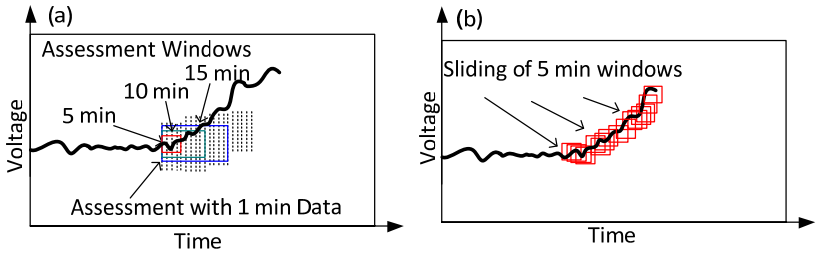

Fig. 4.3. Sliding window based PV impact assessment: (a) 5, 10 and 15-min assessment windows (b) sliding of 5-min windows.

Solar PV impacts in terms of changes in key network parameters will be assessed based on 1-min data logged by smart meters. The 1-min assessment results will then be used to develop a variable sliding window based assessment report. This concept of sliding window is described below using a hypothetical voltage profile time series data shown in Fig. 4.3 with 5-min, 10-min and 15-min assessment windows. The width of the sliding window can be defined by the users to obtain the assessment outcomes in a customised way.

The voltage profile in Fig. 4.3 shows a rising trend due to the integration of solar PV resources. Five consecutive samples of 1-min interval data are used for building the 5-min assessment window; similarly 10 instances of 1-min data are used for 10-min assessment window, and so on. Each of the windows progresses (slide) by 1-min to provide a sliding window based assessment. This is shown in Fig. 4.3(b) for the 5-min window only; other widths will follow the similar pattern. The first window provides the assessment results for 5 time instances, from instance 1 to 5; the second window gives the results for instance 2 to 6 and so on.

The width, W, of a sliding window can be any value between 1 and the number of data points already received, and it is mainly a user defined parameter. In terms of time period, the narrowest width will depend on the resolution of the on-line data available

from the metering systems. For example, if the data is measured in second range, the width of the window can be varied from seconds to minutes to up to hours. On the other hand, if the data is measured in minutes (e.g. 1 minute resolution) then the narrowest width would be in terms of minutes. Resolution of the on-line data is also crucial for assessment of PV output fluctuations and associated impacts. If the time period between two consecutive measurements is higher than the time duration of the fluctuation event, then it will not be visible in the on-line data and the impacts cannot be assessed from such low resolution of the online data. Therefore, the higher the resolution of the online data, the wider would be the choice of the width of an assessment window.

Although for a given resolution of the online data, the width of the assessment window is mainly a user defined parameter, still a suggestion can made on the selection of an appropriate width using the previous measurements of the solar irradiance level. Logically, the width needs to become narrow with the increase of severity of the PV impacts, which depend on the solar irradiance level for a given set of network conditions. Therefore, a suggestion can be made to decrease the width (in terms of time) with the increase of the irradiance level and vice versa.

The advantage of a variable-width sliding window is its adjustability to provide the assessment outcomes in a more customizable way that suits the assessment situation better. For example, in a mostly cloudy day, the impact of PV may not be significantly visible and the user can choose to use a wide assessment window, such as 30 min, or 60 min. On the other hand, in a clear day with the PV units generating at their maximum capacity at noon, when the load demand is usually low, a narrow assessment window, e.g. 10 min, or, 5 min, would be desirable to obtain a closer and tighter view of the PV impacts, such as, a possible violation of the overvoltage limit. In a partly cloudy day, the assessment window can be varied depending on the requirement. For example, if fluctuations in the PV output caused by passing clouds need to be monitored, the width of the assessment window needs to be the narrowest.

4.2.4 Real Time Model of Distribution Networks

A traditional model of a distribution network is an assembly of network components in terms of their admittances combined according to the network topology and the loads imposed at respective buses. With the integration of solar PV resources, the network model will also include PV power injections at buses where PV units are connected. An

off-line model of a distribution network can be constructed from the topological information obtained from Geographic Information System (GIS) maps, the design data of the network, planned or historical load demand data, and nominal or historical output data of PV units. On the other hand, a real time model of a distribution network would need the most recent information and data on the network. A network topology processor will be used for on-line updating of the network admittance model by incorporating any change in the designed topology due to switching and/or outage of network components. Load demand and PV output data will be updated using the on-line data obtained from AMI. The weather data related to PV output will also be available for different types of scenario analysis, or case studies in changed weather conditions.

4.2.5 Fast and Accurate Network Analysis Tool

While solar PV impacts can be investigated based on the online measurements of voltages and power flows, simulation oriented analysis using the real time load and PV generation data can be performed to make an online evaluation of impacts from measured data and compare the results with the actual impacts to check the validity of the real time network models. However, a more important application of the simulation would be to perform "what-if" and "worst-case" scenario analysis by modifying the metered PV generation data. To perform the simulation oriented analysis on-line, the proposed approach needs to utilise an algorithm that is fast but accurate enough so that correct assessment outcomes can be made in time. For example, an on-line assessment tool designed for performing the analysis with 1-min resolution data needs to be able to solve network power flow problem, and then perform post-solution analysis, e.g. assessment of voltage rise, reverse power flow, feeder power loss etc. within 1 minute interval so that the tool is ready to accept the next sample of 1-min resolution data. The current-mismatch variant of Newton-Raphson algorithm [9] will be deployed in the proposed approach as it incurs less computational efforts.

LV distribution networks are typically of three-phase configuration, and more often contains substantial amount of unbalance due to single phase and two phase laterals, load unbalance, and in the recent days due to PV (allocation) related unbalance. Therefore, a three-phase network analysis method [10] will be adopted for the proposed approach that can comprehensively model the LV distribution networks with their true

complexities including the 3-phase 4-wire configuration, single phase and two phase laterals, neutral grounding, single phase and three-phase loads and PV units.

4.2.6 Online Quantification of Impacts through Indices

Each of the solar PV units installed in an LV feeder contributes to the change in network behaviour depending on its capacity. However, to analyse the PV impacts on an overall feeder, a development of numerical indices considering the impacts of all the PV units in a feeder is necessary. The level of PV impact from feeder to feeder will vary depending on the impedance, loading, and level of PV penetration. The use of the numerical indices would also be beneficial to analyse and compare the impacts on different feeders in a distribution system. Indices developed to quantify solar PV impacts in terms of voltage deviation, feeder power flow, MV/LV substation capacity and feeder power loss will be used in the proposed approach. The following proposed indices will be used to investigate the PV impacts using the measured data and also using the results from the load flow analysis for any intended scenario analysis considering changes in the network, such as, increase in PV penetration.

Voltage rise is one of the most discussed impacts of solar PV integration. It can affect the voltage quality of the network by creating a long-duration overvoltage problem [11]. The maximum amount of voltage rise observed among different nodes of a feeder at any given time is used to estimate voltage deviation in the feeder and is defined as the Maximum Voltage Deviation Index (MVDI). At the k^{th} time instant, this can be obtained using,

$$\text{MVDI}(k) = \frac{V^{nom} - V_{\max}(k)}{V^{nom}} \tag{4.2}$$

Here, V^{nom} is the nominal voltage which can either be a constant, or vary according to the load condition or time of the day, based on the operational policy of the utility; $V_{\max}(k)$ is the voltage at the LV feeder node where the maximum amount of voltage variation is observed at the k-th time instant. It is to be noted that MVDI needs to be determined for all the phases separately. The MVDI is an index calculated at any particular instant of time to assess the maximum voltage rise impact of the rooftop solar PV integration in the low voltage network, as given in (4.2). The index is based on the nominal value of the feeder voltage and therefore, it can provide an indication of the deviation of feeder voltage affected by the level of PV penetration. The index can have

both positive and negative value. Without PV integration, the voltages at different points in the feeder are generally lower than the nominal voltage and hence the MVDI will be generally positive. A negative value indicates that the solar PV integration may have produced a voltage-rise. The index can also be used to determine whether the feeder is experiencing overvoltage or undervoltage, by comparing the index with the specified limits for the distribution feeder. For example in Australia, the upper limit is 10% over the nominal value. An MVDI value which is more negative than -0.1 indicates an overvoltage has occurred. Similarly, undervoltage can be indicated by comparing the MVDI with the minimum limit.

An Average Feeder Loading Index (AFLI) of an LV feeder can be formulated as the weighted average of loading levels of all the feeder segments with respect to their lengths. The AFLI at k^{th} instance can be expressed as,

$$\mathrm{AFLI}(k) = \left| \sum_{j=1}^{s} \frac{l_j}{L_f} \times \frac{S_j(k)}{C_j} \right| \tag{4.3}$$

For an LV feeder, the length of the j^{th} segment l_j, total feeder length L_f and load carrying capacity of the j^{th} segment C_j are constants. The AFLI will, therefore, depend only on the complex power flow through all the line segments at the k^{th} time instant, $S_j(k)$, where j = 1, 2…, s and s is the total number of segments in the feeder. The AFLI index provides an average indication of the degree of loading of a given feeder. It indicates the loading of a distribution feeder as a whole, and not for any particular segment. This index can be used to compare the impact on the loading of a given feeder for different scenarios of PV generation. The AFLI value is *zero* if no power flow takes place in the feeder segments. The AFLI value will increase with an increase in feeder power flow to serve the customers. However, with a high penetration of PV resources, AFLI can also increase due to a high amount of reverse power flow.

The amount of the load demand locally served by solar PV units contributes to the release of MV/LV substation capacity of an LV feeder. An index is defined to assess the PV impact on the available capacity of substations using a Substation Reserve Capacity Index (SRCI) as given below.

$$\mathrm{SRCI}(k) = 1 - \frac{\left| S_1^a(k) + S_1^b(k) + S_1^c(k) \right|}{S_{sub}} \tag{4.4}$$

Here, S_1^a, S_1^b, and S_1^c are the complex power flows from phase *a*, *b* and *c* of the LV substation bus and S_{sub} is the rated capacity of the substation. A value of SRCI equal to *one* means substation capacity is fully available whereas a value equal to *zero* means no substation capacity is left unused. With PV units serving local loads, SRCI will decrease with PV integration. However, above a certain level of PV penetration, reverse power flow will cause a higher level of substation capacity to be used and SRCI will decrease.

The import of power from the upstream network will be less due to the availability of local PV generation. Therefore, power loss in the distribution feeder will be reduced. To quantify this, an index is developed using the ratio of the total loss incurred in the feeder to the total load served by the feeder and is referred to as the Feeder Loss to Load Ratio (FLLR), as shown below.

$$\mathrm{FLLR}(k) = \frac{P_{loss}^a(k) + P_{loss}^b(k) + P_{loss}^c(k)}{P_{dem}^a(k) + P_{dem}^b(k) + P_{dem}^c(k)} \tag{4.5}$$

Here, P_{loss}^a, P_{loss}^b and P_{loss}^c are power losses incurred and P_{dem}^a, P_{dem}^b and P_{dem}^c are the load demands in phase a, b and c of an LV feeder. FLLR is an index obtained from the ratio of the loss in the feeder to the load demand of the feeder. Its value increases significantly during midday when the PV output is the highest and the load demand is usually low. During that period, the power loss through the feeder is high due to a high amount of reverse power flow, but since the load demand is typically lower, therefore, the ratio of the loss to the load demand becomes significantly high.

Indices of the Moving Averages (MA) of the variables associated with the PV impact in the sliding windows is required to understand the overall trend of the changes in network behaviour caused by the level of solar PV.

The moving average of the voltage deviation index at any given sliding window, *w,* with a width of *W* can be defined as,

$$\mathrm{MVDI}_w = \frac{\sum_{k=w}^{w+W-1} \mathrm{MVDI}(k)}{W} \tag{4.6}$$

Similarly, the moving averages of the other impact indices, $\mathrm{AFLI_w}$, $\mathrm{SRCI_w}$ and $\mathrm{FLLR_w}$ will be obtained, as given in (4.7)-(4.9). The moving average provides a useful indicator of the long term trend of the variables associated with the PV impact.

$$\mathrm{AFLI}_w = \frac{\sum_{k=w}^{w+W-1} \mathrm{AFLI}(k)}{W} \tag{4.7}$$

$$\mathrm{SRCI}_w = \frac{\sum_{k=w}^{w+W-1} \mathrm{SRCI}(k)}{W} \tag{4.8}$$

$$\mathrm{FLLR}_w = \frac{\sum_{k=w}^{w+W-1} \mathrm{FLLR}(k)}{W} \tag{4.9}$$

4.2.7 Simplified Flowchart of the Proposed On-line Approach

Fig. 4.4 shows a simplified flowchart of the major functions of the proposed approach. The width of the sliding window, W is taken as input from the user. Each of the sliding window, specified by the window counter, w, contains W number of 1-min assessment outcomes. The inner loop, consisting of online data collection, pre-processing, load flow analysis (if required for "what-if" analysis), PV impact assessment through quantification indices, and storing of 1-min results, continues until k becomes equal to W. Once the assessment for the w^{th} sliding window is obtained, results are displayed from w^{th} to $(w+W-1)^{th}$ number of time instances. A summary of the assessment, such as maximum value, minimum value, moving average value etc. for the latest sliding window can be made available for reporting.

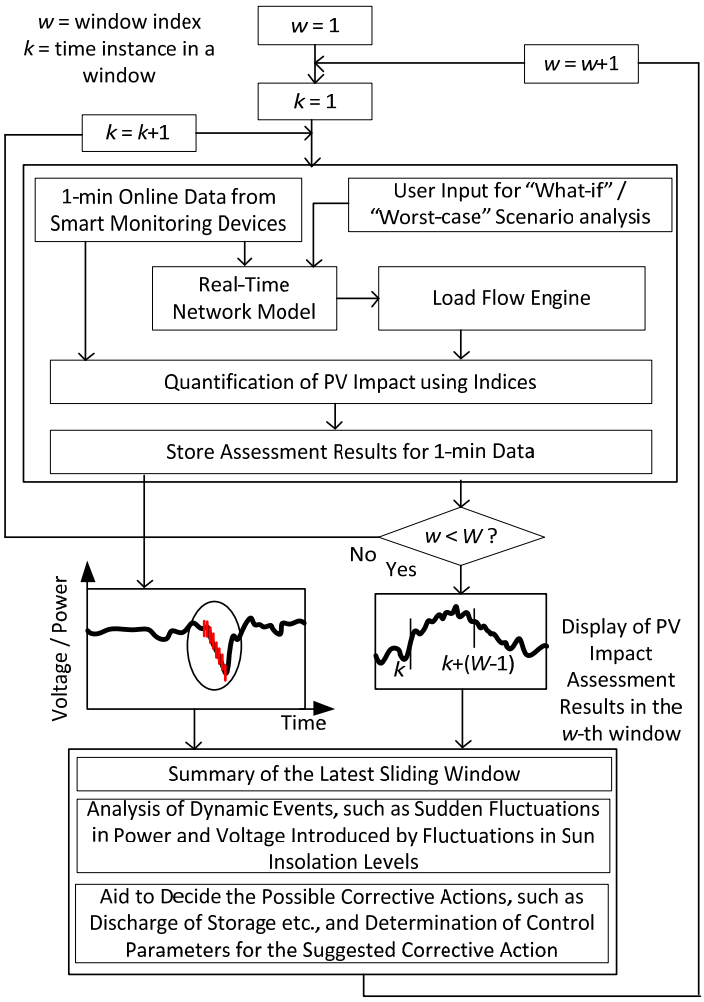

Fig. 4.4. A simplified flowchart of the proposed on-line assessment approach.

4.3 APPLICATION OF THE TOOL IN REAL TIME ENVIRONMENT

With the availability of the real time distribution network model compiled from the most updated information, the proposed approach can be used for determining the network behaviour under any probable changes in PV output, load demand, or even changes in network topology resulting from outage or switching operation. With the capability to assess the solar PV impacts on distribution networks on-line, the proposed approach can also be used for monitoring of dynamic events such as fluctuations induced by passing clouds, etc. Further, this approach may also aid in the decision making (e.g., when to operate a battery energy storage device to mitigate PV output fluctuations and what would be the charging or discharging rates) for compensating the adverse impacts of these dynamic events by proving online assessment of the perturbed parameters. A brief description of these capabilities is provided below.

4.3.1 Dynamic "What-if" Analysis

With an increasing level of solar PV penetration, network operators often need to investigate how the networks would operate under a changed condition of load and PV output. This type of investigation is typically performed using "what-if" type of analysis by first selecting a base case scenario, and then by varying the parameter of interest (for example, the PV output, consumer load, etc), which is similar to a power system security analysis screening process. Conventionally, a base case scenario would typically consist of historical off-line data or synthetic data, and therefore, may not always represent the actual threats of high PV penetration in an operating distribution network. In a real-world scenario, network condition changes with the variations in load demands, PV outputs and network configurations caused by switching operation. Impacts of high PV penetration would be different under different network conditions. Therefore, a static base case using off-line data may not be sufficient to assess high PV penetration impacts. Rather a dynamic base case changing with time and reflecting the actual changes in the network would be needed. The real-time distribution network model obtained using the proposed approach can be used as base case for such a dynamic "what-if" analysis.

A simplified block diagram of the dynamic "what-if" analysis is shown in Fig. 4.5. The proposed online approach compiles time-variant base case scenarios using the real-time load, PV and network data obtained from the actual distribution network using the Advanced Metering Infrastructure. A base case scenario at the k-th time instant will be constructed using the active and reactive load demand, $P_L(k)$ and $Q_L(k)$, the PV output at $P_{PV}(k)$, and the network configuration, each at the k-th time instant. The changed network configuration will affect the network admittance matrix $Y(k)$. The user, e.g., a network operator, would be able to modify the compiled base case scenario to investigate a potential PV penetration scenario to assess the impacts, or, possibility of any threat on the network under that potential scenario. Once the "what-if" analysis for the k-th instant is finished using the load flow engine, results are reported to the operator and the system is ready for analysis for the (k+1)-th instant.

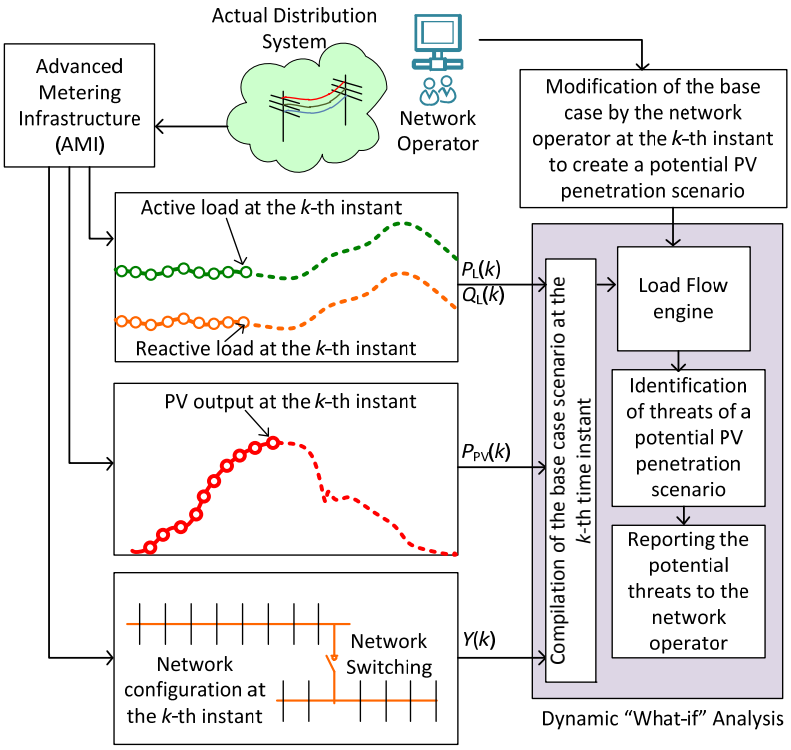

Fig. 4.5. Dynamic "what-if" analysis

4.3.2 Online Monitoring of PV Output Fluctuations

The power output of PV resources depends on the incident sun insolation on PV panels. The PV impacts, therefore, changes throughout the day in accordance with the sun insolation. Any event that creates a sudden change in the sun insolation level, such as passing clouds over the PV installation site [12], eventually produces fluctuations in the PV output and this is reflected in the feeder voltage and power flow. From the collected real-time data, the proposed approach will be able to provide an online assessment of the fluctuating behaviour of network caused by sudden and irregularly variable PV outputs. The ramp rate of the PV output changes during cloud passing can be very high [11] and this will affect the ramp rate of the resulting voltage variation.

Indices are defined to quantify the ramp rate of PV power output variation caused by cloud passing and the resulting voltage variation. A sudden change of the total amount of the PV output in the feeder is considered as a potential impact of PV output fluctuation, which is expressed using Instantaneous Power Ramp Rate (IPRR) with a unit of kW per unit of time, as shown below.

$$\mathrm{IPRR}(k) = \frac{\sum_{i=1}^{n} P_i^{PV}(k) - \sum_{i=1}^{n} P_i^{PV}(k-1)}{t(k) - t(k-1)} \tag{4.10}$$

where, $P_i^{PV}(k)$ is the PV power at the i-th node of the feeder at k-th time instant; i = 1, 2, …, n, where, n is the total number of nodes in the feeder. Positive IPRR indicates an increase of feeder PV generation and negative IPRR indicates a decrease of PV generation. The maximum amount of voltage variation observed in a feeder is used for evaluating the voltage ramp rate. The proposed index is defined as Instantaneous Voltage Ramp Rate (IVRR) that indicates the amount of voltage change between the present and the immediate past instant of measurement. The IVRR is expressed in terms of Volts per unit of time and is calculated using the following equation for the k^{th} time instant.

$$\mathrm{IVRR}(k) = \frac{V_{\max}(k) - V_{\max}(k-1)}{t(k) - t(k-1)} \tag{4.11}$$

In (4.11), $V_{\max}(k)$ is the voltage at the LV feeder node where the maximum amount of voltage variation is observed and $t(k)$ is the time corresponding to k^{th} time instant. The sign of IVRR indicates the direction of voltage ramp; positive sign means an increase in voltage as compared to previous measurement and a negative sign indicates a decrease in voltage. High resolution time series data (in the scale of seconds) would be more suitable for the measurements of IPRR and IVRR. The same mathematical formulations of IPRR and IVRR given in (4.10) and (4.11), respectively, will be applicable when such high resolution data is available. The moving averages of IPRR and IVRR can be calculated in the same way as shown in (4.6)-(4.9) to obtain long term trends of the fluctuations.

4.3.3 Aiding the Decision Making for PV Impact Mitigation

Online monitoring and measurements of PV impacts can be used for real time decision making for mitigation of PV impacts. For example, if any immediate action is to be taken for mitigating the voltage rise caused by PV, the amounts and the exact time references of occurrence of the voltage rise have to be provided to the controllers of the compensating devices; an on-line impact assessment approach would be helpful in this case. Similarly, if storage devices are used for smoothing out the PV fluctuations caused by passing clouds [13], the voltage and power ramp rates available from on-line

measurements can be used for determining the charge and discharge control parameters of storage devices.

A generic conceptual representation of assisting the PV impact mitigation by the proposed approach is shown in Fig. 4.6(a) using the rate of change of a fictitious Fluctuating Variable (FV). The detection of a sudden fluctuation can be performed from the abrupt change in the ramp rate of the FV. A Compensating Action (CA) designed to mitigate the fluctuating effect has to be triggered at the point of detection. The ramp rate of the compensating action will depend on the desired ramp rate of the FV, which is expressed by (4.12) for the *k*-th time instant.

$$\left.\frac{\Delta(\mathrm{CA})}{\Delta t}\right|_k = \left.\frac{\Delta(\mathrm{FV})}{\Delta t}\right|_k^{desired} - \left.\frac{\Delta(\mathrm{FV})}{\Delta t}\right|_k^{actual} \tag{4.12}$$

The ramp rate of the compensating action has to be changed according to the ramp rate of the fluctuating variable at each instant of time. For example, to mitigate the impacts of PV output fluctuation, a compensating action can be implemented using a Community Energy Storage (CES) [14] that may be used for smoothing out the fluctuations in PV generation in the feeder, as shown in Fig. 4.6(b). The ramp rate of the storage discharge power needs to be adjusted using (4.12) based on the IPRR value obtained by (4.10). The discharge ramp rate has to be adjusted at each instant of time based on the most recent IPRR value. Based on the discharge power ramp rate, the discharge current ramp rate of the storage device can be determined at each instant of time and can be sent to the storage controller for implementation. In this way, the proposed approach can aid in the decision making for a real time mitigation of PV impacts. While the proposed assessment approach could be used to assist in the decision making for mitigation of an ongoing PV impact in real time, it would not in itself be able to mitigate the impact, or control the action of mitigation.

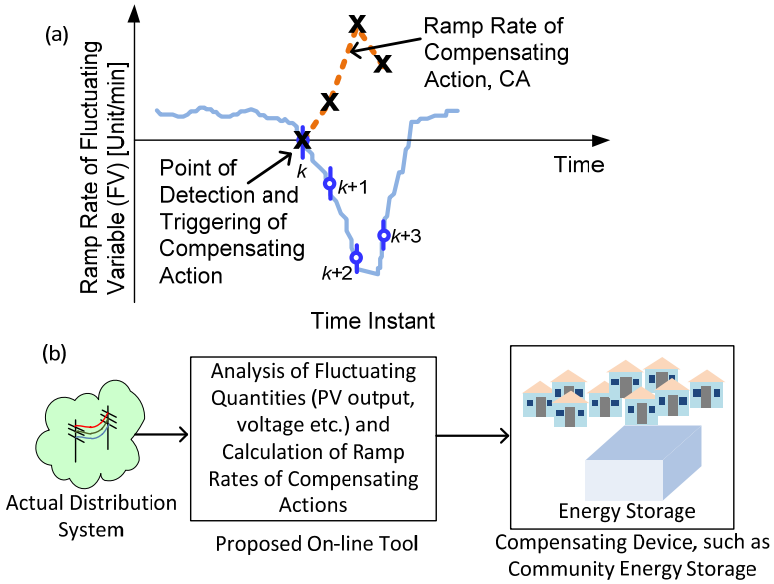

Fig. 4.6. Application of the proposed approach for mitigation of the impact of PV output fluctuations: (a) calculation of ramp rate of a generic compensating action; (b) translation of the idea in terms of a community storage device.

4.4 EXAMPLE APPLICATIONS

The proposed on-line assessment approach is applied on a typical LV distribution feeder in Australia that is connected to a real 11 kV distribution network derived from the distribution system in the South-East part of New South Wales. It is an 80 km long rural system with 3 voltage regulators. The MV network and LV feeder diagrams are shown in Fig. 4.7.

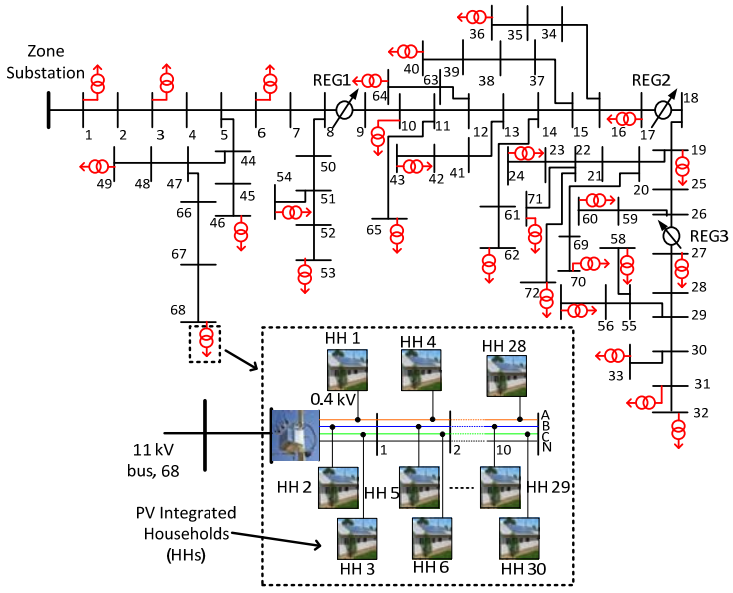

Fig. 4.7. Schematic diagram of the test distribution network.

The LV feeder is connected to bus 68 of the 11 kV network, as marked using an arrow and a rectangular box in Fig. 4.7. It contains households with rooftop PV units. Load profiles captured from a residential LV distribution system in Australia is used to develop voltage dependent household load models. Voltage dependency parameters of typical electric appliances [15] found in residential households were used for an aggregate modelling of the household loads. PV systems, each rated at 4 kW, are integrated with the feeder at different customer premises. The PV inverters are operated at unity power factor. The data of the test feeder is provided in Table 4-I. Though this thesis shows results corresponding to one of the LV feeders, it can be similarly applied for other LV feeders in the network.

TABLE 4-I

TEST LV FEEDER DATA

Feeder Length (metre)	350
Number of Households	30
Pole to Pole Distance (metre)	30-40
Conductor	7/3.00 AAC
MV/LV Transformer Size	160 kVA
PV Module / Inverter	Kyocera / SMA Sunnyboy

4.4.1 Online Monitoring of PV Impacts in Terms of Indices

The indices developed are used to quantify the impact PV has on the network. Fig. 4.8 shows the voltage deviation impact caused by the solar PV on the test feeder in terms of MVDI. The MVDI becomes negative due to the voltage rise caused by PV after 9 AM, as shown in Fig. 4.8(a), and continues to increase in the negative direction. A switch-over to 15-min sliding windows at this time can provide a larger view of the changes in voltage that takes place in the feeder due to the PV penetration. This is shown in Fig. 4.8(b). The MVDIs for all phases reduce to their peak negative levels at about 1 PM, as shown in Fig. 4.8(c). The numerical values of MVDIs indicate that voltage rise is approaching the overvoltage limit of 10%, as specified by Australian standards. Based on the severity of the situation, a 5-min sliding window is chosen for detailed analysis, as shown in Fig. 4.8(d). As mentioned earlier, the width of the window is constrained by the resolution of the data. The resolution of the data used in this chapter of the thesis is 1-minute. A narrower window can be used if a higher resolution data is available.

Although the width of the assessment window is selected at the user's discretion, a feature can be developed in the implementation of the proposed approach to make a suggestion to the operator to narrow down the width with the increase of the irradiance level. This would be useful to pay attention to the voltage rise impact before it reaches a limit violation level.

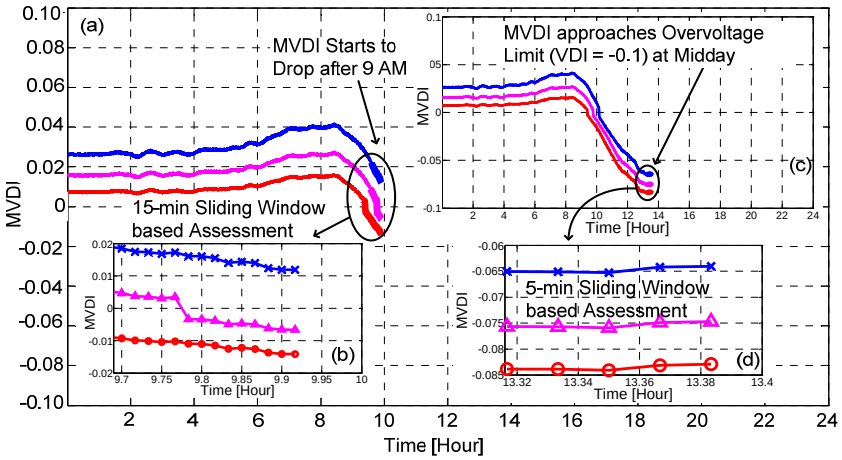

Fig. 4.8. On-line monitoring of voltage deviation caused by PV: (a) Voltage starts to rise above nominal value as indicated by negative MVDI; (b) A 15-min sliding window of the situation in Fig. 4.8(a); (c) MVDI approaches overvoltage limit; (d) A 5-min assessment window to obtain a closer view of the situation in Fig. 4.8(c).

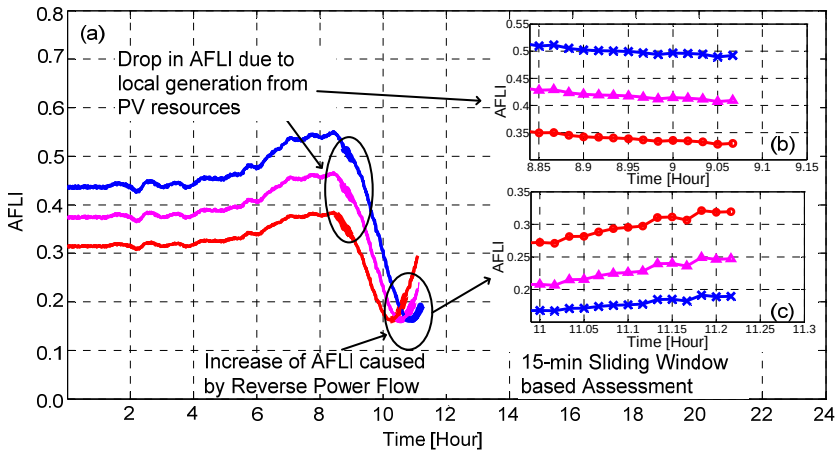

Fig. 4.9. On-line monitoring of feeder loading variation caused by PV: (a) Decrease of AFLI caused by PV units serving local loads and increase of AFLI in the midday caused by reverse power flow; (b) a 15-min sliding window of the decrease in AFLI; (c) a 15-min sliding window of the increase in AFLI

As the loads at the PV connection points are now served locally, less power is imported from the upstream network over the feeder and hence, the feeder loading is reduced. However, with the increase of the PV output power as the day progresses, the loading may increase due to the reverse power flow caused by the surplus power from PV units. Illustrations of these events are presented in Fig. 4.9 in terms of the feeder

loading, quantified using AFLI. The value of AFLI starts to drop at about 9 AM, as shown in Fig. 4.9(a), when the PV units starts to generate power to serve the local load demand. A 15-min assessment window corresponding to this time period is shown in Fig. 4.9(b) that provides a more precise view of the situation. With enough PV output power to exceed the load demand at the PV connection points, the AFLI values starts to increase at about 11 AM. This is shown in Fig. 4.9(a) on a daylong time frame and a detailed view of this is shown in Fig. 4.9(c) using a15-min assessment window.

Similar effect is observed with substation loading, shown in Fig. 4.10 with the index of the remaining capacity of substation, SRCI. The increase in SRCI starting at about 9 AM, as shown in Fig. 4.10(a), indicates the release of substation capacity due to the fact that the PV units are contributing to serve the local loads at the PV connection points. This is followed by a dropping trend from about 11 am due to the loading of the substation caused by the reverse power flow into the upstream network, also shown in Fig. 4.10(a). Both of the increasing and decreasing trends or SRCI are more accurately assessed using 15-min sliding windows, as shown in Fig. 4.10(b) and 10(c), respectively.

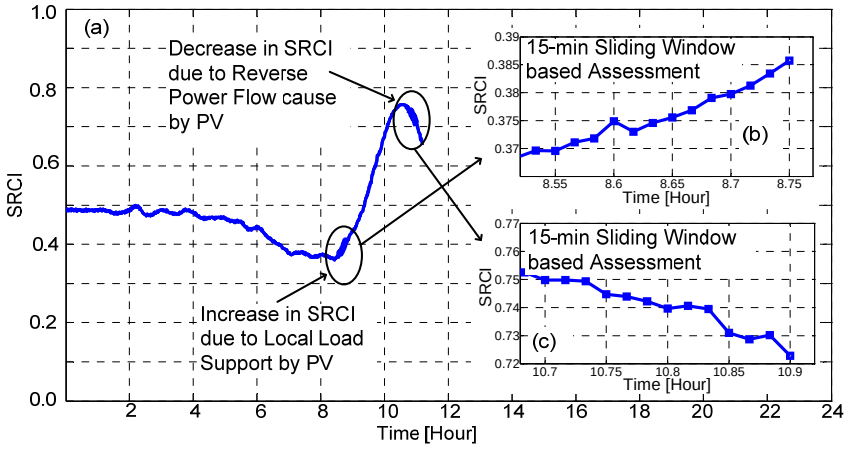

Fig. 4.10. On-line monitoring of substation loading variations caused by PV: (a) Increase of SRCI caused by PV units serving local loads and decrease of SRCI in the midday caused by reverse power flow; (b) a 15-min sliding window of the increase in SRCI; (c) a 15-min sliding window of the decrease in SRCI.

The power loss in the feeder decreases with the reduction in power import from the upstream network with the availability of PV power, which is shown in Fig. 4.11(a) with the drop in FLLR at 9 am in the morning. However, when the surplus power flows through the feeder towards the upstream substation, the power loss in the overall feeder increases, which is shown in Fig. 4.11(a), with the increase in FLLR, at about 11 AM. The increasing and decreasing trends of FLLR are assessed using the 15-min sliding

windows and shown in Fig. 4.11(b) and 11(c).

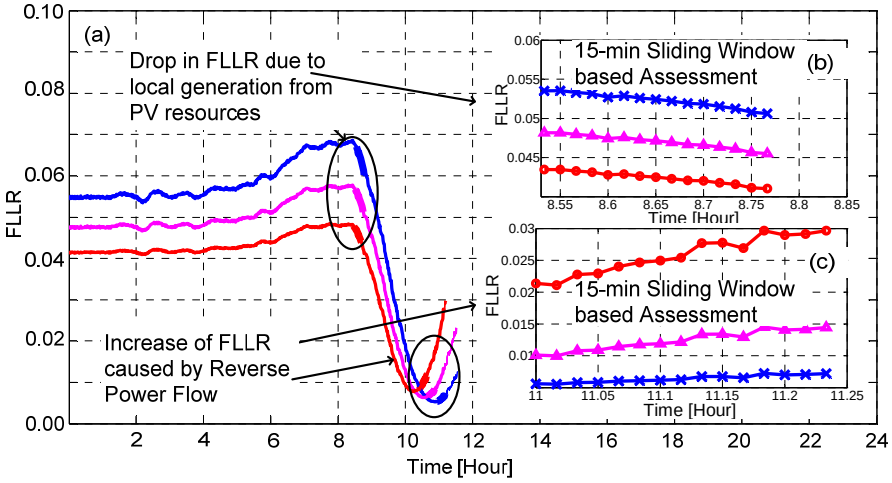

Fig. 4.11. On-line monitoring of feeder power loss variation caused by PV: (a) Decrease of FLLR caused by PV units serving local loads and increase of FLLR in the midday caused by reverse power flow; (b) a 15-min sliding window of the decrease in FLLR; (c) a 15-min sliding window of the increase in FLLR.

Summary of the Latest Sliding Window

Width of Sliding Window		15	min

Impact Indices	Min	Max	Moving Avg
MVDI	-0.063	-0.066	-0.065
AFLI	0.476	0.497	0.486
SRCI	0.220	0.247	0.233
FLLR	0.045	0.050	0.048

Violation of Overvoltage / Under Voltage Limit	No	Yes/No
Detection of Sudden Fluctuation	No	Yes/No
Maximum Voltage Change betn Two Consecutive Measurements	0.424	Volts
Maximum Power Change betn Two Consecutive Measurements	1.61	kW

Fig. 4.12. A summary report of PV impacts in the latest sliding window

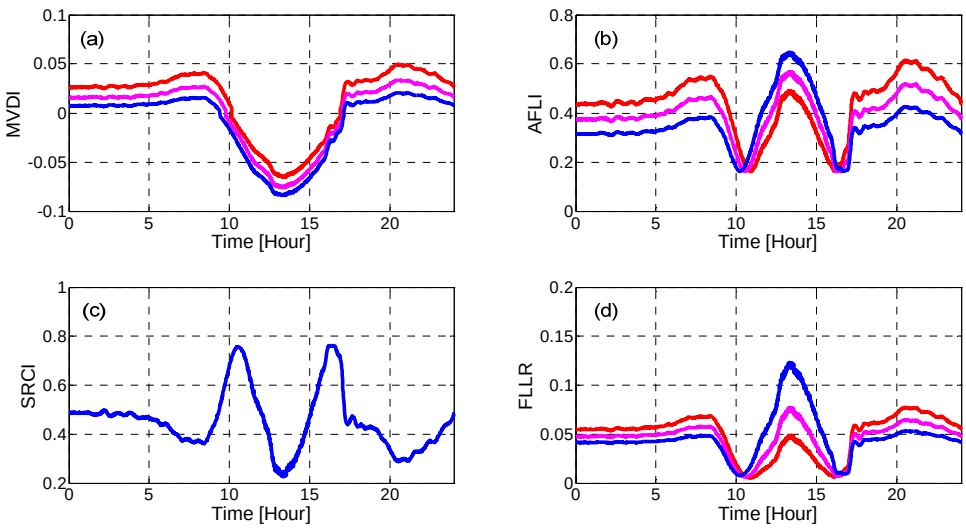

Fig. 4.13. PV impact indices after completion of a 24-hour period: (a) MVDI; (b) AFLI; (c) SRCI; (d) FLLR.

A summary report of the indices for the latest sliding window is available for an overview of the PV impacts as shown in Fig. 4.12. Once the full 24-hour period is completed, the trends of the impact indices and assessment reports over the entire day are available, as shown in Fig. 4.13. Variations in feeder voltage caused by PV is shown in terms of MVDI in Fig. 4.13(a), variations in feeder loading is shown in Fig. 4.13(b) in terms of AFLI, variation of the usage of substation capacity is shown in Fig. 4.13(c) using SRCI, and variations in feeder power loss is shown in Fig. 4.13(d) using FLLR.

4.4.2 Applications of Dynamic "What-if" Analysis

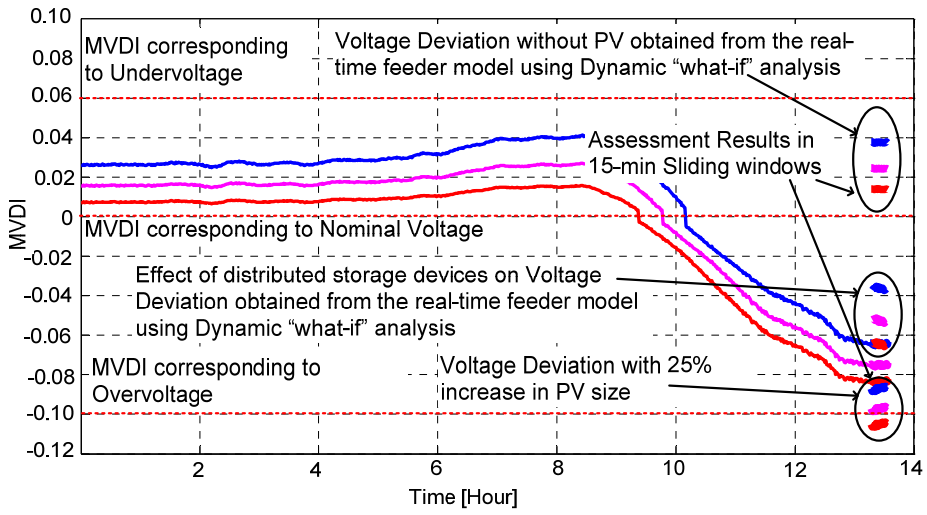

Fig. 4.14. Application of dynamic "what-if" analysis using MVDI

A simple, yet attractive application of the dynamic "what-if" analysis is to investigate how the network would behave without PV penetration to understand how the integration of PV has affected the system operation. For example, an operator might be interested to find out what would be the voltage deviation at midday without PV. This information can be obtained by performing a "what-if" analysis by forcing the PV outputs (which is already known from the on-line measurement) to zero on the real-time network model at midday. The proposed approach was used to perform such an analysis and the results are shown in terms of voltage deviation index in Fig. 4.14. It is shown that without PV, the MVDIs for different phases are within 0.01 to 0.04 at midday which indicates the voltage would be lower than nominal, but within the normal operating range.

Another "what-if" analysis can be performed to investigate the impact of increasing PV generation on real-time basis at about 1 pm. The sizes of solar PV units at different feeder nodes were increased by 25% of the present size. The "what-if" analysis

indicates a violation of the overvoltage limit with this increase in PV size as shown in Fig. 4.14.

A network operator can also use the "what-if" analysis feature to investigate the effectiveness of a potential mitigation strategy. For example, the impact of using distributed storage devices as a voltage rise mitigation strategy can be analysed by incorporating storage device models with the real-time distribution feeder model. Results of such a "what-if" analysis are shown in Fig. 4.14, where storage devices are used in the midday to consume surplus PV power when MVDI values reach nearly at the limit violation level. Distributed storage devices are operated in this case to consume surplus PV power and as a result voltage rise is partially mitigated, as observed from the MVDI values.

4.4.3 Online Impact Assessment of PV Output Fluctuations

The impact indices proposed in this thesis are applied to assess the impact of PV output fluctuations. A practical solar PV output profile obtained from the Renewable Energy Integration Facility at CSIRO Energy Technology in Australia was used for the example application. It is observed in the PV output data that the PV output was distorted by fluctuations in the sun irradiance level.

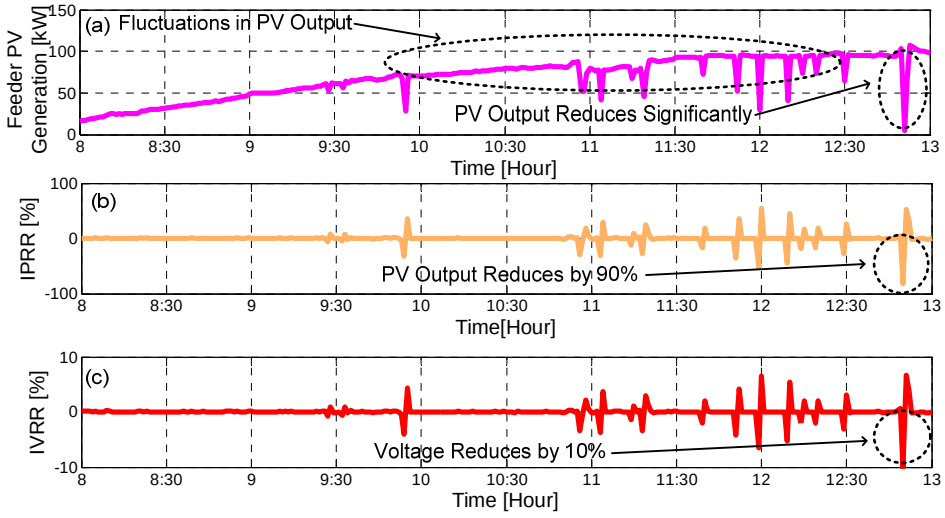

Fig. 4.15. Fluctuations in PV output (a) Fluctuations in total PV generation in the feeder; (b) IPRR in percent of total PV capacity in the feeder; (c) IVRR in percent of the feeder nominal voltage.

The impact of PV output fluctuations on the feeder is shown in Fig. 4.15 in terms of the proposed impact indices. The actual PV generation in kilowatts is shown in Fig. 4.15(a) that shows the PV output fluctuates several times in the period from 9:00 hours

to 13:00 hours. The PV output suddenly reduces to less than 5 kW from about 107 kW at about 12:50 pm. With respect to the total rated PV capacity, this fluctuation is more than 90%, as shown in Fig. 4.15(b). The IVRR caused by such reduction in PV output is shown in Fig. 4.15(c) which shows the voltage reduces by 10%.

A 60-min sliding window, from 12 hours to 13 hours, is used to observe the consecutive fluctuations in a single window, as shown in Fig. 4.16. If fluctuations occur at a higher frequency, a narrower window can be used. The fluctuations in MVDI are shown in Fig. 4.16(a) at the time instances corresponding to the PV output fluctuations in Fig. 4.15(a). Similarly, Fig. 4.16(b), 16(c), and 16(d) show the fluctuations in AFLI, SRCI and FLLR at the same time instances as in MVDI.

In summary, the proposed online approach would be useful for the distribution network operators to observe the impact of the present level of PV penetration on their networks in a real time environment. Using the dynamic "what-if" analysis feature of this approach, the network operators would also be able to understand the impacts of a potential PV penetration level on the present or actual condition of their network. Also, the impacts of ongoing PV output fluctuations on network voltage can be assessed using the proposed online approach as demonstrated through simulation results.

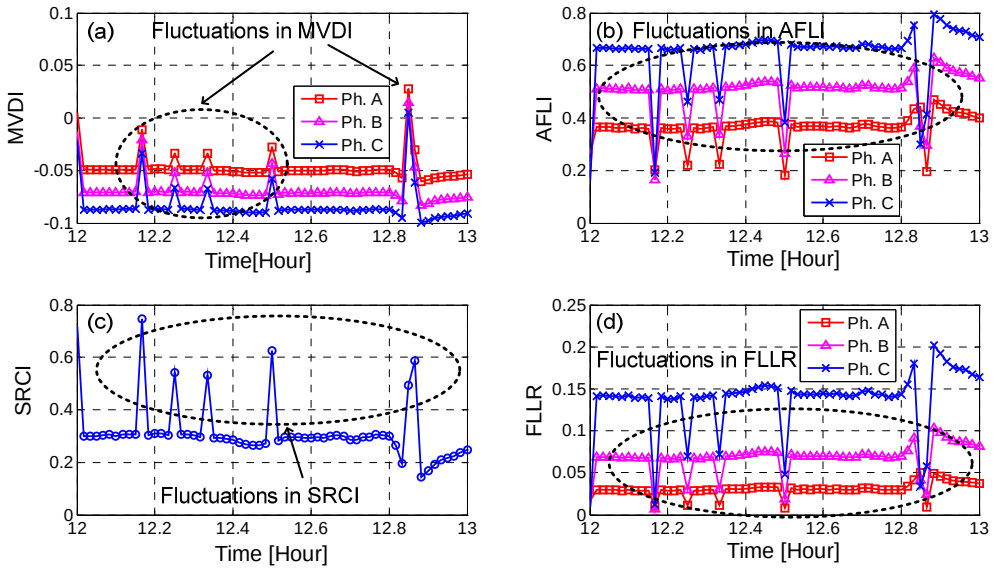

Fig. 4.16. Online assessment PV output fluctuation with impact indices in a 60-min sliding window: (a) MVDI; (b) AFLI; (c) SRCI; (d) FLLR.

4.5 CONCLUSION

A variable-width sliding window based on-line approach has been proposed for

investigation of rooftop solar PV impacts on LV distribution networks. The proposed approach will take on-line network data as input and then will analyse solar PV impacts on the network using a set of proposed impact indices. Using the variable-width sliding window allows the width of the assessment window to be varied depending on the situation. A narrow window can be used during peak PV period, while a wider window can be used during low or no PV output period. This can help to avoid unnecessary monitoring activities. With the availability of most updated network topology, load and PV output data, this approach can make use of real-time models of distribution networks for dynamic "what-if" analysis that would be useful for the assessment of solar PV impacts under a given PV generation scenario using the actual network condition at a given instant of time. A summary report of the assessment outcomes is also available for an 'at-a-glance' view of the impacts over a given period. The information obtained using the proposed approach would be beneficial to implement mitigation actions against adverse impacts of PV penetration, including fluctuations caused by sudden variations in PV output.

REFERENCES

[1] B. H. Chowdhury and A. W. Sawab, "Evaluating the value of distributed photovoltaic generations in radial distribution systems," *Energy Conversion, IEEE Transactions on,* vol. 11, pp. 595-600, 1996.

[2] R. A. Walling, R. Saint, R. C. Dugan, J. Burke, and L. A. Kojovic, "Summary of Distributed Resources Impact on Power Delivery Systems," *IEEE Transactions on Power Delivery* vol. 23, pp. 1636-1644, 2008.

[3] V. H. M. Quezada, J. R. Abbad, and T. G. S. Roman, "Assessment of energy distribution losses for increasing penetration of distributed generation," *Power Systems, IEEE Transactions on,* vol. 21, pp. 533-540, 2006.

[4] J. A. Martinez and J. Mahseredjian, "Load flow calculations in distribution systems with distributed resources. A review," 2011, pp. 1-8.

[5] L. F. Ochoa, A. Padilha-Feltrin, and G. P. Harrison, "Evaluating distributed generation impacts with a multiobjective index," *Power Delivery, IEEE Transactions on,* vol. 21, pp. 1452-1458, 2006.

[6] P. Chiradeja and R. Ramakumar, "An approach to quantify the technical benefits of distributed generation," *Energy Conversion, IEEE Transactions on,* vol. 19, pp. 764-773, 2004.

[7] R. C. Dugan and M. McGranaghan, "Sim City," *Power and Energy Magazine, IEEE,* vol. 9, pp. 74-81, 2011.

[8] S. Zhang, C. Zhang, and Q. Yang, "Data preparation for data mining," *Applied Artificial Intelligence,* vol. 17, pp. 375-381, 2003.

[9] P. A. N. Garcia, J. L. R. Pereira, S. Carneiro, Jr., V. M. da Costa, and N. Martins, "Three-phase power flow calculations using the current injection method," *Power Systems, IEEE Transactions on,* vol. 15, pp. 508-514, 2000.

[10] M. J. E. Alam, K. M. Muttaqi, and D. Sutanto, "A Three-Phase Power Flow Approach for Integrated 3-Wire MV and 4-Wire Multigrounded LV Networks With Rooftop Solar PV," *IEEE Transactions on Power Systems,* vol. 28, pp. 1728-1737, 2013.

[11] "IEEE Recommended Practice for Monitoring Electric Power Quality," *IEEE Std 1159-2009 (Revision of IEEE Std 1159-1995),* pp. c1-81, 2009.

[12] E. Kern Jr, E. M. Gulachenski, and G. A. Kern, "Cloud effects on distributed photovoltaic generation: Slow transients at the Gardner, Massachusetts photovoltaic experiment," *Energy Conversion, IEEE Transactions on,* vol. 4, pp. 184-190, 1989.

[13] T. D. Hund, S. Gonzalez, and K. Barrett, "Grid-Tied PV system energy smoothing," in *Photovoltaic Specialists Conference (PVSC), 2010 35th IEEE*, 2010, pp. 002762-002766.

[14] R. J. Yinger and A. E. Kamiab, "Good Vibrations," *Power and Energy Magazine, IEEE,* vol. 9, pp. 22-32, 2011.

[15] K. P. Schneider and J. C. Fuller, "Detailed end use load modeling for distribution system analysis," in *Power and Energy Society General Meeting, 2010 IEEE*, 2010, pp. 1-7.

Chapter 5

A VERSATILE VOLT-VAR CONTROL STRATEGY FOR SOLAR PV INVERTERS TO SUPPORT DISTRIBUTION NETWORKS WHILE MITIGATING VOLTAGE RISE AT MID-DAY AND VOLTAGE FLUCTUATIONS DURING PASSING CLOUDS

ABSTRACT

A multipurpose reactive power control strategy for solar PV inverters has been proposed for voltage support in distribution networks. The versatility of the proposed approach will allow it to be used for various conditions associated with PV power generation. In the proposed approach, normally the inverters will operate in a dynamic VAr compensation mode for voltage support (including low PV and no PV periods). During surplus PV power in the mid-day, the proposed strategy will control the PV inverters to absorb reactive power for voltage rise mitigation using a droop characteristic approach. During passing clouds, the proposed strategy can mitigate voltage fluctuations by appropriately varying reactive support using a ramp-rate based control. A dynamic model of the proposed PV inverter control has been developed to analyse its performance in terms of fast reactive control and voltage support under various conditions of PV generation. The results of the analysis performed on an Australian distribution system show that the proposed Volt-VAr control strategy can mitigate voltage rise, and improve the voltage profile despite potential vast changes in the sun irradiation during cloud passing and also in the absence of PV output during the evening.

5.1 INTRODUCTION

In recent days, the possibility of the incorporation of reactive power control capability with rooftop solar PV inverters for network support has been reported in the literature [1-6]. Although inverters are limited in size, an appropriate control of the available reactive power can provide considerable benefits in terms of network operation. Previous research e.g. [7], have shown that the voltage rise created by distributed generation can be mitigated by controlling the distributed generator unit to absorb an appropriate amount of reactive power. While controlling the PV inverter to absorb reactive power can mitigate the well-known voltage rise impact arising from a high penetration of rooftop PV resources in distribution networks, the injection of reactive power can be used to support the network voltage when PV power is absent, for example on a cloudy day, or during the evening peak load period.

Several strategies have been proposed in literature for reactive power control of PV inverters, such as *Q*-*V* droop [2-3, 6], power factor control [3-4, 6], and voltage control [3-4]. The *Q*-*V* droop method is a widely used control strategy where the amount of reactive power to be absorbed for mitigation of voltage rise is determined from a pre-specified droop characteristic between the point of common coupling (PCC) voltage and the PV inverter reactive power. Authors in [2] have applied the droop control method to limit the voltage within acceptable limits where the slope of the droop characteristic can be dynamically changed based on the maximum reactive power limit depending on the active power generation. In the power factor control approach, the reactive power output is determined using the active power output and the desired power factor of the inverter. A strategy for controlling the reactive power based on PV inverter active power is used in [5] for voltage rise mitigation in coordination with an energy storage unit. A combination of voltage and active power generation based *Q*-droop characteristic has been proposed in [1] for mitigation of voltage rise.

The dependency on the ambient irradiance condition makes solar PV generation subject to sudden fall and rise during cloud passing period resulting in a high ramp-rate operation. Such fluctuations of PV output can cause significant voltage fluctuation [8], particularly in weak radial systems. Earlier works have mainly concentrated on the voltage rise created by a slow variation of PV output with the progress of the day. A smart inverter is proposed in [6] where the simulation results indicate that voltage

fluctuations can be reduced by VAr support. Therefore, a control feature that explicitly caters for the high ramp-rate variations of PV output needs to be included with a reactive power control strategy so that the available reactive capacity can be exploited for various support functions for the network, including voltage fluctuation mitigation.

The contribution of this thesis is to develop a versatile reactive power control strategy that will be able to provide an appropriate reactive power support to meet various conditions associated with PV power generation, including the absence of PV in the evening. A dynamic VAr control approach is proposed for normal VAr support over the 24 hours period depending on the power drawn from the grid by the loads. This will include the voltage support during evening peak load period. Instead of using a *Q-V* droop, a reverse power flow versus reactive power droop characteristic is proposed for voltage rise mitigation during the period of surplus PV power. A strategy based on PV output ramp-rate is proposed for reactive power control during the period of cloud passing. A coordinated control strategy is developed for smooth transition among the various control modes, such as the transition from excess PV power to low PV power during passing clouds, so that high and unwanted step changes in reactive power can be avoided. The proposed strategy will therefore provide a better performance under diverse conditions of PV generation compared to other traditional strategies where explicit attention is not given to address the high ramp-rate operations of the inverter VAr support function. To investigate the performance of the proposed strategy in providing fast reactive support during passing clouds in the presence of physical device time lags, a dynamic model of the inverter reactive power control loop is developed. The dynamics of the voltage regulator are also modeled to study the impact of the proposed strategy on the regulator operation. An Australian distribution system is used to test the validity of the proposed approach.

5.2 THE PROPOSED REACTIVE POWER CONTROLLER

The proposed reactive power controller will have three modes of operation. Normally the controller will operate in Mode 1, which is a dynamic reactive power control mode to provide voltage support, as necessary. Mode 2 will be used to mitigate voltage rise produced by reverse power flow. If significant PV output fluctuations appear when the controller is in Mode 1/Mode 2 operation, a ramp-rate based voltage support will be provided using Mode 3. The amount of VAr support during different modes of

operation will depend on the available reactive power capacity of the inverter. The description of the control modes and the *Q*-capacity limits applicable to these modes are described below.

5.2.1 Mode 1: Dynamic VAr Compensation Mode for Feeder Voltage Support

In general, when there is no voltage rise caused by a high PV output producing reverse power flow, or no voltage fluctuation caused by PV output fluctuations, the proposed strategy will normally operate in a dynamic VAr compensation mode for feeder voltage support. According to this mode, reactive power support will be provided by a PV inverter if the voltage at the inverter connection point falls below a threshold. The design philosophy behind this mode is based on the idea that the only customers in a feeder who are contributing to create low voltage in the network by drawing power from the grid during low or no PV period (e.g. during the evening peak) will provide compensation to this by injecting VAr. If a household does not contribute to voltage drop because of having *zero* demand, then using the PV inverter of that household for VAr support may impose an issue of financial interest, because any increase of operating hour of the inverter will cause a decrease in the designed lifetime making it financially less efficient for the owner of the PV inverter. It is obvious that under bilateral arrangements between the grid operator and the customer, the households with PV inverters can participate in the ancillary services market. However, such an environment has not been considered in the present phase of this work.

The amount of reactive power support will dynamically vary depending on the power drawn by the customer from the grid (forward power, P_F, determined using the load demand P_L and PV inverter power, P_{PV}). The ratio of the voltage sensitivity with active power (σ_{VP}) to the voltage sensitivity with reactive power (σ_{VQ}) will be included in the VAr control function to determine the appropriate amount of VAr support necessary to compensate for the voltage drop produced by drawing active power from the grid. The VAr support function is developed in such a way that the user can control how much VAr will be injected at the detection of low voltage using a control parameter C_1 and how the VAr injection will vary during the peak load period, using a control parameter C_2. The expression of dynamic VAr support is given below.

$$Q_{\mathrm{INV}}(k)=\left(\frac{\sigma_{VP}}{\sigma_{VQ}}\right)\times P_{\mathrm{F}}(k_{\mathrm{VL}})\times\left[C_1+C_2\times\left\{\frac{P_{\mathrm{F}}(k)}{P_{\mathrm{F}}(k_{\mathrm{VL}})}-1\right\}\right] \tag{5.1}$$
$$P_{\mathrm{F}}(k)=P_{\mathrm{L}}(k)-P_{\mathrm{PV}}(k)$$

where, $P_{\mathrm{F}}(k_{\mathrm{VL}})$ is the forward power at the time instant when a voltage lower than a limit is detected, $P_{\mathrm{F}}(k)$ is the forward power at the k-th instant, C_1 is a parameter to determine the amount of reactive power support when the voltage lower than the limit is first detected and C_2 is a parameter to determine how the reactive power will be increased with the increase of power drawn from the grid once the lower voltage limit is detected. The expression in (5.1) indicates that the proposed strategy would be applicable for VAr support during no PV (at night, $P_{\mathrm{PV}} = 0$), and also during low PV (in the early morning/evening, $P_{\mathrm{PV}}>0$) periods. An approach for obtaining the parameter C_1 and C_2 is illustrated in Fig. 5.1. A forward power profile of the household where the PV inverter is installed can be obtained using historical load demand and PV output profiles, as shown in Fig. 5.1(a). The voltage profile at the household, also shown in Fig. 5.1(a), corresponding to the forward power profile is analysed to determine the time instant k_{VL} when the voltage falls below the specified limit.

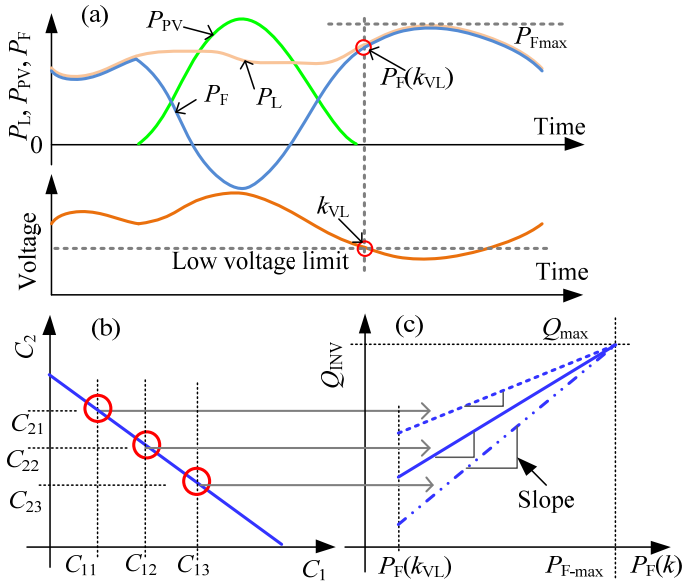

Fig. 5.1. Dynamic VAr compensation mode for voltage support. (a) Historical forward power profile and voltage profile. (b) Relation between C_1 and C_2. (c) Relation between PF and QINV under different selections of (C_1, C_2).

The inverter will start to inject VAr from this time instant. According to (5.1), for a given set of values of σ_{VP}, σ_{VQ} and a given forward power profile, the amount of VAr at

the time instant k_{VL} is controlled using the value of C_1.

The value of the parameter C_1 can be selected from a range (0 to C_{1max}), where C_{1max} is obtained from (5.1) by replacing Q_{INV} with Q_{max} and replacing $P_F(k)$ with $P_F(k_{VL})$, as given below.

$$C_{1max} = \frac{Q_{max}}{P_F(k_{VL})} \times \frac{\sigma_{VQ}}{\sigma_{VP}} \tag{5.2}$$

where, Q_{max} is the capacity of the PV inverter under consideration. The selection of the value of C_1 will vary, depending on a number of site specific considerations, e.g., how severe is the specified low voltage limit for the system under consideration and how much VAr support needs to be given at the first detection of low voltage. Once the value of C_1 is selected, the value of C_2 is determined using (5.1) by replacing Q_{INV} with Q_{max} and replacing $P_F(k)$ with P_{Fmax}, as given below.

$$C_2 = \left(\frac{Q_{max}}{P_F(k_{VL})} \times \frac{\sigma_{VQ}}{\sigma_{VP}} - C_1 \right) \times \left(\frac{P_F(k_{VL})}{P_{Fmax} - P_F(k_{VL})} \right) \tag{5.3}$$

For a selected set of (C_1, C_2), how the inverter reactive power, Q_{INV}, will be increased with the increase of forward power, P_F, up to the maximum forward power P_{Fmax}, can be determined using (5.1). P_{Fmax} is obtained from the historical P_F profile, as shown in Fig. 5.1(a). Once the inverter starts to inject VAr upon detection of the low voltage limit, the VAr injection afterwards is governed by the variation of P_F. Further, as indicated by (5.1) the VAr injection is independent of the voltage level, as the voltage will not be controlled using any feedback arrangement based on a voltage set-point. Therefore, the VAr injection will not be switched off even when the voltage is improved above the low voltage threshold. The only time the VAr injection will stop is when the forward power goes below its level when the low voltage was first detected. Fig. 5.1(b) shows three sets of (C_1, C_2) and the corresponding Q_{INV} characteristics. For the set (C_{11}, C_{21}) in Fig. 5.1(a), C_1 is low and therefore a low value of Q_{INV} is injected for voltage support when a low voltage is first detected. However, Q_{INV} increases at a high rate with the increase of P_F, as indicated by the slope of the Q_{INV} in Fig. 5.1(b). For the sets (C_{12}, C_{22}) and (C_{13}, C_{23}), C_1 is increased and therefore higher amount of power is injected at the first detection of low voltage. However, due to the limit of Q_{max}, the slope of Q_{INV} is lower than before. The combination of (C_1, C_2) is user-defined and will govern the distribution

of Q-capacity over the range of variations in power drawn from the grid for voltage support.

Although this thesis has used the variation of active power for determining the amount of reactive power support in (5.1) - (5.3), the apparent power can also be used for the same purpose. This would be beneficial, particularly for industrial feeders with high reactive power consumption.

5.2.2 Mode 2: Droop Mode during Surplus PV Power Operation

The cause of the voltage rise impact of solar PV is mainly the reverse power flow created by excess PV power at the PV connection point. Therefore, a reverse power flow based reactive power droop control method is used to mitigate the voltage rise. Similar to Mode 1 operation, the design philosophy for Mode 2 is based on the idea that only the customers in a feeder that are contributing to create voltage rise in the network by producing reverse power flow will provide mitigation action by consuming VAr. The amount of the reactive power output for droop mode operation can be obtained using the expression given below.

$$Q_{\text{INV}}(k) = \begin{cases} Q_{\min} + P_{\text{R}}(k)\dfrac{Q_{\max} - Q_{\min}}{P_{\text{R-UL}} - P_{\text{R-LL}}}, \text{if } P_{\text{R-LL}} < P_{\text{R}}(k) < P_{\text{R-UL}} \\ Q_{\max}, \text{if } P_{\text{R}}(k) \geq P_{\text{R-UL}} \end{cases} \tag{5.4}$$

where, Q_{INV} is the amount of reactive power obtained from a droop characteristic, P_{R} is the reverse power flow, $Q_{\min}$ and $Q_{\max}$ are the minimum and maximum reactive power respectively, $P_{\text{R-LL}}$ and $P_{\text{R-UL}}$ are the lower and upper limit of reverse power flow respectively. For a given range of reverse power flow, the slopes of Q_{INV} will vary for different values of reactive capacities ($Q_{\max 1}$, $Q_{\max 2}$, $Q_{\max 3}$) as shown in Fig. 5.2(a). Again, for a given $Q_{\max}$, the slopes of Q_{INV} will vary for different ranges of reverse power flow as shown in Fig. 5.2(b).

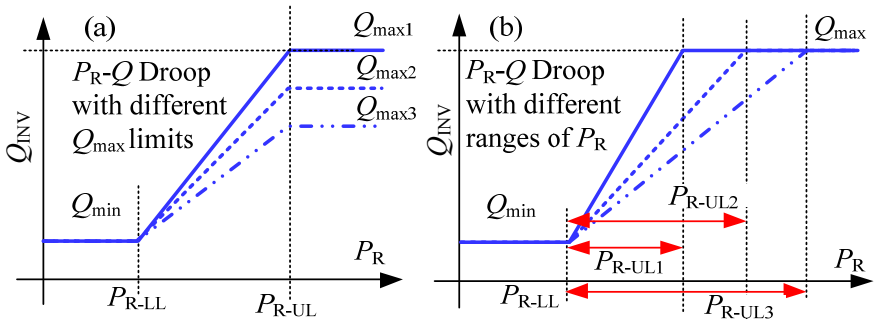

Fig. 5.2. Reverse power flow based reactive power droop characteristics. (a) For different Q capacities. (b) For different ranges of reverse power flow.

5.2.3 Mode 3: Ramp-rate Mode for Voltage Fluctuation Mitigation

When the PV units experience shading effects due to passing clouds, PV power fluctuation may become severe and can create significant voltage fluctuations in weak radial feeders. During such power and voltage fluctuations, the reactive power of the PV inverter will be controlled using the ramp-rate of the PV panel power P_{DC} to provide fast and appropriate reactive power support as given below.

$$Q_{INV}(k) = Q_{INV}(k-1) - \lambda \times \left(\frac{\sigma_{VP}}{\sigma_{VQ}}\right) \times \frac{dP_{DC}}{dt}(k), \text{if} \left|\frac{dP_{DC}}{dt}(k)\right| \geq \text{PVRR}_{lim} \tag{5.5}$$

where, λ a user defined scale factor that can increase or decrease the ramp-rate of the inverter reactive power; (dP_{DC}/dt) is the ramp-rate of the PV panel output power; and PVRR_{lim} is a threshold of PV output ramp-rate, beyond which the ramp-rate mode will be applied. The ratio of σ_{VP} to σ_{VQ} is included in (5.5) to determine the appropriate amount of VAr support necessary to compensate for the sudden drop in voltage produced by sudden reduction of PV power generation due to cloud passing. If $\lambda = 1$ the ramp-rate of the inverter reactive power is controlled according to the ramp-rate of the PV panel output. However, if $\lambda > 1$, then the ramp-rate is scaled up which would be useful in providing additional reactive power support within the inverter capacity limit. The value of λ can be determined dynamically for using the maximum available Q-capacity at any given instant using the expression given below.

$$\lambda(k) = -\frac{Q_{max}(k) - Q_{INV}(k-1)}{\frac{dP_{DC}}{dt}(k) \times \left(\frac{\sigma_{VP}}{\sigma_{VQ}}\right)} \tag{5.6}$$

The ratio of the voltage sensitivity to the active and reactive power has been incorporated in (5.5) to consider the change in voltage created by change in PV power generation. Such sensitivities strongly depend on the R/X ratio of the feeders as discussed in [9-10]. For a given feeder, such sensitivities can be obtained by injecting active and reactive power and observing the changes in voltage, as proposed in [9] by one of the co-authors.

5.2.4 A Coordinated Control for Smooth Transition among Control Modes

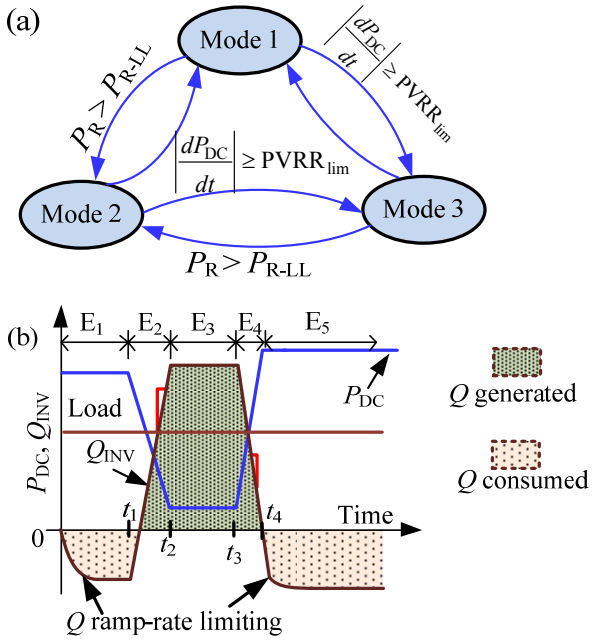

Fig. 5.3. (a) Mode transition diagram. (b) Illustration of Mode2/3 transitions.

A mode transition diagram is used is Fig. 5.3(a) to show the transitions among control modes. The inverter normally operates in Mode 1 that injects VAr to improve feeder voltage according to (5.1). During the Mode 1 operation, if a reverse power flow beyond a certain level appears (P_R>$P_{R\text{-}LL}$), then the control system enters into Mode 2 operation and consumes reactive power according to (5.4). At any moment of Mode 1 or Mode 2 operation, if the PV output fluctuates at a ramp-rate higher than $PVRR_{lim}$, then Mode 3 is triggered that provides reactive power support to mitigate voltage fluctuation according to (5.5). The activation of Mode 3 by detecting a negative ramp-rate of P_{DC} caused by a sudden reduction in PV output suggests that there will be a low PV period at the end of the negative ramping event. The reactive power support is continued during the low PV period for a user defined support interval τ_S. The amount

of τ_S is only limited by the ratings and specifications of the inverter components. In general, τ_S needs to be selected in such way that it is larger than most of the short-term cloud passing events. The expression for continuing the VAr support is given below.

$$Q_{\text{INV}}(k) = Q_{\text{INV}}(k-1), \text{if } t(k) - t(k-j) \le \tau_S \tag{5.7}$$

where, $t(k)$ is the time at the k-th instant, $t(k\text{-}j)$ is the time at a previous $(k\text{-}j)$-th instant when the most recent ramp-rate of P_{DC} less than the threshold of -PVRR_{lim} was detected; τ_S is the predefined support interval. The reason for using $t(k)$ rather than the instant, k, is to indicate 'time' in (5.7) since the support interval τ_S is defined in unit of time (minute or second).

If any positive ramping event is not detected within the support period τ_S due to a continuously cloudy condition in the day, then the system returns to Mode 1 control and injects VAr to provide voltage support, as necessary.

A ramp-rate limiter, given in (5.8), is used during operation in Mode 1 and 2, and also during the mode transitions 1-2, 2-1, 3-1 and 3-2 to avoid any high step change in reactive power generation/consumption, which may create voltage fluctuation itself. The ramp-rate limiter function is not applied in Mode 3 operation and in the transitions from other modes to Mode 3 operation to avoid any unwanted VAr consumption or injection which may deteriorate voltage drop or voltage rise during high ramp-rate operations.

$$Q_{\text{INV}}(k) = \begin{cases} Q_{des}(k), \text{if } -Q_{\Delta-\max} < |Q_{\text{INV}}(k-1)| - |Q_{\text{des}}(k)| < Q_{\Delta-\max} \\ Q_{\text{INV}}(k-1) + \dfrac{|Q_{\text{INV}}(k-1)| - |Q_{des}(k)|}{n}, \text{otherwise.} \end{cases} \tag{5.8}$$

where, $Q_{des}(k)$ is the desired Q at time instant k, $Q_{\Delta\text{-max}}$ is the allowable ramp-rate of Q; and, n is the step number to limit the step change of Q.

An illustration of the coordinated transitions between Mode 2 (voltage rise mitigation mode) and Mode 3 (voltage fluctuation mitigation mode) is provided in Fig. 5.3(b) using a fictitious PV output profile. Mode 1/Mode 2 transitions do not contain any fast ramping events and is less complex to deal with.

The total time period of the PV output profile is divided into five events, E_1 to E_5. In

the event E_1 from time $t = 0$ to t_1, the PV output P_{DC} is such that it produces a reverse power flow high enough to cause the inverter to absorb reactive power according to the droop characteristic in Mode 2. However, to prevent any sudden change in Q_{INV}, a ramp-rate limiter is applied, as given in (5.8). During the event E_2 from time $t = t_1$ to t_2, the P_{DC} sharply falls at a ramp-rate lower than $-PVRR_{lim}$. During this event, Q_{INV} is controlled using Mode 3. In the event E_3 from time $t = t_2$ to t_3, the P_{DC} remains at the level attained at time t_2. During this period, Q support continues over the support interval and Q_{INV} is determined using (5.7). During the event E_4 from time $t = t_3$ to t_4, the P_{DC} increases at a ramp-rate higher than the limit $PVRR_{lim}$; Q_{INV} in this period is controlled using Mode 3. In the event E_5 for time $t \geq t_4$, the P_{DC} remains at the level attained at t_4 and produces reverse power flow. Therefore, Q_{INV} control is transferred from Mode 3 to Mode 2 through the ramp-rate limiter in (5.8).

5.2.5 Dynamic VAr Capacity Limit under Varying PV Output

Although rooftop PV systems at low voltage feeders are usually operated at unity power factor, in the recent days, the incorporation of VAr capability with LV level inverter installations are currently being considered by utilities. For a PV inverter to provide VAr support, additional capacity needs to be incorporated so that the inverter can generate/consume reactive power even when rated active power is being produced [4]. For a given inverter, the maximum reactive power capacity at the rated active power operation can be obtained from (5.9), and is shown in Fig. 5.4(a).

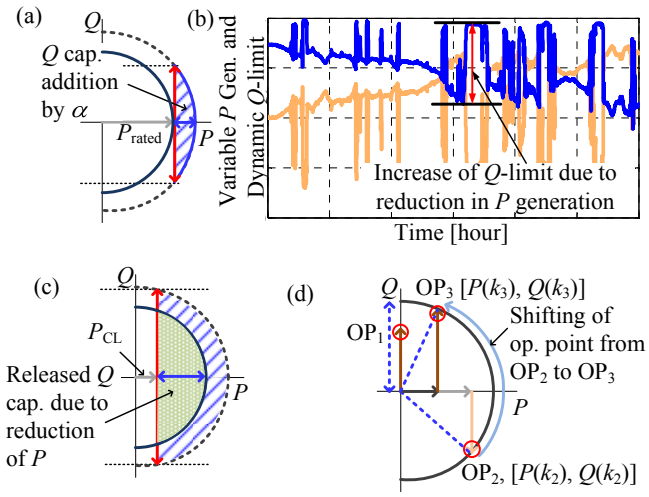

Fig. 5.4. (a) Q-capacity addition. (b) Variable Q-limit. (c) Q-capacity realse during cloud passing/low PV period. (d) Shifting of operating modes.

$$Q_{\max} = P_{rated}^{\mathrm{PV}}\left(\sqrt{\alpha^2 + 2\alpha}\right) \tag{5.9}$$

where, $Q_{\max}$ is the maximum reactive power at rated PV output P_{rated}^{PV}, α is the additional capacity as a proportion of the rated active power output of the PV system, incorporated for reactive support.

The reactive support capability is increased during passing clouds or low PV period due to the less production of active power, as shown in Fig. 5.4(b). Therefore, reactive capacity can be released for generating more VAr output, as shown in Fig. 5.4(c), which can provide further voltage support to the network. The Q-limit at a given instant of cloudy or low PV period, k, can be determined using the following expression.

$$Q_{\max}(k) = \sqrt{[(1+\alpha)\times P_{rated}]^2 - [P_{\mathrm{CL}}(k)]^2} \tag{5.10}$$

where, the left hand side term under the square root sign is the capacity of the inverter and $P_{\mathrm{CL}}(k)$ is the active power during time instant k of the cloudy or low PV period. For Mode 2 operation, $Q_{\max}$ obtained by (5.9) will be considered as the Q-limit, because it would not be wise to absorb more Q for voltage rise mitigation when active power production is lower than P_{rated} and therefore more Q-capacity is available. For Mode 2 and 3, the dynamic Q-limit determined by (5.10) will be applied to take advantage of the maximum Q-availability for voltage support.

For a given inverter capacity, the operating points corresponding to the three modes of operation are shown in Fig. 5.4(d). The operating point OP_1 corresponds to a time instant k_1 when the inverter reactive power is controlled using Mode 1 operation. The operating point OP_2 corresponds to time instant k_2 when inverter active power $P(k_2)$ produces a reverse power flow and $Q(k_2)$ is determined using Mode 2 control. The operating point OP_3 corresponds to the time instant k_3 when inverter active power is reduced to $P(k_3)$ at a high ramp-rate due to cloud passing. To provide adequate reactive support, the inverter operates in Mode 3 where $Q(k_3)$ is determined using (5.5). Transitions through the trajectories among operating points are performed using a PI controller designed in Section 5.3.

5.3 SYSTEM MODELLING FOR PERFORMANCE EVALUATION OF THE PROPOSED REACTIVE POWER CONTROL STRATEGY

To investigate the effectiveness of the proposed control strategy for reactive power support, network analysis will be performed using both steady-state and dynamic approach. In the steady-state approach, a series of steady-state models of the network will be solved for each time instant under consideration. In the dynamic approach, the dynamic behaviour of the network between two given instants will be investigated using a differential-algebraic model of the system.

The steady-state network model at a given k-th time instant is developed using the network admittance matrix $\mathbf{Y}$, voltage regulator tap T_{REG}, active and reactive loads P_{L}, Q_{L}, and, active and reactive power of PV inverters P_{INV}, Q_{INV} at that time instant as given below.

$$\begin{bmatrix} 0 \\ 0 \end{bmatrix} = \begin{bmatrix} \dfrac{(P_{\mathrm{L}} - P_{\mathrm{INV}})V_{\mathrm{re}} - (Q_{\mathrm{L}} - Q_{\mathrm{INV}})V_{\mathrm{im}}}{{V_{\mathrm{re}}}^2 + {V_{\mathrm{im}}}^2} - \phi_{\mathrm{re}}(\mathbf{Y}, T_{\mathrm{REG}}, V_{\mathrm{re}}, V_{\mathrm{im}}) \\ -\dfrac{(P_{\mathrm{L}} - P_{\mathrm{INV}})V_{\mathrm{im}} + (Q_{\mathrm{L}} - Q_{\mathrm{INV}})V_{\mathrm{r}}}{{V_{\mathrm{re}}}^2 + {V_{\mathrm{im}}}^2} - \phi_{\mathrm{im}}(\mathbf{Y}, T_{\mathrm{REG}}, V_{\mathrm{re}}, V_{\mathrm{im}}) \end{bmatrix} \tag{5.11}$$

where, V_{re} and V_{im} are the real and imaginary components of voltage, and ϕ_{re} and ϕ_{im} are functions representing real and imaginary components of calculated network currents. The model in (5.11) is a steady-state current injection model of the network developed by the authors and the details can be found in [11]. By solving (5.11), V_{re} and V_{im} can be obtained for each instant of time under consideration.

For the dynamic analysis, the values of P_{INV} and Q_{INV} are determined from the state variables representing the dynamic behaviour of the PV inverter, as described in the subsection below.

5.3.1 Dynamic Modelling and Control of PV Inverter

A dynamic model of the PV inverter is necessary to understand the performance of the proposed strategy in the context of practical system components that are subject to physical device time lags. Detailed switching models of the power electronic converters are used in power-electronics based investigations where high frequency switching transients are of interest. However, as the main interest in this thesis is to investigate the

performance of the proposed strategy in the presence of physical device time lags only, the modelling of the fast switching dynamics is excluded and only the ac-side current control dynamics are considered.

In a PV inverter control system, the synchronously rotating current/voltage signals are decomposed into direct (d) and quadrature (q) axis components using a Phase-Locked-Loop (PLL) function which regulates the q-axis component of the inverter connection point voltage (v_q) to be *zero* in steady state when the frequency determined by the PLL becomes equal to the grid frequency [12]. Therefore, the d-axis component of voltage (v_d) for inverter control can be directly obtained from the magnitude of voltage at the PV connection point as shown in [13]. Regulation of v_q to *zero* makes it possible to control the real power by controlling d-axis current (i_d), and reactive power by controlling q-axis current (i_q) only, as the active and reactive power of the PV inverter are related to i_d and i_q and these are expressed as below.

$$\begin{bmatrix} P_{INV} \\ Q_{INV} \end{bmatrix} = \begin{bmatrix} v_d & v_q \\ v_q & -v_d \end{bmatrix} \begin{bmatrix} i_d \\ i_q \end{bmatrix} \tag{5.12}$$

The block diagrams of the i_d and i_q controller, including the reactive power control loop is shown in Fig. 5.5. If the DC link voltage dynamics is not considered, the reference current $i_{d\text{-ref}}$ can be obtained from the PV panel DC power P_{DC} as given below.

$$i_{d\text{-ref}} = \frac{P_{DC}}{v_d} \tag{5.13}$$

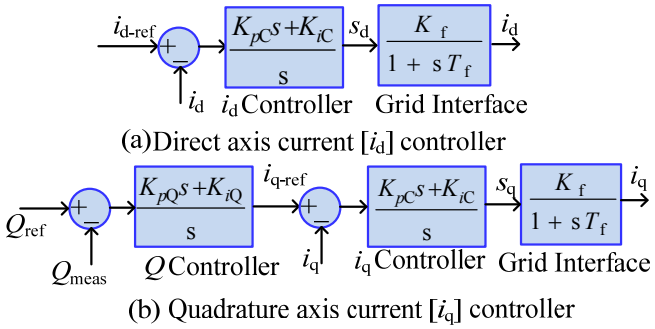

Fig. 5.5. PV inverter current controllers. (a) d-axis current controller. (b) q-axis current controller with reactive power controller.

The reference current $i_{q\text{-ref}}$ is obtained by processing the difference between the reference reactive power Q_{ref} (determined by the proposed strategy) and Q_{meas} ($-v_d \times i_q$)

through a PI controller. The differences between the actual dq-axis currents and reference dq-axis currents are processed through PI controllers to produce the signals s_d and s_q to obtain dq-axis components of the inverter control signals m_d and m_q. The dq-axis currents are related to the control signals m_d, m_q, dc-link voltage V_{dc}, v_d and v_q as given below.

$$\begin{bmatrix} \frac{di_d}{dt} \\ \frac{di_q}{dt} \end{bmatrix} = \begin{bmatrix} -\frac{R_f}{L_f} & \omega \\ -\omega & -\frac{R_f}{L_f} \end{bmatrix} \times \begin{bmatrix} i_d \\ i_q \end{bmatrix} + \frac{1}{L_f} \times \begin{bmatrix} 0.5 m_d V_{DC} - v_d \\ 0.5 m_q V_{DC} - v_q \end{bmatrix} \tag{5.14}$$

where, R_f and L_f are the resistance and reactance of the grid coupling filter. To decouple the dynamics of i_d and i_q, m_d and m_q are defined as given below [12].

$$m_d = \frac{2\left(s_d - L_f \omega i_q + v_d\right)}{V_{DC}}, \text{and } m_q = \frac{2\left(s_q + L_f \omega i_d + v_q\right)}{V_{DC}} \tag{5.15}$$

Using (5.14) and (5.15), the current controller outputs s_d and s_q can be related to i_d and i_q through the first order dynamics of the grid coupling filter whose gain and time constants can be obtained from R_f and L_f. Differential equations describing the inverter control dynamics are given below.

$$\frac{di_d}{dt} = \frac{1}{T_f} \times \left(K_f s_d - i_d\right) \tag{5.16a}$$

$$\frac{ds_d}{dt} = -K_{pC} \times \frac{1}{T_f} \times \left(K_f s_d - i_d\right) + K_{iC} \times \left(i_{d\text{-ref}} - i_d\right) \tag{5.16b}$$

$$\frac{di_q}{dt} = \frac{1}{T_f} \times \left(K_f s_q - i_q\right) \tag{5.16c}$$

$$\frac{ds_q}{dt} = K_{pC} \times \left[\frac{di_{q\text{-ref}}}{dt} - \frac{1}{T_f} \times \left(K_f s_q - i_q\right)\right] + K_{iC} \times \left(i_{q\text{-ref}} - i_q\right) \tag{5.16d}$$

$$\frac{di_{q\text{-ref}}}{dt} = -K_{pQ} v_d \frac{1}{T_f} \times \left(K_f s_q - i_q\right) + K_{iQ} \times \left(Q_{ref} - v_d i_q\right) \tag{5.16e}$$

Here, K_{pC} and K_{iC} are the current regulator parameters; T_f and K_f are the time constant and gain of the grid coupling filter; K_{pQ} and K_{iQ} are the reactive power controller parameters.

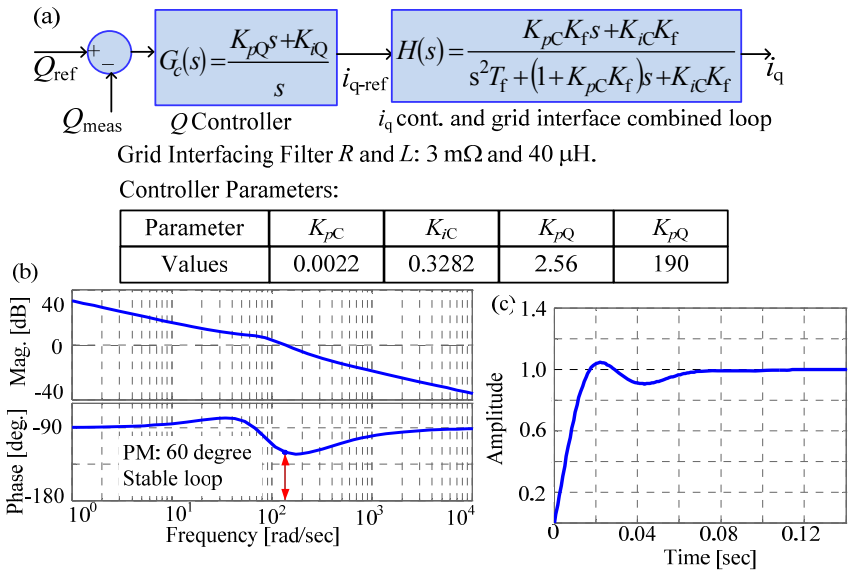

Fig. 5.6. Reactive power controller dynamic performance (a) Controller transfer function. (b) Open loop frequency response. (c) Closed loop step response.

Simplifying the control loop in Fig. 5.5(b) from the output of the Q controller to the output of the grid interface gives the transfer function $H(s)$ shown in Fig. 5.6(a). This transfer function is used to obtain the reactive power control parameters K_{pQ} and K_{iQ}. The MATLAB Simulink PID control design tool is used to obtain the initial controller parameters based on 60° phase margin and reference tracking algorithm [14]. With the initial controller parameters, loop shaping technique is used to tune the parameters further. The frequency response characteristics of the open loop system consisting of $G_c(s)$ and $H(s)$ are shown in Fig. 5.6(b) that shows a phase margin of 60° which indicates a stable loop according to [14]. A step response of the closed loop system is shown in Fig. 5.6(c) that shows an overshoot of less than 10% and rise time of around 20 msec. Parameters of the PI controllers for i_d, i_q, and Q are provided in Fig. 5.6(a).

This chapter of the thesis focuses on developing a strategy for VAr control of the distributed PV inverters at the LV customer households where only the dynamics of P-Q control loops have been modeled and the loads at the inverter connection points are actually measured in real time. Therefore, the VAr control is based on local measurements of actual load. The controller only operates based on local load and PV generation, and does not consider the impact of the dynamics of loads at other locations.

5.3.2 Step Voltage Regulator (SVR) Dynamics

The dynamics of the operation of a step voltage regulator in a distribution network can be modeled using the following expression.

$$T_{\mathrm{REG}}(k)=\begin{cases} T_{\mathrm{REG}}(k-1)+1, \text{if } V_{\mathrm{LC}} > (1+BW)V_{\mathrm{UL}} \text{ for } t \geq \tau_D \\ T_{\mathrm{REG}}(k-1)-1, \text{if } V_{\mathrm{LC}} < (1-BW)V_{\mathrm{LL}} \text{ for } t \geq \tau_D \\ T_{\mathrm{REG}}(k-1), \text{otherwise} \end{cases} \tag{5.17}$$

where, $T_{\mathrm{REG}}(k)$ is the voltage regulator tap at the k-th instant; V_{LC} is the load centre voltage; V_{UL} and V_{LL} are the voltage upper limit and lower limit, respectively; BW is a control bandwidth, and τ_{D} is the tap changer time delay. Modelling of the voltage regulator is performed using transfer admittance method [15]. The value of $T_{\mathrm{REG}}(k)$ is used to modify the regulator transfer admittance and the modifications are incorporated with the network admittance matrix , as indicated in (5.11) using ϕ_{re} and ϕ_{im} to reflect the effect of tap operation on network voltage. The modifications performed on the admittance matrix elements are given below.

$$\begin{aligned} Y_{\mathrm{ps}}(k) &= Y_{\mathrm{ps}}(k-1)-(\alpha-\beta)y_{\mathrm{REG}} \\ Y_{\mathrm{ss}}(k) &= Y_{\mathrm{ss}}(k-1)-(\beta^2-\alpha^2+2\alpha-2\beta)y_{\mathrm{REG}} \\ \text{where, } \alpha &= \frac{T_{\mathrm{REG}}(k-1)}{1+T_{\mathrm{REG}}(k-1)}, \beta = \frac{T_{\mathrm{REG}}(k)}{1+T_{\mathrm{REG}}(k)} \end{aligned} \tag{5.18}$$

where, the regulator is connected between bus p and s, Y_{ps} is the mutual admittance between bus p and s, Y_{ss} is the self admittance of bus s, y_{REG} is the transfer admittance of the regulator.

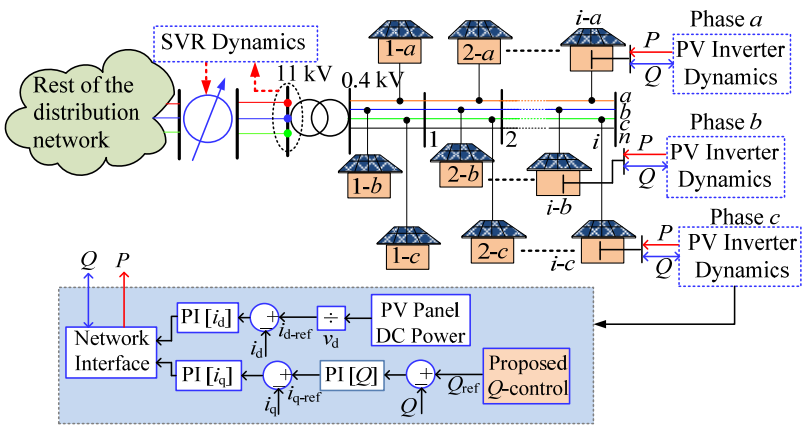

Fig. 5.7. An integrated network model showing the integration of voltage regulator and PV inverter

dynamics.

A schematic diagram showing the network integration of voltage regulator dynamics and PV inverter dynamics is shown in Fig. 5.7 which will be used for investigating the dynamics of the distribution network with the effect of the proposed reactive power control strategy including the impact on the voltage regulator tap operation.

5.4 APPLICATION EXAMPLES

An Australian distribution test system from the South-East part of New South Wales is used to verify the proposed reactive power control approach. A schematic diagram of the test system, including the configuration of an LV feeder from the system, is shown in Fig. 5.8. All the households in the LV feeder contain rooftop PV inverters. The dynamic model of the PV inverter control system developed in this thesis is integrated in all of the PV inverters in the LV feeder. The analysis presented in this thesis corresponds to the household (HH16) in the LV feeder connected to bus 28, which is at the immediate downstream to the step voltage regulator REG3 connected between bus 26 and 27.

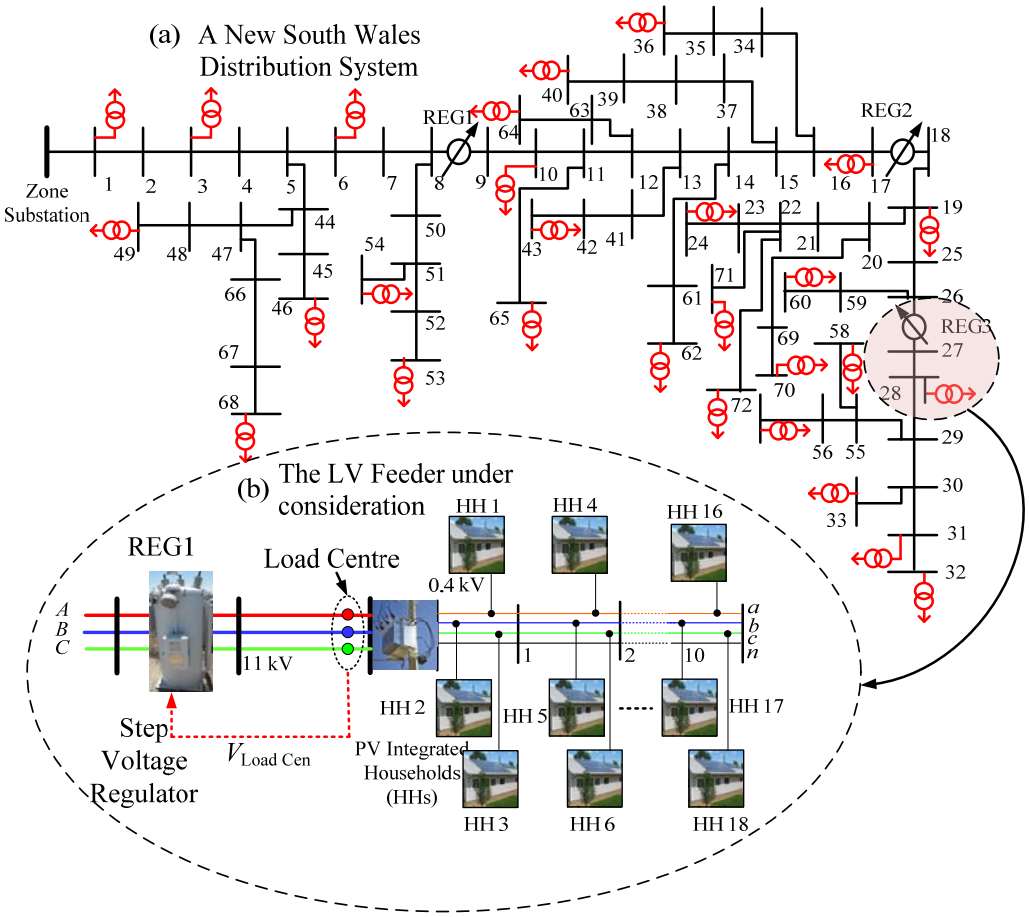

Fig. 5.8. An Australian distribution system. (a) The MV system. (b). An LV feeder in the MV system.

A realistic PV output profile with a 1-second resolution, collected from the Oahu Island, Hawaii on the 18th of March 2010 by NREL [16] is used for testing the proposed strategy. The load data is captured from a real LV residential feeder in New South Wales.

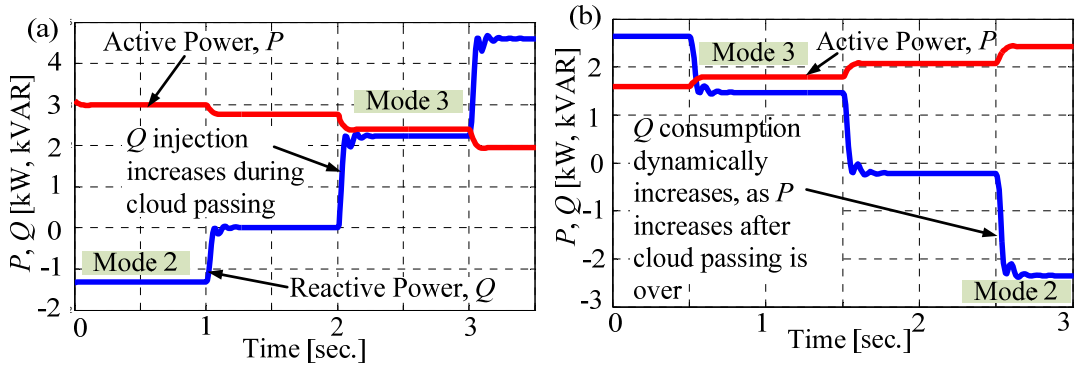

Fig. 5.9. Reactive power support profile obtained from the dynamic model. (a) During reduction of PV output power. (b) During increase of PV output power.

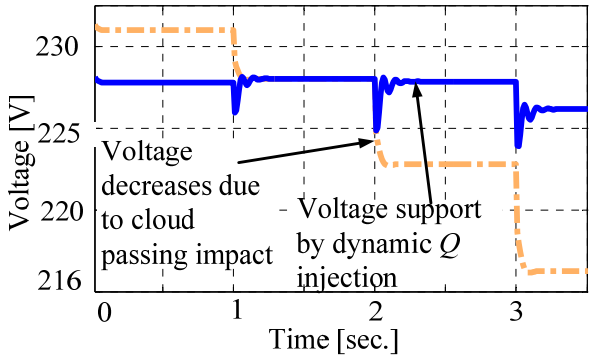

Fig. 5.10. Dynamic behaviour of the PCC voltage at the household HH16.

Using the differential-algebraic model of the integrated network, the dynamic changes of PV inverter reactive power in response to PV inverter active power change is investigated. Fig. 5.9(a) shows how the reactive power is increased in response to a sudden decrease in active power caused by the reduction in the irradiance level. Initially the controller was in Mode 2 for controlling the consumption of reactive power for voltage rise mitigation caused by reverse power flow. With the sudden reduction of PV output power, the controller switches to Mode 3 operation and starts to generate reactive power. At the end of the negative ramping event, the controller continues the *Q*-support over the low PV period until a positive ramping event is detected. Fig. 5.9(b) shows that the controller was initially in Mode 3 for providing reactive support during the low PV

period between the negative and positive ramping events. As the PV output starts to increase at the end of cloud passing, a positive ramping event is detected. Then the controller starts to reduce the Q-injection, and eventually starts to consume Q, which is then followed by a transition to Mode 2 for voltage rise mitigation. The dynamic behaviour of the PCC voltage at household HH16 as a result of the reactive power control is shown in Fig. 5.10 that shows, without reactive power support, the decrease in PCC voltage is higher.

To understand the effectiveness of the proposed strategy in providing network support under different weather conditions, a longer term analysis is performed using quasi-steady-state simulation by solving the load-flow model of the network at each instant of time. A 570-second window from the real PV output profile used in the dynamic simulation is used for the long term quasi-steady-state analysis.

As shown in Fig. 5.11, the PV output profile consists of events such as, a high PV output producing reverse power flow, a sharp decrease in the PV output due to the starting of the passing cloud period, a low PV output during cloudy sky, and a sharp increase in PV output at the end of the passing cloud period. When the PV output is high and produces reverse power flow, reactive power is consumed according to Mode 2 to mitigate voltage rise. While this approach consumes VAr from the system, at the same time it injects active power to the system which relieves the system from active power supply burden. Therefore the system capacity will be relieved. As the present version of this work mainly concerns PV inverter installations at the LV distribution level which would be connected to the high voltage transmission system through large sub-transmission networks with numerous VAr support devices (capacitor banks, SVC, STATCOM etc.), the impact of the VAr demand created by the proposed strategy on the transmission system operation would be insignificant.

When the PV output decreases sharply at a high ramp-rate at the starting of the cloud passing period, the reactive power generation also increases sharply because of triggering the control Mode 3, to mitigate the sudden decrease in voltage. Following the sudden decrease in PV output, when the PV active power generation remains low for a certain period of time, the reactive power support is continued over that period according to (7). When the PV output again sharply increases at the end of the cloud passing, reactive power is consumed according to Mode 3 control for mitigating sharp

increase in voltage. Once the PV output ramping event is over, the reactive power is controlled according to Mode 2 to consume reactive power to mitigate voltage rise.

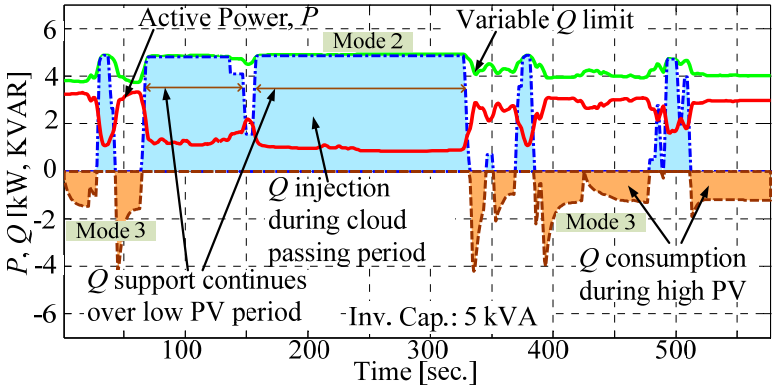

Fig. 5.11. Control of reactive power according to the proposed strategy under different conditions of PV generation.

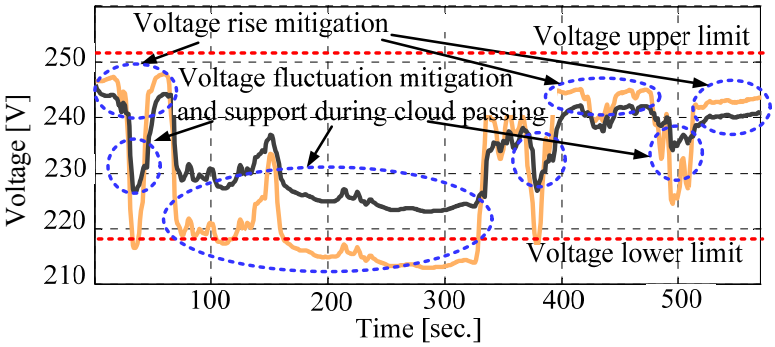

Fig. 5.12. PCC voltage at HH16 without the regulator REG3 operation.

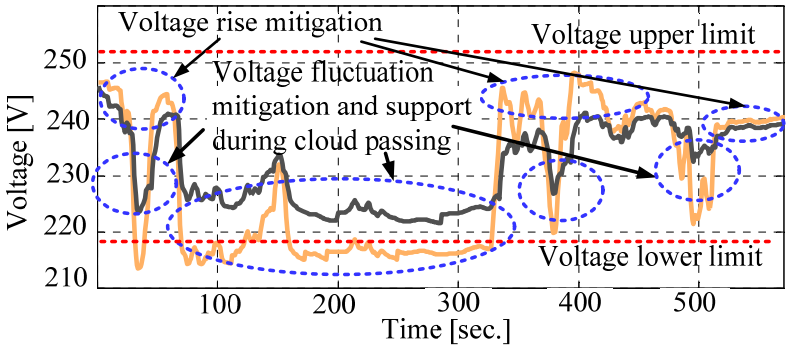

Fig. 5.13. PCC voltage at HH16 with the regulator REG3 operation.

The impact of the proposed strategy on the PCC voltage of household HH16 in the LV feeder is shown in Fig. 5.12 (without the operation of the regulator) and in Fig. 5.13 (with the operation of the regulator). The mitigation of voltage rise by consuming reactive power, mitigation of voltage fluctuation by ramp-rate control of reactive power

(generation /consumption) and voltage support during intermittent low PV generation are identified in Fig. 5.12. The voltage profile for the same PCC in household HH16 is shown in Fig. 5.13, where the impact of the upstream step voltage regulator is considered. Due to the voltage regulator operation, the LV feeder voltage without VAr support is improved during the cloudy period. Fig. 5.12 and 5.13 also show that with appropriate reactive power support, the voltage profile does not exceed the operational limits.

The proposed versatile VAr control strategy not only features the capabilities to provide dynamic VAr compensation for voltage support (Mode 1), voltage rise mitigation (Mode 2) and voltage fluctuation mitigation (Mode 3), but also ensures smooth transitions among the control modes so that the mode transitions do not create any fluctuation or abrupt change in voltage. The performance of the proposed strategy is compared in Fig. 5.14 with that using the simple reactive power to PV active power (Q-P) droop and the reactive power to voltage (Q-V) droop.

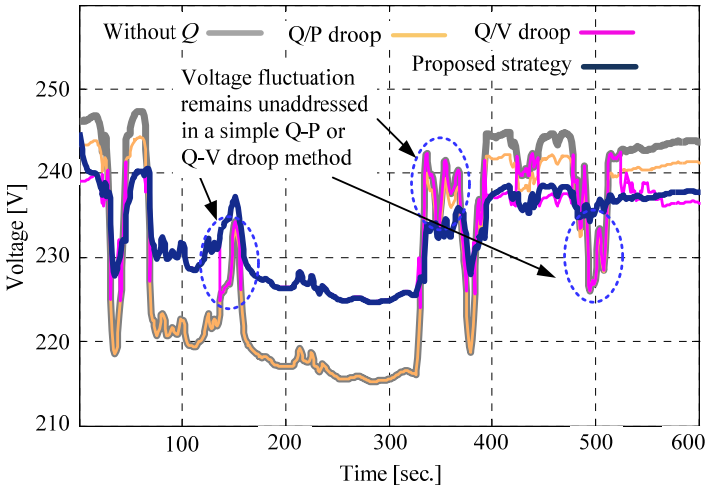

Fig. 5.14. Comparison of the proposed strategy with Q-P and Q-V regulation modes.

In the Q-P regulation mode, the inverter will consume VAr in proportion to the active power generation of the inverter to mitigate voltage rise. However, when the inverter experiences fluctuations in the active power generation due to unstable weather conditions, the amount of reactive power (Q) will also experience fluctuation at the same proportion and this will also be reflected in the voltage, as shown in Fig. 5.14.

In a Q-V regulation mode, the inverter will consume or generate VAr according to a Q-V droop characteristic. However, the Q-V droop itself will not cater for the fluctuations created by the shifting of operating points from a high voltage (Q-

consumption) to a low voltage (Q-generation) region. As the high voltage to low voltage transition can appear quite often and at a high ramp-rate in a practical PV generation scenario, the problem of the voltage fluctuation will still remain unaddressed, as shown in Fig. 5.14. In contrast, the proposed strategy carefully controls the mode transitions and in-mode operations using strategic applications of a ramp-rate limiting function. Therefore, an overall satisfactory performance in voltage support, voltage rise mitigation and fluctuation reduction can be achieved using the proposed method.

The benefit of the reactive power support on the voltage regulator operation is shown in Fig. 5.15 and 5.16. The total reactive power support from the all the distributed inverters in the downstream LV feeder, shown in Fig. 5.15(a), aids to keep the load centre [MV Bus 27] voltage profile of the regulator REG3 within the regulator control limits, shown in Fig. 5.15(b). Therefore, the tap operation is reduced as shown in Fig. 5.16. The cumulative tapping profile showing the total number of tap operations performed at the end of the period under consideration indicates a significant reduction in tap operation with the proposed strategy which will eventually result in less maintenance of voltage regulators.

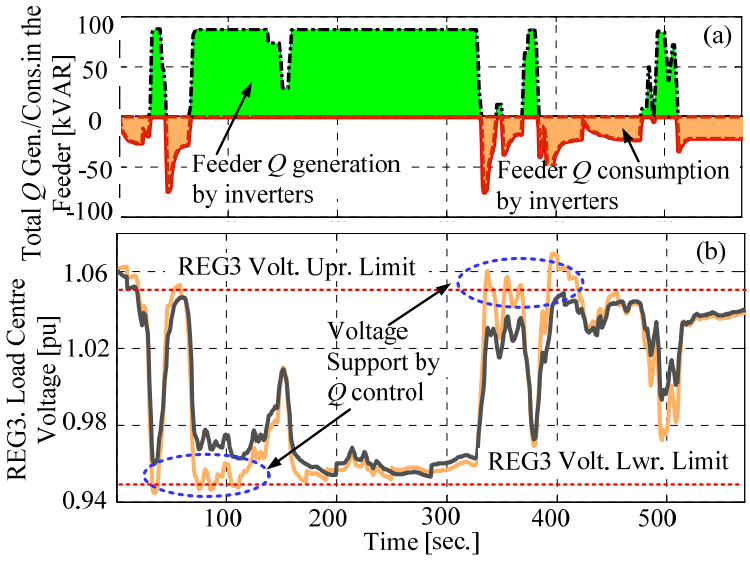

Fig. 5.15. Impact of the proposed reactive power control strategy on REG3 load centre voltage. (a) Total reactive power generation and consumption in the feeder. (b) Load centre [Bus 27] voltage profile.

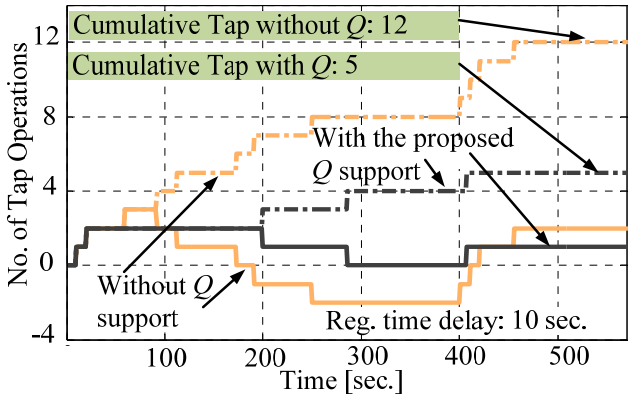

Fig. 5.16. REG3 tap operation profile.

The application of the proposed control strategy for VAr support during a low voltage period using Mode 1 control is investigated and the results are presented in Fig. 5.17. A one hour period is selected from 20:00 hour to 21:00 hour that contains the peak load demand of the demand curve used in this thesis.

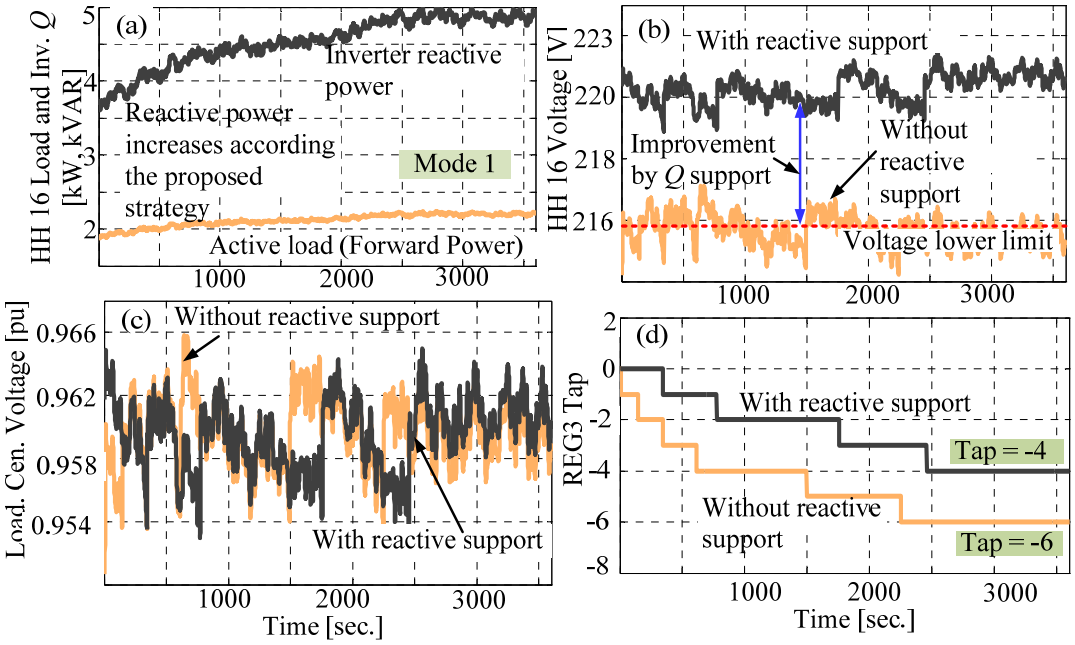

Fig. 5.17. Effects of reactive power support from PV inverters during evening load period. (a) Reactive power profile. (b) Voltage improvement at the PV inverter connection point at the LV customer location. (c) REG3 load centre voltage profile. (d) REG3 tap operation.

The power drawn from the grid and VAr support profile from the inverter at the household HH16 is shown in Fig. 5.17(a), and the voltage improvement achieved by the VAr support during this period shown in Fig. 5.17(b). Without the VAr support, the voltage profile is at the edge of the lower voltage limit, whereas with the VAr support

the voltage profile does not exceed the limit. Due to this VAr support, the load centre voltage also improves in such a way that the tap operation is reduced, as presented in Fig. 5.17(c) and (d).

Although VAr support from customer installed distributed PV inverters is a highly discussed topic, most distribution utilities are yet to allow this to happen in their networks. In autonomous microgrids, however, this concept could be more realistic.

5.5 CONCLUSIONS

A versatile reactive power control strategy has been developed in this thesis for use with solar PV inverters in distribution networks for providing VAr support. The main contribution of this thesis lies in the suitability of the proposed strategy for providing VAr support under different conditions associated with PV power generation using three control modes. In normal operation, the proposed controller will be in a dynamic VAr compensation mode to provide voltage support (if necessary) to the network by controlling the VAr injection depending on the power drawn from the grid by the loads connected to the PCC. The dynamic VAr compensation function considers the inverter's VAr capacity limit and the user's input to control the VAr injection appropriately over the low voltage period. To mitigate the voltage rise during surplus PV power operation, the proposed strategy will pass on the control to a VAr consumption mode that uses a reverse power flow based droop characteristic developed in this chapter. In addition, the proposed controller will switch to a ramp-rate based mode to provide a fast and appropriate level of reactive power support for mitigation of voltage fluctuation during passing clouds. In this thesis, the ramp-rate of the PV output is used for developing an appropriate reactive control strategy for fluctuation mitigation. A coordination strategy is developed that ensures that the inverter VAr control function and mode transitions do not create any fluctuation, which may be observed when traditional strategies are used, when specific attention is not given to ramp-rate control and smooth mode transitions. The results of the analysis indicate that the proposed reactive power control strategy is able to operate under various operating modes of solar PV (e.g. normal condition, excess PV power generation, passing clouds and low or no PV power output) to provide useful reactive support for voltage improvement. Simulation results have also revealed that implementation of the proposed versatile Volt-VAr strategy, if adopted in solar PV inverters, can reduce the number of tap

changing operations of step voltage regulators at the immediate upstream MV networks.

However, additional capacity needs to be incorporated into the PV inverter to provide or consume VAr for network support. A trade-off analysis needs to be carried out to determine how to justify the extra cost for incorporating the additional VAr capacity. One possibility is for incentives to be provided to encourage those installing PV's to make the decision to choose a PV system with reactive support capability. Another possibility is for the regulatory authorities who are keen to promote higher penetration of PV to develop a more sustainable and decentralised electricity supply system subsidizes the extra cost. However, proposing any incentive/penalty scheme or subsidies based on Q generation/consumption would be a complex task and will need ancillary market oriented detailed studies. Therefore, such proposals will be considered in our future works.

REFERENCES

[1] E. Demirok, P. González, K. H. B. Frederiksen, D. Sera, P. Rodriguez, and R. Teodorescu, "Local Reactive Power Control Methods for Overvoltage Prevention of Distributed Solar Inverters in Low-Voltage Grids," *IEEE Journal of Photovoltaics* vol. 1, pp. 174-182, 2011.

[2] P. Jahangiri and D. C. Aliprantis, "Distributed Volt/VAr Control by PV Inverters," *IEEE Transactions on Power Systems* vol. 28, pp. 3429-3439, 2013.

[3] F. Katiraei and M. R. Iravani, "Power Management Strategies for a Microgrid With Multiple Distributed Generation Units," *IEEE Transactions on Power Systems* vol. 21, pp. 1821-1831, 2006.

[4] Y. Liu, J. Bebic, B. Kroposki, J. de Bedout, and W. Ren, "Distribution System Voltage Performance Analysis for High-Penetration PV," in *IEEE Energy 2030 Conference*, Atlanta, GA, USA, 17-18 Nov., 2008, pp. 1-8.

[5] G. Mokhtari, A. Ghosh, G. Nourbakhsh, and G. Ledwich, "Smart Robust Resources Control in LV Network to Deal With Voltage Rise Issue," *IEEE Transactions on Sustainable Energy* vol. 4, pp. 1043-1050, 2013.

[6] J. W. Smith, W. Sunderman, R. Dugan, and B. Seal, "Smart inverter volt/var control functions for high penetration of PV on distribution systems," in *IEEE/PES Power Systems Conference and Exposition (PSCE)*, Phoenix, AZ, USA, 20-23 Mar., 2011, pp. 1-6.

[7] P. M. S. Carvalho, P. F. Correia, and L. A. F. Ferreira, "Distributed Reactive Power Generation Control for Voltage Rise Mitigation in Distribution Networks," *IEEE Transactions on Power Systems* vol. 23, pp. 766-772, 2008.

[8] H. Sugihara, K. Yokoyama, O. Saeki, K. Tsuji, and T. Funaki, "Economic and Efficient Voltage Management Using Customer-Owned Energy Storage Systems in a Distribution Network With High Penetration of Photovoltaic Systems," *IEEE Transactions on Power Systems,* vol. 28, pp. 102-111, 2013.

[9] M. A. Kashem and G. Ledwich, "Distributed generation as Voltage support for single wire Earth return systems," *Power Delivery, IEEE Transactions on,* vol. 19, pp. 1002-1011, 2004.

[10] R. Tonkoski, D. Turcotte, and T. H. M. El-Fouly, "Impact of High PV Penetration on Voltage Profiles in Residential Neighborhoods," *IEEE Transactions on Sustainable Energy,* vol. 3, pp. 518-527, 2012.

[11] M. J. E. Alam, K. M. Muttaqi, and D. Sutanto, "A Three-Phase Power Flow Approach for Integrated 3-Wire MV and 4-Wire Multigrounded LV Networks With Rooftop Solar PV," *IEEE Transactions on Power Systems,* vol. 28, pp. 1728-1737, 2013.

[12] A. Yazdani and P. P. Dash, "A Control Methodology and Characterization of Dynamics for a Photovoltaic (PV) System Interfaced With a Distribution Network," *IEEE Transactions on Power Delivery,* vol. 24, pp. 1538-1551, 2009.

[13] Mathworks. (Oct 2012). *STATCOM (Phasor Model)* [Online]. Available: http://www.mathworks.com.au/help/physmod/sps/examples_v2/statcom-phasor-model.html

[14] Mathworks. (Oct. 2013). *PID tuning algorithm for linear plant model* [Online]. Available: http://www.mathworks.com.au/help/control/ref/pidtune.html

[15] L. Powell, *Power System Load Flow Analysis*. Mexico, USA: McGraw-Hill, 2005.

[16] NREL. *1-Second Global Horizontal Irradiance Oahu, Hawaii* [Online]. Available: http://www.nrel.gov/midc/oahu_archive/

Chapter 6

MITIGATION OF ROOFTOP SOLAR PV IMPACTS AND EVENING PEAK SUPPORT BY MANAGING AVAILABLE CAPACITY OF DISTRIBUTED ENERGY STORAGE SYSTEMS

ABSTRACT

A high penetration of rooftop solar photovoltaic (PV) resources into low-voltage (LV) distribution networks creates reverse power-flow and voltage-rise problems. This generally occurs when the generation from PV resources substantially exceeds the load demand during high insolation period. This thesis has investigated the solar PV impacts and developed a mitigation strategy by an effective use of distributed energy storage systems integrated with solar PV units in LV networks. The storage is used to consume surplus solar PV power locally during PV peak, and the stored energy is utilised in the evening for the peak-load support. A charging/discharging control strategy is developed taking into account the current state of charge (SoC) of the storage and the intended length of charging/discharging period to effectively utilise the available capacity of the storage. The proposed strategy can also mitigate the impact of sudden changes in PV output, due to unstable weather conditions, by putting the storage into a short-term discharge mode. The charging rate is adjusted dynamically to recover the charge drained during the short-term discharge to ensure that the level of SoC is as close to the desired SoC as possible. A comprehensive battery model is used to capture the realistic behaviour of the distributed energy storage units in a distribution feeder. The proposed PV impact mitigation strategy is tested on a practical distribution network in Australia and validated through simulations.

6.1 INTRODUCTION

Solar photovoltaic (PV) resources are the most commonly observed form of distributed generation (DG) at the residential customer premises in low voltage (LV) distribution networks. Depending on their capacity, the rooftop solar PV units serve part of the loads locally that reduces the stress on the distribution feeder and improve system performance by reducing feeder loss and releasing system capacity. However, a high penetration level of PV resources can impose several challenges for distribution network operators, such as, reverse power-flow and voltage-rise problems at LV networks [1-4].

If the PV generation is greater than the local demand at the point of common coupling (PCC), the excess power from PV inverters may produce reverse power flow in the feeder that would create voltage-rise [2, 4]. With a high penetration of rooftop PV resources at LV level, there is a possibility of the upper voltage limit violation. Solutions are required to reduce the overvoltage problem caused by the rooftop solar PV so that the penetration level can be increased while preserving a compliance with the system operation limits.

Active power curtailment [5] and reactive power consumption [6] have been proposed for voltage-rise mitigation. Active power curtailment may not be an economically attractive solution, while reactive power consumption may create additional loss in the feeder due to higher current flow [7]. Authors in [8] have proposed a reactive power based voltage control technique to mitigate the voltage-rise and also discussed the limitations of their technique. Authors in [9] have proposed a control strategy for a coordinated operation of the energy storage systems and On-Load Tap Changers (OLTCs) for voltage-rise mitigation, that reduces tap changer operation stress and feeder power loss. However, an aggregate model of the secondary LV circuits was used and the details of storage charging and discharging profiles were not presented, as the focus of the paper was mainly on control coordination. The application of storage devices integrated with residential PV systems was proposed in [10] to store the surplus power from the PV array during noon time and hence reducing the energy loss associated with the excess power from the solar PV. This operation can also reduce the reverse power flow and voltage-rise problems during peak PV generation by injecting less power to the grid and storing the excess energy in the battery storage. Stored energy

could be used to support the evening peak load by serving the local loads and hence reducing the stress on the grid. An investigation of voltage-rise mitigation is presented in [11] using detailed models of solar PV and battery storage devices. However, a constant-rate charging/discharging strategy was used in [11] that caused the storage device to consume or generate a constant power over the charging or discharging period, irrespective of the PV generation and the load demand variations.

In this thesis, a new charging/discharging strategy is proposed for storage devices integrated with rooftop PV systems that can better match the PV generation and load profile. The proposed strategy is more advantageous for PV impact mitigation and evening load support compared to the traditional constant charging/discharging strategy. To wisely use the limited capacity of the storage device, while operating it according to the proposed strategy, a methodology is developed to obtain the appropriate charging/discharging rates. The proposed charging/discharging strategy would also be able to mitigate sudden changes in PV output (due to unstable weather conditions, such as, cloud passing) by operating the storage in a short-term discharge mode. The proposed strategy can also track the deviation of the actual State of Charge (SoC) of the energy storage device with the expected level of SoC at any given time instant. If the deviation of the actual SoC is more than a specified level, an adjustment of the charging/discharging rate is performed to compensate for such a deviation. This will ensure a better utilization of the available storage capacity. The proposed control strategies are verified using an Australian distribution system where the LV secondary circuits are explicitly modeled using distributed household loads, rooftop solar PV arrays and distributed storage systems.

6.2 ANALYSIS OF PCC OPERATION

A simple feeder shown in Fig. 6.1(a) is used to illustrate the voltage-rise issues produced by the solar PV units in a distribution feeder. The PV panels and storage devices are connected to the PCCs through Power Conditioning Systems (PCS) that perform Maximum Power Point Tracking (MPPT), storage control and DC/AC conversion. Initially, the storage devices are considered to be absent. Without PV, a voltage drop would occur along the feeder, as shown in Fig. 6.1(b). With PV, if all the loads are locally served by the PV generations at each of the PCCs, the voltage profile would be nearly flat as in Fig. 6.1(c). However, if the PV generation exceeds the load

demand, especially at the furthest end of the feeder, then the power will flow back from the feeder to the upstream network and this can cause the voltage to rise, as shown in Fig. 6.1(d).

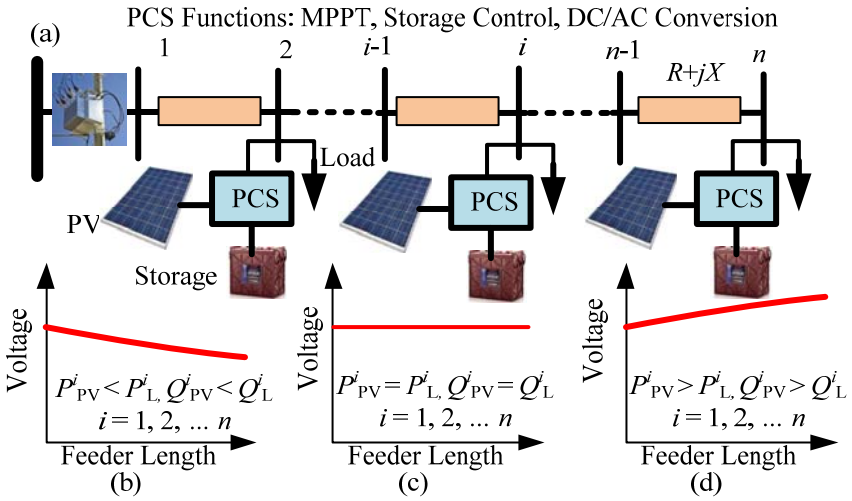

Fig. 6.1. Voltage profile along feeder with different PV generation. (a) single line diagram of feeder; (b) voltage drop (c) flat voltage profile (d) voltage-rise.

A four quadrant P-Q diagram shown in Fig. 6.2(a) is used to illustrate the PCC operation under different PV penetration levels where the active power (P) and the reactive power (Q) of the PV inverter can be fully controlled. From the perspective of a power injection, the loads and the power injections from the solar PV are shown in the negative and positive P and Q axes, respectively. Hence, a PCC operating in the 1st quadrant behaves like a source, and in the 3rd quadrant behaves like a load. Therefore, a 1st quadrant operation of the PCC would normally cause a voltage-rise, and a 3rd quadrant operation would cause a voltage drop. However, a 2nd quadrant or a 4th quadrant operation would cause the PCC to be either a P-sink and Q-source, or a P-source and Q-sink, respectively. A 2nd quadrant operation may cause a voltage-rise with a net positive Q injection if the network is highly reactive, whereas, a 4th quadrant operation may cause a voltage-rise if the network is highly resistive.

The net complex power injection at the i-th node, S^i_{NI}, can be expressed as,

$$S^i_{NI} = \left(P^i_{PV} - P^i_L\right) + j\left[\sqrt{\left(S^i_{PV}\right)^2 - \left(P^i_{PV}\right)^2} - Q^i_L\right] \tag{6.1a}$$

where, $P^i_{PV} + jQ^i_{PV}$ is the complex power generated by the PV inverter at the i-th node, S^i_{PV} is the PV inverter capacity, and $P^i_L + jQ^i_L$ is the load connected at this node.

However, for a unity power factor (UPF) operation of the inverter where the reactive (Q) injection/absorption is *zero*, (6.1a) can be simplified as given in (6.1b).

$$S^{i}_{\mathrm{NI}} = \left(P^{i}_{\mathrm{PV}} - P^{i}_{\mathrm{L}}\right) - jQ^{i}_{\mathrm{L}} \tag{6.1b}$$

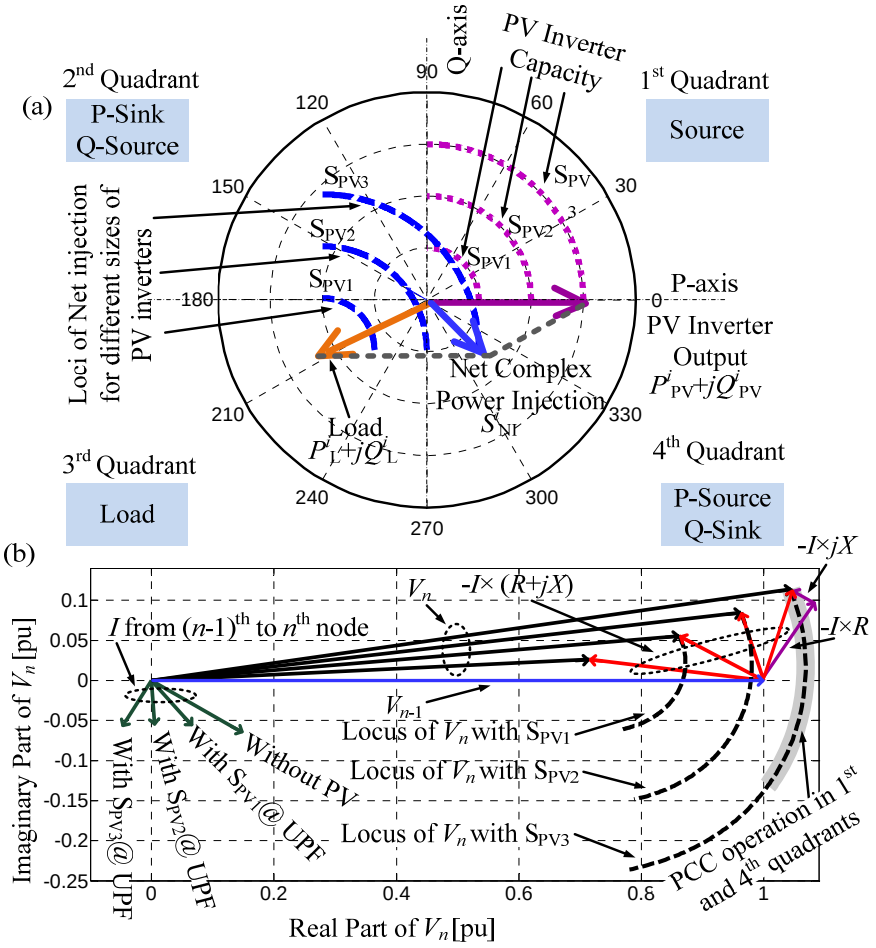

Fig. 6.2. Loci of net power injection and voltage. (a) Net power injection with different PV capacity; (b) Voltage for different amount of PV injection.

To investigate the effects of varying the outputs of the PV inverter on the PCC operation, the potential apparent capacities of PV inverter (S_{PV}) of 0.5, 1.0 and 1.5 times the load active power are considered, and denoted with S_{PV1}, S_{PV2}, and S_{PV3}, respectively, as shown using the dotted circular lines in the 1st quadrant. The active power output of the PV inverter in the P-axis is varied from the rated capacity to *zero* in the 1st quadrant of Fig. 6.2(a). The remaining capacity is used for reactive power injection. Considering a fixed load and the variations of PV inverter output as stated for each of the inverter capacities, S_{PV1}, S_{PV2}, and S_{PV3}, the tips of the net power injection vectors obtained using (6.1a) are plotted as the loci of the net injections in Fig. 6.2(a). These loci represent the operating points of the PCC as the PV inverter output varies.

For an inverter capacity S_{PV1}, less than the load active power, the PCC operation remains within the 2nd and 3rd quadrant for the entire range of the PV inverter output variations. For an inverter capacity S_{PV2}, equal to the load active power, the operating point of the PCC starts at the edge of the 3rd quadrant when the inverter active power output is at the rated value, and gradually shifts into the 2nd quadrant, as the inverter output is varied. For an inverter capacity S_{PV3}, higher than the load active power, the PCC operation traverses through the 4th, 1st and 2nd quadrant, but does not enter into the 3rd quadrant. This indicates that for such an inverter capacity, the PCC may behave either as a PQ-source, or a P-source Q-sink, or a P-sink Q-source, but it will not behave like a load.

Ideally, for a highly resistive distribution circuit, the reverse power flow and voltage-rise problem would exist while the operating point of the PCC is located in the 1st and the 4th quadrant. This can be illustrated using a 2-node segment of the feeder in Fig. 6.1(a), from the (*n*-1)-th to the *n*-th node. A load and a PV inverter are connected at the *n*-th node and the output of the inverter is varied according to the capacity curves in the 1st quadrant of Fig. 6.2(a). The line impedance ($R+jX$) corresponds to a highly resistive distribution circuit and the load power factor used is similar to that of a low voltage residential feeder load. The voltages at the *n*-th node are obtained using a load flow analysis. The vector diagram of the voltages at these nodes is given by (6.2) and is shown in Fig. 6.2(b) using $V_{n\text{-}1}$ as the reference vector.

$$V_n = V_{n-1} - [I \times (R + jX)] \tag{6.2}$$

The tips of the voltage vector at the *n*-th node, V_n, are plotted in Fig. 6.2(b) for the variations in PV output for the three potential capacities of the PV inverter, S_{PV1}, S_{PV2}, and S_{PV3}, and indicated as the loci of the V_n. The voltage-rise is only observed for S_{PV3}, which is higher than the load active power and when the net P injection is positive. This is shown as the shaded region of the V_n locus for S_{PV3}. Therefore, a mechanism that can reduce the active power output of the solar PV inverter can help to mitigate the voltage-rise issue. This can be achieved by absorbing part of the solar PV inverter output in the storage device.

6.3 THE APPLICATION OF DISTRIBUTED ENERGY STORAGE FOR MITIGATION OF SOLAR PV IMPACTS

Storage devices will reduce the net active power injection so that the PCC operating point shifts towards the 2nd and 3rd quadrant where a voltage-rise would not be typically expected for a highly resistive distribution circuit. The shift of the net injection vector due to the addition of storage devices in the feeder of Fig. 6.1(a) is shown in Fig. 6.3(a) and the corresponding voltage vector at the *n*-th node is shown in Fig. 6.3(b). The addition of the storage device mitigates the voltage-rise by storing the surplus power from the solar PV in the storage device. During the evening peak load period, the net injection vector would be shifted from the 3rd quadrant to the right towards the 4th quadrant, as shown in Fig. 6.4(a).

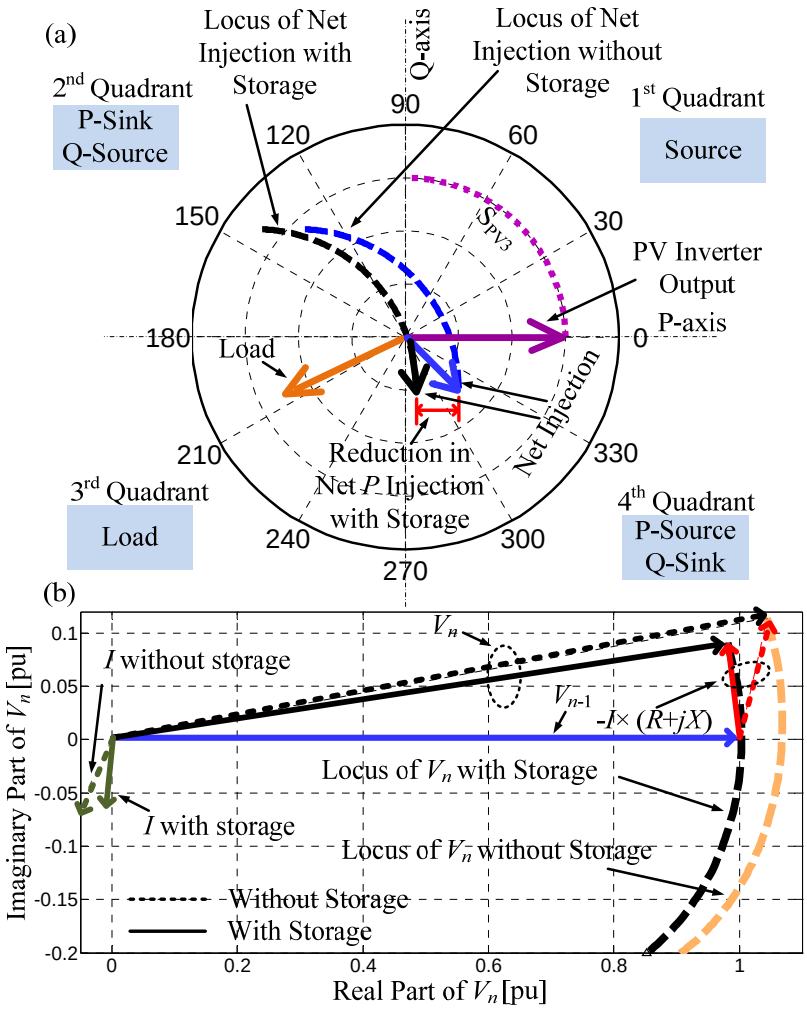

Fig. 6.3. A four quadrant net power injection diagram with storage. (a) Net injection in charging operation; (b) Voltage locus in charging operation.

The corresponding voltage vector diagram is shown in Fig. 6.4(b) showing the voltage improvement that can be obtained with the storage device. If the remaining capacity of the inverter can be used for reactive power injection, as shown in the net injection locus of Fig. 6.4(a), a further improvement in voltage could be observed, as shown in the voltage locus of Fig. 6.4(b).

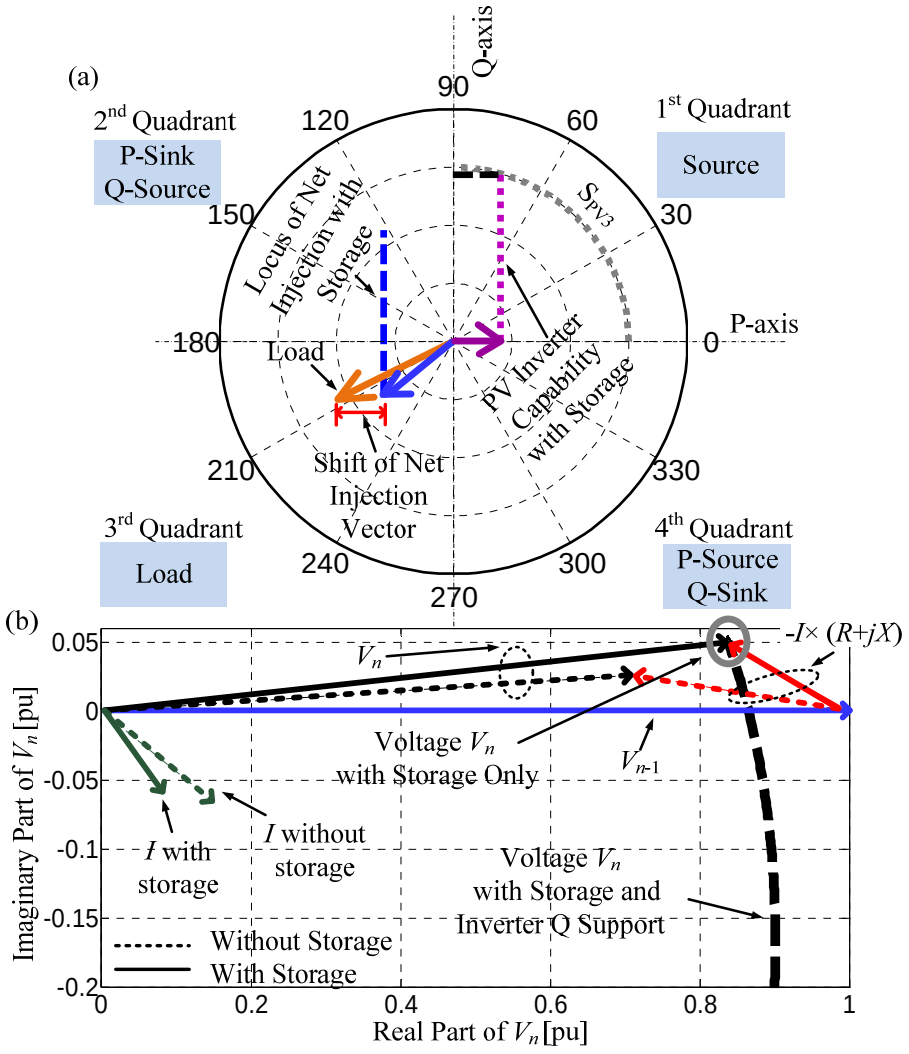

Fig. 6.4. Four quadrant net power injection diagram with storage: (a) Net injection in charging operation; (b) Voltage locus in discharge operation.

6.3.1 Modelling of Battery Storage Device for Rooftop Solar PV System

Rooftop PV installations at LV customer premises mainly consist of the solar PV modules that produce DC power from solar insolation, and a Power Conditioning System (PCS) that accomplishes multiple functions including maximum power point tracking, DC-AC conversion and filtering. For an integrated storage device coupled

with the DC side of the rooftop PV system, as used in this chapter of the thesis, the PCS will also function as the charge/discharge controller. A detailed description of the rooftop PV system modelling is presented in a previous paper of the authors [11] and is therefore not included here. More focus has been given on the modelling of storage devices and its charging/discharging strategies.

The modelling of the battery storage device involves obtaining the non-linear characteristics of the battery voltage as a function of the battery State of Charge (SoC) [12] at a given charging/discharging rate, as shown in Fig. 6.5 [13], for typical lead-acid batteries. In Fig. 6.5, C is the capacity of battery storage unit in Ampere-hour (Ah).

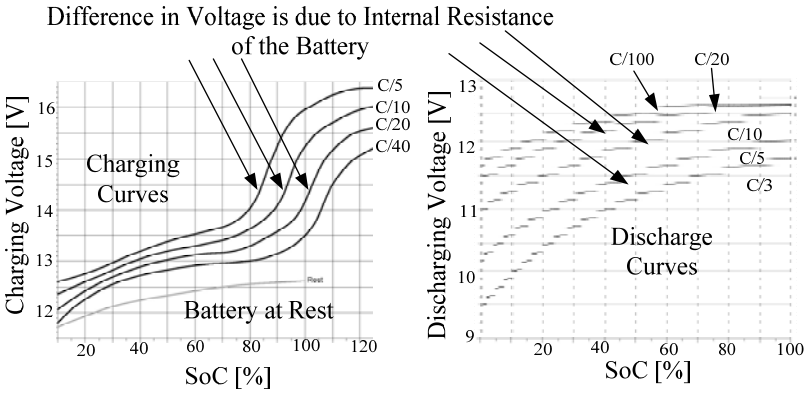

Fig. 6.5. Charge and discharge characteristic of a typical battery storage unit.

Fig. 6.5 shows that the battery voltage characteristics are different for the different charging/discharging rates due to the internal resistance of the battery [14]. The battery voltage varies throughout the whole range of SoC, as the internal resistance is a function of SoC [15]. When the battery is at rest the voltage becomes lower, as shown in the charging characteristics in Fig. 6.5 [13]. As no charging current flows when the battery is at rest, voltage drop across the internal resistance would be ideally zero. The manufacturer supplied battery characteristic curves are segregated into exponential, nominal and end of nominal regions in [16], and a set of parameters is obtained to fit the characteristic curves containing the segregated regions. This model requires only three points to be taken from the manufacturer supplied curve. The model used in [16] uses the same characteristics for both charging and discharging operation. However, as shown in Fig. 6.5, the voltage value when charging, is different to that when discharging for a given SoC, because when the battery is discharged, the energy used to charge the battery is not fully recovered [17]. Furthermore, the internal resistance of the

battery storage is different at charged and discharged states [18]. In this thesis, separate charging/discharging curves and different internal resistances at charged and discharged states are considered to develop a more realistic battery model.

The battery voltage at a given charging/discharging rate can be expressed using (6.3) involving the battery capacity C_B, the present SoC, the battery internal resistances at charged state and at discharged state, R_{BC} and R_{BD}, the change in internal resistance for per unit change in SoC, ρ, and the battery current, I_B.

$$V_B = \begin{cases} V_{B0} + I_B(R_{BD} - \rho \times \text{SoC}), \text{in charging operation} \\ V_{B0} - I_B(R_{BC} + \rho \times \text{SoC}), \text{in discharge operation} \end{cases} \tag{6.3}$$

where, the no-load battery voltage, V_{B0} is given by [16],

$$V_{B0} = V_{BC} - K \times \frac{C_B}{C_B - \text{SoC}} + Ae^{-B \times \text{SoC}} \tag{6.4}$$

where, V_{BC} is the battery constant voltage; K is the polarization voltage; A is the exponential zone voltage; and B is the exponential zone time constant.

Methods for determining V_{B0}, K, A, and B are described in [16]. The model used in this thesis requires first to obtain the set of parameters V_{B0}, K, A, and B for both charging and discharging curves at a given standard rate. The obtained parameters are then used in (6.3) and (6.4) to obtain the characteristic curves at the required charging and discharging rates.

The present SoC can be found from the previous SoC of the battery, the battery current, and the time interval between the previous and the present charging states as given in (6.5),

$$\text{SoC}(t + \Delta t) = \begin{cases} \text{SoC}(t) + I_B \Delta t, \text{in charging operation} \\ \text{SoC}(t) - I_B \Delta t, \text{in discharge operation} \end{cases} \tag{6.5}$$

6.3.2 Determination of the Maximum Charging Rate for Storage

Battery storage devices store the surplus power from solar PV units during charging operation. This reduces the amount of active power injection into the grid. The injection of real power into the grid, P_{inj}, for a given level of load, PV output and battery storage

unit can be obtained using (6.6).

$$P_{inj} = -P_L + \eta_{inv}(P_{PV} - \mathrm{CR} \times V_B) \tag{6.6}$$

where, P_L is the active power of load, P_{PV} is the active power output of the PV module, η_{inv} is the PV inverter efficiency, CR is the battery charging rate, i.e., the battery current and V_B is the battery voltage.

A study was conducted to determine the amount of P_{inj} with a 1-kW load, which is a typical midday load of a residential household, and a 3-kW PV system. The values of P_{inj} at different charging rates are shown in Fig. 6.6 for a 12-V, 250-Ah battery.

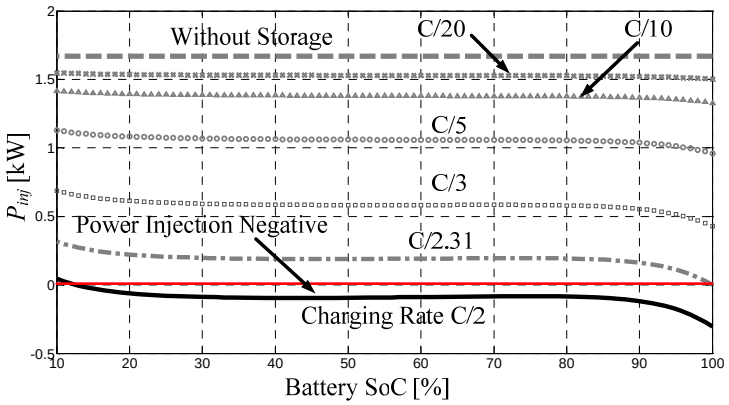

Fig. 6.6. The variation of power injection into grid at different charging rates.

The amount of grid injection decreases as the charging rate increases and this contributes to a mitigation of voltage-rise. However, beyond a certain level of charging rate, the battery power input will exceed the available surplus power from the PV resulting in a negative PV power injection into the grid. Fig. 6.6 shows that a charging rate of C/2.31 will result in a negative P_{inj} at 100% SoC level of the battery, which is undesirable. The maximum allowable charging rate is the one at which the real power injection into the grid is *zero*, that is, all the surplus power is consumed by the storage during its charging operation. This rate could be obtained from (6.6) by substituting *zero* for P_{inj}, as given in (6.7).

$$\mathrm{CR}_{\max} = \left| -\frac{(P_{L\min} - \eta_{inv} P_{PV\max})}{\eta_{inv} \times V_B^{\mathrm{Full}}} \right| \tag{6.7}$$

In (6.7), $P_{L\min}$ is the minimum level of load within the PV generation period, $P_{PV\max}$ is the maximum amount of solar PV generation in the same period, and V_B^{Full} is the battery

voltage at the 100% SoC. V_B^{Full} is a function of the charging rate and hence (6.7) is solved numerically to find CR_{max}.

6.3.3 A New Strategy for the Charging/Discharging of Storage Devices

In a clear sunny day, the PV output increases gradually as the day progresses, reaches its peak during midday, and gradually decreases after midday. The surplus power at the PCC would also follow a similar trend. Therefore, a charging strategy where the charging rate gradually increases with the progress of the day, reaches its peak level during midday, and gradually decreases after the midday, would be more effective for PV impact mitigation, compared to a traditional constant charging strategy. Similarly, a discharging strategy where the discharging rate gradually increases from the start of the evening period, reaches its peak level during the evening peak load, and gradually decreases with the decrease of evening load, would be more effective for peak load support compared to a constant discharging strategy.

Further, since the energy storage devices have limited capacity (Ah) or energy (kWh), it is important to use it wisely. Charging the energy storage devices too fast, when there is reverse power flow, may cause the battery to be full too soon and therefore may result in unacceptable reverse power flow and a voltage-rise at an inconvenient time, for example at peak insolation period. But too slow charging of the storage device, when there is reverse power flow, may cause some of the capacity of the battery to be left unused.

A new charging/discharging strategy is proposed to better match the surplus PV generation/evening load profile. The methodology to obtain the appropriate charging/discharging rates to wisely use the limited storage capacity is described below using Fig. 6.7. Fig. 6.7(a) shows the load and the PV output profile at a given PCC, where the PV output is higher than the load demand for a period of the day, *T*. During this period, a surplus power will be available at the PCC. According to the proposed strategy, the storage device will be charged over the period *T*. The charging rate will be increased from *zero* at the start of the period *T*, (when the storage SoC is at the maximum depth of discharge DoD_{max}) at a Slope of Charging Rate (SCR) defined in per-unit of time, until the SoC reaches a threshold level, ToS_1. This is shown in Fig. 6.7(b). From this point, the storage will be charged at a constant saturated charging rate, CR_{Sat}. Once the SoC reaches the second threshold, ToS_2, less capacity of the storage is

available and therefore the charging rate will be decreased using the same SCR, until the storage device attains the state of maximum charge, SoC_{max}, at the end of period T.

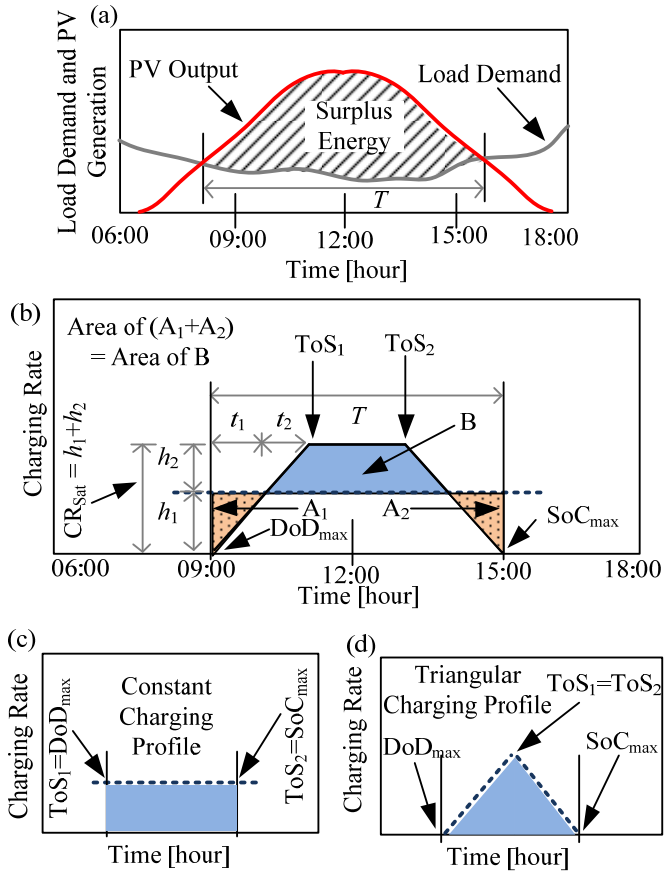

Fig. 6.7. Proposed charging/discharging strategy. (a) load and PV generation profile; (b) methodology to obtain charging/discharging rates; (c) a constant charging profile; (d) a triangular charging profile.

According to this strategy, the charging rate at the k-th time instant can be expressed as given in (6.8).

$$\mathrm{CR}(k)=\begin{cases}\mathrm{CR}(k-1)+\mathrm{SCR}, \text{if } \mathrm{SoC}(k-1)\le \mathrm{ToS}_1\\ \mathrm{CR}_{\mathrm{Sat}}, \text{if } \mathrm{ToS}_1<\mathrm{SoC}(k-1)<\mathrm{ToS}_2\\ \mathrm{CR}(k-1)-\mathrm{SCR}, \text{if } \mathrm{SoC}(k-1)\ge \mathrm{ToS}_2\\ 0, \text{if } \mathrm{SoC}(k-1)\ge \mathrm{SoC}_{\max}\end{cases} \tag{6.8}$$

To obtain the appropriate values of the parameters SCR and CR_{Sat} to be used in (6.8), the following facts are considered.

The amount of charge lost for not charging the battery at a constant charging rate over the entire charging period will have to be recovered in the overall charging period. Mathematically, this constraint can be expressed using the geometrical relationships in

Fig. 6.7(b) as given below.

$$h_2^{\,2} + (2h_1 - T \times \mathrm{SCR}) \times h_2 + h_1^{\,2} = 0 \tag{6.9}$$

where, h_1 is the constant charging rate that charges the battery in T amount of time, h_2 is the amount of increase in the constant charging rate to recover the charge lost for not using the constant charging rate over the whole charging period.

Again, the charge stored during the constant charging period is equal to the amount of charge between the first and second threshold of SoC, ToS_1 and ToS_2 respectively. This can be expressed using (6.10) below.

$$(h_1 + h_2) \times \left(T - \frac{2h_1}{\mathrm{SCR}} - \frac{2h_2}{\mathrm{SCR}} \right) - (\mathrm{ToS}_2 - \mathrm{ToS}_1) \times \mathrm{C} = 0 \tag{6.10}$$

It is observed that in (6.9) and (6.10), h_2 and SCR are the only unknown parameters; h_1 is known from the battery capacity, and T is the period for which the battery is intended to be charged, which can be estimated from historical load and PV output profile as shown in Fig. 6.7(a), ToS_1 and ToS_2 are the choices to shape the charging rate profile. Therefore, h_2 and SCR can be obtained by solving (6.9) and (6.10) simultaneously using a Newton based numerical technique. By varying the difference between ToS_1 and ToS_2, different charging profiles can be obtained and the pattern of usage of the available storage capacity can be controlled. For example, if ToS_1 and ToS_2 are set to DoD_{max} and SoC_{max}, respectively, a constant charging profile is obtained, as shown in Fig. 6.7(c). Again, if the difference between ToS_1 and ToS_2 is *zero*, then a triangular charging profile is obtained, as shown in Fig. 6.7(d).

A similar strategy will be followed for the discharge operation; however, in this case the discharge rate (DR) will be increased at a Slope of Discharge Rate (SDR) defined in per-unit of time, until the SoC drops to ToS_2 from the SoC_{max} level, and then the discharge will continue at a constant saturated discharge rate DR_{Sat}. When the SoC drops below ToS_1, the battery discharge rate is decreased at the same SDR until DoD_{max} is reached. At a given k-th instant, this can be expressed as,

$$\mathrm{DR}(k)=\begin{cases}\mathrm{DR}(k-1)+\mathrm{SDR}, \text{if } \mathrm{SoC}(k-1)\geq \mathrm{ToS}_2\\ \mathrm{DR}_{\mathrm{Sat}}, \text{if } \mathrm{ToS}_2>\mathrm{SoC}(k-1)>\mathrm{ToS}_1\\ \mathrm{DR}(k-1)-\mathrm{SDR}, \text{if } \mathrm{SoC}(k-1)\leq \mathrm{ToS}_1\\ 0, \text{if } \mathrm{SoC}(k-1)\leq \mathrm{DoD}_{\max}\end{cases} \tag{6.11}$$

The values of SDR and $\mathrm{DR_{Sat}}$ can be obtained from (6.9)-(6.10). In this case, T will be the intended period of discharge. This is the duration of the peak load support and will depend on the limited amount of the stored energy in the battery. To make an effective use of the available stored energy, it needs to be discharged in a period that includes the maximum evening peak, as shown in Fig. 6.8.

An estimate of the discharge period, T, can be obtained initially using the historical load curves of the specific household where the storage device is to be installed. If the available energy is fully discharged during the evening peak, the following expression will hold true.

$$\eta_B\times(\mathrm{SoC}_{\max}-\mathrm{DoD}_{\max})\times V_B-\int_{t_1}^{t_2}P_L(t)dt=0 \tag{6.12}$$

where, $(t_2 - t_1) = T$, as shown in Fig. 6.8, $t_{\max}$ is the time of occurrence of the maximum demand, V_B is the nominal battery voltage, η_B is the battery energy efficiency and $P_L(t)$ is the load demand at time, t. T can be obtained by solving (6.12) iteratively and can be used in (6.9) and (6.10) to obtain SDR and $\mathrm{DR_{Sat}}$. Normally, the time of occurrence of the peak load and the length of evening load period would not be significantly different between two consecutive days. Therefore, once the system is installed and commissioned using the initial historical load curve, the information on t_1 and t_2 can be updated daily from measurements at the PCC to accurately estimate the intended period of discharge.

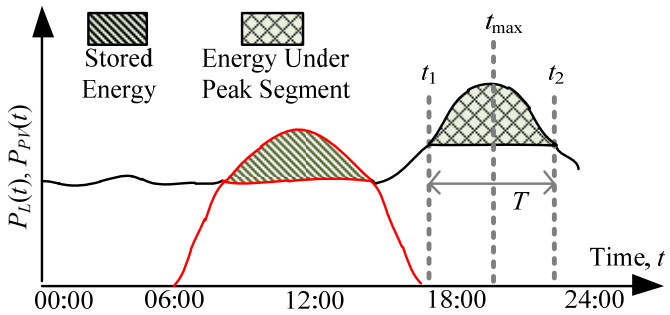

Fig. 6.8. Determination of evening peak support interval.

The flow chart of the charge and discharge control system for a given time step is shown in Fig. 6.9(a) and 9(b), respectively. The storage device is normally charged if there is no sudden decrease in PV output at the PCC and also a reverse power flow greater than a threshold level is found. The charging rate is obtained using (6.8) based on the parameters obtained from (6.9)-(6.10). The storage is normally discharged if the PCC voltage is found to be lower than a threshold level and also when no sudden dip in the PCC voltage is observed, as shown Fig. 6.9(b). The discharge rate is obtained using (6.11) based on the parameters obtained from (6.9)-(6.10).

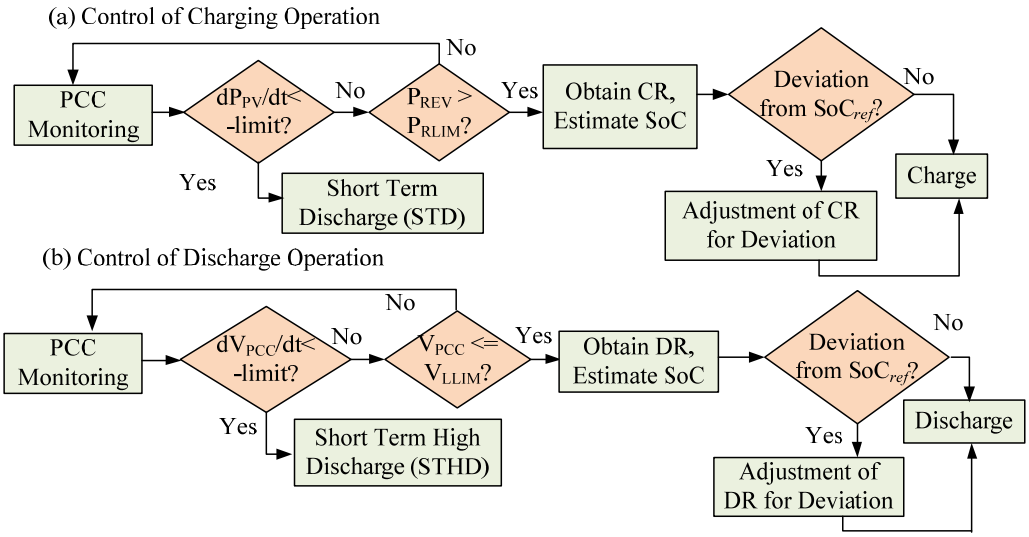

Fig. 6.9. Storage control flow charts. (a) charging operation (b) discharging operation

The PV output may be suddenly decreased by irregularities in the sun irradiance levels due to unstable weather conditions causing fluctuations in the PCC net power and voltage. In the event of a sudden decrease in the PV output, the storage is put into a short-term discharge (STD) mode, as shown in Fig. 6.9(a). The short-term discharge-support is limited to avoid a significant drainage of charge.

To ensure an effective use of the available storage capacity, it is necessary to make-up for the charge lost during the short- term discharge period, and also during the unavailability of enough surplus power at the PCC caused by changing cloudiness of the sky. The lost charge can be replenished by adjusting the charging rate at each instant of time to attain a reference SoC level. The reference SoC level is the one which is not affected by any unstable weather condition and can be obtained using the charging rate expressions given in (6.8). The strategy for performing the adjustment in charging rate is shown in Fig. 6.10.

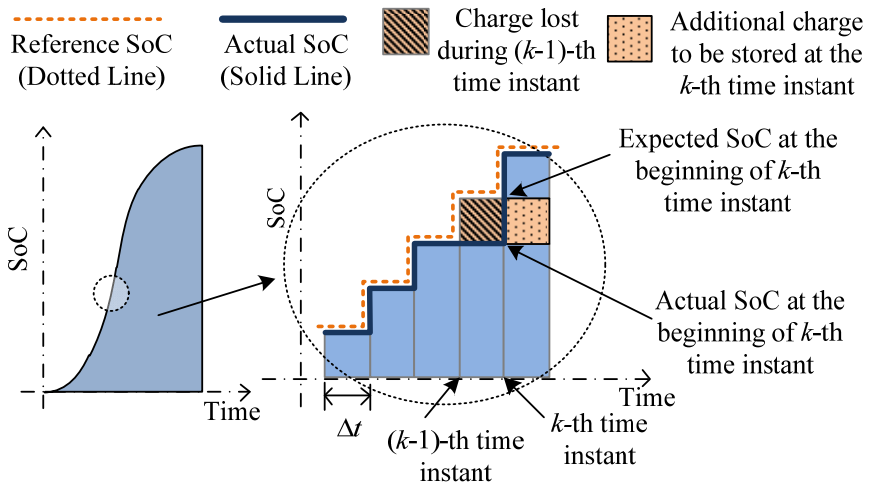

Fig. 6.10. Adjustment of charging rate to make-up for charge lost due to unstable weather condition.

If the storage is not charged at the (k-1)-th time instant, the SoC will remain at the same value as in the previous time instant. Again, if the storage is discharged at the (k-1)-th time instant, the SoC level will be reduced than the previous SoC. Therefore, an adjustment of the charging rate has to be performed at the beginning of the k-th time instant to make-up for the charge not stored, or lost, during the (k-1)-th instant, as given below.

$$\mathrm{CR}'(k) = \mathrm{CR}(k) + \varepsilon \times \frac{\mathrm{SoC}_{ref}(k) - [\mathrm{SoC}(k-1) + \mathrm{CR}(k) \times \Delta t]}{\Delta t} \tag{6.13}$$

where, $\mathrm{CR}'(k)$ is the adjusted charging rate, SoC_{ref} is the reference level of SoC, Δt is the time between two consecutive time instants, and ε is a parameter defining the percentage of the deviation to be met which can be controlled to limit the adjustment in the charging rate, if required. This adjustment of charging rate ensures an effective utilization of a storage device compared to a constant charging rate strategy in the event of irregularities in PV output which is difficult to anticipate.

Similarly, in the evening, it may be required to discharge the storage at a rate higher than the normal rate to support any abrupt voltage drop, such as a voltage-dip event caused by a sudden increase in the load demand. In this situation, the storage is put into at a short-term high discharge (STHD) mode as presented in Fig. 6.9(b), depending on the intensity of the sudden increase in the momentary load demand. This will result an additional charge to be drained during the higher discharge operation. Therefore, the discharge rate is adjusted by using (6.14) to reduce the deviation with the reference SoC

level.

$$DR'(k) = DR(k) - \varepsilon \times \frac{SoC_{ref}(k) - [SoC(k-1) - DR(k) \times \Delta t]}{\Delta t} \quad (6.14)$$

All of the distributed storage units in the feeder operate according to the control strategy described above, based on the local information at the PCC, such as the PV output, the local demand, and the PCC voltage.

Although this thesis proposes a storage control strategy based on local parameters only, a coordinated control strategy of multiple storage devices in the feeder may also be possible if a communication system become available as envisaged in the future smart grid. In such a coordinated operation, the storage devices at different locations would be able to exchange information on the available storage capacity and the surplus power at different PCCs using the communication systems, to make a better use of the total storage capacity available in the feeder to store an optimum amount of total excess PV generation in the feeder.

The present thesis mainly discusses the mitigation of reverse power flow caused by active power injection from rooftop solar PV in LV distribution feeders, resulting in the avoidance of a voltage-rise, although the system does not intentionally control the voltage. As there is no voltage control set-point in the proposed strategy, it is different than an on load tap-changer or voltage regulator located in medium voltage system where a feed-back arrangement is used to control the voltage at the load centre. For the same reason, it will not interfere with the operation of the on load tap-changer or the voltage regulator. The only effect of this controller is to make the on-load tap changer and the voltage regulator to have less switching operation and hence less stress. With a communication system, the battery storage system can be coordinated with the on-load tap changer as presented in [9].

6.4 CASE STUDIES

A distribution network containing medium and low voltage feeders has been extracted from a New South Wales Distribution system in Australia to investigate the applicability of the proposed mitigation strategy. This is an 80 km long 11 kV rural network with three series voltage regulators. A single line diagram of the network is

shown in Fig. 6.11. One of the LV feeders is shown in detail in a dashed circular shape. The LV feeder data used for analysis are presented in Table 6-I.

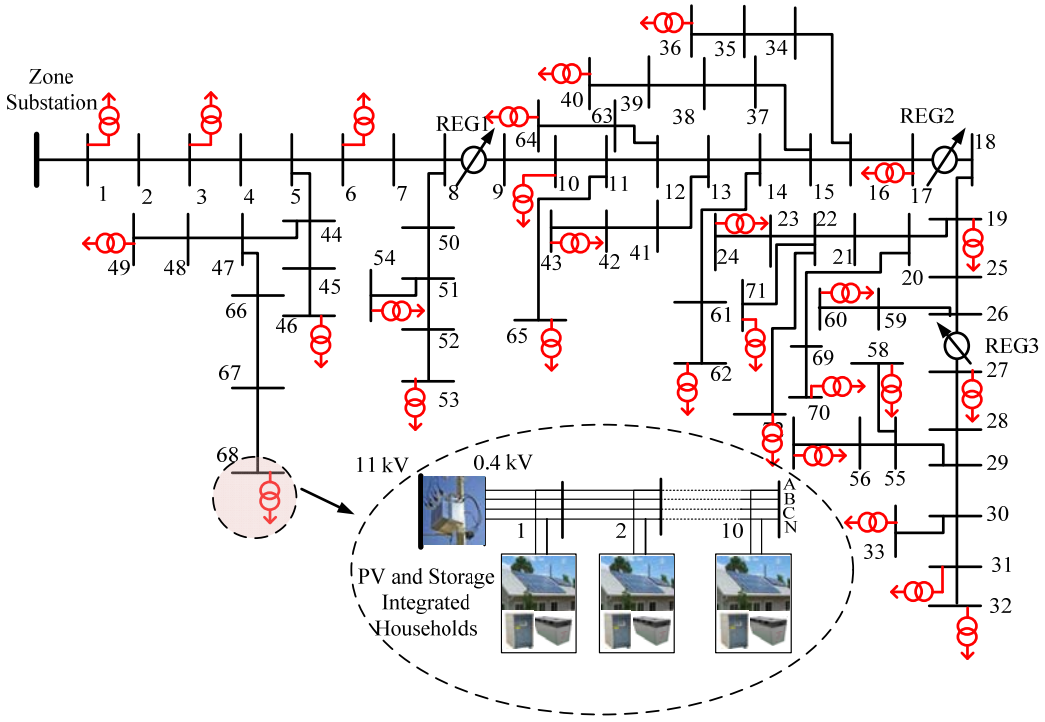

Fig. 6.11. A practical distribution system in Australia.

Typical electric appliances used in residential households were used to model the aggregate loads at the different phases of the test feeder. The PV system sizes at the residential households were limited within 4 kW range and operated at unity power factor. The selection of a proper sizing methodology for energy storage is a complex task and may require optimization process, as discussed in [19]. In this research, a lead-acid energy storage device rated at 250 Ah, 24 V, was integrated at each of the rooftop PV system which is a typical size for residential rooftop PV applications in Australia for a PV rating of 2-4 kW [20]. The standard charging/discharging curves of a 12-V lead-acid battery available in [13] were used to model a 24-V lead-acid battery using the method described in section 6.3.1 and the obtained charging/discharging curves are shown in Fig. 6.12. The specifications of the charging/discharging control strategy are given in Table 6-II. The charging/discharging parameters CR_{Sat}, DR_{Sat}, SCR, and SDR are calculated using (6.9)-(6.10).

TABLE 6-I

DATA OF A TYPICAL AUSTRALIAN LOW VOLTAGE FEEDER

Feeder Length (metre)	350
Pole to Pole Distance (metre)	30-40
Conductor	7/3.00 AAC
MV/LV Transformer Size	160 kVA
PV Size (kW)	2-4 kW
PV Module Manufacturer	Kyocera
Inverter Manufacturer	SMA Sunnyboy
Battery Storage Model	Lead-acid Trojan L-16W
Battery Storage Voltage (V)	2×12
Battery Storage Capacity (Ah)	250

TABLE 6-II

SPECIFICATIONS OF CHARGING/DISCHARGING CONTROL STRATEGY

Parameter	Value
CR_{Sat}, DR_{Sat}	C/6.56, C/3.34
SCR, SDR (per minute)	0.1619, 0.6243
Charging and Discharging Profile	Triangular
ToS_1, ToS_2	70%, 70%
SoC_{max}, DoD_{max}	100%, 40%
ε for CR, DR compensation	100%

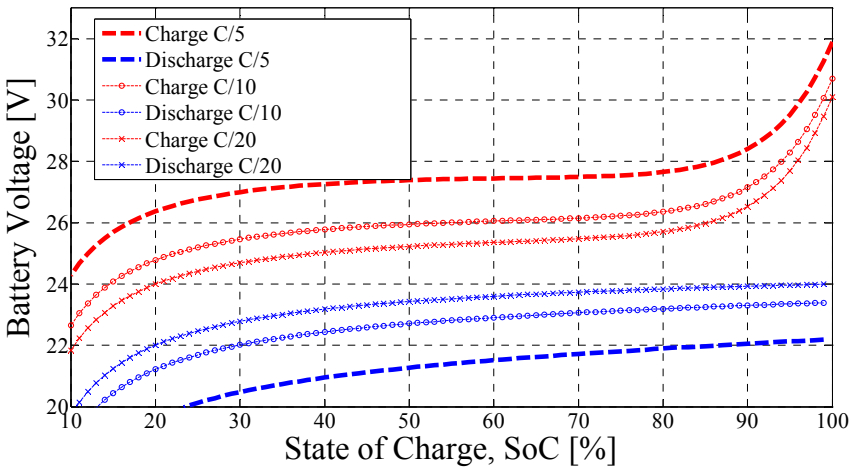

Fig. 6.12. Charge/discharge curves of a 24-V lead acid battery modeled for different charging/discharging rates.

The network analysis is performed using a three-phase four-wire power-flow tool

[21] developed by the authors, based on the current mismatch variant of the Newton-Raphson power flow algorithm [22]. The proposed storage control strategy is tested with steady-state simulations of the test network at each instant of time under consideration.

To test the developed methodology in a realistic PV generation environment, a solar PV output profile captured on the 9th of February 2011, in the Renewable Energy Integration Facility, CSIRO Energy Technology, Australia, is used. The PV output, the load demand, the energy storage power and the net active power injection into the grid from 8:00 hours to 24:00 hours for the PCC corresponding to phase *a* of node 10 of the test LV feeder is shown in Fig. 6.13(a). The PV output was distorted by the sudden changes in the sun irradiance level. It is assumed that the SoC of the storage device is at DoD_{max} at the start of the simulation.

The storage starts to charge at about 9:00 hours by detecting a reverse power flow larger than a set threshold of 0.1 kW at the PCC. Using a triangular charging profile, the charging rate increases at the SCR specified in Table 6-II until it attains $ToS_{1,}$ which is 70% of the total battery capacity. The SoC profile is shown in Fig. 6.13(b). Due to the triangular charging profile, the second threshold ToS_2 is also 70%, and therefore, the charging rate starts to decrease from this point at the same SCR until the charging rate becomes *zero*. Due to the power consumed by the storage in the charging operation, the active power injection into the grid without storage (dotted blue line) in Fig. 6.13(a) is higher than the active power injection with storage (solid blue line).

Within the charging period, several fluctuations in PV output appear, as marked using the dotted circular shapes in Fig. 6.13(a). The proposed control strategy detects the sudden changes in PV output and places the storage in a short-term discharge mode, as observed by the negative spikes in the battery power shown in Fig. 6.13(a). This counteracts the sudden fluctuations in the PV power. As a result, the fluctuations in surplus power injection at the PCC are also reduced, as observed by comparing the solid and dotted blue lines in Fig. 6.13(a). The drops in the SoC levels in the zoomed box in Fig. 6.13(b) indicate the short-term discharges. It is also observed in Fig. 6.13(b) that the SoC level without the charging rate adjustment does not reach the SoC_{max} level.

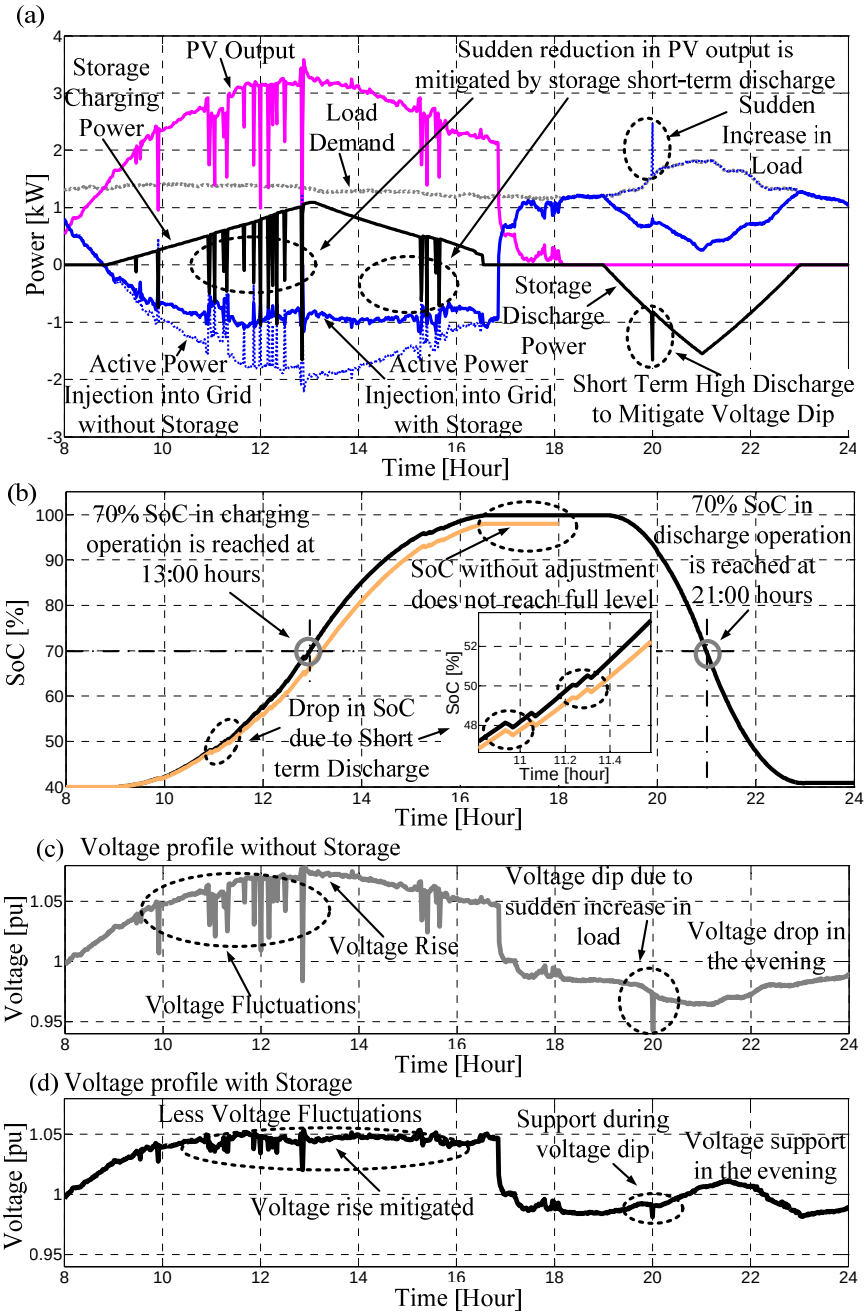

Fig. 6.13. (a) Load demand, PV output, storage power and active power injection into grid; (b) SoC profile; (c) Voltage profile without storage; (d) Voltage profile with storage.

The discharge operation starts at 19:00 hours by detecting the drop of PCC voltage below a threshold level. Using a triangular discharge profile, the discharge rate increases at the SDR defined in Table 6-II until the SoC drops to 70% of the SoC and then decreases at the same SDR until DoD_{max} is reached. The discharge power of storage and the SoC during the discharge operation is shown in Fig. 6.13(a) and 13(b), respectively. A sudden increase in the PCC load (due to an event such as a motor start) is observed in Fig. 6.13(a) at about 20:00 hours. This is partly mitigated by putting the

storage in a short-term high discharge mode, as observed in Fig. 6.13(a) by a momentary increase in storage discharge power.

The PCC voltage profile with and without storage is shown in Fig. 6.13(c) and 13(d), respectively. The voltage-rise during the peak PV generation, the voltage fluctuations during the sudden reductions in PV output, the voltage drop during the evening peak and a voltage dip due to a sudden increase in the load are observed in Fig. 6.13(c). Fig. 6.13(d) shows that the voltage-rise is reduced by the charging operation; the voltage fluctuations are reduced by the short-term discharging operation; the voltage profile is improved during evening peak by the discharging operation; and the voltage dip is partly mitigated by the short-term high discharge operation.

A comparison of the reverse power flow at the secondary side of LV substation connected at bus 68 in Fig. 6.11 with and without distributed storage devices is shown in Fig. 6.14. It is observed that the reverse power flow with storage devices is reduced by 44% compared to the case without storage devices.

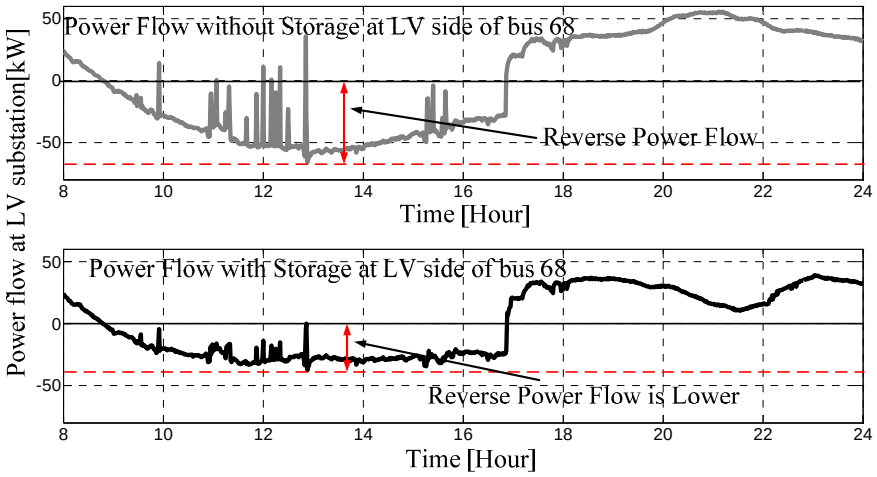

Fig. 6.14. Reverse power flow mitigation with storage.

The reduction in reverse power flow is limited due to the size of the installed storage devices. With a sufficient storage capacity, it is possible to totally eliminate the reverse power. The only limitation is the cost of the energy storage system. A trade-off analysis between the cost of the energy storage and the impacts of the reverse power flow and voltage-rise in the system has to be performed to find the optimum size of the energy storage system. Further, it is important to note that the reverse flow is a complex function of time, load demand and sun insolation. The result in Fig. 6.14 is only for a

particular day, a particular load demand and the given sun insolation profile. The size of the energy storage system (250 Ah, 24 V) has been found to be adequate for the size of PV modules chosen in terms of the acceptable Australian voltage limits.

A case is studied in Fig. 6.15 where the PV generation drops down to such a low level for a certain period that no surplus power is available at the PCC for the storage to be charged during that time. The PV output profile is obtained from the same source (Renewable Energy Integration Facility at CSIRO), and the data was captured on the 8th February, 2011.

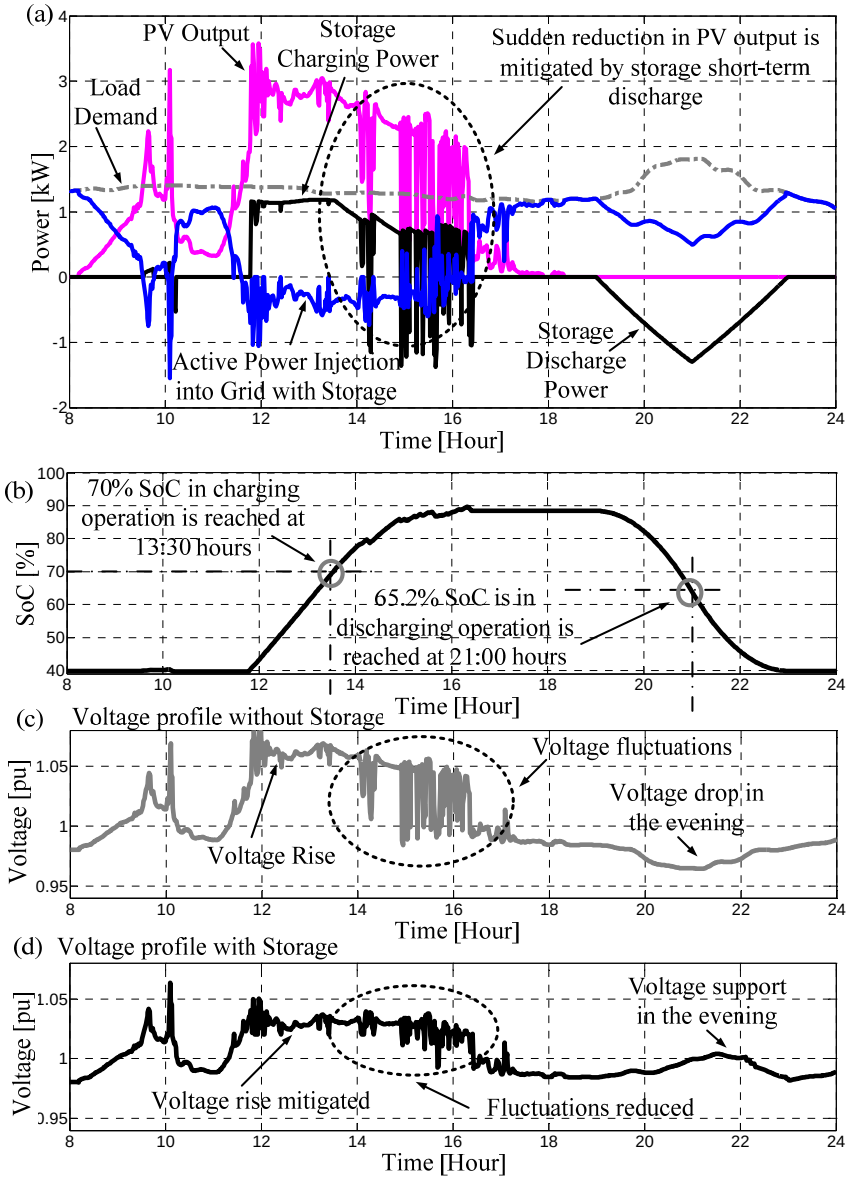

Fig. 6.15. (a) Load demand, PV output, storage power and active power injection into grid; (b) SoC profile; (c) Voltage profile without storage; (d) Voltage profile with storage.

As shown in Fig. 6.15(a), the PV output drops below the load demand in the period from 10:00 hours to about 11:30 hours. At this time, no reverse power is available at the PCC and the storage device is not charged. The PV output again exceeds the load demand from about 11:45 hours and the storage device consumes the surplus power available at the PCC. The storage charging follows a triangular profile. The charging rate starts to decrease once 70% SoC level is reached at about 13:30 hours, as shown in Fig. 6.15(b). It is important to observe that due to multiple short-term discharge operations from 14:00 hours to 16:30 hours, and the unavailability of surplus PV power from 16:30 hours, the desired SoC_{max} level is not reached at the end of the charging period. The SoC level in this scenario reaches to about 88.5%. To ensure that the available stored charge is used wisely to serve the evening peak load, the discharge parameters are re-calculated using (6.9)-(6.11). In this case, the discharge rate starts to decrease when the SoC drops to 65.2% (not to 70% that would be the case for full SoC level) at 21:00 hours as shown in Fig. 6.15(b). The mitigation of voltage-rise, the reduction of voltage fluctuations, and voltage support during the evening peak demand are shown in Fig. 6.15(c) and 15(d).

The usefulness of the proposed charging strategy is shown in Fig. 6.16 for the same PV output profile in terms of the utilization of battery capacity and the mitigation of voltage-rise. Fig. 6.16(a) shows that the storage power consumption is higher with the charging rate adjustment than that without the adjustment, because according to (6.13), the charging rate is adjusted to be higher than the normal charging rate to recover the charge not stored during the time of unavailability of surplus PV power. Also, the storage power consumption is higher with the proposed strategy than that with the constant charging strategy during peak PV generation period.

Fig. 6.16(b) shows that at the end of the charging period, 28% higher utilization of the storage capacity is achieved by the proposed adjustment strategy when compared to the constant charging strategy (220Ah instead of 150Ah). However, if the adjustment is not performed to account for unstable weather condition, the utilization of the battery capacity would not be significantly higher than constant charging rate, as shown in Fig. 6.16(b). Fig. 6.16(c) shows that the proposed strategy can mitigate voltage-rise better than that using the constant charging rate, particularly during peak PV period in the midday.

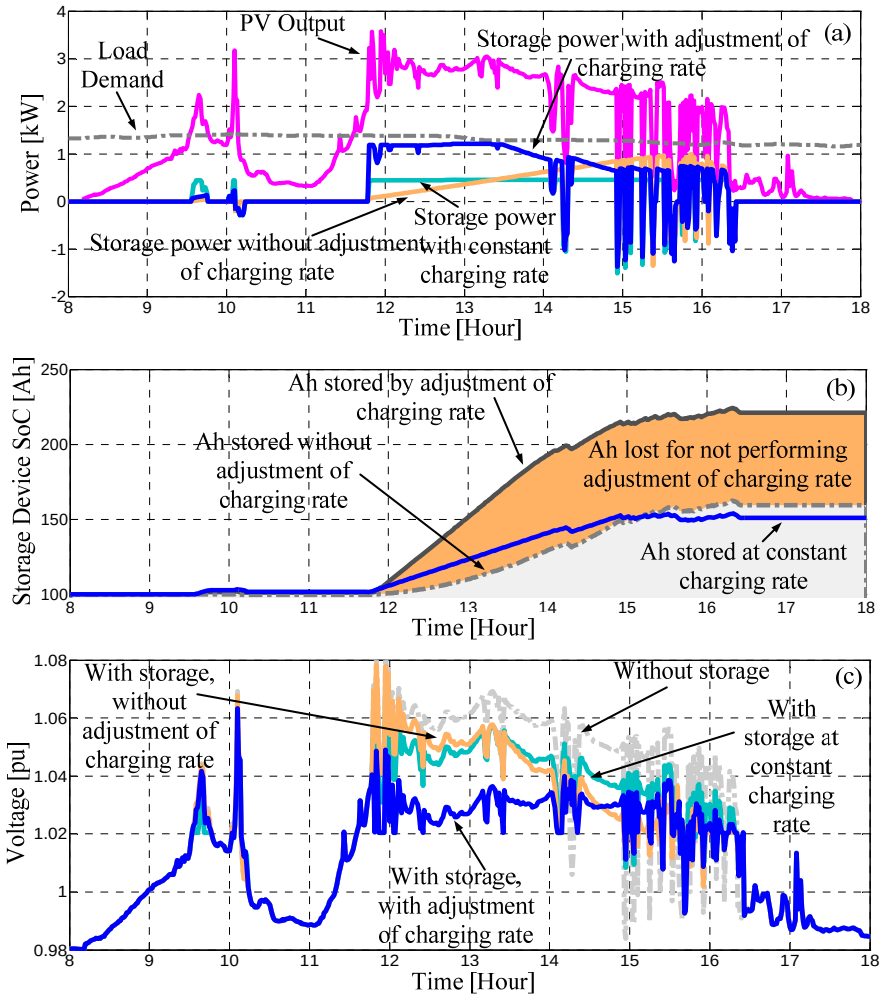

Fig. 6.16. Usefulness of the proposed charging strategy. (a) effect on power consumed by storage in charging operation; (b) utilization of battery capacity (c) voltage rise mitigation performance.

The methodology proposed in this thesis is generic in nature and can be adapted for any integrated PV and storage system connected to the PCC. It can be used by the distribution network operators as a general guideline for the charging/discharging of storage devices integrated at the LV customer premises with rooftop PV. It can also be applied for operation of the energy storage devices in autonomous distribution systems and microgrids. Further, a graphical user interface can be developed to allow network operators to input the relevant information such as the intended length of charging/discharging period and the shape of the charging/discharging profile, the PV irradiance data, the PV rating, the PV inverter characteristics, the energy storage data, such as rating, charging/discharging characteristics, SoC_{max}, DoD_{max}. It is envisaged that with the availability of smart meters and monitoring devices, especially with the introduction of Advanced Metering Infrastructure [23], the low voltage distribution networks will be automated using a two-way communication with the utility system.

Through this arrangement, the AMI interface can communicate with network control center and the required parameters for storage controller can be made available. In such an environment, the distributed storage devices will be able to mitigate the PV impacts using the continuously updated control parameters. A manual can be developed and used to inform the operators on how to input the correct data to the graphical user interface to obtain a generic charging/discharging strategy for an integrated PV and storage system under consideration.

6.5 CONCLUSION

A new strategy for charging/discharging of storage devices has been proposed in this thesis for rooftop PV impact mitigation and evening peak load support. The proposed strategy can match the PV output/evening load profile better than the traditional constant charging/discharging strategy. A methodology has been developed to obtain the appropriate charging/discharging rates based on the current SoC level of the storage device and the intended charging/discharging period to wisely utilise the limited capacity of storage device. Further, the proposed strategy can mitigate sudden changes in PV output due to unstable weather conditions by putting the storage in a short-term discharge operation mode. It can also track and compensate for the deviation of the storage SoC from the desired level of SoC. Simulation results demonstrate that the proposed mitigation strategy can effectively mitigate the negative impacts of solar PV, can support the evening peak-time load demand while utilizing the available capacity of the storage device.

REFERENCES

[1] A. Canova, L. Giaccone, F. Spertino, and M. Tartaglia, "Electrical Impact of Photovoltaic Plant in Distributed Network," *IEEE Transactions on Industry Applications* vol. 45, pp. 341-347, 2009.

[2] M. Thomson and D. G. Infield, "Network Power-Flow Analysis for a High Penetration of Distributed Generation," *IEEE Transactions on Power Systems* vol. 22, pp. 1157-1162, 2007.

[3] R. Tonkoski, D. Turcotte, and T. H. M. El-Fouly, "Impact of High PV Penetration on Voltage Profiles in Residential Neighborhoods," *IEEE Transactions on Sustainable Energy,* vol. 3, pp. 518-527, 2012.

[4] R. A. Walling, R. Saint, R. C. Dugan, J. Burke, and L. A. Kojovic, "Summary of Distributed Resources Impact on Power Delivery Systems," *IEEE Transactions on Power Delivery* vol. 23, pp. 1636-1644, 2008.

[5] R. Tonkoski, L. A. C. Lopes, and T. H. M. El-Fouly, "Coordinated Active Power Curtailment of Grid Connected PV Inverters for Overvoltage Prevention," *IEEE Transactions on Sustainable Energy,* vol. 2, pp. 139-147, 2011.

[6] E. Demirok, P. González, K. H. B. Frederiksen, D. Sera, P. Rodriguez, and R. Teodorescu, "Local Reactive Power Control Methods for Overvoltage Prevention of Distributed Solar Inverters in Low-Voltage Grids," *IEEE Journal of Photovoltaics* vol. 1, pp. 174-182, 2011.

[7] Y. Liu, J. Bebic, B. Kroposki, J. de Bedout, and W. Ren, "Distribution System Voltage Performance Analysis for High-Penetration PV," in *IEEE Energy 2030 Conference*, Atlanta, GA, USA, 17-18 Nov., 2008, pp. 1-8.

[8] P. M. S. Carvalho, P. F. Correia, and L. A. F. Ferreira, "Distributed Reactive Power Generation Control for Voltage Rise Mitigation in Distribution Networks," *IEEE Transactions on Power Systems* vol. 23, pp. 766-772, 2008.

[9] L. Xiaohu, A. Aichhorn, L. Liming, and L. Hui, "Coordinated Control of Distributed Energy Storage System With Tap Changer Transformers for Voltage Rise Mitigation Under High Photovoltaic Penetration," *IEEE Transactions on Smart Grid,* vol. 3, pp. 897-906, 2012.

[10] Y. Ueda, K. Kurokawa, T. Tanabe, K. Kitamura, K. Akanuma, M. Yokota, and H. Sugihara, "Study on the Over Voltage Problem and Battery Operation for Grid-connected Residential PV Systems," in *22nd European Photovoltaic Solar Energy Conference*, Milan, Italy, 2007.

[11] M. J. E. Alam, K. Muttaqi, and D. Sutanto, "Distributed Energy Storage for Mitigation of Voltage-rise Impact caused by Rooftop Solar PV," in *IEEE PES General Meeting*, San Diego, California, USA, 22-26 July, 2012.

[12] I. Papic, "Simulation Model for Discharging a Lead-acid Battery Energy Storage System for Load Leveling," *Energy Conversion, IEEE Transactions on,* vol. 21, pp. 608-615, 2006.

[13] R. Perez, "Lead-acid Battery State of Charge vs. Voltage," *Home Power,* vol. 36, pp. 66-69, 1993.

[14] G. M. Masters, *Renewable and Efficient Electric Power Systems*. New Jersey: Wiley-IEEE Press, 2004.

[15] N. K. Medora and A. Kusko, "Dynamic Battery Modeling of Lead-Acid Batteries using Manufacturers' Data," in *Telecommunications Conference, 2005. INTELEC '05. Twenty-Seventh International*, 2005, pp. 227-232.

[16] O. Tremblay, L. A. Dessaint, and A. I. Dekkiche, "A Generic Battery Model for the Dynamic Simulation of Hybrid Electric Vehicles," in *Vehicle Power and Propulsion Conference, 2007. VPPC 2007. IEEE*, 2007, pp. 284-289.

[17] R. Rynkiewicz, "Discharge and Charge Modeling of Lead Acid Batteries," in *Fourteenth Annual Applied Power Electronics Conference and Exposition*, Dallas, TX, USA, 14-18 Mar, 1999, pp. 707-710 vol.2.

[18] D. Linden and T. B. Reddy, "Handbook of Batteries," *New York,* 1995.

[19] Y. Ru, J. Kleissl, and S. Martinez, "Storage Size Determination for Grid-Connected Photovoltaic Systems," *accepted for a future issue of IEEE Transactions on Sustainable Energy* 2012.

[20] K. Y. Khouzam, "Technical and Economic Assessment of Utility Interactive PV Systems for Domestic Applications in South East Queensland," *IEEE Transactions on Energy Conversion,* vol. 14, pp. 1544-1550, 1999.

[21] M. J. E. Alam, K. M. Muttaqi, and D. Sutanto, "A Three-Phase Power Flow Approach for Integrated 3-Wire MV and 4-Wire Multigrounded LV Networks with Rooftop Solar PV," *Accepted for a future issue of IEEE Transactions on Power Systems*.

[22] D. R. R. Penido, L. R. de Araujo, S. Carneiro, J. L. R. Pereira, and P. A. N. Garcia, "Three-Phase Power Flow Based on Four-Conductor Current Injection Method for Unbalanced Distribution Networks," *IEEE Transactions on Power Systems* vol. 23, pp. 494-503, 2008.

[23] R. C. Dugan and M. McGranaghan, "Sim City," *Power and Energy Magazine, IEEE,* vol. 9, pp. 74-81, 2011.

Chapter 7

A NOVEL APPROACH FOR RAMP-RATE CONTROL OF SOLAR PV USING ENERGY STORAGE TO MITIGATE OUTPUT FLUCTUATIONS CAUSED BY CLOUD PASSING

ABSTRACT

The variability of solar irradiance with a high ramp-rate, caused by cloud passing, can create fluctuation in the PV output. In a weak distribution grid with a high PV penetration, this can create significant voltage fluctuations. Energy storage devices are used to smooth out the fluctuation using traditional moving average control. However, moving average does not control the ramp-rate directly; rather the ramp-rate depends on previous values of PV output. This thesis proposes a strategy where the ramp-rate of PV panel output is used to control the PV inverter ramp-rate to a desired level by deploying energy storage (which can be available for other purposes, such as storing surplus power, countering voltage rise, etc). During the ramping event, the desired ramp-rate is governed by controlling the energy storage based on an inverse relationship with the PV panel output ramp-rate to improve the fluctuation mitigation performance. In contrast to the moving average method, the proposed strategy is able to control the desired ramp-rate independent of the past history of the PV panel output. A dynamic model of the PV-storage integrated system is developed to verify the proposed strategy in the presence of physical device time lags. The proposed strategy is verified using simulation results based on an Australian distribution system. A laboratory experiment is also conducted to validate the concept of the proposed control strategy.

7.1 INTRODUCTION

Solar photovoltaic power generation can be highly variable in nature due to the irregularities in the sun irradiance level caused by cloud passing. Although the investigation on PV output variability has been continuing for a long time as evidenced in [1-2], it is still being addressed as an issue of contemporary interest [3], especially with a high penetration level of PV resources. Recent operating experiences from La Ola Island PV plant [4] has revealed that the ramp-rate of the PV output can be as high as 63% of the rated capacity/minute, whereas it was intended to limit the ramp-rate up to 30% of the rated capacity /minute [4]. To avoid any negative impact of such a high ramp-rate on the distribution system, the PV penetration was limited to 50% of the PV plant capacity [4]. The one-second resolution irradiance data collected from Oahu Island by NREL [5] shows that the irradiance level can fluctuate with a ramp-rate of more than 50% between two consecutive measurements. A PV output ramp-rate of 20% of the rated capacity/second is recorded in a study [6] conducted on a system in Mesa del Sol, New Mexico. In Australia, the Commonwealth Scientific and Industrial Research Organisation (CSIRO) has reported [7] that the PV output ramp-rates can be up to 8% of the rated capacity/second at various locations. With a high penetration of grid-connected PV resources in weak radial distribution systems, such high ramp-rate variations of the PV output can introduce significant voltage fluctuations [8]. Therefore, ramp-rate control strategies to reduce fluctuations in PV outputs and the resulting voltage fluctuations in PV integrated distribution systems are necessary in order to increase the PV penetration level in the networks.

Different kinds of energy storage technologies have been proposed for smoothing of PV output, such as, electric double-layer capacitor (EDLC) [9-11], superconducting magnetic energy storage [12], fuel cell [13], and battery energy storage [14-15]. A moving average based ramp-rate control is proposed in [9] for smoothing PV output fluctuations using EDLC. The moving average method was also used in [14] for controlling battery energy storage to reduce PV fluctuations. An exponential moving average has been used in [16] that gives more weight on the recent values of the fluctuating PV output. A modified Euler type moving average model is proposed in [11] for prediction of moving average values for a hybrid system with PV, fuel cell, EDLC and battery. Controlling an energy storage device using traditional moving average

method can reduce PV output fluctuation, but it may not necessarily control the PV output to a desired ramp-rate. Also, a moving average with a long averaging window would require a storage device to operate to match the difference between the actual PV output and the moving average, even if the actual PV output is not significantly fluctuating. The battery and charging facility available in an electric-vehicle has been used in [15] to mitigate the short-term intermittency using a high-pass filter for fluctuation mitigation. In this method, the ramp-rate of PV inverter is limited using the characteristics of the filter, such as the corner frequency. A dynamic filtering controller and dynamic rate limiter approach is used in [17] for smoothing of PV and wind power generation fluctuations.

In [18], the power delivered/absorbed by energy storage for ramp-rate control is determined using a battery State of Charge (SoC) versus allowable ramp-rate droop characteristic for generic renewable resources, where the allowable ramp-rate is related to the SoC, but not directly related to the renewable resource ramp-rate. An application of this strategy for a utility scale PV plant is demonstrated in [19]. Fluctuation mitigation using moving average control and a first-order low pass filter is presented in [20] where the SoC of the energy storage device is maintained within a range by modifying the energy storage power output using a gain parameter, which requires tuning. The impact of different storage time constants has also been investigated using time constants up to 30 seconds. Authors in [6] have applied both ramp-rate control and moving average method for intermittency mitigation of the aggregate output of a distribution system with several distributed resources including an energy storage system. There is no unique strategy for PV output smoothing, as it depends on many factors including cost and response time of the compensating resource and system operation policy [6]. Also, the delay in data transmission can cause less smooth output or may even add more fluctuation to the aggregate output [6]. However, if the fluctuation is mitigated at the PV connection point with local information, the transmission of data would not be necessary.

The contribution of this thesis is to propose a new method for mitigation of PV inverter output fluctuation by ramp-rate control using energy storage. The energy storage system may be available for other purposes, such as storing excess energy for use when the sun is not available, mitigating voltage rise, etc [21]. The novelty of the proposed approach is an algorithm to control the ramp-rate of the PV output fluctuation

using the appropriate strategies during the ramping and post-ramping event. During a ramp-down or ramp-up event**,** the energy storage system is controlled based on an inverse characteristic of the desired ramp-rate of PV inverter with respect to the ramp-rate of the PV panel output to improve the fluctuation mitigation performance. Once the ramping event is over, the energy storage system will be controlled using a SoC droop characteristic to consider the available capacity in selecting the desired ramp-rate. Unlike the traditional moving average method, the proposed strategy does not have a memory effect and therefore the storage devices can be controlled according to the requirement at each instant of time without being influenced by the PV panel output at the previous instants or without affecting the compensating power at a future time instant**.** A dynamic model of the PV-storage integrated system is developed using first order representations of storage device and PV inverter, and is integrated with the distribution network model to test the validity of the proposed strategy in a dynamic environment with physical device time-lags. Voltage fluctuation mitigation achieved by applying the proposed control strategy is also investigated. The proposed control strategy is verified using a daylong quasi-steady-state and dynamic simulation based on an Australian distribution system and also using a basic experimental setup.

7.2 LIMITATIONS OF TRADITIONAL MOVING AVERAGE METHOD IN RAMP-RATE CONTROL

Traditionally, moving average is used to smooth out a fluctuating variable. Energy storage device has been controlled by a moving average method for smoothing PV output fluctuations in [14, 20]. Although this is a traditionally accepted way to reduce the fluctuations in PV output, it requires the energy storage device to inject/absorb power even if the PV output is not fluctuating significantly. Also, such moving average strategy does not control the ramp-rate directly. These points are discussed further below.

It is well-known that moving average has a memory effect. Depending on the length of the averaging window, a moving average would highly depend on the past history and therefore, may be significantly different than the present value of the fluctuating variable. For PV output smoothing, the integrated storage device will have to operate to make-up for the aforementioned difference between the actual PV output and the moving average. Numerically, a moving average with a w-length window contains only

(1/w) % of the present value of the fluctuating variable. A realistic PV output from Oahu Island, Hawaii on the 18th of March 2010, available from NREL [5] and its 20-min [9] moving average is shown in Fig. 7.1. Although the PV output does not fluctuate significantly during the time periods in the red circles, the moving average values during these times still deviate significantly from the actual PV outputs due to the memory effect of the moving average method. To make-up for this deviation, energy storage device needs to operate more than necessary.

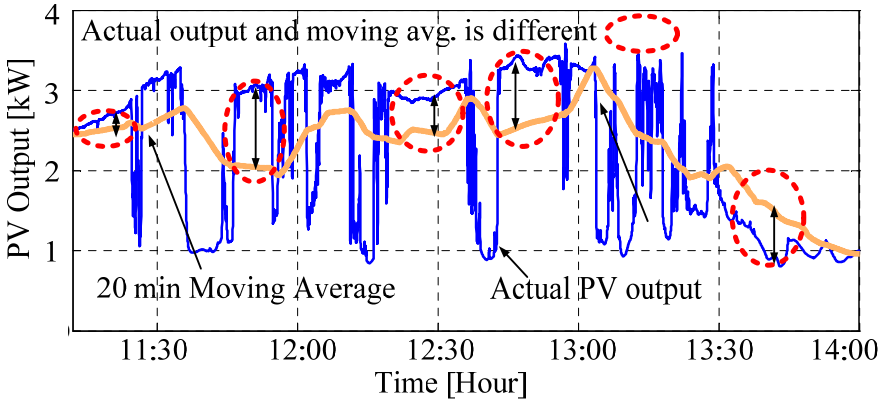

Fig. 7.1. Actual PV output and a 20-min moving average.

Further, with a given window length w, the moving average method may not provide a desired ramp-rate; rather the ramp-rate will depend on the past history of the fluctuating PV output. The ramp-rate of the moving average of a variable PV output at the k-th time instant can be defined using the following expression.

$$\begin{aligned} MoRR(k) &= \frac{1}{w} \times \frac{\sum_{i=0}^{w-1} P_{DC}(k-i) - \sum_{i=0}^{w-1} P_{DC}(k-1-i)}{t(k)-t(k-1)} \\ &= \frac{1}{w} \times \frac{P_{DC}(k) - P_{DC}(k-w)}{t(k)-t(k-1)} \end{aligned} \tag{7.1}$$

where, $MoRR(k)$ is the ramp-rate of the moving average of PV panel DC output, w is the length of the moving average window in terms of the number of data points, P_{DC} is the PV panel DC output and $t(k)$ is the time corresponding to the k-th time instant. Observing (7.1), it is clear that the ramp-rate obtained by following a moving average of the PV output depends on the PV output at the k-th and (k-w)-th instant. Although, a significantly low ramp-rate can be obtained by following a moving average with a long window, it is not directly related to the actual desired level.

7.3 THE PROPOSED RAMP-RATE CONTROL STRATEGY

7.3.1 Concept of the Proposed Ramp-rate Control Strategy

In the proposed ramp-rate control strategy, a compensation power will be added with the PV panel DC power to control the ramp-rate of the PV inverter output within a desired level at any instant of time. The basic concept of the ramp-rate control strategy is explained in Fig. 7.2.

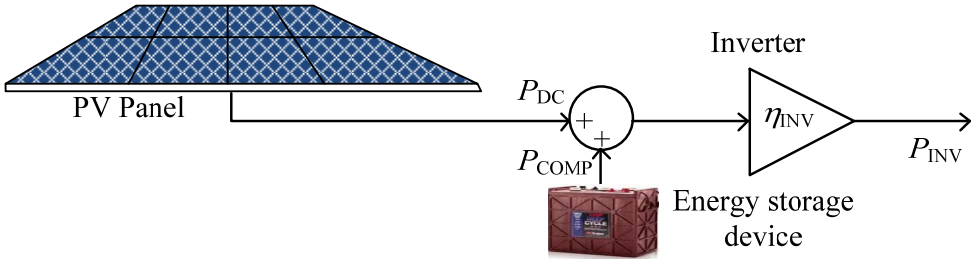

Fig. 7.2. Conceptual schematic of the proposed ramp-rate control strategy.

Based on Fig. 7.2, the PV inverter output P_{INV} can be obtained from the PV panel DC power P_{DC} and the compensation power P_{COMP} using the following expression.

$$P_{INV} = \eta_{INV} \times (P_{DC} + P_{COMP}) \tag{7.2}$$

In Fig. 7.2 and (7.2), η_{INV} is the inverter efficiency. Taking the time derivative of (7.2) at both sides, the ramp-rate of P_{INV} can now be related with the ramp-rate of P_{COMP} and P_{DC}, as given in (7.3).

$$\frac{dP_{INV}}{dt} = \eta_{INV} \times \left[\frac{dP_{DC}}{dt} + \frac{dP_{COMP}}{dt} \right] \tag{7.3}$$

where, $\frac{dP_{INV}}{dt}$ is the PV inverter output ramp-rate, $\frac{dP_{DC}}{dt}$ is the PV panel DC power output ramp-rate, and $\frac{dP_{COMP}}{dt}$ is the compensation power ramp-rate.

To control the ramp-rate of the PV inverter output within a desired level, the ramp-rate of P_{COMP} can be controlled using the expression derived from (7.3), as given below.

$$\frac{dP_{COMP}}{dt} = \frac{1}{\eta_{INV}} \times \left[\left. \frac{dP_{INV}}{dt} \right|_{des} - \eta_{INV} \times \frac{dP_{DC}}{dt} \right] \tag{7.4}$$

where, $\left.\frac{dP_{\text{INV}}}{dt}\right|_{des}$ is the desired ramp-rate of the PV inverter. If the desired ramp-rate of the inverter output is set to zero, then PV inverter output will not be allowed to change at all. For smoothing purpose, the desired ramp-rate is set to a small negative value during a ramp-down event of the PV module output, and to a small positive value during a ramp-up event of the PV module output as described later.

The expression given in (7.4) is the basic control equation that will be followed to control the ramp-rate of PV inverter output. However, the following modifications are made to accommodate practical situations.

(*a*) To allow for the slow variations of P_{DC} with the progress of the day, a dead-band function '*f*' is incorporated with (7.4) that will force the ramp-rate of P_{DC} to be *zero* if it is within an acceptable limit, defined using the desired ramp-rate of P_{INV}, as shown below.

$$f\left(\frac{dP_{\text{DC}}}{dt}\right)=\begin{cases}0, \text{if } \eta_{\text{INV}}\times\left|\frac{dP_{\text{DC}}}{dt}\right|\le\left.\frac{dP_{\text{INV}}}{dt}\right|_{des}\\ \frac{dP_{\text{DC}}}{dt}, \text{otherwise}\end{cases} \tag{7.5}$$

(*b*) Observing (7.4) it is apparent that when the ramp-rate of P_{DC} is *zero*, considering the dead-band function mentioned in modification (*a*), the ramp-rate of P_{COMP} will be governed by the desired ramp-rate of P_{INV}. However, when the ramp-rate of P_{DC} is *zero*, then if P_{COMP} has already attained such a level that removal of P_{COMP} itself would not create an unacceptable fluctuation in P_{INV}, then it will not be necessary to change P_{COMP} for the ramp-rate control. Therefore, the ramp-rate of P_{COMP} can be made zero during this situation. To accommodate this, a switching function *S*, as given below, is incorporated with (7.4).

$$S=\begin{cases}0, \text{if } |P_{\text{COMP}}|<\left.\frac{dP_{\text{INV}}}{dt}\right|_{des} \text{ and } f\left(\frac{dP_{\text{DC}}}{dt}\right)=0\\ 1, \text{otherwise}\end{cases} \tag{7.6}$$

The modified control equation incorporating the dead-band function '*f*' and the switching function '*S*' can be described using the expression below.

$$\frac{dP_{\text{COMP}}}{dt} = S \times \left[\frac{1}{\eta_{\text{INV}}} \times \left\{ \left. \frac{dP_{\text{INV}}}{dt} \right|_{des} - \eta_{\text{INV}} \times f\left(\frac{dP_{\text{DC}}}{dt} \right) \right\} \right] \tag{7.7}$$

The inverter efficiency η_{INV} will depend on the power output of the inverter. The efficiency curve for a given inverter over a range of operating power can be obtained from the manufacturer or developed through testing. As the desired P_{INV} at any given instant is known, η_{INV} at the desired P_{INV} can be taken from the efficiency curve and can be used in (7.7) to control the ramp-rate of P_{COMP} at the necessary level.

Considering a discrete time representation, the ramp-rate of P_{DC} at the k-th instant can be determined using the expression below.

$$\frac{dP_{\text{DC}}}{dt}(k) = \frac{[P_{\text{DC}}(k) - P_{\text{DC}}(k-1)]}{t(k) - t(k-1)} \tag{7.8}$$

where, $t(k)$ is the time at the k-th instant.

The value of the switching function is also incorporated with P_{COMP} to force it to *zero* when the conditions of $S = 0$ are satisfied, as given in (7.6). P_{COMP} at the k-th instant can be obtained using (7.9).

$$P_{\text{COMP}}(k) = S \times \left[P_{\text{COMP}}(k-1) + \frac{dP_{\text{COMP}}}{dt}(k) \times \{t(k) - t(k-1)\} \right] \tag{7.9}$$

To illustrate the proposed ramp-rate control strategy, a fictitious PV output fluctuation shown in Fig. 7.3(a) is used, where the PV panel output decreases at a ramp-rate of PVRR_1 kW/sec from time t_1 to t_2, remains constant at the level reached at time t_2 up to time t_3, and again increases from time t_3 to time t_4 at a ramp-rate of PVRR_2 kW/sec. After reaching time t_4, the PV output remains constant. To control the ramp-rate of P_{INV}, (7.7) and (7.9) are used to produce the appropriate amount of P_{COMP}. The desired ramp-rate of P_{INV} is defined as the Maximum Allowable Ramp-rate (MARR) in W/sec. To apply the proposed strategy to any size of PV plant, the ramp-rate units can also be defined in % of the rated PV capacity/sec. Before time t_1, P_{DC} remains at a stable state. Therefore, the ramp-rate of P_{COMP} is *zero* according to (7.7), and remains *zero*. From time t_1 to t_2, P_{DC} sharply decreases with a ramp-rate of PVRR_1. During this time the ramp-rate of P_{COMP} is determined using PVRR_1 and MARR. At time t_2, PVRR_1 becomes *zero*, but P_{COMP} is not *zero* yet. Therefore, the ramp-rate of P_{COMP} from time t_2

to t_3 is determined using MARR only. From time t_3 to t_4, P_{DC} sharply increases with a ramp-rate of $PVRR_2$. During this time, P_{COMP} is controlled with a ramp-rate determined using $PVRR_2$ and MARR. After time t_4, $PVRR_2$ becomes *zero*, however, P_{COMP} is not *zero* yet. Therefore, from time t_4 P_{COMP} is controlled using MARR only. At time t_5, P_{COMP} becomes *zero* and the ramp-rate of P_{DC} is also *zero*. Therefore, the ramp-rate of P_{COMP} is *zero* after t_5 which keeps P_{COMP} at *zero*.

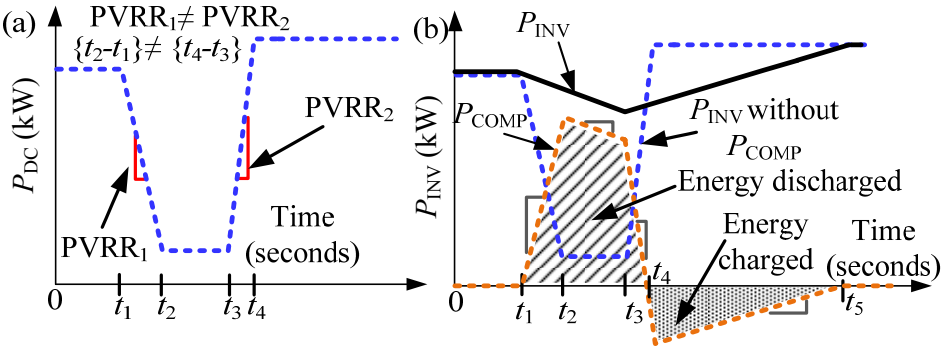

Fig. 7.3. An illustration of the proposed ramp-rate control strategy. (a) A hypothetical PV output fluctuation. (b) PV inverter output with appropriately controlled P_{COMP} to limit the P_{INV} ramp-rate within a desired level.

For moving average control, P_{COMP} at a given k-th instant depends on the previous values of P_{DC} within the averaging window, w, as given below.

$$P_{COMP}(k) = \frac{\sum_{i=0}^{w-1} P_{DC}(k-i)}{w} - P_{DC}(k) \tag{7.10}$$

Therefore, if moving average is applied to control the ramp-rate of the fluctuation shown in Fig. 7.3(a), then P_{COMP} at $t>t_1$ will actually depend on the P_{DC} values before t_1. It will not directly depend on the required P_{COMP} to control the ramp-rate at a desired level. According to (7.10), P_{COMP} is only controllable using the length of the averaging window w. The higher the number w is chosen, the more is the smoothing effect. However, if a high w is chosen for improving fluctuation mitigation performance at the k-th instant, it not only impacts the P_{COMP} at the k-th instant, but also at all the future time instants. For example, if w is increased by Δw to increase the smoothing effect at the k-th instant, then at any future $(k+j)$-th instant, the deviation of P_{COMP} due to the increase of w (i.e., Δw) will be,

$$\Delta P_{\mathrm{COMP}}(k+j)=\left|\frac{\sum_{i=0}^{w+\Delta w-1}P_{\mathrm{DC}}(k+j-i)}{w+\Delta w}-\frac{\sum_{i=0}^{w-1}P_{\mathrm{DC}}(k+j-i)}{w}\right| \tag{7.11}$$

The deviation ΔP_{COMP} at the (k+j)-th instant is solely due to the increase of w at the k-th instant. For a given Δw, this deviation will remain in effect for all future time instants even if it is not necessary because of acceptable variations in P_{DC}.

In contrast, according to the proposed ramp-rate control strategy, the amount of P_{COMP} to control the ramp-rate at a given k-th instant can be governed by the desired ramp-rate of P_{INV} for the k-th instant only and it does not impact the future ramp-rates. According to (7.9), P_{COMP} at the k-th time instant is,

$$P_{\mathrm{COMP}}(k)=S\times\left[P_{\mathrm{COMP}}(k-1)+\phi\left(\frac{dP_{\mathrm{INV}}}{dt}(k)\bigg|_{des}\right)\right] \tag{7.12}$$

In (7.12), $\phi(\cdot)$ denotes a function that determines the ramp-rate of P_{COMP} for obtaining the desired ramp-rate of P_{INV} at the given ramp-rate of P_{DC}. The value of $\phi(\cdot)$ is obtained using (7.7). As the proposed strategy does not have a memory effect, P_{COMP} can be changed at each instant dynamically based on the requirement. This advantage is used in this thesis to improve the fluctuation mitigation performance.

7.3.2 Improvement of the Fluctuation Mitigation Performance

For a given PV output fluctuation, the duration of the ramping event is inversely proportional to the ramp-rate of the PV output, because the higher the ramp-rate, the faster the PV output changes from one stable state to another stable state. As the time duration for a high-rate ramping event is very short, the amount of energy needed to be used for ramp-rate control is small. Therefore, during the ramping event, the MARR can be reduced in an inverse proportion to the PV panel output ramp-rate (PVRR) to improve the fluctuation mitigation performance without discharging a significant amount of storage capacity. Such an inverse characteristic is given in (7.13) and shown in Fig. 7.4(a).

$$\mathrm{MARR}_{\rho}(k)=\begin{cases}|\mathrm{PVRR}(k)|, \text{if } |\mathrm{PVRR}(k)|<\mathrm{RR}_{\mathrm{lim}}\\ \dfrac{\gamma}{|\mathrm{PVRR}(k)|}, \text{if } |\mathrm{PVRR}(k)|\geq\mathrm{RR}_{\mathrm{lim}}\end{cases} \tag{7.13}$$

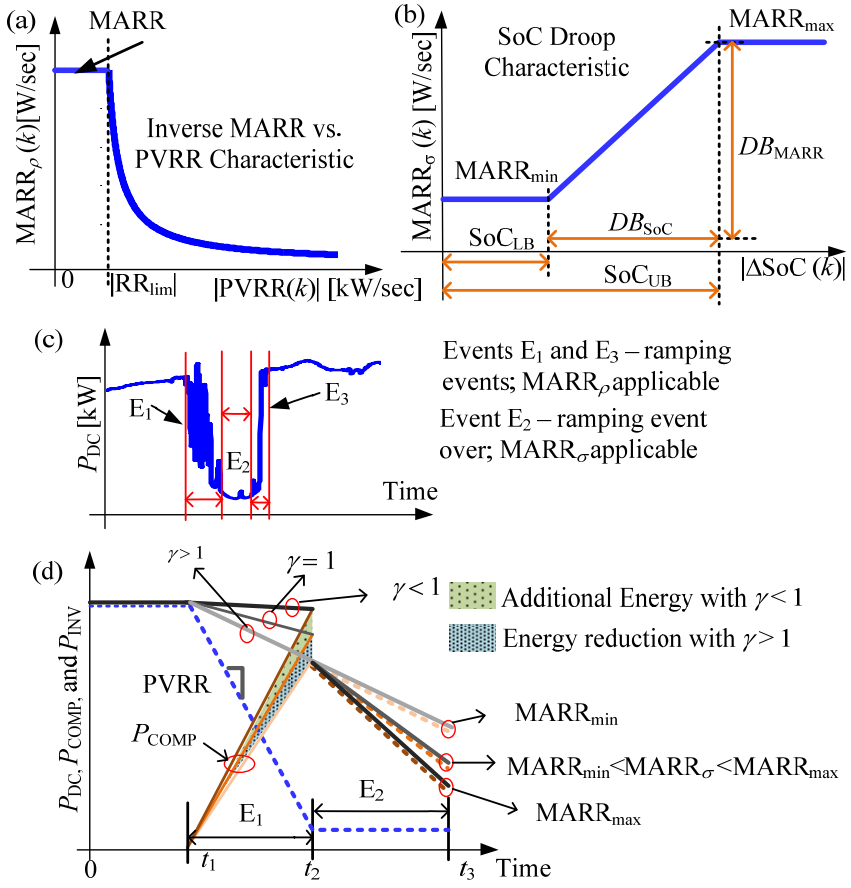

Fig. 7.4. Ramping event dependent selection of MARR. (a) During the ramping event. (b) After the ramping event. (c) Application of MARR$_\rho$ and MARR$_\sigma$ (d) The effect of γ and MARR versus SoC droop on ramp-rate control.

In (7.13), MARR$_\rho$ is the inverse characteristic based desired ramp-rate, to be applied during the ramping event and γ is a factor to control the degree of inverse characteristic; RR$_{lim}$ is a threshold of ramp-rate of P_{DC} beyond which the inverse characteristic is applied. RR$_{lim}$ should be set to a value higher than the ramp-rate of slow variations of P_{DC} to allow P_{INV} to vary with the progress of the day. Once the ramping event is over, the P_{COMP} can be brought to *zero* with an MARR determined using a SoC droop characteristic as given by (7.14) and shown in Fig. 7.4(b).

$$\text{MARR}_\sigma(k)=\begin{cases}\text{MARR}_{\min}, \text{if } |\Delta\text{SoC}(k)|<\text{SoC}_{\text{LB}}\\ \text{MARR}_{\min}+\dfrac{DB_{\text{MARR}}}{DB_{\text{SoC}}}\times\left[|\Delta\text{SoC}(k)|-\text{SoC}_{\text{LB}}\right],\\ \qquad\qquad \text{if } \text{SoC}_{\text{LB}}\le|\Delta\text{SoC}(k)|\le\text{SoC}_{\text{UB}}\\ \text{MARR}_{\max}, \text{if } |\Delta\text{SoC}(k)|>\text{SoC}_{\text{UB}}\end{cases} \tag{7.14}$$

In (7.14), MARR$_\sigma$ is a SoC droop based desired ramp-rate, to be applied once the

ramping event is over; DB_{MARR} and DB_{SoC} are the dead-bands of MARR and SoC, respectively; $\mathrm{SoC}_{\mathrm{LB}}$ and $\mathrm{SoC}_{\mathrm{UB}}$ are the lower and upper bands of SoC, respectively, and $|\Delta \mathrm{SoC}(k)|$ is the absolute value of the deviation between $\mathrm{SoC}(k\text{-}1)$ and a user defined reference $\mathrm{SoC}_{\mathrm{ref}}$. Using the absolute deviation makes the droop characteristic applicable for change of SoC in either direction.

Fig. 7.4(c) identifies the ramping events in a real PV output fluctuation and shows the event driven application of MARR_{ρ} and MARR_{σ} to control the ramp-rates. $\mathrm{SoC}_{\mathrm{LB}}$ defines the amount of energy available for controlling the ramp-rate at $\mathrm{MARR}_{\mathrm{min}}$ before entering the droop characteristic. Therefore, $\mathrm{SoC}_{\mathrm{LB}}$ should be set to a value that represents a sufficient amount of energy to control the ramp-rate at $\mathrm{MARR}_{\mathrm{min}}$ (during the worst-case fluctuation) for a certain amount of time that allows for any back up power to come online or any sensitive load to be shut down safely. $\mathrm{SoC}_{\mathrm{UB}}$ should be set up to a value that represents a substantial portion of the energy needed to control the ramp-rate (during the worst-case fluctuation) before exceeding the saturation limit of the droop characteristic ($\mathrm{MARR}_{\mathrm{max}}$).

The effect of the parameter γ in (7.13) and the parameters $\mathrm{MARR}_{\mathrm{min}}$ and $\mathrm{MARR}_{\mathrm{max}}$ in (7.14) on the fluctuation mitigation performance is shown in Fig. 7.4(d) using a fictitious PV fluctuation containing a ramping event E_1 (time t_1 to t_2) at a ramp-rate PVRR, followed by a low PV event E_2 (time t_2 to t_3). During the event E_1, MARR_{ρ} is applicable which is determined by γ. If $\gamma = 1$, MARR_{ρ} is in direct inverse relation with the ramp-rate of P_{DC}. If $\gamma < 1$, the degree of the inverse characteristic increases, and therefore, P_{INV} is improved compared to $\gamma = 1$. However, this will be performed at the expense of additional energy discharged from the storage device as shown in Fig. 7.4(d) using the shaded region. If $\gamma > 1$, the degree of the inverse characteristic decreases, and therefore, P_{INV} is reduced compared to $\gamma = 1$, but at the same time a smaller amount of energy is discharged from the storage device, as shown in Fig. 7.4(d). Although for high ramp-rate events, the variation of storage energy discharge is not significant, it provides the user a control over the fluctuation mitigation performance of the proposed strategy.

During the event E_2, P_{COMP} slowly decreases at MARR_{σ} determined from the SoC droop characteristic in (7.14). For a given fluctuation, $\mathrm{MARR}_{\mathrm{min}}$ is selected as MARR_{ρ} so that P_{INV} can be reduced at the same ramp-rate as it reduces during event E_1, which

provides a smooth transition in ramp-rate control from event E_1 to E_2. However, if $|\Delta SoC|$ is higher than SoC_{LB}, then $MARR_{\sigma}$ is increased and therefore, P_{INV} reduces at a higher ramp-rate as shown in Fig. 7.4(d). $MARR_{max}$ in (7.14) needs to be set to a value that allows for the slow variations of P_{DC}, as mentioned for selecting RR_{lim} in (7.13).

The discussions presented above provide only basic guidelines for selection of the control parameters for the proposed strategy. In general, these parameters are user defined and can vary depending on the scenario.

7.3.3 Energy Utilization for the Control of Ramp-rate

The amount of energy to be utilised by an energy storage device for controlling the ramp-rate will mainly depend on the PV panel output power, P_{DC}, just prior to start of the fluctuation, and the maximum allowable ramp-rate, MARR. A relation of the energy usage for ramp-rate control to the rated output of a PV panel is established and discussed below using Fig. 7.5. To consider a worst case fluctuation, a PV output power having a sudden fall from the rated value of $P_{DC\text{-}rated}$ to *zero* at time $t_1$is shown in Fig. 7.5(a). In this case it is assumed that P_{DC} does not return to its previous value due to a likely phenomenon of a sustained cloudy period, after time t_1. According to the proposed strategy, the PV inverter output will be slowly reduced at the maximum allowable ramp-rate MARR and will become *zero* at time t_2, instead of suddenly dropping to *zero*. The value of MARR will be determined depending on the situation as shown in Fig. 7.4.

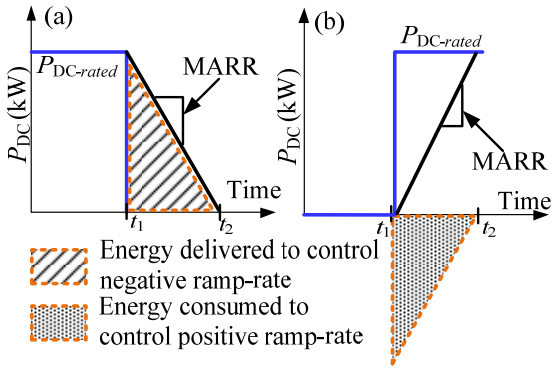

Fig. 7.5. Energy utilization in the proposed ramp-rate control strategy. (a) During negative ramp-rate control. (b) During positive ramp-rate control.

The energy to be discharged by the storage device in controlling the ramp-rate is shown in Fig. 7.5(a) using a shaded area. A similar type of worst case scenario for

positive ramp-rate is shown in Fig. 7.5(b), where the PV output suddenly increases from *zero* to $P_{DC\text{-}rated}$ at time t_1. In this case, the positive ramp-rate of the P_{INV} is controlled by charging the energy storage with certain amount of energy, as indicated using a shaped area in Fig. 7.5(b). The energy utilised for ramp-rate control, E_{RRC} (Wh) can be derived using the expression given below.

$$E_{RRC} = \frac{\sum_{i=1}^{N_{tot}} (P_{DC\text{-}rated} - i \times \text{MARR})}{3600} \tag{7.15a}$$

where, N_{tot} is the total number of time-steps between time t_1 (seconds) and t_2 (seconds), which can be determined using,

$$N_{tot} = \frac{P_{DC-rated}}{\text{MARR}} \tag{7.15b}$$

In (7.15a), 3600 is used to bring the unit to kWh, as the calculations are being performed in per second unit. A plot of the E_{RRC} for rated PV capacities up to 5 kW is derived using (7.15) for different values of MARR and is shown in Fig. 7.6. Increase of energy utilization for ramp-rate control with increase in PV capacity and decrease in MARR is observed in Fig. 7.6.

Instead of using $P_{DC\text{-}rated}$, $P_{DC}(k)$ can be used in (7.15) to determine the energy required to control the ramp-rate from the present value of P_{DC}. The amount of energy determined in this way can be identified as an Energy Buffer (E_{Buff}) to approximately check the minimum amount of capacity need to be present in the storage to control the ramp-rate according to the proposed strategy.

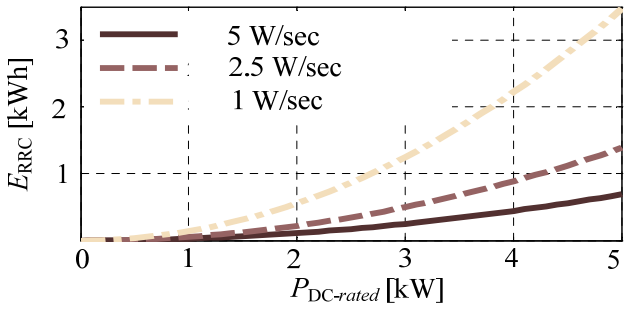

Fig. 7.6. Variations of the energy utilization for ramp-rate control with different rated PV output at different MARR.

7.3.4 The Flow Chart of the Proposed Control Strategy

The flowchart of the proposed ramp-rate control strategy for a given k-th time instant is shown in Fig. 7.7. The ramp-rate of P_{DC} at the k-th instant PVRR(k) is calculated using (7.8), and based on this $MARR_{\rho}$ is calculated using (7.13). If PVRR(k) is equal to or higher than $MARR_{\rho}$, S is set to 1 and the ramp-rate of P_{COMP} is determined using (7.7) and in this case the desired ramp-rate is replaced with $MARR_{\rho}$. If PVRR(k) is found lower than $MARR_{\rho}$, then a test is performed to find if removal of P_{COMP} would create an unacceptable fluctuation in P_{INV}. If 'Yes', then S is set to 1 and the ramp-rate of P_{COMP} is determined using (7.7), but in this case the desired ramp-rate is replaced with $MARR_{\sigma}$, determined from (7.14). If 'No', then the ramp-rate of P_{COMP} is determined using (7.7) with $S = 0$. The ramp-rate of $P_{COMP}(k)$ is applied to determine $P_{COMP}(k)$ using (7.9). With the value of $P_{COMP}(k)$ obtained, the present level of SoC is checked. If it is found within the lower (SoC_{LL}) and upper (SoC_{UL}) limits of SoC, obtained using the Maximum Depth of Discharge (DoD_{max}), the Maximum State of Charge (SoC_{max}), and buffer energy E_{Buff}, then a charge/discharge operation is performed depending on the sign of $P_{COMP}(k)$. According to the proposed strategy, a *+ve* sign means discharge, and *–ve* sign means charge. Once the discharging/charging decision for the time instant is made and the storage is put into operation, the control system proceeds with a transition into the next time instant.

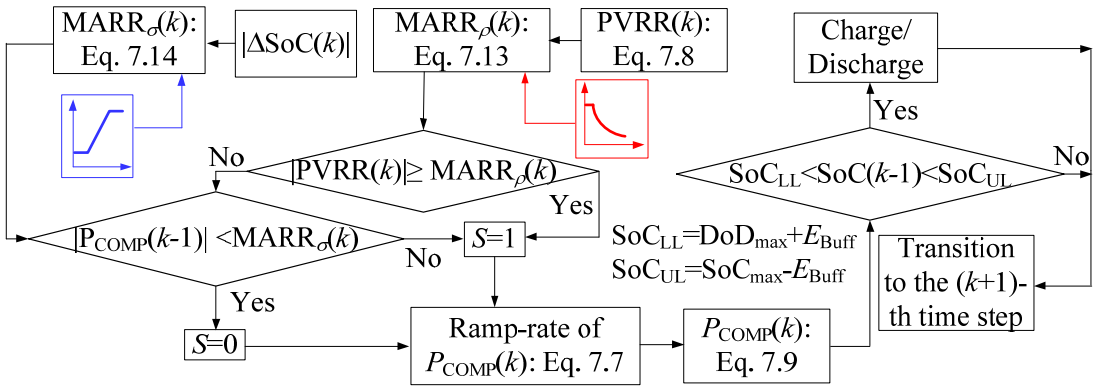

Fig. 7.7. Flow chart of the proposed ramp-rate control strategy.

Although this thesis has mainly concentrated on the application of battery energy storage, the fundamental idea of ramp-rate control proposed in this thesis would be applicable for other type of energy storage (such as ultra-capacitor).

7.3.5 Dynamic Model of PV-Storage Integrated System

The development of a dynamic model is necessary to understand the performance of the proposed strategy in the context of practical system components that are subject to physical device time lags. Detailed switching models of the power electronic converters are used in power-electronics based investigations where sub-cycle phenomena are of interest. However, for the scope of the investigations of this thesis, such fast dynamics are not of interest. Therefore, a simplistic dynamic model of the PV-storage integrated system is developed, as shown in Fig. 7.8, that represents the time-lag related to the associated devices and components. The dynamic model consists of four states which are the PI controller output (y_1), the storage power output (y_2), storage power output measurement signal (y_3), and the PV inverter output (y_4). The state equations are given below.

$$\frac{dy_1}{dt} = -K_P \times \frac{1}{T_{\text{meas}}} \times (y_2 - y_3) + K_I \times (P_{\text{COMP-ref}} - y_3) \tag{7.16a}$$

$$\frac{dy_2}{dt} = \frac{1}{T_{\text{sto}}} \times (y_1 - y_2) \tag{7.16b}$$

$$\frac{dy_3}{dt} = \frac{1}{T_{\text{meas}}} \times (y_2 - y_3) \tag{7.16c}$$

$$\frac{dy_4}{dt} = \frac{1}{T_{\text{inv}}} \times (\eta_{\text{inv}}[P_{\text{DC}} + y_2] - y_4) \tag{7.16d}$$

where, $P_{\text{COMP-ref}}$ is the reference to the PI controller; T_{inv} is the inverter time constant; T_{sto} is the storage time constant; T_{meas} is the storage output measurement circuit time delay; K_P and K_I proportional and integral gain of the PI controller.

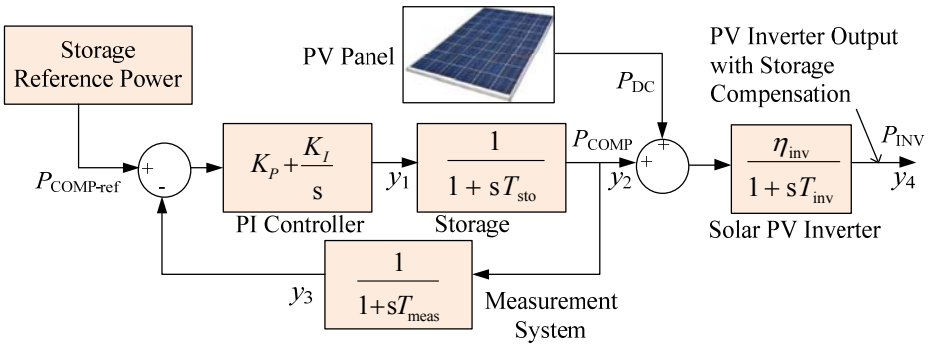

Fig. 7.8. A dynamic model of the PV-storage integrated system to consider the effect of physical device time-lags.

It is necessary that the energy storage device responds to the charging/discharging commands as fast as possible to control the ramp-rate satisfactorily. Studies have shown that battery energy storage devices, such as NaS, Li-ion, and Valve-Regulated Lead-Acid (VLRA) batteries, have response time in the order of milliseconds [22-23]. Therefore, it is expected that with an appropriate selection of the energy storage device, the ramp-rate can be controlled according to the requirements. Using the developed dynamic model, the impact of different storage response times on ramp-rate control can be investigated.

The PI controller is tuned to have a low rise time so that the fast response time of the storage device can be effectively used for fluctuation mitigation. The initial controller parameters are obtained using the open-loop frequency response of the linearised plant model. The tuning task is performed with the aid of Simulink Automatic PID tuner [24] that performs the initial tuning based on a reference tracking algorithm while keeping a trade-off between performance and robustness. Once the initial parameters are obtained, further tuning is performed to reduce the rise time.

This thesis has mainly discussed the concept of the proposed strategy and its system level application. To carry out a component level detailed design, practical issues, such as battery power losses, heat generated, and DC-link voltage fluctuations caused by high current pulses during high-ramp rate operations, need to be considered.

7.4 APPLICATION EXAMPLE OF THE PROPOSED RAMP-RATE CONTROL STRATEGY

To analyse the performance of the proposed strategy in a distribution network environment, a low voltage (LV) distribution feeder extracted from the New South Wales distribution system is considered. All the households in the LV feeder are assumed to have rooftop PV units with integrated battery storage devices. A typical 12 kWh Valve Regulated Lead Acid battery is used for simulation. Energy storage devices are modeled incorporating the non-linear voltage versus SoC characteristics and the effect of internal resistance, as described in [21]. The LV feeder under study is shown in Fig. 7.9. The results shown correspond to the PV output fluctuations in household no. 28 (HH 28) connected to phase *a,* bus 10 of the LV feeder.

The PV output data correspond to the irradiance profile of the 18th of March, 2010,

captured by NREL in the Oahu Island, Hawaii [4]. For simplicity, constant inverter efficiency (89.5%) is used in the simulations. To select the ramp-rate threshold limit to apply the inverse characteristic in (7.13), RR_{lim} is selected by observing the ramp-rate during slow variation of P_{DC} from 7:00 hours to 9:00 hours. During this time frame, more than 99% of the ramp-rates were less than 3 W/sec, as shown in Fig. 7.10(a). Therefore, to allow for this variation, RR_{lim} is set to a higher value of 5 W/sec. $MARR_{max}$ in (7.14) is also set to 5 W/sec for the same purpose.

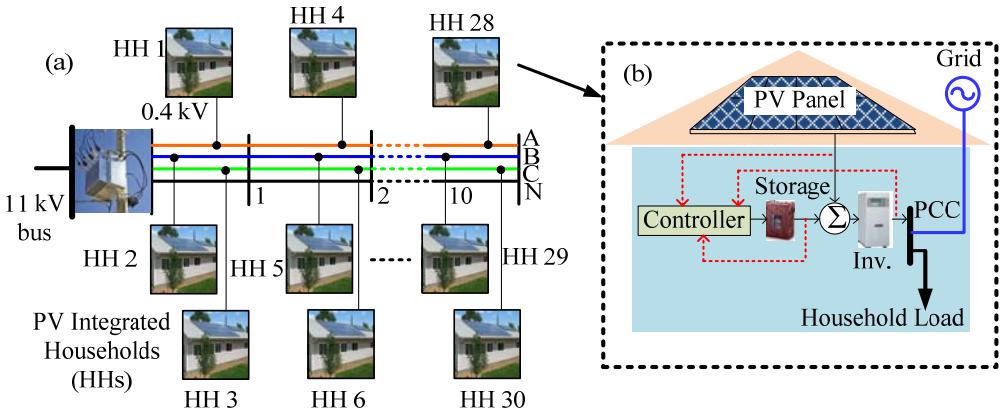

Fig. 7.9. Network integration model of the PV-storage dynamic system. (a) The test LV feeder. (b) Schematic of the system inside a household.

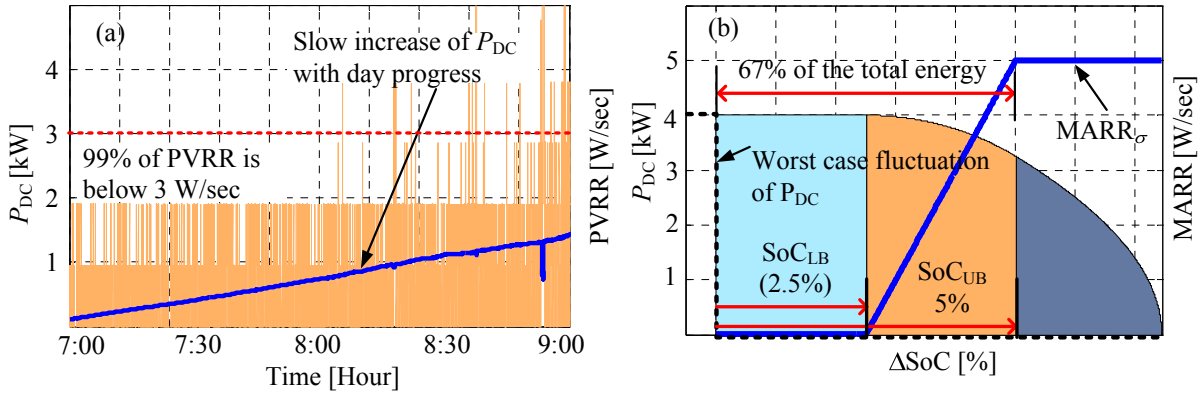

Fig. 7.10. PVRR during slow variation with the progress of the day. (a) Energy used to control the worst case fluctuation and $MARR_{\sigma}$ characteristic.

Simulation trials have been run using a range of $0.1 \leq \gamma \leq 50$. For $\gamma \leq 1$, fluctuation mitigation performance does not improve much, whereas with $\gamma > 1$, deterioration of the fluctuation mitigation performance appears with $\gamma \geq 20$. The value of γ has been selected as 5 (with Watt to kW conversion: 0.005). The storage devices are allowed to operate between a typical range of 40% to 100% SoC. To allow for charging and

discharging for ramp-rate control, SoC_{ref} is set to 70%, which is at the mid-point of the allowable range of SoC. The SoC bands, SoC_{LB} and SoC_{UB}, are selected considering the worst case fluctuation of P_{DC} from the rated value (4 kW for the PV systems in the network under study) to *zero* at the worst-case ramp-rate of $P_{DC\text{-}rated}$/sec and after the fall, P_{DC} does not recover due to a continuous cloudy period. The P_{DC} profile with the storage support is shown in Fig. 7.10(b), where the ramp-rate control is performed according to (7.14), as shown using the $MARR_{\sigma}$ profile. SoC_{LB} is set to 2.5% which corresponds to the amount of energy that can control the ramp-rate at the value of $MARR_{min}$ for about 5 minutes which is sufficient for bringing emergency power online or disconnecting sensitive loads safely. SoC_{UB} is set to 5% which accounts for about 67% of the total energy used for bringing P_{DC} to zero at a controlled ramp-rate. The parameters used for the simulation of the proposed ramp-rate control strategy are given in Table 7-I in the Appendix. Initially, the results of the quasi-steady state simulations using 1-sec resolution data are presented to investigate the validity of the strategy over a daylong variation. Later, dynamic simulation results in milliseconds time-frame are presented.

PV panel DC power, P_{DC} (multiplied by the inverter efficiency), the storage compensation power P_{COMP}, and the inverter output P_{INV} are shown in Fig. 7.11(a) and 11(b) for the moving average control and the proposed strategy, respectively. For moving average control, a 20-min moving average [9] of P_{DC} is used.

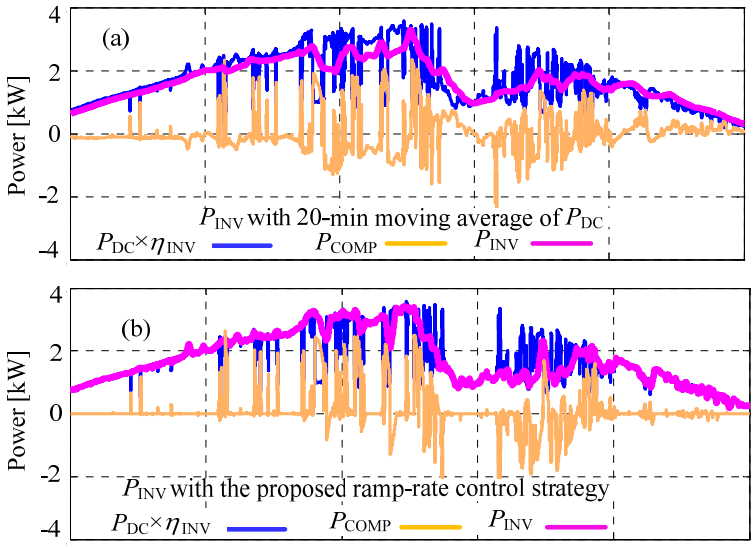

Fig. 7.11. Mitigation of PV output fluctuation. (a) Using moving average. (b) Using the proposed ramp-rate control strategy.

In general, both of the methods (moving average and the proposed approach) can

mitigate the fluctuations in PV output, as observed from Fig. 7.11. However, detailed investigations reveal the specific advantages of the proposed approach. Fig. 7.12(a) shows P_{DC} and P_{INV} profiles in a shorter window, from 10:00 hour to 13:00 hour.

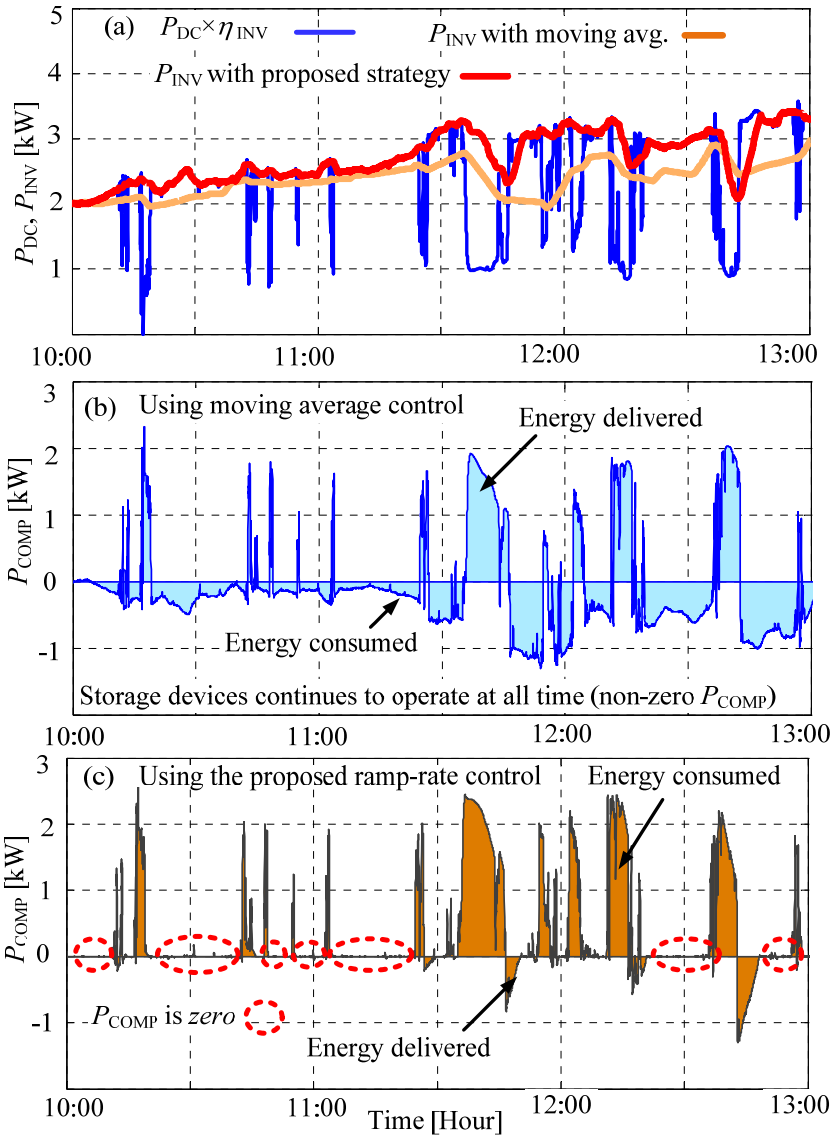

Fig. 7.12. Mitigation of PV output fluctuation. (a) P_{DC} and P_{INV} profiles. (b) P_{COMP} with moving average control. (c) P_{COMP} with the proposed strategy.

According to the proposed strategy, P_{INV} tracks P_{DC} when the ramp-rate of P_{DC} does not exceed the desired ramp-rate at that time. Therefore, the proposed strategy does not need to operate the storage at all the times. In contrast, (7.10) suggests that the moving average method needs to continue the storage operation due to the past history of P_{DC}, even if it is not necessary as the ramp-rate is within desired limit. This is observed from P_{COMP} profiles in Fig. 7.12(b) for the moving average methods and 12(c) for the proposed approach. In Fig. 7.12(c), *zero* values of P_{COMP} are highlighted using dotted

circular shapes. Examining the P_{COMP} profiles it is found that according to the proposed strategy, the storage device operates for about 50% less time in the 10 hours period (from 8:00 to 18:00 hrs) in comparison to the moving average method. This can contribute to increase the lifetime of a battery storage device.

The percentage ratio of P_{INV} to P_{DC}, based on the profiles in Fig. 7.12(a), is compared between the proposed approach and moving average method in Fig. 7.13. Due to the dependency of previous P_{DC} values, P_{INV} obtained from the moving average method is different (lower) than P_{DC}, even during the periods when P_{DC} exhibits very low fluctuation. In contrast, the proposed approach tracks P_{DC} in those periods and therefore, the P_{INV} to P_{DC} ratio is higher using the proposed approach, as compared to the moving average method.

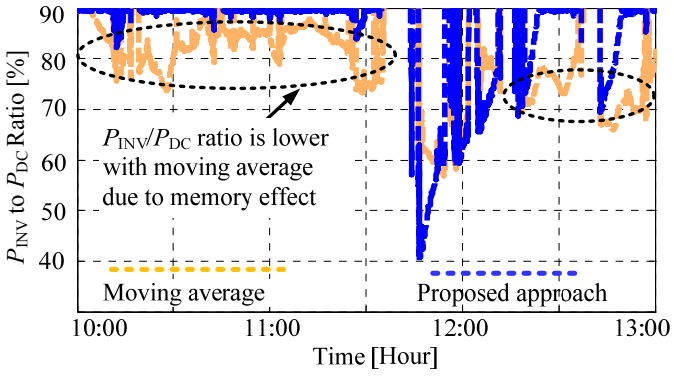

Fig. 7.13. P_{DC} to P_{INV} ratio.

The ramp-rate profiles of P_{DC} and P_{INV} from 10:00 hour to 13:00 hour are shown in Fig. 7.14(a); the ramp-rates of P_{INV} can be controlled within a specified limit by operating the storage device according to the proposed strategy. The ramp-rates of P_{INV} with 20-min moving average control of storage device are compared with those obtained using the proposed strategy in Fig. 7.14(b) for the time period when the maximum negative and positive ramp-rates in P_{DC} appeared. For reference, the ramp-rate of P_{DC} is also included in Fig. 7.14(b). During the negative fluctuation of P_{DC} with a ramp-rate of -1.767 kW/sec, the proposed strategy controls the P_{INV} ramp-rate at -0.0028 W/sec which comes from the inverse characteristic in (7.13). With the 20-min moving average, the ramp-rate of P_{INV} is -1.485 W/sec, which is not controlled at this value; rather it is produced as a result of the previous P_{DC} samples over the last 20 min period. During the positive ramping event at 1.725 kW/sec, the ramp-rate with the proposed strategy is 0.0029 W/sec which is controlled using (7.13), whereas, with the

moving average it is 0.0183 W/sec, which is not actually controlled to this value. Although the moving average method provides significant fluctuation mitigation at the expense of operating the storage device all the time, the proposed strategy provides better mitigation during the time of fluctuation with a high ramp-rate (such as the one shown in Fig. 7.14).

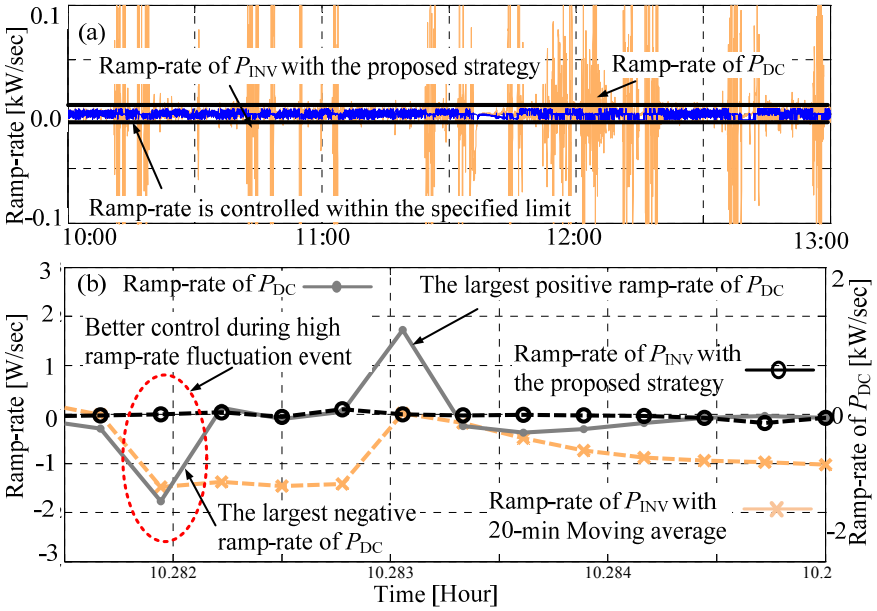

Fig. 7.14. Ramp-rate control. (a) The ramp-rate profiles of P_{DC} and P_{INV}. (b) Comparison of the P_{INV} ramp-rates obtained using the moving average control and the proposed strategy.

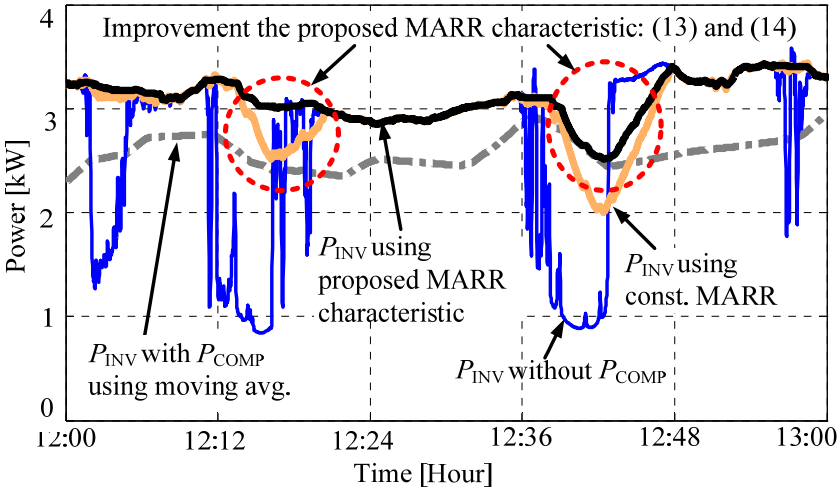

Fig. 7.15. The usefulness of the proposed inverse characteristic in the improvement of fluctuation mitigation.

The usefulness of the proposed MARR characteristics in (7.13) and (7.14) can also be observed in Fig. 7.15 where the PV output fluctuation mitigation using the proposed

inverse MARR characteristic from 12:00 hours to 13:00 hours is compared with a constant MARR value of 5 W/sec. The proposed inverse MARR and SoC droop based characteristics can mitigate the fluctuation better than a constant MARR value. For reference, the fluctuation mitigation using the 20-min moving average is also included in Fig. 7.15.

The PCC voltage profile at household no. 28 (HH 28) of the test feeder from 10:00 hours to 13:00 hours is shown in Fig. 7.16(a). For reference, P_{COMP} profile is also shown in Fig. 7.16(b). When sharp decrease in PCC voltage appears as a result of sudden decrease in PV output, energy storage device is discharged to control the high negative ramp-rates. This action mitigates the associated voltage dips. Again, when sharp rise in PCC voltage appears due to sudden increase in PV output, energy storage device is charged to control the positive ramp-rates and this action mitigates the sharp voltage rise as well. Without the proposed ramp-rate control strategy, the voltage ramp-rate at 10 hr : 16 min : 54 sec (when the largest negative ramp-rate in the PV output appeared) is -9.3 V/sec and at 10 hr : 16 min : 58 sec (when the largest positive ramp-rate in PV output appeared) is 9.1 V/sec. Controlling the ramp-rate of PV output using the proposed strategy, the PCC voltage ramp-rate is reduced to less than 0.1 mV/sec.

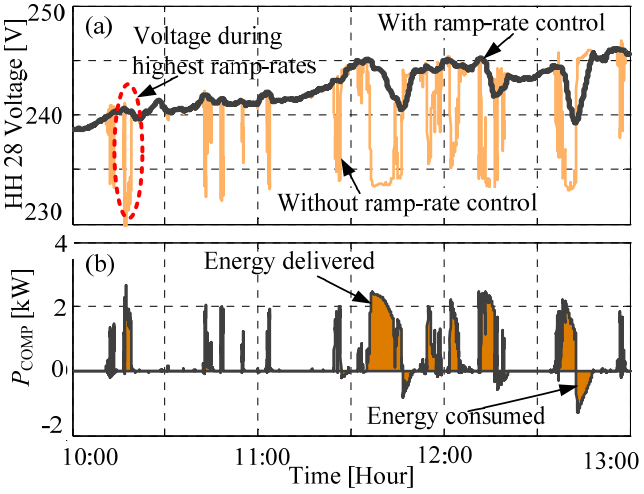

Fig. 7.16. Mitigation of PCC voltage fluctuation using the proposed strategy. (a) PCC voltage profile. (b) P_{COMP} profile.

The validation of the proposed strategy in a dynamic environment is tested using the proposed PV-storage integrated system model using 1 millisecond time step and the

results are presented in Fig. 7.17. The largest ramp-rate observed in the PV output data used for the daylong simulation is used for this purpose. The dynamic simulation is performed with the data shown in Table 7-II in the Appendix.

The PV output decreases at a ramp-rate of -1.767 kW/sec at 10 hr : 16 min : 54 sec. Fig. 7.17(a) shows that following the negative ramp-rate of P_{DC}, P_{COMP} increases within a few milliseconds time to increase the P_{INV} at the level that maintains the desired ramp-rate MARR$_\rho$ specified at the time. After 4 seconds time, the P_{DC} again increases with a ramp-rate of 1.725 kW/sec at 10 hr : 16 min : 58 sec. Fig. 7.17(b) shows that following the positive ramp-rate of P_{DC}, P_{COMP} decreases to the level necessary to maintain the desired ramp-rate of P_{INV} at that time. The impact of the storage time constant T_{sto} is also shown in Fig. 7.17; P_{INV} with T_{sto} of 5 milliseconds settles down faster and with less swing as compared to the P_{INV} with T_{sto} of 20 milliseconds. Therefore, a storage device with a fast response time is necessary for a satisfactory mitigation of the fluctuation.

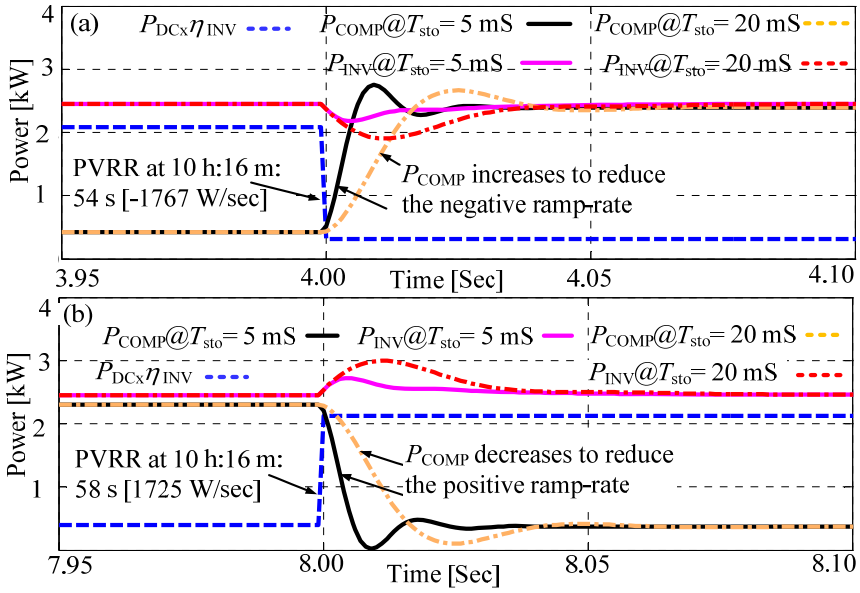

Fig. 7.17. Performance analysis using the proposed dynamic model. (a) Negative ramp-rate control; (b) Positive ramp-rate control.

7.5 EXPERIMENTAL RESULTS

An experimental set-up with a controllable DC power source simulating the PV panel DC power, an Ultratech 12V 7Ah sealed lead-acid battery, a charge/discharge controller (Model: CM3024Z), a PowerBright 400W, 12V DC to 220V AC inverter (Model:

ERP400-12), and a Chroma programmable AC/DC electronic load (Model: 63804) is used to verify the main concept of the proposed approach. The experimental set-up is shown in Fig. 7.18. The waveforms are captured using an Agilent Infiniivision (Model: DSO7034A) series oscilloscope.

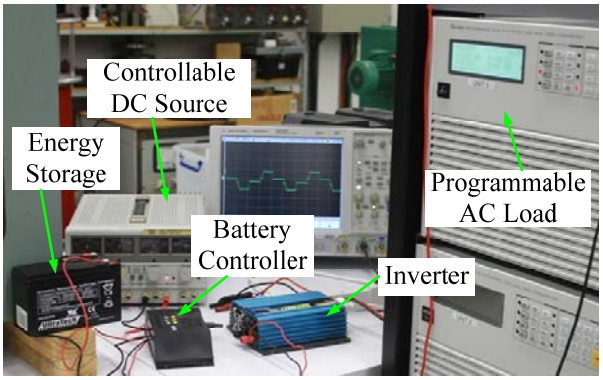

Fig. 7.18. Experimental set-up for verification of the proposed strategy.

A segment of the real PV generation profile used to obtain the simulation results is used for the experiment where the highest negative and positive ramp-rate of P_{DC} is included. A scale factor is used to scale down the simulation data to comply with the ratings of the equipment. The data points obtained from the simulation are shown in Fig. 7.19(a) that shows that from the 2nd to the 3rd data point, the PV output decreases at a ramp-rate of -55%/sec of the rated output, then remains at low values of less than 15% of the rated output from the 3rd to 6th data point. Then it increases at a ramp-rate of 53%/sec of the rated output from the 6th to the 7th data point. With the proposed control approach, P_{COMP} is controlled using (7.13) from the 2nd to the 3rd data points and from the 6th to 7th data points (ramping events). From the 3rd to the 6th data point (post-ramping event), P_{COMP} is controlled using (7.14). As a result of controlling P_{COMP} according to the proposed strategy, the ramp-rate of P_{INV} is maintained at such a low value over the period of fluctuation (1st to 7th data point) that P_{INV} remains nearly constant, as shown in Fig. 7.19(a). The captured waveforms of the DC source current, I_{DC}, the battery current, I_{COMP}, and the inverter current I_{INV} at the points (P_1), (P_2), and (P_3) identified in Fig. 7.19(a), are shown in Fig. 7.19(b). The time differences among the data points are represented using dashed lines. The decrease of I_{DC} from P_1 to P_2 caused by cloud passing is compensated by the increase of I_{COMP} and therefore, I_{INV} remains nearly constant from P_1 to P_2. The increase of I_{DC} from P_2 to P_3, when the cloud passing is over, makes I_{COMP} to decrease. Therefore, I_{INV} remains nearly constant from

P_2 to P_3.

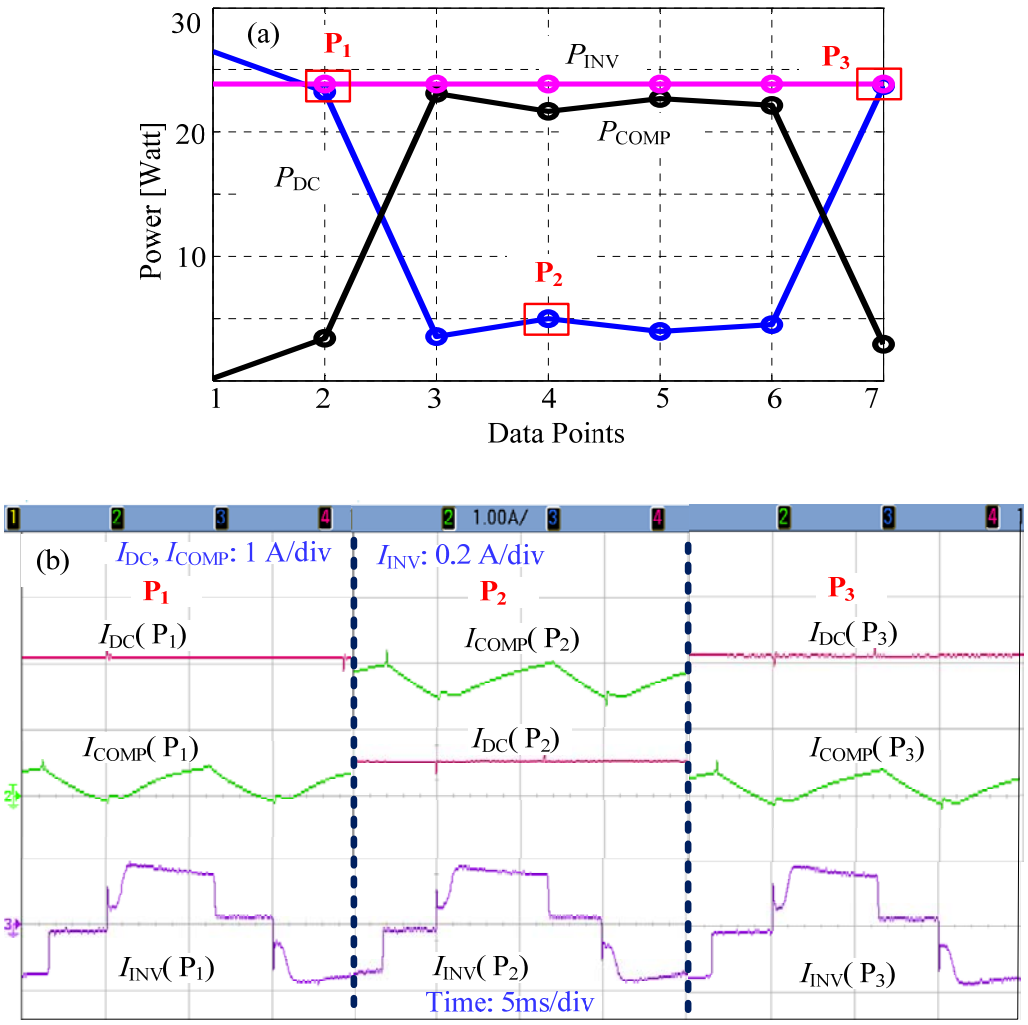

Fig. 7.19. Experimental results (a) Data points for experimental verification. (b) Captured current waveforms for points P_1, P_2 and P_3.

The results from this experiment indicate that the proposed strategy would be able to control the ramp-rate of P_{INV} by appropriately controlling the P_{COMP} support.

7.6 CONCLUSION

This thesis has proposed a new approach for PV inverter ramp-rate control using an integrated energy storage device. Unlike the traditional moving average method, which is biased by the previous values and does not directly control the ramp-rate at a desired level, the proposed method can limit the ramp-rate within a desired level. An inverse characteristic of the desired ramp-rate with the PV panel output ramp-rate is proposed to improve the fluctuation mitigation performance during the ramping event. Once the

ramping event is over, the desired ramp-rate is switched to a droop characteristic with SoC so that the available capacity is taken into account while controlling the ramp-rate. Simulation results show that the mitigation of the PV output fluctuation achieved by the proposed ramp-rate control strategy is comparable to those obtained using the moving average method, while not using the energy storage all the time. Also, during very high ramp-rate events, the proposed strategy can provide tighter control of the ramp-rate due to the inverse characteristic. The mitigation of voltage fluctuation in weak networks caused by PV output fluctuation using the proposed method is also demonstrated. The validity of the proposed strategy has been verified in a dynamic environment using a dynamic model of the PV-storage integrated system developed in this chapter. The results from a laboratory experiment using a PV inverter, a battery storage system, and an electronic load demonstrates that the proposed approach is able to control the PV inverter ramp-rate by providing appropriate support from the storage device.

APPENDIX

TABLE 7-I

SIMULATION PARAMETERS OF THE PROPOSED CONTROL STRATEGY

Parameter	Value
$\|RR_{lim}\|$, γ	5 W/sec, 0.005
SoC_{ref}, SoC_{LB}, SoC_{UB}, DB_{SoC}	70%, 2.5%, 5%, 2.5%
$MARR_{min}$, $MARR_{max}$, DB_{MARR}	MARRρ, 5 W/sec, (5-$MARR_{min}$)
SoC_{max}, DoD_{max}	100%, 40%

TABLE 7-II

PARAMETERS USED FOR DYNAMIC SIMULATION

Parameter	Value
T_{inv}, T_{sto}, T_{meas}	20 mS, 5 mS, 3 mS
K_P, K_I	2.30, 470

REFERENCES

[1] W. Jewell and R. Ramakumar, "The Effects of Moving Clouds on Electric Utilities with Dispersed Photovoltaic Generation," *IEEE Transactions on Energy Conversion,* vol. EC-2, pp. 570-576, 1987.

[2] E. C. Kern, E. M. Gulachenski, and G. A. Kern, "Cloud effects on distributed photovoltaic generation: slow transients at the Gardner, Massachusetts photovoltaic experiment," *IEEE Transactions on Energy Conversion,* vol. 4, pp. 184-190, 1989.

[3] C. Trueblood, S. Coley, T. Key, L. Rogers, A. Ellis, C. Hansen, and E. Philpot, "PV Measures Up for Fleet Duty : Data from a Tennessee Plant Are Used to Illustrate Metrics That Characterize Plant Performance," *IEEE Power and Energy Magazine,* vol. 11, pp. 33-44, 2013.

[4] J. Johnson, B. Schenkman, A. Ellis, J. Quiroz, and C. Lenox.Sandia National Laboratories. *Initial Operating Experience of the La Ola 1.2-MW Photovoltaic System* [Online]. Available: http://energy.sandia.gov/wp/wp-content/gallery/uploads/SAND2011-8848_Lanai_DOE_Report_FINAL.pdf

[5] NREL. *1-Second Global Horizontal Irradiance Oahu, Hawaii* [Online]. Available: http://www.nrel.gov/midc/oahu_archive/

[6] S. Abdollahy, A. Mammoli, F. Cheng, A. Ellis, and J. Johnson, "Distributed compensation of a large intermittent energy resource in a distribution feeder," in *IEEE PES Innovative Smart Grid Technologies*, Washington, DC, USA, 24-27 Feb. 2013, pp. 1-6.

[7] S. Sayeef, S. Heslop, D. Cornforth, T. Moore, S. Percy, J. K. Ward, A. Berry, and D. Rowe.CSIRO. (June 2012). *Solar intermittency: Australia's clean energy challenge. Characterising the effect of high penetration solar intermittency on Australian electricity networks.* [Online]. Available: https://publications.csiro.au/rpr/download?pid=csiro:EP121914&dsid=DS1

[8] H. Sugihara, K. Yokoyama, O. Saeki, K. Tsuji, and T. Funaki, "Economic and Efficient Voltage Management Using Customer-Owned Energy Storage Systems in a Distribution Network With High Penetration of Photovoltaic Systems," *IEEE Transactions on Power Systems,* vol. 28, pp. 102-111, 2013.

[9] N. Kakimoto, H. Satoh, S. Takayama, and K. Nakamura, "Ramp-Rate Control of Photovoltaic Generator With Electric Double-Layer Capacitor," *IEEE Transactions on Energy Conversion* vol. 24, pp. 465-473, 2009.

[10] T. Kinjo, T. Senjyu, N. Urasaki, and H. Fujita, "Output levelling of renewable energy by electric double-layer capacitor applied for energy storage system," *IEEE Transactions on Energy Conversion,* vol. 21, pp. 221-227, 2006.

[11] T. Monai, I. Takano, H. Nishikawa, and Y. Sawada, "A collaborative operation method between new energy-type dispersed power supply and EDLC," *IEEE Transactions on Energy Conversion,* vol. 19, pp. 590-598, 2004.

[12] K. S. Tam, P. Kumar, and M. Foreman, "Enhancing the utilization of photovoltaic power generation by superconductive magnetic energy storage," *IEEE Transactions on Energy Conversion,* vol. 4, pp. 314-321, 1989.

[13] S. Rahman and K. S. Tam, "A feasibility study of photovoltaic-fuel cell hybrid energy system," *IEEE Transactions on Energy Conversion,* vol. 3, pp. 50-55, 1988.

[14] T. D. Hund, S. Gonzalez, and K. Barrett, "Grid-Tied PV system energy smoothing," in *Photovoltaic Specialists Conference (PVSC)*, Honolulu, HI, USA, 20-25 Jun., 2010, pp. 2762-2766.

[15] J. Traube, L. Fenglong, D. Maksimovic, J. Mossoba, M. Kromer, P. Faill, S. Katz, B. Borowy, S. Nichols, and L. Casey, "Mitigation of Solar Irradiance Intermittency in Photovoltaic Power Systems With Integrated Electric-Vehicle Charging Functionality," *IEEE Transactions on Power Electronics,* vol. 28, pp. 3058-3067, 2013.

[16] S. G. Tesfahunegn, Ø. Ulleberg, P. J. Vie, and T. M. Undeland, "PV Fluctuation Balancing Using Hydrogen Storage–a Smoothing Method for Integration of PV Generation into the Utility Grid," *Energy Procedia,* vol. 12, pp. 1015-1022, 2011.

[17] L. Xiangjun, H. Dong, and L. Xiaokang, "Battery Energy Storage Station (BESS)-Based Smoothing Control of Photovoltaic (PV) and Wind Power Generation Fluctuations," *IEEE Transactions on Sustainable Energy,* vol. 4, pp. 464-473, 2013.

[18] C. J. Coe, A. N. Hurst, M. I. Hardin, M. C. Such, and R. T. Jennings.(Nov. 2011, US Patent 20110273129). *Managing Renewable Power Generation* [Online]. Available: https://docs.google.com/viewer?url=www.google.com/patents/US20110273129.pdf

[19] C. A. Hill, M. C. Such, C. Dongmei, J. Gonzalez, and W. M. Grady, "Battery Energy Storage for Enabling Integration of Distributed Solar Power Generation," *IEEE Transactions on Smart Grid,* vol. 3, pp. 850-857, 2012.

[20] A. Ellis, D. Schoenwald, J. Hawkins, S. Willard, and B. Arellano, "PV output smoothing with energy storage," in *Photovoltaic Specialists Conference (PVSC)*, Austin, TX, USA., 3-8 Jun., 2012, pp. 1523-1528.

[21] M. J. E. Alam, K. M. Muttaqi, and D. Sutanto, "Mitigation of Rooftop Solar PV Impacts and Evening Peak Support by Managing Available Capacity of Distributed Energy Storage Systems," *Accepted for a future issue of IEEE Transactions on Power Systems*.

[22] H. Chen, T. N. Cong, W. Yang, C. Tan, Y. Li, and Y. Ding, "Progress in electrical energy storage system: A critical review," *Progress in Natural Science,* vol. 19, pp. 291-312, 2009.

[23] B. Espinar and D. Mayer.International Energy Agency. July 2011. *The role of energy storage for mini-grid stabilization* [Online]. Available: http://www.iea-pvps-task11.org/HTMLobj-187/Act_24_Final.pdf

[24] Mathworks. (Oct. 2013). *PID tuning algorithm for linear plant model* [Online]. Available: http://www.mathworks.com.au/help/control/ref/pidtune.html

Chapter 8

MITIGATION OF NEUTRAL CURRENT AND NEUTRAL POTENTIAL RISE IN 4-WIRE MULTIGROUNDED LV NETWORKS UNDER UNBALANCED ALLOCATION OF ROOFTOP SOLAR PV USING ENERGY STORAGE

ABSTRACT

An unbalanced allocation of 1-phase rooftop photovoltaic (PV) units have the potential to exacerbate the existing neutral current and neutral potential in low voltage (LV) 4-wire multigrounded distribution networks. In spite of balanced loads, a high PV unbalance can create considerable neutral current and neutral potential rise. Traditional mitigation strategies have certain limitations to mitigate the combined effect of load and PV unbalance. To address this unbalance effect, energy storage is applied as a potential strategy against the neutral current and neutral potential under a high penetration of unbalanced rooftop PV allocation. Two novel mitigation approaches are proposed: one is using distributed storage devices connected to each PV unit, suitable for use in an existing network, and the other is a Community Energy Storage (CES) system connected to all the PV systems installed in an LV feeder, suitable for new networks or future grids. A power balancing algorithm is developed to perform the balancing operation while minimizing power drawn from the energy storage. A charge/discharge control strategy is developed that will continuously balance and dynamically adjust the power exchange with the grid in a real time and mitigate the neutral current and neutral potential rise. An Australian LV distribution system is used to verify the proposed approach and results are presented.

8.1 INTRODUCTION

Neutral current flow in low voltage (LV) 4-wire multigrounded distribution networks is a known problem among distribution system research community and protection engineers. The fundamental frequency component of the neutral current is mainly produced by load unbalance [1] and unbalanced impedances of the network. The unbalanced phase currents do not sum up to *zero*, and the resultant neutral current flows through the neutral conductor and neutral grounding resistances causing health and safety concerns. Besides the fundamental component, harmonic components produced by the magnetization of distribution transformers and non-linear loads can increase the neutral current to be even higher than the phase current [1]. In a healthy distribution system, the neutral grounding resistances would be small and therefore, a reasonable amount of neutral current produced by inherent unbalances of a distribution feeder would not increase the neutral potential significantly. However, if the neutral grounding resistances elevate, for example due to bonding with a non-metallic water piping system [2], the neutral potential or Neutral-to-Ground Voltage (NGV) can become significant. A high NGV value can damage sensitive electronic and computing equipment due to the common-mode noise effect [3]. Manufacturers of computing equipment have specified 0.5 V [3] as the limit of common-mode noise; a more stringent limit of 0.1 V is reported in [4]. NGV and other forms of stray voltages are also detrimental for human beings [5] and farm animals [6]. To ensure a safe and reliable operation of distribution networks, neutral current and NGV rise have to be treated with due importance.

In addition to the legacy of load and network unbalance, a high penetration of single phase rooftop solar PV units can worsen the classical neutral current and neutral (or earth) potential. Residential rooftop PV system size is primarily proposed by the customer during the application process. Due to a rapid growth of the number of PV connection requests, distribution utilities in Australia are not always in a position to perform detailed analysis of the impact of each PV connection, especially if the PV system is small (less than 5 kW) [7]. The main attention is given on the transformer size so that the proposed connection does not cause exceeding the limit. Therefore, a direct control to accomplish a balanced allocation of PV systems to different phases of a feeder may not always be practiced. Hence, a highly unbalanced allocation of PV units may appear which can create a large neutral current and hence, the NGV can rise to

exceed the acceptable limit.

Several methods for the mitigation of neutral current and neutral potential rise have been reported in the literature [6, 8-11]. The balancing of loads [8-9, 11] is a traditional mitigation method used for the reduction of neutral current produced by the load unbalance, although in practice it is very difficult to have 100% load balance [11]. Other forms of traditional mitigation techniques, such as re-sizing of neutral conductor [8, 11], improving grounding system [8, 11] or installation of equipotential planes [6, 8, 10], may need significant additional material and can increase installation costs. Further, the variability of PV generation would make it difficult to balance the combined effect of load and PV unbalance using the traditional mitigation techniques that are mainly of "static" type, and does not change with the variation of PV output. Therefore, new mitigation strategies need to be developed to balance out the combined unbalance produced by rooftop solar PV units and load demands.

Energy storage has been used in [12] to mitigate voltage unbalance in LV networks. In a previous work [13], the authors have explored the application of distributed energy storage devices integrated with rooftop PV systems for the mitigation of neutral current and NGV problems. However, the detailed method for charging/discharging control was not shown in [12]. The concept of Community Energy Storage (CES) system [14] is becoming popular among the utilities [15]. It entails utility deployment of modular energy storage systems where one CES system is connected with multiple customers in a feeder to serve as a back-up power source, and also for different ancillary support including the buffering of customers' PV/wind energy and time shifting of energy for PEV charging [15]. With an appropriate control strategy, the CES system can also be used for mitigating neutral current and neutral potential rise problems.

This thesis proposes the application of energy storage devices for mitigation of neutral current and neutral potential rise in LV distribution networks under an unbalanced allocation of 1-phase PV resources. At first, the shortcomings of the traditional mitigation strategies in providing effective solutions for neutral current and neutral potential rise caused by PV units will be discussed. Considering the limitations of the traditional strategies, two new solution approaches are developed in this thesis: one is the distributed energy storage based mitigation strategy for existing distribution networks and the other is the CES based solution approach suitable for new networks or

future grids. The main contributions of this thesis are to develop an algorithm to minimise the power consumption/delivery by the energy storage while mitigating the neutral current and NGV rise problems, and to develop a charging/discharging strategy using the proposed power balancing algorithm to provide a dynamic mitigation effect under variable load and PV unbalance. The proposed approach will be analysed for their effectiveness in mitigating the neutral current and neutral potential problems in the context of Australian LV distribution systems.

8.2 NEUTRAL CURRENT AND NEUTRAL POTENTIAL CREATED BY UNBALANCED ALLOCATION OF ROOFTOP SOLAR PV UNITS

A three-phase 4-wire multigrounded LV feeder containing PV integrated households is considered in Fig. 8.1. The neutral current produced at any given bus can be obtained from the expression below.

$$\begin{aligned} I_{\mathrm{N}}^{n} &= -\left(I_{\mathrm{net}}^{a} + I_{\mathrm{net}}^{b} + I_{\mathrm{net}}^{c}\right) \\ I_{\mathrm{net}}^{p} &= \frac{\left(P_{\mathrm{L}}^{p} - P_{\mathrm{PV}}^{p}\right) - j\left(Q_{\mathrm{L}}^{p} - Q_{\mathrm{PV}}^{p}\right)}{\left(V_{\mathrm{re}}^{p} - V_{\mathrm{re}}^{n}\right) - j\left(V_{\mathrm{im}}^{p} - V_{\mathrm{im}}^{n}\right)}, p \in \{a,b,c\} \end{aligned} \tag{8.1}$$

where, I_{N}^{n} is the neutral current at the given bus; $I_{\mathrm{net}}^{a}, I_{\mathrm{net}}^{b}$, and I_{net}^{c} are the net currents in phase *a*, *b* and *c*; P_{L}, P_{PV} are the active load and active power of the PV inverter at the respective phases; Q_{L}, Q_{PV} are the reactive power of the load, and reactive power of the PV inverter at the respective phases; V_{re} and V_{im} are the real and imaginary components of the respective phase and neutral voltages.

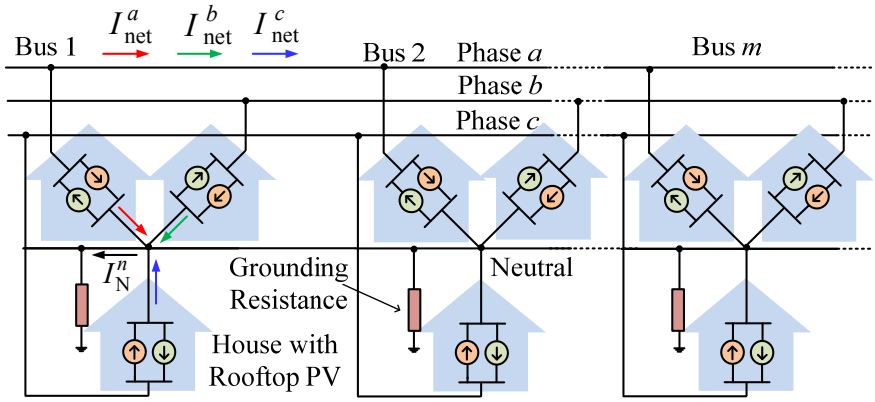

Fig. 8.1. Neutral current in a 4-wire multigrounded LV feeder produced by unbalanced load and PV allocation.

Observing (8.1), it is clear that the neutral current can still be produced even if the loads are fully balanced. To investigate how only PV unbalance can create neutral current and voltage problem, a feeder similar to the one shown in Fig. 8.1 is considered where the loads are perfectly balanced. The outputs of the PV units in phase *a* are varied from *zero* to twice the outputs of the PV units in phase *b* and *c* using a scaling factor λ. The net current vectors I_{net}^{a}, I_{net}^{b}, I_{net}^{c} and the neutral current obtained from the net currents according to (8.1) for such variations of PV output are shown in Fig. 8.2(a) using compass plots. Current Unbalance Factor (CUF) defined using the following expression [16] is used to measure the current unbalance created by PV unbalance.

$$CUF = \frac{\sqrt{|I_{\text{ns}}|^2 + |I_{\text{zs}}|^2}}{|I_{\text{ps}}|} \times 100\%, \begin{bmatrix} I_{\text{ps}} \\ I_{\text{ns}} \\ I_{\text{zs}} \end{bmatrix} = \frac{1}{3}\begin{bmatrix} 1 & a & a^2 \\ 1 & a^2 & a \\ 1 & 1 & 1 \end{bmatrix}, a = e^{j\left(\frac{2\pi}{3}\right)} \tag{8.2}$$

where, I_{ps}, I_{ns} and I_{zs} are positive, negative and *zero* sequence currents, respectively. The left and right hand side compass plots in Fig. 8.2(a) correspond to the cases with λ = 0 and λ = 2, respectively, that represents two extreme cases of current unbalance (CUF: 400% and 70%) and therefore shows high neutral current. The middle compass plot corresponds to the case with λ = 1, where the net currents are balanced and the neutral current is approximately *zero*.

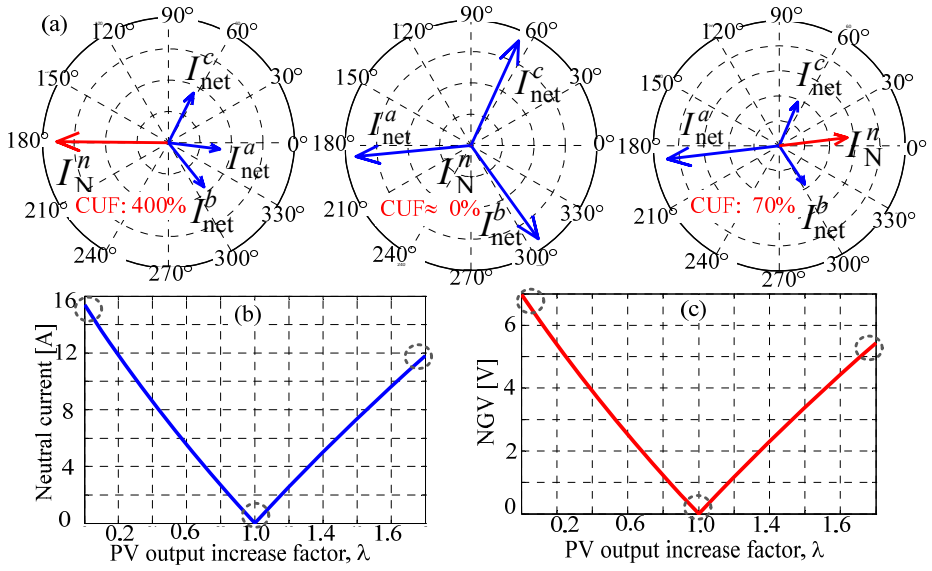

Fig. 8.2. Effect of PV unbalance on neutral current and voltage. (a) The vector diagrams of net currents and neutral current. (b) Neutral current. (c) NGV.

The neutral current and neutral to ground voltage (NGV) profiles with the increase of

λ are shown in Fig. 8.2(b) and (c), respectively. The neutral current and NGV value increases for 0<λ<1 and 1>λ>2, with a theoretically *zero* value when PV outputs are balanced (i.e. λ = 1). The above unbalance condition will worsen if the loads are also unbalanced, as it aggravates further the neutral current and neutral potential rise created by unbalanced allocation of the PV units. Therefore, a dynamically adjustable balancing strategy is needed so that the combined unbalance effect introduced by the unbalanced load and unbalanced solar PV allocations can be reduced in real-time that will mitigate the neutral current and NGV rise in the 4-wire multi-grounded distribution feeders.

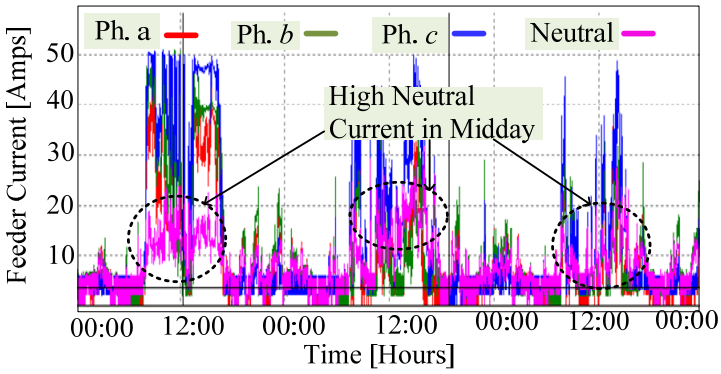

Fig. 8.3. Captured unbalanced phase currents and neutral current profiles in a distribution feeder in Australia.

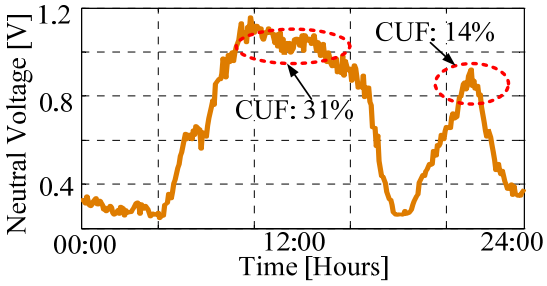

Fig. 8.4. Simulated neutral voltage in an Australian distribution system caused by unbalanced rooftop PV allocation.

Neutral current problem caused by a high penetration of unbalanced rooftop PV would be significant during midday due to high PV output. A typical feeder current profile with rooftop PV, captured by an Australian distribution utility, is shown in Fig. 8.3 where it is observed that the neutral current increases during midday due to a large level of current unbalance introduced by mostly PV systems.

In a previous study [17], authors found that neutral voltage can exceed the acceptable

level of 0.5 V [3] in a feeder with an unbalanced allocation of PV units. The neutral grounding resistances in the feeder were increased because of bonding with non-metallic water reticulation system [2]. A profile of the neutral potential from an LV bus of the system studied in [17] is shown in Fig. 8.4. It is observed that the value of NGV during midday and during evening peak load exceeds the acceptable limit of 0.5 V. The current unbalance factors are also high during those periods as shown in Fig. 8.4.

8.3 LIMITATIONS OF TRADITIONAL TECHNIQUES FOR MITIGATION OF NEUTRAL POTENTIAL RISE FOR PV APPLICATION

Several methods for mitigation of neutral current and neutral potential related issues have been reported in the literature. The traditional techniques for mitigation of neutral current and neutral potential rise can be categorised into four groups [6]: (a) by mitigation of the conditions that cause or worsen NGV, e.g., load balancing, re-sizing of conductors, improvement of neutral grounding etc.; (b) by nullifying the current that produces NGV; (c) by gradient control using equipotential planes; and (d) by electrical isolation. A typical 4-wire multigrounded Australian LV feeder is used to investigate the effectiveness of some common traditional mitigation strategies.

To create a load unbalance, phase *a* and phase *c* loads of the feeder are assumed to be 15% higher and 6% lower than phase *b* loads, respectively. To create a higher level of PV unbalance as compared to load unbalance, the sizes of the PV units in phase *a* and phase *c* are assumed to be around 25% higher and 10% lower, respectively, than the PV units in phase *b*. To analyse the impact of the increase in the neutral grounding resistances, a value of 10 ohm is used for all grounding resistances, based on the discussion presented in [2]. Fig. 8.5 shows the results of applying the traditional mitigation strategies that presents five typical NGV profiles identified by letters (A) to (E). Profile (A), corresponding to NGV value without rooftop PV, shows that the value of NGV during midday is around 0.8 V due to the light load demand and in the evening around 1.2 V due to the heavy load demand. Profile (B) corresponds to the NGV value with rooftop PV, but without any mitigation strategy, where the value of NGV during midday exceeds 1.7 V. Profiles (C) to (E) correspond to the simulation results of the traditional mitigation strategies as described below.

8.3.1 Load Balancing

According to this strategy, loads are allocated in such a manner that the differences among the phase currents are reduced [8-9]. As a result, neutral current and neutral potential is reduced. Practically it is impossible to achieve a 100% load balancing [11]. In the presence of rooftop PV units, the load balancing will involve load and PV balancing, which becomes more complex. A perfect re-distribution of load and PV units among the different phases may not be achievable because this requires modification of existing connections. Also, the load balancing by connection modification is a static type of solution which would not be effective in the presence of variable PV, and also due to a high growth rate of PV penetration. This will change the network condition for which load balancing has been achieved by configuring the load connections.

Considering the physical limitations of load balancing, it is assumed that the rearrangement of load and PV reduces the previous unbalances by 50%. The value of NGV with such re-arrangement reduces to 0.8 V approximately during midday and to 0.6 V approximately in the evening, as shown in profile (C). During midday, the value of NGV with load balancing is still above the limit.

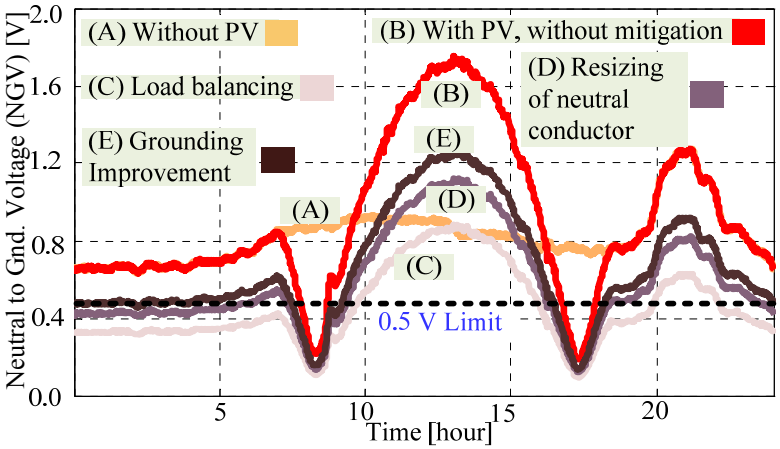

Fig. 8.5. NGV profiles with different traditional mitigation strategies.

8.3.2 Re-sizing of Neutral Conductor

Depending on the current path impedance, the neutral current flow is divided into two parts: one flows through the neutral conductor and the other flows through the neutral grounding resistance. If the neutral conductor is re-sized to have a lower impedance, the current flow through the neutral conductor will be increased and less current will flow

through the grounding resistance. Therefore, the level of NGV will be reduced [8]. However, a resizing of the neutral conductor will involve additional material and construction cost. Also, the rating of the new neutral conductor selected based on a given PV penetration scenario may become inadequate before the expected planning period due to a high growth rate of PV penetration. The neutral wire impedance in the test feeder is reduced by 50% by increasing its size. As a result, the NGV value is reduced to 1.0 V during midday and 0.8 V in the evening, as shown in profile (D). Therefore, during the PV peak generation period, the value of NGV is still over the limit.

8.3.3 Improvement of Grounding System

This method aims to reduce the impedances of the grounding system so that the level of NGV is reduced for the same current flow [8]. Improvement of grounding system would be highly capital intensive, as it would incur additional grounding materials and construction costs over multiple locations in a distribution feeder. The neutral grounding resistance at each node of the test feeder is reduced to a typical value of 1.0 ohm. Even with such a reduced value, the NGV is found to be higher than 1.2 V during midday and higher than 0.8 V during the evening peak, as shown in profile (E).

8.3.4 Isolation Transformer

In this method, a separate transformer is used to isolate the source and load side, by not bonding the primary and secondary side neutrals, so that the primary side NGV cannot be propagated into the secondary side [6, 8, 10-11]. However, this may cause an adverse effect on the protection of the load side of the transformer following lightning strike, system fault or wiring error [8]. The PV system producing a variable current over the day may increase the complexity of the new protection system design. Therefore, a trade-off analysis between the merits and demerits of isolation transformer method needs to be performed prior to implementation.

8.3.5 Equipotential Planes

In this method, a conductive wire mesh is installed over the area where the NGV problems appear and most of the conductive materials in that area are bonded with the mesh, to produce a level surface having the same electrical potential throughout, such

that no potential difference exists on the surface [6, 8, 10]. Though this method does not mitigate the original cause of the neutral current and voltage problems, as long as one is on the surface, the potential of danger is removed [6, 8]. To achieve the benefits of the equipotential plane, a proper installation of the plane is essential, which involves additional grounding materials, wire mesh and new construction costs. Traditionally this method has been used in farms to protect animals from the hazards of the neutral potential rise. However, if this method is chosen for PV integrated households, each of the households in the feeder will have to install this wire mesh. This may not be feasible for each and every PV system owner, especially if the house is already constructed.

8.3.6 Active Suppression by Current Nullifying Device

In this method, an active device is used to inject a current at some point in the neutral grounding system and the current is adjusted to cancel out the NGV [6]. The active current injection device consumes power from the distribution system. It also has the disadvantages of maintenance difficulty and high initial cost. Moreover, due to a high growth rate of PV penetration, control limits and ratings of the active suppression device may need to be changed more frequently than expected, which would increase the cost.

The results from the above investigations indicate that the traditional mitigation techniques may not be adequate for mitigating neutral current and voltage problems in the presence of a high penetration of single phase PV units. To address this, two novel mitigation strategies are developed in this thesis, as presented below.

8.4 PROPOSED DISTRIBUTED ENERGY STORAGE BASED MITIGATION STRATEGY FOR AN EXISTING NETWORK

In this strategy, storage devices are integrated with each of the PV systems installed in a feeder, as shown in Fig. 8.6. Each of the households of a given phase in a given bus is connected to the households in the other two phases in the same bus through communication link. For balancing operation, it is intended to charge/discharge the storage devices such that the power exchange with grid (reverse power flow during high PV period or forward power flow during low or no PV period) becomes equal for all the three phases at each bus in the LV feeder.

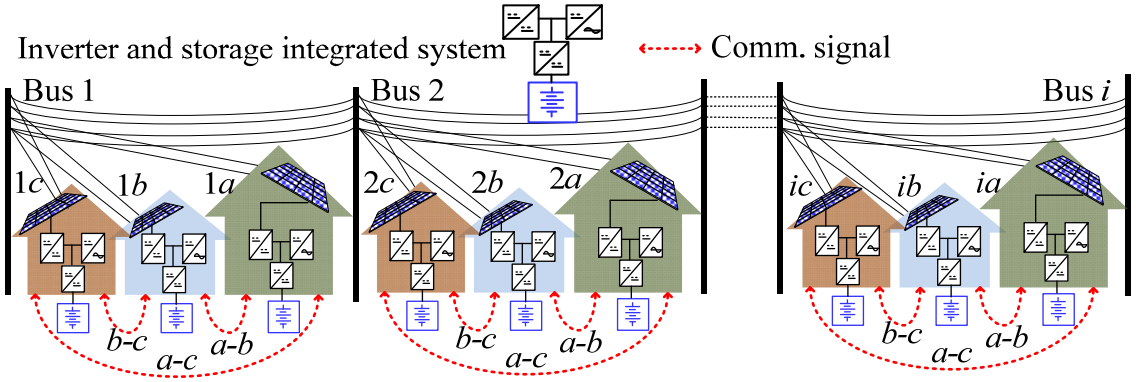

Fig. 8.6. Schematic diagram of the proposed distributed storage based strategy for mitigation of NC and NGV problems.

A method to determine the amount of power to be consumed or delivered by each of the storage device for the balancing operation is developed below.

8.4.1 Development of a Power Balancing Algorithm based on Charging/Discharging of Distributed Storage

Assume that the power to be exchanged with the grid (P_{grid}) at each of the phases at the i-th bus will have to be made equal to a reference power $P_{\text{grid}}^{\text{ref-}i}$ .The amount of power to be consumed/delivered by the storage device at each of the phases for this purpose can be obtained as given below.

$$\begin{bmatrix} P_{\text{ES}}^{ia} \\ P_{\text{ES}}^{ib} \\ P_{\text{ES}}^{ic} \end{bmatrix} = P_{\text{grid}}^{\text{ref-}i} - \begin{bmatrix} P_{\text{grid}}^{ia} \\ P_{\text{grid}}^{ib} \\ P_{\text{grid}}^{ic} \end{bmatrix} = P_{\text{grid}}^{\text{ref-}i} - \begin{bmatrix} P_{\text{L}}^{ia} - P_{\text{PV}}^{ia} \\ P_{\text{L}}^{ib} - P_{\text{PV}}^{ib} \\ P_{\text{L}}^{ic} - P_{\text{PV}}^{ic} \end{bmatrix} \tag{8.3}$$

where, P_{ES} is the power absorbed/delivered by the energy storage, P_{L} is the load active power, P_{PV} is the inverter active power, all for the respective phases.

If all the phases experience reverse power flow (-ve P_{grid}, during high PV period), then the balancing is performed by the charging operation, as shown in Fig. 8.7(a), whereas, balancing is performed by the discharging operation if power is drawn from the grid at all the phases (+ve P_{grid}, during low or no PV period), as shown in Fig. 8.7(b). It is expected to minimise the power used for balancing operation so that less amount of storage capacity is required. The value of $P_{\text{grid}}^{\text{ref-}i}$ that minimises the total amount of power usage from the three distributed storage devices in a bus can be obtained by solving a constrained minimization problem as formulated below.

$$\text{minimise}: \sum_{p\in\{a,b,c\}} \left|P_{\text{ES}}^{ip}\right|, \text{s.t.}: \tag{8.4a}$$

$$\begin{bmatrix} 0 \\ 0 \\ 0 \end{bmatrix} = -\begin{bmatrix} 1 & -1 & 0 \\ 0 & 1 & -1 \\ -1 & 0 & 1 \end{bmatrix}\begin{bmatrix} P_{\text{ES}}^{ia} \\ P_{\text{ES}}^{ib} \\ P_{\text{ES}}^{ic} \end{bmatrix} + \begin{bmatrix} P_{\text{grid}}^{ia} - P_{\text{grid}}^{ib} \\ P_{\text{grid}}^{ib} - P_{\text{grid}}^{ic} \\ P_{\text{grid}}^{ic} - P_{\text{grid}}^{ia} \end{bmatrix} \tag{8.4b}$$

$$\left(P_{\text{ES}}^{ia} \times P_{\text{ES}}^{ib}\right) \geq 0,\ \left(P_{\text{ES}}^{ib} \times P_{\text{ES}}^{ic}\right) \geq 0,\ \left(P_{\text{ES}}^{ic} \times P_{\text{ES}}^{ia}\right) \geq 0 \tag{8.4c}$$

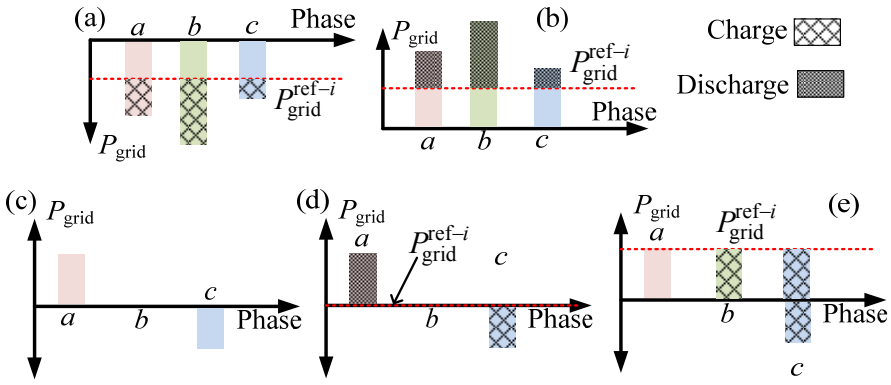

Fig. 8.7. Grid power exchange scenarios (a) P_{grid} at all phases <0. (b) P_{grid} at all phases >0. (c) Mixed type of P_{grid}. (d) Balancing by charging and discharging. (e) Balancing by only charging.

The equality constraint in (8.4b) ensures that an equal power exchange with the grid at all the phases (power balancing) and the inequality constraints in (8.4c) ensures the correct decision is made on the storage operation (charging or discharging). According to the solutions obtained from (8.4), if all the phases experience the same type of power exchange with the grid (either reverse power or forward power), the total power for the balancing operation at a given *i*-th bus can be minimised if the reference power exchange with the grid is obtained using (8.5).

$$P_{\text{grid}}^{\text{ref-}i} = min\left(\left|P_{\text{grid}}^{ia}\right|, \left|P_{\text{grid}}^{ib}\right|, \left|P_{\text{grid}}^{ic}\right|\right) \tag{8.5}$$

However, depending on load demand and PV generation, a bus may experience a mixed type of P_{grid}. For example in Fig. 8.7(c), phase *a, b* and *c* have +ve, 0 and -ve P_{grid}, respectively. For this case, balancing can be performed using a combination of charging and discharging [Fig. 8.7(d)] operation, or using either of those [Fig. 8.7(e) shows charging only]. For these cases (8.4) needs to be solved to select the option that ensures the minimum power consumption or delivery by the battery storage devices.

Once P_{ES} is obtained using (8.3)-(8.5), the charging/discharging rate of the battery at the phase 'p' of the i-the bus can be obtained using the expression below.

$$I_{\mathrm{ES}}^{ip} = \frac{P_{\mathrm{ES}}^{ip}}{V_{\mathrm{ES}}^{ip}} = \frac{P_{\mathrm{ES}}^{ip}}{f\left(\mathrm{SoC}_{\mathrm{ES}}^{ip}, C_{\mathrm{ES}}^{ip}, \mathbf{p}_{\mathrm{ES}}^{ip}\right)} \tag{8.6}$$

where, I_{ES}^{ip} is the charging rate of the energy storage, $p \in \{a,b,c\}$, V_{ES}^{ip} is the battery voltage which is a function of the battery $\mathrm{SoC}_{\mathrm{ES}}^{ip}$, C_{ES}^{ip} is the capacity of the battery, and $\mathbf{p}_{\mathrm{ES}}^{ip}$ is a set of battery modelling parameters. The details of the battery modelling approach used in this thesis are provided in a previous work [18] of the authors.

8.4.2 A Control Strategy for Charging/Discharge Operation

The control strategy for charging/discharging of the distributed storage connected at a given i-th bus and p-th phase is shown in Fig. 8.8 using a flowchart for a given k-th time instant. The amount of the grid power exchange (P_{grid}) at the p-th phase (from measurement) and the other two phases is continuously monitored (through communication). If P_{grid} at all the phases are less than *zero*, this indicates a reverse power flow (during high PV period) at the phases and therefore power balancing is performed by charging operation. The appropriate charging rates for the balancing operation are obtained using (8.6), based on the values obtained from (8.3) and (8.5). Then the charging operation is performed if the present SoC is less than the maximum allowable state of charge of the battery ($\mathrm{SoC}_{\mathrm{max}}$). If P_{grid} at all the phases are higher than *zero*, this indicates a forward power flow (during low or no PV period) at the phases and therefore power balancing is performed by discharging operation. Discharging rates for the balancing operation are obtained using (8.3), (8.5) and (8.6), and the discharge operation is performed if the present SoC is higher than the maximum depth of discharge of the battery ($\mathrm{DoD}_{\mathrm{max}}$). If P_{grid} at the phases have forward and reverse power flow, then (8.4) is solved to find the total power for charging and discharging options. Then the balancing operation is performed by the option that requires the minimum amount of total power.

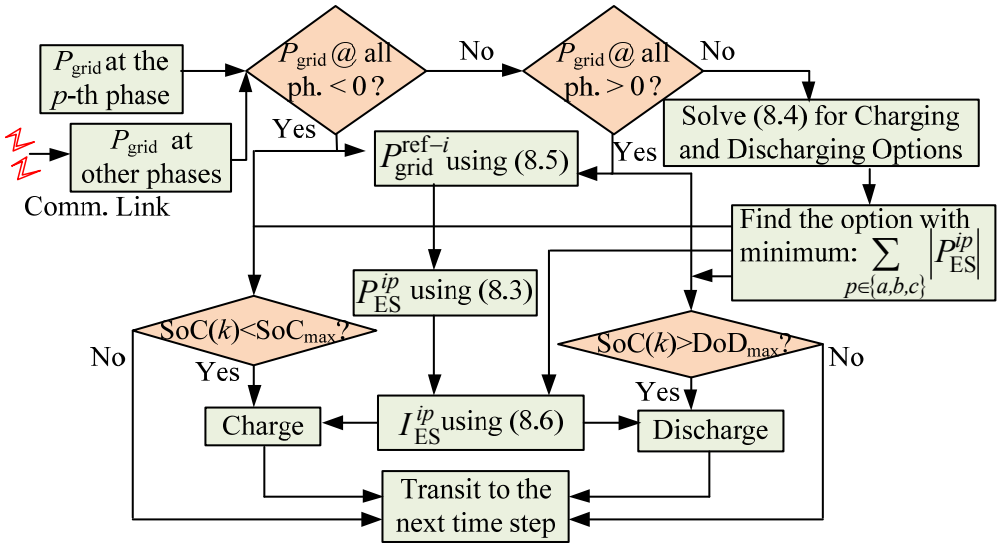

Fig. 8.8. The balancing control strategy with distributed storage.

8.5 PROPOSED COMMUNITY ENERGY STORAGE BASED MITIGATION STRATEGY FOR FUTURE NETWORKS

To avoid the issues of using distributed storage devices installed at the customer premises to solve neutral current/voltage problem, which is mainly a utility concern, utility installed Community Energy Storage (CES) system is proposed as another potential mitigation strategy. According to this strategy, each rooftop PV system installed in the same feeder will be connected to a CES system dedicated to serve the customers at the whole LV feeder, as shown in Fig. 8.9.

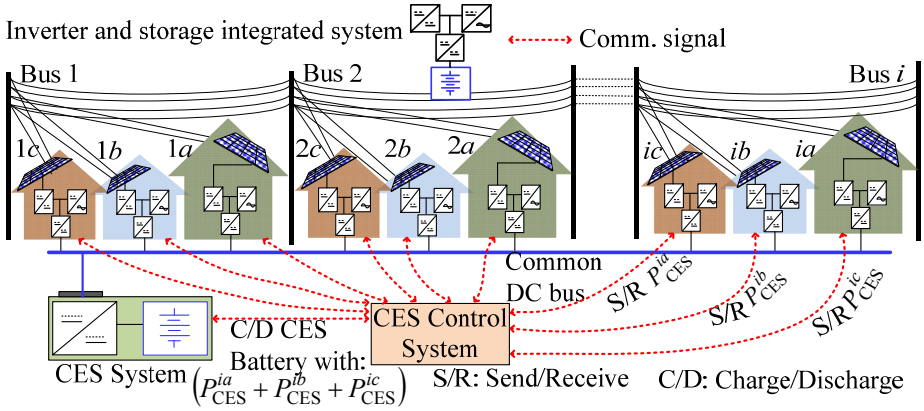

Fig. 8.9. Schematic diagram of the proposed CES system based strategy for mitigation of neutral current and NGV problems.

The power connection between the CES and the PV system will be through a common DC bus connected to the bi-directional DC/DC converter of the PV system. DC distribution grids are being proposed in the literature [19] where such DC bus will

become available.The CES control system will collect measurement signals such as load, PV generation etc. from all of the PV connection points and will determine the amount of power to be absorbed/delivered by the CES system from/to each of the PV systems.

Using a power balancing algorithm (described later), the control system determines the power to be absorbed from the individual households. Then commands are issued to the bi-directional DC/DC converters of the PV systems at phase *a*, *b* and *c* to send power $P_{\mathrm{CES}}^{ia}, P_{\mathrm{CES}}^{ib}, P_{\mathrm{CES}}^{ic}$, respectively, to the CES system. At the same time, a command is issued to the CES system to charge the CES battery with a power equal to $\left(P_{\mathrm{CES}}^{ia} + P_{\mathrm{CES}}^{ib} + P_{\mathrm{CES}}^{ic}\right)$. In addition to the communication links, this strategy will also need a certain level of control access to operate the customer PV systems to send/receive power to/from the CES battery. With an advanced level deployment of smart grid technologies and with arrangements between the customers and the utility, this type of strategy can be adopted in new or future distribution grids.

The amount of power to be consumed or delivered at each of the phases of a given *i*-th bus for balancing operation can be obtained as given below.

$$\begin{bmatrix} P_{\mathrm{CES}}^{ia} \\ P_{\mathrm{CES}}^{ib} \\ P_{\mathrm{CES}}^{ic} \end{bmatrix} = P_{\mathrm{grid}}^{\text{ref-}i} - \begin{bmatrix} P_{\mathrm{grid}}^{ia} \\ P_{\mathrm{grid}}^{ib} \\ P_{\mathrm{grid}}^{ic} \end{bmatrix}, P_{\mathrm{grid}}^{\text{ref-}i} - \begin{bmatrix} \left(P_{\mathrm{L}}^{ia} + P_{\mathrm{B}}^{ia}\right) - P_{\mathrm{PV}}^{ia} \\ \left(P_{\mathrm{L}}^{ib} + P_{\mathrm{B}}^{ib}\right) - P_{\mathrm{PV}}^{ib} \\ \left(P_{\mathrm{L}}^{ic} + P_{\mathrm{B}}^{ic}\right) - P_{\mathrm{PV}}^{ic} \end{bmatrix} \tag{8.7}$$

In (8.7), $P_{\mathrm{grid}}^{\mathrm{ref}-i}$ is the reference power exchange for bus *i*, P_{CES} is the power absorbed by the CES, P_{B} is the power consumed or delivered by the local energy storage device (if any), all for the respective phases.

The reference power exchange with the grid for each of the buses to minimise the total amount of balancing power to be absorbed/delivered by the CES system from the whole feeder can be obtained from a constrained minimization problem combining all the buses, as given below.

$$\text{minimise}: \left(\sum_{i=1}^{m} \sum_{p \in \{a,b,c\}} P_{\mathrm{CES}}^{ip} \right), \text{s.t.}: \tag{8.8a}$$

$$\begin{bmatrix}\mathbf{0}\\ \mathbf{0}\\ \vdots\\ \mathbf{0}\end{bmatrix}=-\begin{bmatrix}\mathbf{A}_{\text{CES}}^{1} & \mathbf{0} & \cdots & \mathbf{0}\\ \mathbf{0} & \mathbf{A}_{\text{CES}}^{2} & \cdots & \mathbf{0}\\ \vdots & \vdots & \ddots & \vdots\\ \mathbf{0} & \mathbf{0} & \cdots & \mathbf{A}_{\text{CES}}^{m}\end{bmatrix}+\begin{bmatrix}\mathbf{P}_{\text{grid}}^{1}\\ \mathbf{P}_{\text{grid}}^{2}\\ \vdots\\ \mathbf{P}_{\text{grid}}^{m}\end{bmatrix} \tag{8.8b}$$

$$\begin{gathered}\left(P_{\text{CES}}^{1a}\times P_{\text{CES}}^{1b}\right)\geq 0,\ \left(P_{\text{CES}}^{1b}\times P_{\text{CES}}^{1c}\right)\geq 0,\ \left(P_{\text{CES}}^{1c}\times P_{\text{CES}}^{1a}\right)\geq 0\\ \left(P_{\text{CES}}^{2a}\times P_{\text{CES}}^{2b}\right)\geq 0,\ \left(P_{\text{CES}}^{2b}\times P_{\text{CES}}^{2c}\right)\geq 0,\ \left(P_{\text{CES}}^{2c}\times P_{\text{CES}}^{2a}\right)\geq 0\\ \vdots\\ \left(P_{\text{CES}}^{ma}\times P_{\text{CES}}^{mb}\right)\geq 0,\ \left(P_{\text{CES}}^{mb}\times P_{\text{CES}}^{mc}\right)\geq 0,\ \left(P_{\text{CES}}^{mc}\times P_{\text{CES}}^{ma}\right)\geq 0\end{gathered} \tag{8.8c}$$

where,

$$\mathbf{A}_{\text{CES}}^{i}=\begin{bmatrix}0 & -1 & 0\\ 0 & 1 & -1\\ -1 & 0 & 1\end{bmatrix},\ \mathbf{P}_{\text{CES}}^{i}=\begin{bmatrix}P_{\text{CES}}^{ia} & P_{\text{CES}}^{ib} & P_{\text{CES}}^{ic}\end{bmatrix}^{T}$$

$$\mathbf{P}_{\text{grid}}^{i}=\left[\left(P_{\text{grid}}^{ia}-P_{\text{grid}}^{ib}\right)\ \ \left(P_{\text{grid}}^{ib}-P_{\text{grid}}^{ic}\right)\ \ \left(P_{\text{grid}}^{ic}-P_{\text{grid}}^{ia}\right)\right]^{T}$$

$$i=1,2,\cdots m$$

According to the values of $\mathbf{P}_{\text{CES}}^{i}$ obtained by solving (8.8), the reference power exchange with grid for a given *i*-th bus $P_{\text{grid}}^{\text{ref}-i}$ can be obtained as given below.

$$P_{\text{grid}}^{\text{ref-}i}=min\left(\left|P_{\text{grid}}^{ia}\right|,\left|P_{\text{grid}}^{ib}\right|,\left|P_{\text{grid}}^{ic}\right|\right) \tag{8.9}$$

With the total amount of power to be consumed or delivered by the CES system dedicated for the whole feeder, the charging/discharging rate (battery current) of the CES battery can be obtained using the expression below.

$$I_{\text{CES}}=\frac{\sum_{i=1}^{m}\sum_{p\in\{a,b,c\}}P_{\text{CES}}^{ip}}{V_{\text{CES}}}=\frac{\sum_{i=1}^{m}\sum_{p\in\{a,b,c\}}P_{\text{CES}}^{ip}}{f(\text{SoC},C_{\text{CES}},\mathbf{p})} \tag{8.10}$$

where, I_{CES} is the charging/discharging rate of the CES, V_{CES} is the CES voltage which is a function of the battery SoC, C_{CES} is the capacity of the CES battery, and **p** is a set of battery modelling parameters.

The control strategy for the charging/discharging of the CES system for the balancing operation is shown in Fig. 8.10. The values of P_{grid} at all the buses are collected through the communication link. Similar to the distributed storage based strategy, the balancing is performed by a charging operation if P_{grid} at all the buses are negative, and similarly balancing is performed by a discharging operation if P_{grid} at all the buses are positive. A

summation operator is used to determine the total power to be absorbed or delivered by the CES battery. Then the charging/discharging operation is performed using the rates determined by (8.10), and with the necessary checks of the SoC limits. For a mixed combination of positive and negative P_{grid}, (8.8) has to be solved for charging and discharging options to select which option uses minimum power. Once the operation requiring the minimum power is determined, the charging/discharging operation is performed in the similar way as described before.

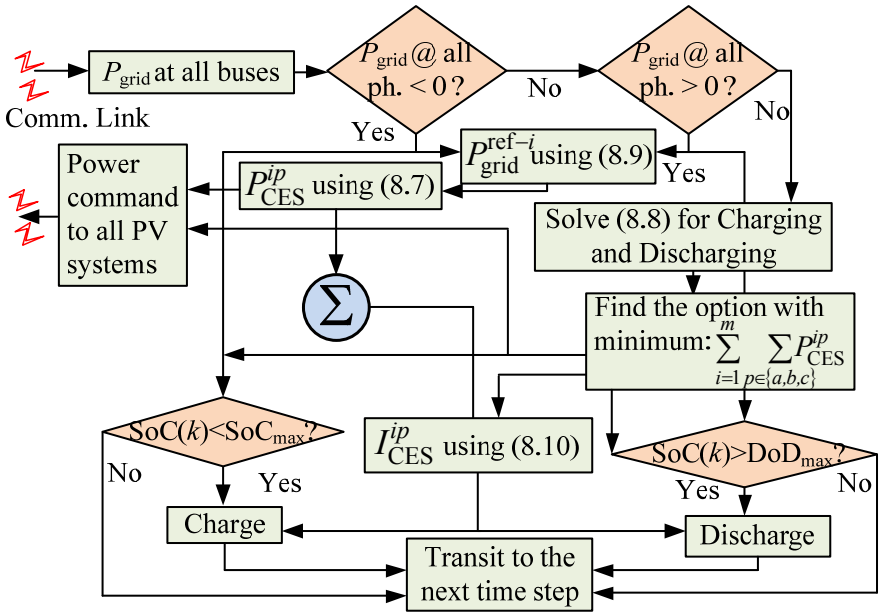

Fig. 8.10. The balancing control strategy with CES.

8.6 APPLICATION EXAMPLES

A typical Australian distribution feeder used in section 8.3 for investigating the traditional mitigation strategies is also used for the verification of the proposed strategies. A detailed description of the test feeder is provided in [18]. For the analysis of distributed storage based strategy, 3 to 8 kWh sealed lead acid battery (a typical Australian size and type for residential or small PV systems) is used depending on the load and PV size at different phases. For the community storage based approach, Li-Ion battery is considered and the size is determined from the total amount of energy used in the whole feeder for the balancing operation.

8.6.1 Distributed Storage Based Mitigation Strategy

The distributed storage devices installed in the test LV feeder is controlled according

to the proposed power balancing algorithm. P_{grid} profiles for the three phases in the substation-end bus of the test feeder and the reference power exchange with the grid determined based on the P_{grid} profiles using (8.3) to (8.5) are shown in Fig. 8.11 (a). During the periods of mixed P_{grid} values (+ve and -ve), as marked using blue circles, the storage devices are controlled using (8.4) as shown in the flowchart in Fig. 8.8. The SoC profile of the storage device in phase *a* of the substation-end bus is shown in Fig. 8.11(b); the DoD_{max} (35%) and SoC_{max} (100%) limits are checked while performing the charging/discharging operation.

The power delivered/absorbed by the distributed storage devices of the substation-end bus of the LV feeder is shown in Fig. 8.12. The shaded areas indicate the energy used in the charging/discharging operation. The time corresponding to the charging/discharging operations are also identified over the 24 hour period in Fig. 8.12. The energy stored during the charging operation over the daytime is discharged during the nighttime. Depending on the amount of stored energy, the period of the discharge operation can be determined for a given load demand profile. If the stored energy is adequate, the balancing support can be continued over the late night to early morning, as shown in Fig. 8.12. However, if the amount of stored energy is not adequate, the balancing support could only be provided during the peak load period, when the neutral current and the NGV problems are most severe due to a high amount of load unbalance.

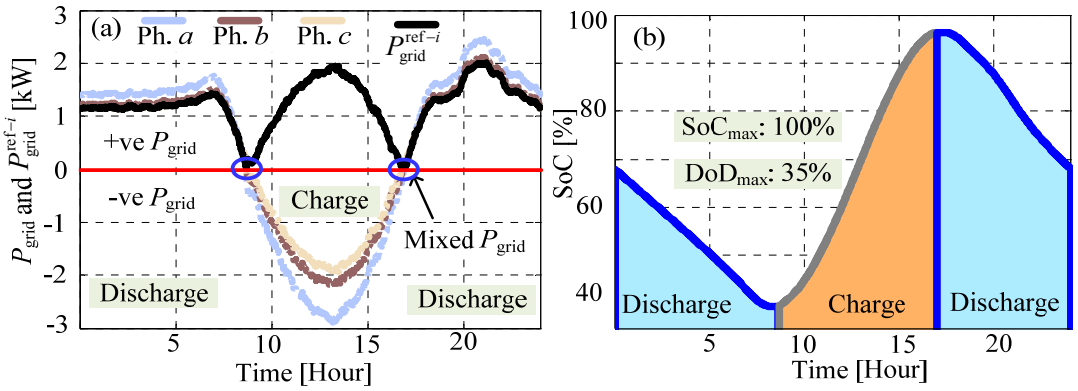

Fig. 8.11. Charge and discharge operation of energy storage. (a) P_{grid} and P_{grid}^{ref-i} profile. (b) SoC profile during charge and discharge operation.

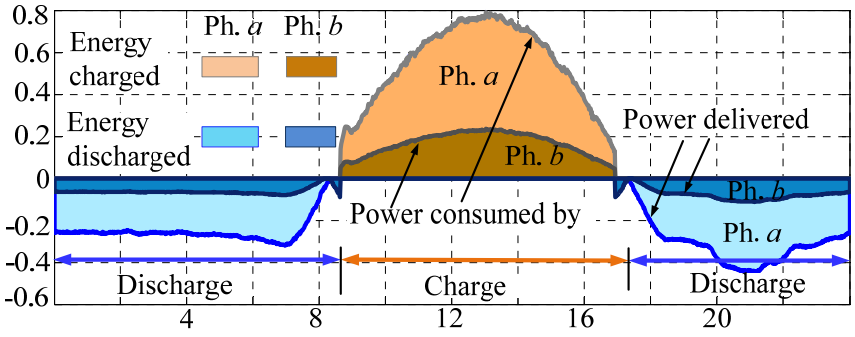

Fig. 8.12. Power absorbed/delivered by distributed storage devices.

Fig. 8.13(a) shows the feeder current flow without any mitigation. It is observed that during midday and also during the evening peak period, the currents in the three phases are unbalanced, with a Current Unbalance Factor (CUF) of 14% and 10%, respectively. These unbalanced phase currents produce a high neutral current. The current unbalance is reduced by the balancing action of the storage units (CUF value reduced to 3.6% and 2.8%, respectively) and, the neutral current is also reduced as shown in Fig. 8.13(b). The reduction of neutral current will mitigate the neutral potential rise problem.

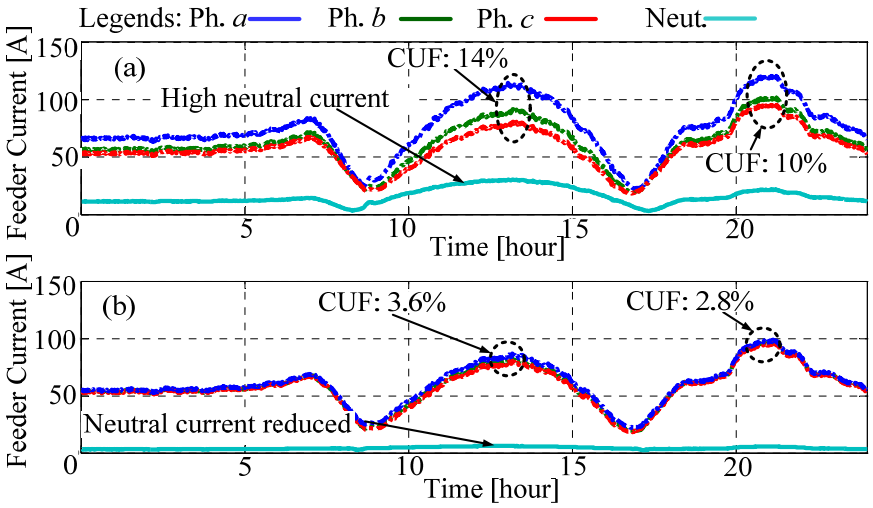

Fig. 8.13. Phase and neutral current flow through the test feeder; (a) without mitigation; (b) with mitigation by distributed storage devices.

The NGV profiles at the substation-bus and at the remote-end bus of the LV feeder without balancing action are compared in Fig. 8.14 with the NGV profiles at the same buses with balancing action. It is observed that with the power balancing operation, the NGV values are reduced significantly during midday PV peak and also during the evening peak load period. For reference, the NGV profiles at the other buses of the LV feeder have also been included in Fig. 8.14. It is found that the proposed mitigation

strategy has reduced the NGV values all over the LV feeder below the limit of 0.5 V.

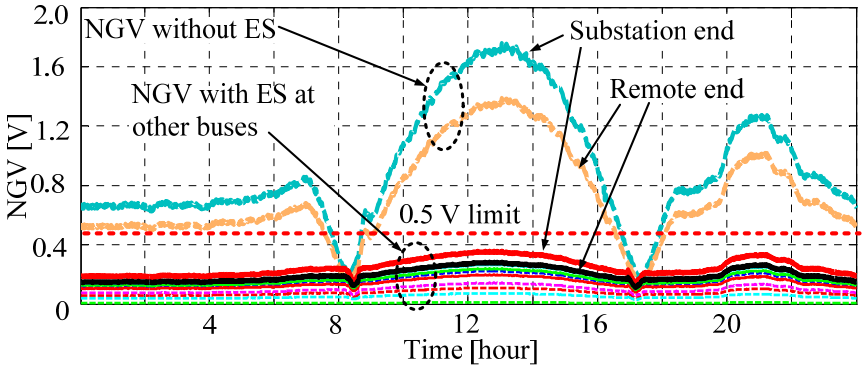

Fig. 8.14. NGV with the mitigation by distributed energy storage.

8.6.2 Community Energy Storage Based Mitigation Strategy

To verify how a CES based approach performs to mitigate the neural current and voltage problems, a CES system is integrated to the test LV feeder. The size of the CES battery is assumed to be 100 kWh based on the energy requirement for the whole feeder calculated using the energy used from the distributed storage devices.

It is observed in Fig. 8.15(a) that the neutral current is reduced by the balancing action of the CES and the corresponding reduction in NGV is shown in Fig. 8.15(b). The total power for balancing operation during the load and PV unbalance over the day, and the total power for the balancing operation during load unbalance over the night are shown in Fig. 8.16. The energy used for charging/discharging operation is also shown in Fig. 8.16 using the shaded regions.

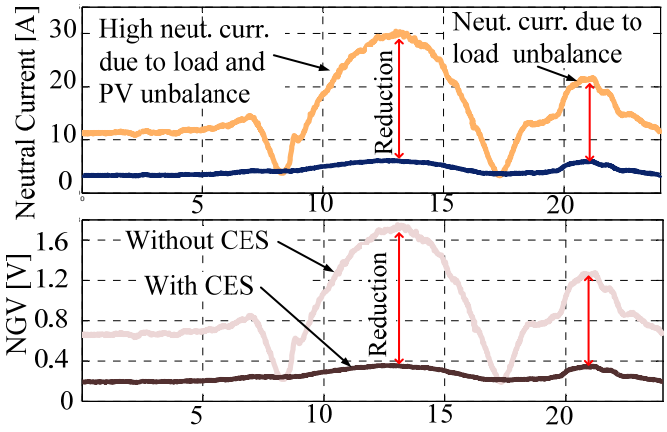

Fig. 8.15. Neutral current and voltage with and without mitigation by the CES system (a) Neutral current (b) Neutral-to-ground voltage.

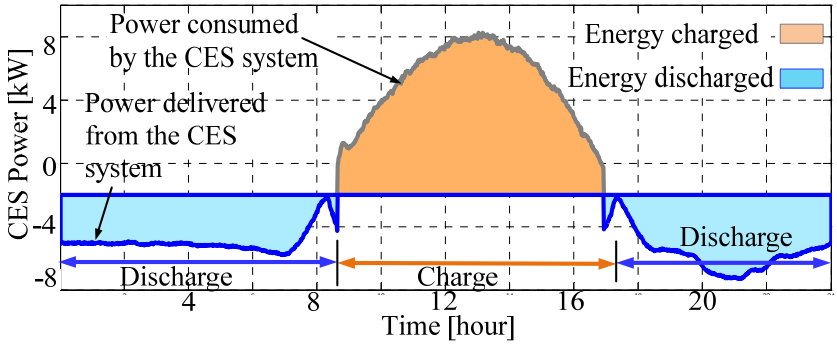

Fig. 8.16. Power absorbed/delivered by the CES system.

Both strategies can be used for the mitigation of the neutral current and neutral potential rise problems, as observed in the analysis results. The distributed storage strategy will need communication among the storage devices connected to the same bus only. But this strategy will use the storage devices installed at the customer premises. Therefore, the issues related to solving a utility concern by using customer installed storage devices need to be resolved through mutual agreement. Even if the storage devices are installed by the utility, access and maintenance would be another issue. For the CES based strategy, power and control/communication connections between the CES and all the PV systems in the feeder will be needed. However, with the prospect of deploying smart grid technologies in the future, such arrangements would be possible. Also, for the CES based strategy, a central storage device will be shared among all the PV systems and therefore, cross-coupling among the phases would be possible for the balancing operation.

The proposed strategies perform the mitigation of the neutral current and NGV problems by storing surplus energy during PV peak period and releasing the stored energy during the evening peak load. In addition to mitigating NGV problem, this operation brings the benefit of partially mitigating voltage rise impact of PV and also supports the evening peak load.

8.7 CONCLUSIONS

This thesis has developed a novel strategy for the mitigation of the neutral current and neutral potential problems in 4-wire multigrounded LV networks under unbalanced allocation of rooftop PV using battery energy storage. Investigations showed that the traditional mitigation strategies are not able to reduce the neutral potential below the

acceptable level, because these strategies do not directly act to mitigate the combined effect of load and PV unbalance, especially with the PV variability. With this background, energy storage system has been proposed to dynamically balance the power exchange with the grid in the three phases so that the neutral current and NGV problems are reduced. Both distributed storage connected to each PV system and a central community storage system for the whole feeder, have been considered as potential strategies. A constrained minimization based power balancing algorithm has been developed to balance the net power exchange with the grid utilizing the minimum amount of storage power. A control strategy has been developed based on the balancing algorithm to control the energy storage devices to provide an appropriate balancing effect under varying load and PV unbalance. Analysis performed using an Australian distribution feeder proves that both strategies are able to reduce the neutral current, which results in the mitigation of the NGV problem.

REFERENCES

[1] J. C. Balda, A. R. Oliva, D. W. McNabb, and R. D. Richardson, "Measurements of neutral currents and voltages on a distribution feeder," *IEEE Transactions on Power Delivery,* vol. 12, pp. 1799-1804, 1997.

[2] J. Werda, J. Chan, and P. Freeman. *Electrical Earthing - Risk Management Strategies for the Water Industry, presented at the 2nd Annual Water Industry Engineers and Operators Conference, Newcastle, NSW, Australia, 8-10 April, 2008.* [Online]. Available: http://www.wioa.org.au/conference_papers/08_nsw/documents/johnwerda.pdf

[3] T. M. Gruzs, "A survey of neutral currents in three-phase computer power systems," *IEEE Transactions on Industry Applications* vol. 26, pp. 719-725, 1990.

[4] Power & Systems Innovation, Inc. *Power Quality - The Basics* [Online]. Available: http://www.psihq.com/iread/pqbasics.htm

[5] D. W. Zipse, "The hazardous multigrounded neutral distribution system and dangerous stray currents," in *IEEE Industry Applications Society 50th Annual Petroleum and Chemical Industry Conference*, Houston, TX, USA, 15-17 Sep., 2003, pp. 23-45.

[6] United States Dept. of Agriculture. *Effects of Electrcal Voltage/Current on Farm Animals* [Online]. Available: http://naldc.nal.usda.gov/download/CAT92970513/PDF

[7] Ergon Energy. (May 2014). *Solar PV system connections: Assessment criteria* [Online]. Available: https://www.ergon.com.au/your-home/connections/renewable-energy-system-connection/assessment-criteria

[8] EPRI. *Elevated Neutral-to-Earth Voltage, Urban Contact Voltage and Other Perceptibility Concerns for Humans and Animals* [Online]. Available: http://strayvoltage.epri.com/index.asp

[9] G. Ahmadi and S. M. Shahrtash, "Neutral to earth voltage reduction methods in three-phase four wire distribution systems," in *International Conference on Electrical and Electronics Engineering*, Bursa, Turkey, 5-8 Nov., 2009, pp. I-134-I-138.

[10] T. C. Surbrook, N. D. Reese, and A. M. Kehrle, "Stray Voltage: Sources and Solutions," *IEEE Transactions on Industry Applications,* vol. IA-22, pp. 210-215, 1986.

[11] B. Jamali, R. Piercy, and P. Dick.Kinectrics Inc. *Stray Voltage Mitigation* [Online]. Available: http://www.ontarioenergyboard.ca/OEB/_Documents/EB-2007-0709/report_Kinectrics_20080530.pdf

[12] K. H. Chua, L. Yun Seng, P. Taylor, S. Morris, and W. Jianhui, "Energy Storage System for Mitigating Voltage Unbalance on Low-Voltage Networks With Photovoltaic Systems," *IEEE Transactions on Power Delivery,* vol. 27, pp. 1783-1790, 2012.

[13] M. J. E. Alam, K. Muttaqi, and D. Sutanto, "Effectiveness of Traditional Mitigation Strategies for Neutral Current and Voltage Problems under High Penetration of Rooftop PV," in *IEEE PES General Meeting*, Vancouver, British Columbia, Canada, Jul. 21 - 25, 2013.

[14] O. C. Onar, M. Starke, G. P. Andrews, and R. Jackson, "Modeling, controls, and applications of community energy storage systems with used EV/PHEV batteries," in *IEEE Transportation Electrification Conference and Expo*, Dearborn, MI, USA, 18-20 Jun 2012, pp. 1-6.

[15] S&C Electric Company. *Community Energy Storage Systems: Meeting the Need for Energy Storage at the Grid's Edge* [Online]. Available: http://www.sandc.com/edocs_pdfs/EDOC_070868.pdf

[16] A. D. Kolagar, P. Hamedani, and A. Shoulaie, "The effects of transformer connection type on voltage and current unbalance propagation," in *Power Electronics and Drive Systems Technology*, Tehran, Iran, 15-16 Feb., 2012, pp. 308-314.

[17] M. J. E. Alam, K. M. Muttaqi, and D. Sutanto, "A Three-Phase Power Flow Approach for Integrated 3-Wire MV and 4-Wire Multigrounded LV Networks With Rooftop Solar PV," *IEEE Transactions on Power Systems,* vol. 28, pp. 1728-1737, 2013.

[18] M. J. E. Alam, K. M. Muttaqi, and D. Sutanto, "Mitigation of Rooftop Solar PV Impacts and Evening Peak Support by Managing Available Capacity of Distributed Energy Storage Systems," *IEEE Transactions on Power Systems,* vol. 28, pp. 3874-3884, November 2013.

[19] S. Grillo, V. Musolino, L. Piegari, E. Tironi, and C. Tornelli, "DC Islands in AC Smart Grids," IEEE Transactions on Power Electronics vol. 29, pp. 89-98, 2014.

Chapter 9

CONCLUSIONS AND DIRECTIONS FOR FUTURE WORKS

This thesis has developed comprehensive and realistic approaches for the analysis of solar photovoltaic (PV) impact on distribution networks, and has proposed new mitigation strategies against the potential impacts. General conclusions of the thesis and directions of future works are provided below.

9.1 CONCLUDING REMARKS

A new approach for modelling and analysis of integrated 3-wire medium voltage (MV) and 4-wire mutigrounded low voltage (LV) networks with solar PV resources has been developed in **Chapter 2**. This approach can provide the PV impact analysis results more accurately than traditional power flow methods where the wiring configurations are not considered in the actual form, and the impact of neutral grounding resistances are not considered. This approach can assess the PV impact on the LV networks where the PV resources are integrated, and also on the upstream medium voltage (MV) networks where the impact can potentially propagate, in a single analysis platform.

A novel and intelligent approach has been developed in **Chapter 3** combining a new time series approximation method (SAX) and data mining techniques for a realistic assessment of solar PV impact using real network data available from smart grid measurements. The developed approach can be used to extract the appropriate portion of the data from a large volume of smart grid measurements to perform solar PV impact assessment with less computational burden. Using the developed intelligent approach, PV impacts, such as, voltage rise, reverse power flow, and voltage fluctuations can be identified in a computationally efficient manner from a large database. The identified data can be used for further detailed analysis.

A variable width sliding window based online approach has been developed in

Chapter 4 for PV impact assessment in LV distribution networks. The developed approach can provide an assessment of distribution network performance using the new performance indices developed in Chapter 4. Using the proposed approach, utilities can update the offline investigation outcomes performed at the planning stage for designing appropriate mitigation actions. The proposed approach can also be applied to perform a dynamic "what-if" analysis online to understand the threats of a potential PV penetration scenario and the effectiveness of a prospective mitigation action.

A versatile reactive power control strategy for solar PV inverters has been developed in **Chapter 5** to provide network support under various conditions associated with PV power generation. The proposed strategy can: (a) mitigate voltage rise during surplus PV generation period by controlling the reactive power consumption using a droop based mode, (b) provide fast reactive power support during cloud passing periods for voltage fluctuation mitigation using a ramp-rate based mode, and, control the reactive power injection for voltage support during low or no PV period using a dynamic VAr compensation mode. A coordination strategy developed in Chapter 5 ensures smooth transition among the control modes while providing reactive power support under intermittent PV power generation.

A new charging/discharging control strategy has been developed in **Chapter 6** for battery energy storage systems to mitigate the PV impact and support the evening peak, while ensuring an effective use of a limited storage capacity. The proposed strategy can control the shape of the battery capacity usage profile by appropriately varying the charging/discharging rates to better match the load and PV generation profiles in comparison to the traditional charging/discharging strategies. Moreover, the strategy can dynamically adjust the charging/discharging rates that ensure an effective use of the limited storage capacity in an event of unstable weather condition, e.g., cloud passing.

A novel strategy for controlling energy storage devices for the mitigation of PV output fluctuation has been developed in **Chapter 7.** The proposed strategy is able to provide an appropriately controlled fluctuation mitigation support during the ramping and post-ramping events of a fluctuation. Unlike the traditional moving average based methods, the proposed strategy does not have a memory effect and therefore, can control the fluctuation mitigation support without being affected by previous PV outputs. The ramp-rate of a PV inverter output can be controlled at a desired level using

this strategy. The voltage fluctuations at the PV system connection point, caused by cloud passing, can also be mitigated using the proposed strategy.

Energy storage based new strategies have been developed in **Chapter 8** to mitigate the neutral current and neutral potential problems arising from a high penetration of PV resources allocated in an unbalanced pattern. Limitations of traditional strategies for mitigating the neutral potential rise problem under variable load and PV generation are discussed. Using the two developed strategies (one is using distributed storage for each PV system in a feeder and the other is utilising a community storage device for all the PV systems in a feeder), the neutral current and neutral potential rise are controlled through power balancing in all phases and mitigated using the minimum amount of battery power.

9.2 DIRECTIONS FOR FUTURE WORKS

General directions for future work are provided below.

- The current-injection based non-linear power flow equations have been formulated in this thesis to apply for a generalised assessment of solar PV impact. Therefore, constraints related to any particular PV impact have been relaxed. The proposed power flow approach can be extended to an "optimal power flow" framework using the constraints related to any specific PV impact to determine the optimal parameters of potential mitigation strategies against the specific impact under consideration.

- This thesis has concentrated on the impacts of distributed solar PV resources integrated in the low voltage (LV) distribution grids and the potential propagation of the impacts into the upstream medium voltage (MV) networks. With the deployment of utility scale large solar PV farms in the MV distribution grids, the nearby LV distribution grids can be affected. Investigations can be performed to study how the impact of large solar PV installations in the MV level can propagate into the LV level. The advantage of the LV/MV integrated analysis of the power flow approach proposed in this thesis can be used for this. However, appropriate models of the large solar PV farms and suitable approaches for assessment of the MV-to-LV impact propagation have to be developed.

- While developing the PV impact mitigation strategies using battery energy storage,

this thesis has mainly concentrated on the limitations of the traditional strategies and made an effort to overcome those using typical sizes of battery in the residential distribution feeders. Methods for determining the appropriate sizes of the energy storage devices to use with the storage based mitigation strategies proposed in this thesis can be developed. Optimisation based approaches could be useful in this regard.

- Although the fundamental idea of the PV inverter ramp-rate control proposed in this thesis is suitable for energy storage devices in general, the detailed control strategies and dynamic models developed are suitable for battery energy storage. The basic ramp-rate control concept in this thesis can be extended for emerging type of energy storage devices, such as, ultra capacitor. The dynamic response of the new energy storage devices need to be modeled and appropriate control variables need to be identified to map the new strategy on the proposed ramp-rate control concept.

- The control strategies developed in this thesis to be used with distributed energy storage devices for PV impact mitigation can be extended to Community Energy Storage systems deployment in the new or future distribution grids. These strategies can also be extended for large battery energy storage systems in a transmission network based deployment to mitigate the intermittency effect and ramp-rate control of large utility scale solar PV farms.

- This thesis has investigated the impact of small distributed PV inverters in the LV networks on the operation of the voltage regulators in the upstream MV networks. With advanced control features (e.g., voltage control), large inverters used in the utility scale solar PV farms in the MV networks can interact with the voltage control devices in medium voltage and the high voltage (HV) sub-transmission networks. Suitable dynamic models capturing the control features of the large scale inverters can be developed to investigate the potential MV-MV and MV-HV interactions and to design appropriate strategies and controllers for mitigation of interactions and improvement of system stability